An Experimental Investigation of Steady and Unsteady Flow Field in an Axial Flow Turbine

M. Zaccaria and B. Lakshminarayana
Pennsylvania State University
University Park, Pennsylvania

ABSTRACT

A better understanding of the turbine flow field is needed in order for turbine designers to increase the efficiency and to improve the performance of turbines. This has been hampered by the fact the present knowledge of the axial flow turbine flow field is not adequate. Several of the major areas that need more investigation include turbine secondary flow, turbine nozzle and rotor wakes and rotor-stator interaction. In view of this need, the three-dimensional steady flow field in a turbine nozzle has been investigated experimentally with an emphasis on the nozzle secondary flow and the nozzle wakes. The two-dimensional unsteady flow field in a turbine rotor has also been investigated experimentally at midspan with an emphasis on the interaction of the nozzle wake with the rotor flow field. The nozzle wake decay upstream and in the rotor passage and the rotor wake decay characteristics were also measured and analyzed.

The nozzle flow was measured at several axial locations. These measurements were carried out using a five hole probe, a two-component laser doppler velocimeter (LDV) and a single sensor hot wire. The static pressure on the nozzle endwall and vane surfaces were also measured. Based on these measurements, the nozzle secondary flow is found to be weak at midchord. At the nozzle exit, two secondary flow loss cores (casing and hub passage vortices) dominate the flow field. The casing passage vortex is larger in area than the hub passage vortex, while the hub passage vortex has a higher maximum loss than the casing passage vortex, which is contrary to the results of linear cascades (where the casing and hub passage vortices are identical.) Radial inward flow was observed over the whole passage, which was more pronounced in the wake. The nozzle wake decay was compared to the decay of other turbomachinery blade wakes. The nozzle

wake is shown to decay much faster than a compressor cascade wake, an annular turbine cascade wake or a turbine nozzle wake with a large nozzle-rotor spacing. This is due to the presence of a rotor in close vicinity. The radial variation of nozzle wake total velocity defects shows larger velocity defects in the hub and casing secondary flow regions. These large defects results from the interaction of the passage vortices and the wake which cause deeper and wider wakes.

The steady and the unsteady flow field in the rotor was also measured at midspan using a two-component LDV. Measurements were acquired at 37 axial locations from just upstream of the rotor to one chord downstream of the rotor. The propagation of the nozzle wake through the rotor passage was captured by this method. As the nozzle wake enters the rotor passage it becomes bowed because the convection velocity at midpitch is higher than that near the rotor leading edge. As the nozzle wake travels further through the passage, it becomes distorted with the region of the nozzle wake near the rotor suction surface moving faster than the region near the pressure surface. The region of the nozzle wake near the rotor suction side continues to move faster than the region near the rotor pressure side, until the nozzle wake has turned more than 30 degrees from its orientation at the rotor inlet. It is now spread out along the rotor pressure surface from midchord to the trailing edge. This in contrast to other measurements of the nozzle wake in the turbine rotor passage, where at the rotor exit, the nozzle wake still spans the rotor passage in the pitchwise direction, extending from the pressure to suction surface. The reason for the difference is that the turbine rotor employed has a much larger ratio of the suction surface velocity to pressure surface velocity than the other researchers' turbines, which causes the region of the nozzle wake near the suction surface to travel much more rapidly than the region of the nozzle wake near the

rotor pressure surface. Thus the nozzle wake rotates about the region of the nozzle wake near the pressure surface, ending up spread out along the pressure surface.

As the nozzle wake travels through the rotor flow field, the magnitude of the velocity defect grows until close to midchord, after which it decreases. This is contrary to the common theory that the nozzle wake would continuously decay as it travels through the rotor passage. Also, the nozzle wake total relative unsteadiness does not decrease steadily as the nozzle wake travels through the rotor passage. Instead, it increases and decreases as the nozzle wake travels through the rotor passage.

High values of relative total unresolved unsteadiness were observed near the rotor leading edge, which result from an increase in the production of unresolved unsteadiness due to large mean flow gradients near the leading edge. High values of relative total unresolved unsteadiness were also observed near the rotor pressure surface. This increase in unresolved unsteadiness is due to the interaction of the nozzle wake with the pressure surface boundary layer, along with the concave curvature effects, which destabilize the flow.

The rotor wake decay characteristics were also analyzed. Correlations are presented which match the decay of the various wake properties. The rotor wake velocity defect decays rapidly in the trailing edge region, becoming less rapid in the near and the far wake regions. The rotor wake velocity defect decays according to the inverse of the square route of streamwise distance downstream of the rotor. The decay of the maximum unresolved unsteadiness and maximum unresolved velocity cross correlation is very rapid in the trailing edge region and this trend slows in the far wake region. While the interaction of the nozzle wake with the rotor wake does not influence the decay rate of the various wake properties, it does change the magnitude of the properties.

TABLE OF CONTENTS

LIST OF FIGURES

LIST OF TABLES

xxii

NOMENCLATURE

B   Bias error

C   Nozzle axial chord at midspan

C_L Nozzle axial chord

C_p Nozzle static pressure coefficient $\left(p - P_{o_1}\right) \big/ 0.5\rho V_{x_1}^2$

C_{p2} Nozzle static pressure coefficient $\left(p - P_{o_1}\right) \big/ 0.5\rho V_2^2$

$C_{p_{pitch}}$ Pitch angle calibration coefficient for five hole probe

$C_{p_{yaw}}$ Yaw angle calibration coefficient for five hole probe

$C'_{p_{static}}$ Static pressure calibration coefficient for five hole probe

$C'_{p_{total}}$ Total pressure calibration coefficient for five hole probe

H   Spanwise distance $\left(R - R_h\right) \big/ \left(R_t - R_h\right)$

H   Shape factor

j   Individual measurement window location in the rotor passage

k   Kinetic energy

k   Nozzle/rotor position

L   Semi-wake width

L_s Maximum pitchwise width of the passage vortex from the wake center

M   Mach number

$\dot{m}$ Mass flow rate

n   Total number of measurements in each measurement window

NB   Number of rotor blades

NRP   Number of nozzle/rotor positions

NW   Number of measurement windows

NWB   Number of measurement windows per blade

P   Precision error

p   Static pressure on nozzle surface

PS   Pressure surface

P_{atm} Atmospheric pressure

R   Radius

Re   Reynolds number

S   Percentage pitchwise distance in nozzle passage (Percentage pitchwise distance from nozzle pressure surface to nozzle suction surface)

S   Percentage pitchwise distance from the wake center at midspan (positive on pressure side, negative on suction side)

S   Precision error

S_r Percentage pitchwise distance in rotor passage (Percentage pitchwise distance from rotor pressure surface to rotor suction surface)

SS   Suction surface

Tu   Turbulence intensity, $\dfrac{\sqrt{\left(\overline{u'^2}+\overline{v'^2}\right)}}{V} \times 100\%$

Tu_r Relative total unresolved unsteadiness, $\dfrac{\sqrt{\left(\overline{u'^2}+\overline{v'^2}\right)/2}}{W} \times 100\%$

Tu_t Total unresolved unsteadiness, $\dfrac{\sqrt{\left(\overline{u'^2}+\overline{v'^2}\right)/2}}{U_m} \times 100\%$

U   Uncertainty

U_m Blade speed at midspan

u'   Fluctuating (unresolved) velocity in axial direction

$\tilde{u}$ Periodic velocity in axial direction

V   Absolute total velocity

v'   Fluctuating (unresolved) velocity in tangential direction

v'_x Fluctuating (unresolved) velocity in axial direction

v'_θ Fluctuating (unresolved) velocity in tangential direction

$\tilde{v}$ Periodic velocity in tangential direction

V_c Defect in absolute velocity at the wake center normalized by U_m

$(V_r)_{ref}$ Radial velocity at midspan passage, midspan

V_{sec} Secondary Velocity

W   Relative total velocity

W_c Defect in relative velocity at the wake center normalized by U_m

X   Axial distance from nozzle leading edge at midspan

X_L Axial distance from nozzle leading edge

X_r Axial distance from rotor leading edge at midspan

Y   Percentage pitchwise distance in the rotor wake with wake center equal to zero

Z   Axial distance from nozzle or rotor trailing edge normalized by nozzle or rotor axial chord, respectively

α Absolute tangential flow angle or yaw angle (measured from axial direction)

α_p Primary flow angle

α_o Nozzle vane outlet angle

β Relative tangential flow angle or yaw angle (measured from axial direction)

β_o Rotor blade outlet angle

γ Radial flow angle

δ^* Displacement thickness

ε Dissipation

θ Momentum thickness

ζ Total pressure loss coefficient $(P_{o1} - P_o)/0.5\rho V_{x1}^2$

η Efficiency

ρ Density

Ψ Total pressure loss coefficient $\left(P_{o1} - P_{o_3}\right)\big/0.5\,\rho U_m^2$

Ψ_{LOSS} Total pressure loss coefficient $\left(P_{o1} - P_o\right)\big/0.5\,\rho U_m^2$

Ψ_s Static pressure drop coefficient $\left(p_1 - p\right)\big/0.5\rho U_m^2$

Ψ_d Static pressure difference in the wake $\left(p_{max} - p_{min}\right)\big/\left(p_{max} - p_{min}\right)_{te}$

ω Vorticity

ω_s Streamwise vorticity (Equation 4.5, normalized by C/V_{X1})

ω_{s_m} Streamwise vorticity at midspan

ω_{sec} Secondary vorticity (Equation 5.1, normalized by C/V_{X1})

Subscripts

1	Inlet to nozzle
2	Exit to nozzle
3	Exit of rotor
b	blade
h	Hub
i	Instantaneous
l	local
m	Midspan
max	Maximum
min	Minimum
n	Normal
r	Rotor
ref	Reference conditions
rev	Revolution
s	Streamwise
s	Stator

sec   Secondary flow

o   Total

r,θ,x Radial, tangential, axial directions

t   Tip

te   Trailing edge

Superscripts

—   Circumferentially mass-averaged properties (Chapters 3, 4 and 5)

—   Ensemble-averaged properties (Chapters 2, 6 and 7)

=   Area-averaged properties (Chapters 3, 4 and 5)

=   Time-averaged properties (Chapters 2, 6 and 7)

∩   Circumferentially mass-averaged properties (Chapters 6 and 7)

...   Cycle-averaged properties

'   Fluctuating quantity

~   Periodic quantity

^   Aperiodic quantity

∪   Phase-locked averaged

*   Nondimensionalized variable

ACKNOWLEDGEMENTS

CHAPTER 1

INTRODUCTION

The major goals of the axial flow turbine designer are to increase the aerodynamic, thermal and mechanical performance of the turbine, and to lower manufacturing effort and cost. To increase the turbine performance, a better understanding of the flow field is needed. This has been hampered by the fact the present knowledge of the axial flow turbine flow field, especially the rotor flow field is not adequate. The flow field is complex being three-dimensional and unsteady, with the presence of laminar, transitional and turbulent regions near the blade surface. Some of the three-dimensional effects present include a three-dimensional boundary layer which can be laminar, transitional or turbulent, shock wave boundary layer interaction, radial density (or temperature) gradient, non-uniform entry flow and temperature field, steady and unsteady flow, and leakage and secondary flows. The three-dimensional viscous flows and turbulence effects are mainly caused by the three-dimensional boundary layers on blades and wakes, annulus wall and hub wall boundary layers, shock boundary layer interaction, and secondary flows in annulus wall and hub wall boundary layers. The presence of a horseshoe vortex at the leading edge combined with thick blades and high turning makes the flow field truly complex. There are many other basic problems related to turbines that remain unresolved, including rotor-stator interaction and its effect on the flow field, unsteady heat transfer and flow induced vibration.

The other goal of the turbine designer is to lower manufacturing effort and cost, which means a reduction in the size, weight and number of blades. This requirement can only be met by reducing the blade row spacing and the number of stages, which involves increasing the aerodynamic stage loading. Reducing the

blade weight also results in decreasing the blade height. Thus the aspect ratio (the ratio of the blade height to the blade chord) of the blade decreases causing an increase in three dimensional viscous effects in the turbine flow field. This reduction in size and weight of the turbine also results in a decreasing gap between the nozzle and rotor, thus causing an increase in rotor-stator interaction effects. Thus a better understanding of the turbine flow field is essential for more efficient design of turbines.

1.1 Turbine Flow Field

The turbine flow field is very complex as is described above. Thus it is useful to describe the axial flow turbine flow field before proceeding. The flow field in the nozzle is described first. At the center of the blade passage, away from the blade surfaces and endwalls, no significant viscous effects are taking place. This region is basically inviscid and is called the inviscid core region. Along the blade surfaces, a three-dimensional boundary layer develops, which transforms into a three-dimensional wake downstream of the nozzle. The turning of the endwall boundary layers inside the nozzle induces three dimensional viscous flow effects called secondary flows. After the flow exits the nozzle it enters the rotor. The interaction of the nozzle wakes with the rotor and the interaction of the nozzle and rotor potential flow fields is called rotor-stator interaction. The rotor flow field is similar to the nozzle, except that it has the additional effects of the rotor rotation and the nozzle wake propagation through the rotor passage.

Though the turbine inviscid flow field is understood well, the turbine secondary flow and wakes along with the turbine rotor-stator interaction are not completely understood as of yet. A complete description of these turbine flow field

phenomena and why they need to be investigated further is provided below.

1.1.1 Secondary Flow

Secondary flow in turbines is associated with the endwall flow and arises due to the turning of the endwall boundary layer by the blade row. This flow is highly three-dimensional and contains numerous vortices, including the passage vortex, the horseshoe vortex, the trailing filament and trailing shed vortices and the corner vortex.

Figure 1.1 describes the classical secondary flow vortex system of Hawthorne (1955). It includes the passage, the trailing filament and trailing shed vortices. A comprehensive review and analysis of classical secondary flow theory is given by Horlock and Lakshminarayana (1973). The passage vortex is a result of the flow turning in the blade passage. The deflection of the flow in the inviscid region generates a cross-channel pressure gradient, from pressure to suction side, which is balanced by the centrifugal force in this region. But in the endwall boundary layer, the velocity of the flow decreases, and since the pressure in the boundary layer is the same as that of the inviscid core flow, the radius of curvature of the streamlines must decrease near the endwalls in order for the centrifugal and pressure force to be in equilibrium. Thus a cross flow is generated from the pressure to suction surface which rolls up into a vortex core to form a passage vortex. There are two passage vortices in each passage, one at each endwall, which rotate opposite to each other. The strength of the passage vortex is a function of the main flow turning, the thickness of the incoming end-wall boundary layer, and the velocity gradient. Presence of the passage vortex causes over-turning of the flow near the endwalls and underturning of the flow away from the wall.
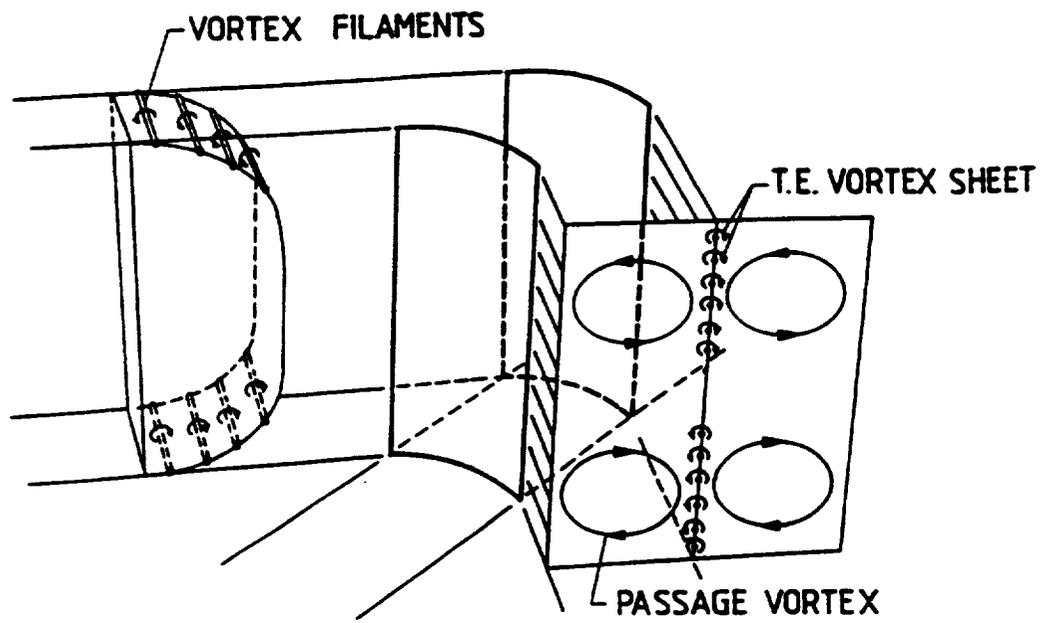
Figure 1.1. Classical Secondary Flow Model of Hawthorne (1955)

The trailing filament vortices and the trailing shed vorticity compose the vortex sheet at the trailing edge. The trailing filament vortices are generated due to the stretching of the inlet vortex filaments when passing through the cascade withdifferent velocities between the suction side and the pressure side. The trailing shed vorticity is caused by the spanwise change of blade circulation. The trailing shed vortices are shed all along the blade span, whereas the trailing filament vortices are confined to the endwall region. Together, these two vortices form a vortex sheet with the same sense of rotation, but opposite to that of the passage vortex.

The horseshoe vortex is caused by the rolling up of the inlet boundary layer as it approaches the leading edge of the blade. It is called this because of its shape. The physical presence of the blade causes the flow approaching the blade to decelerate. A direct consequence of this flow deceleration is that the incoming endwall boundary layer has to negotiate an adverse pressure gradient. Thus, the inlet boundary layer (and the associated vorticity normal to the freestream) grows rapidly and separates to form a horseshoe vortex. One leg of the horseshoe vortex wraps itself around the pressure side of the blade, while the other leg wraps itself around the suction side. Although the horseshoe vortex is a well known phenomena, its existence in the turbine flow field has only been realized recently. According to Sieverding (1985b), Klein (1966) was the first person to identify the horseshoe vortex in a turbine passage, calling it a stagnation point vortex. (see top of Figure 1.2). But it was Langston et al. (1977) who first presented a detailed analysis of the development of the horseshoe vortex. The bottom of Figure 1.2, from Langston (1980), shows the horseshoe vortex.

The corner vortex is the vortex that rotates in the opposite sense to the passage vortex and is located right in the endwall/suction side corner. It is caused

LAMINAR SEPARATION
BUBBLE

STAGNATION POINT
VORTEX

PASSAGE VORTEX

KLEIN'S MODEL

STREAM SURFACE

INLET BOUNDARY
LAYER

ENDWALL

PASSAGE VORTEX

ENDWALL
CROSSFLOW

COUNTER VORTEX
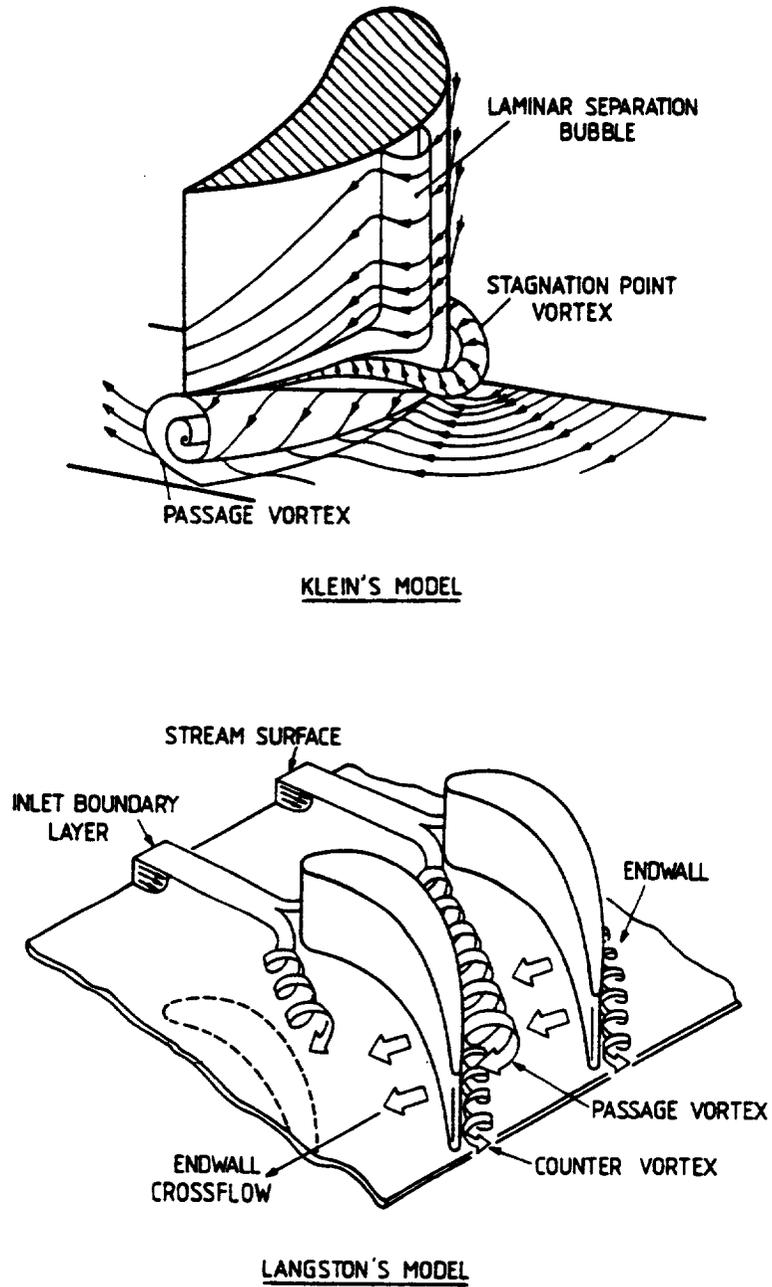
LANGSTON'S MODEL

Figure 1.2. Endwall Flow Models by Klein (1966) and Langston (1980)

by the fact that the overturning of the flow near the endwall is so extreme that the flow interferes almost at a right angle with the blade suction surface. Sieverding (1985b) states that this interaction is similar to the one causing the boundary layer ahead of the leading edge to roll up into a horseshoe vortex. Because it is so small, it is hard to see, but its existence is often shown by a characteristic reduction of the overturning near the endwall, as shown in Figure 1.3a. Figure 1.3b shows endwall limiting streamlines indicating the generation of the corner vortex. The overturning at the endwall is such that the limiting streamlines interfere at almost a right angle with the blade suction surface near the position of maximum surface curvature.

The interaction of all these vortices causes the flow in the nozzle passage to be very complex and highly three-dimensional. Many researchers have conducted experiments to try to understand the nozzle flow field. Until the late 1970's, most of this research was limited to surveys of flow conditions upstream and downstream of the turbine cascade, which is called the "control volume approach". Since no measurements were made within the blade passage, researchers had to infer from the inlet and exit measurements the processes occurring inside the cascade passages. Numerous loss correlations were developed from experiments using the control volume approach, but since these correlations were not based on the actual physics of the flow field, there were major discrepancies between the various correlations. There was no sound basis on which to decide what correlation to use for the performance of a particular turbine stage. This was strongly criticized by several researchers including Sieverding (1985a).

Researchers thus realized that only by obtaining a better physical understanding of the evolution of secondary flow both inside and outside of the blade passage could accurate predictions of the losses occurring in the turbine be calculated. Several research programs were started in the mid 1970's to take

(a)

(b)
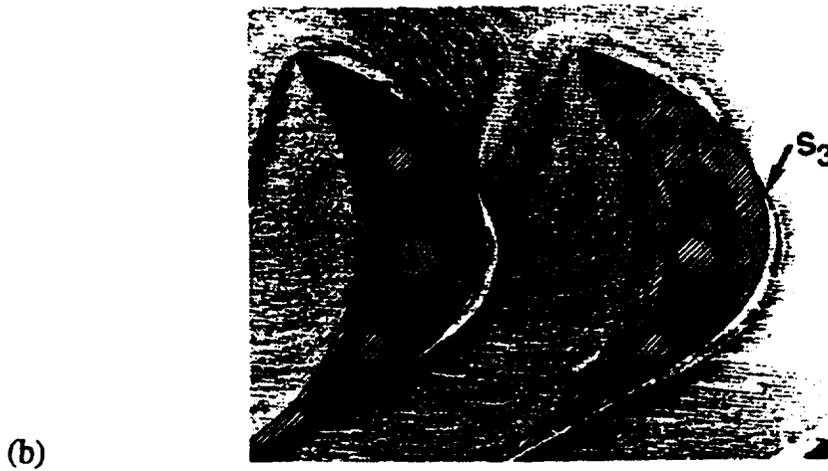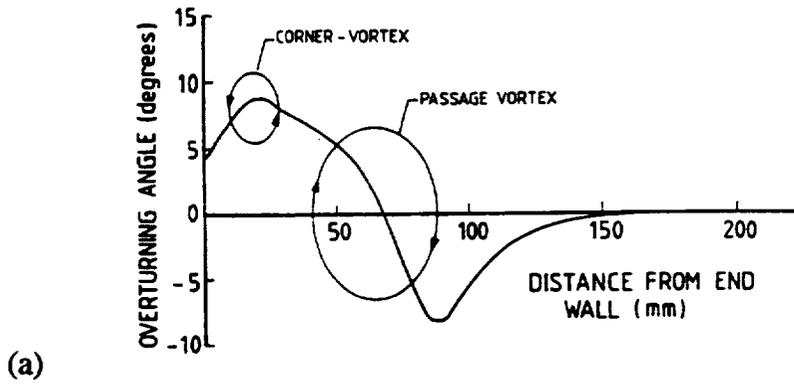
Figure 1.3. Corner Vortex:

(a) Reduction of Overturning Near Endwall Due to Corner Vortex (from Gregory-Smith and Graves, 1983)

(b) Endwall Limiting Streamlines Indicating Generation of Corner Vortex (from Belik, 1975)

detailed measurements of the endwall flow development. Most of this work was conducted in linear cascades. Sieverding (1985b) gives an excellent review of the research conducted in turbine cascades in order to provide an understanding of the basic aspects of secondary flows in turbine cascades. Sharma and Butler (1987) also present a detailed description of the evolution of secondary flow in a turbine cascade. From these and other researchers, a description of the flow field in a linear turbine cascade is presented as follows.

The incoming boundary layer at both endwalls separates at the leading edge of the nozzle, forming a horseshoe vortex with two counter rotating legs, the pressure side leg and the suction side leg. This is shown in Figure 1.4. As the pressure side leg enters the vane passage, it is convected toward the suction surface of the vane, due to the pressure gradient between the pressure and suction surfaces. It meets the suction surface near the minimum static pressure point, lifts off the endwall and grows rapidly as it travels along the suction surface. As the pressure side leg moves across the passage, it merges with the passage vortex, while entraining low energy boundary layer fluid from the endwall and blade surfaces. Most of the fluid from the inlet endwall boundary layer is trapped in the passage and horseshoe vortex. Since all of the fluid particles from the inlet boundary layer have either become part of the passage and horseshoe vortices or been convected toward the suction side, a new boundary layer starts at the endwall downstream of the separation line defined by the passage vortex (see Figure 1.5). The suction leg of the horseshoe vortex follows the contour of the blade suction surface, until it reaches the point where the pressure side leg of the horseshoe vortex meets the suction side. At this point, the suction side leg of the horseshoe vortex leaves the endwall and orbits around the outer edge of the passage vortex, as it moves downstream. It is hard to detect this downstream of the vane, since it loses intensity
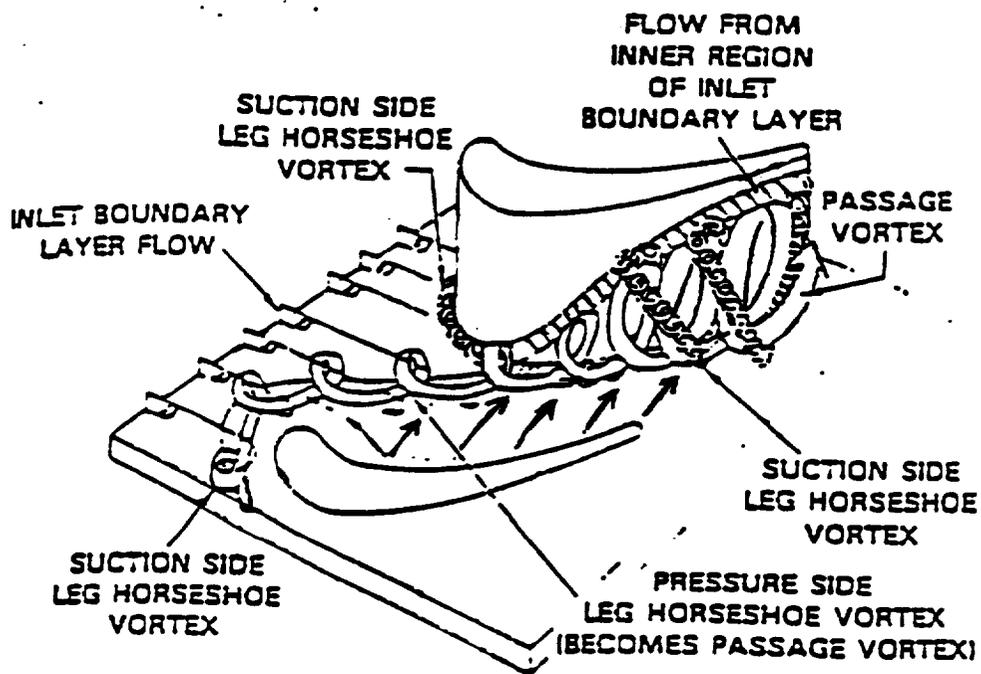
Figure 1.4. Cascade Endwall Flow Structure (from Sharma and Butler, 1987)
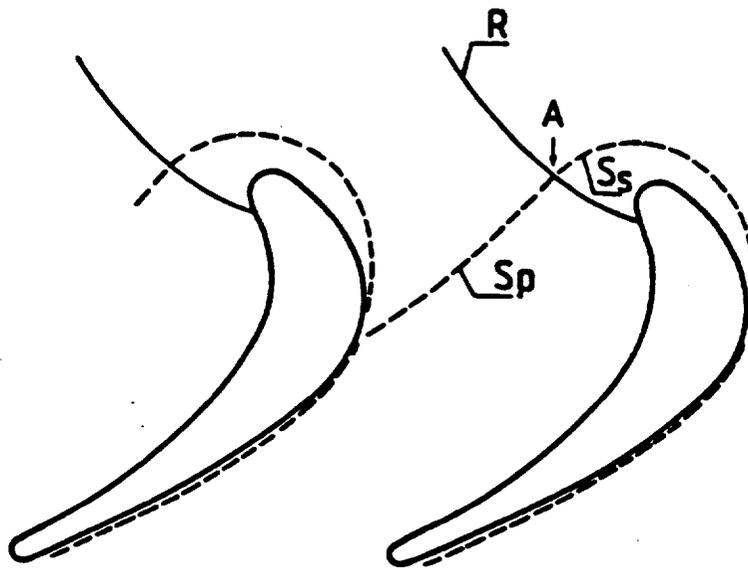
Figure 1.5. Endwall Three-Dimensional Separation and Reattachment Lines (from

Langson et al., 1977)

in contact with the passage vortex.

The separation lines on the endwall are shown in Figure 1.5 (from Sieverding (1985b), based on the endwall ink traces of Langston et al. (1977)). The flow field is divided into distinct regions through the three-dimensional separation lines S and the reattachment lines R (stagnation streamline) with the separation saddle point A at their intersection. The horseshoe and the passage vortices form behind the separation line S, with the pressure side leg of the horseshoe vortex and the passage vortex forming behind S_p (starting from A) and the suction side leg of the horseshoe vortex behind S_s.

While this is a good description of the flow in a linear cascade, it is not an accurate one of the flow in a real turbine nozzle. Important turbine parameters such as a radial pressure gradient that can be the same order of magnitude as the pitchwise pressure gradient and radial variation in blade loading, which are present in an actual nozzle, do not exist in a linear cascade. Also, Boletis and Sieverding (1984) show that the presence of a downstream rotor causes local changes to the outlet flow of an annular cascade. Though there have been a few investigations carried out in annular cascades, most of them have been in configurations where there is no rotor behind the nozzle such as Yamamoto and Yanagi (1986), Binder and Romey (1982) and Sieverding, Van Hove and Boletis (1984). Even fewer measurements have been completed in nozzles with a rotor downstream and they were all carried out with a nozzle-rotor spacing that is much larger than is found in modern axial flow turbines, such as the experiments done by Richards and Johnson (1988) and by Joslyn and Dring (1990). Thus more work needs to be done in annular turbine nozzles with a downstream rotor and a realistic nozzle-rotor spacing.

1.1.2 Turbine Blade Wakes

An understanding of turbine nozzle and rotor wakes are also important for the efficient design of axial flow turbomachinery used in land, space, naval and aircraft applications. A major cause of noise and vibration characteristics of turbomachinery is caused by wakes. Turbine wakes represent a source of loss in efficiency, since the mixing of the wakes with the freestream dissipates energy. The three-dimensional characteristics of the wake, the decay characteristics and the path that it follows is important in the design of the following blade rows. This information is essential for both the prediction of the aerodynamic and mechanical performance of a turbine and for building quieter turbomachines. An understanding of the wake development and its decay is also essential because of the role it plays in the rotor-stator interaction (see below).

Both the nozzle and rotor wakes are three-dimensional. In the nozzle wake, shown in Figure 1.6, the radial component results from an imbalance between the pressure and centrifugal forces within the shear layer. The tangential velocity decreases as the surface of the nozzle is approached, and thus the centrifugal force decreases, while the radial pressure gradient remains constant. This imbalance between the centrifugal and the pressure forces sets up a radial inward flow, which continues even in the wake. On the other hand, the radial velocity is outward in a turbine rotor wake due to the centrifugal force. Although there has been extensive research done on compressor wakes (see Reynolds (1978), and Ravindranath (1979), for a complete literature survey on compressor wake research), not much work has been done on turbine wakes. Mee et al. (1990) measured the wake of a linear cascade at midspan at six axial locations. Sitaram and Govardhan (1986) reported the wake of a turbine rotor cascade blade at midspan at seven axial
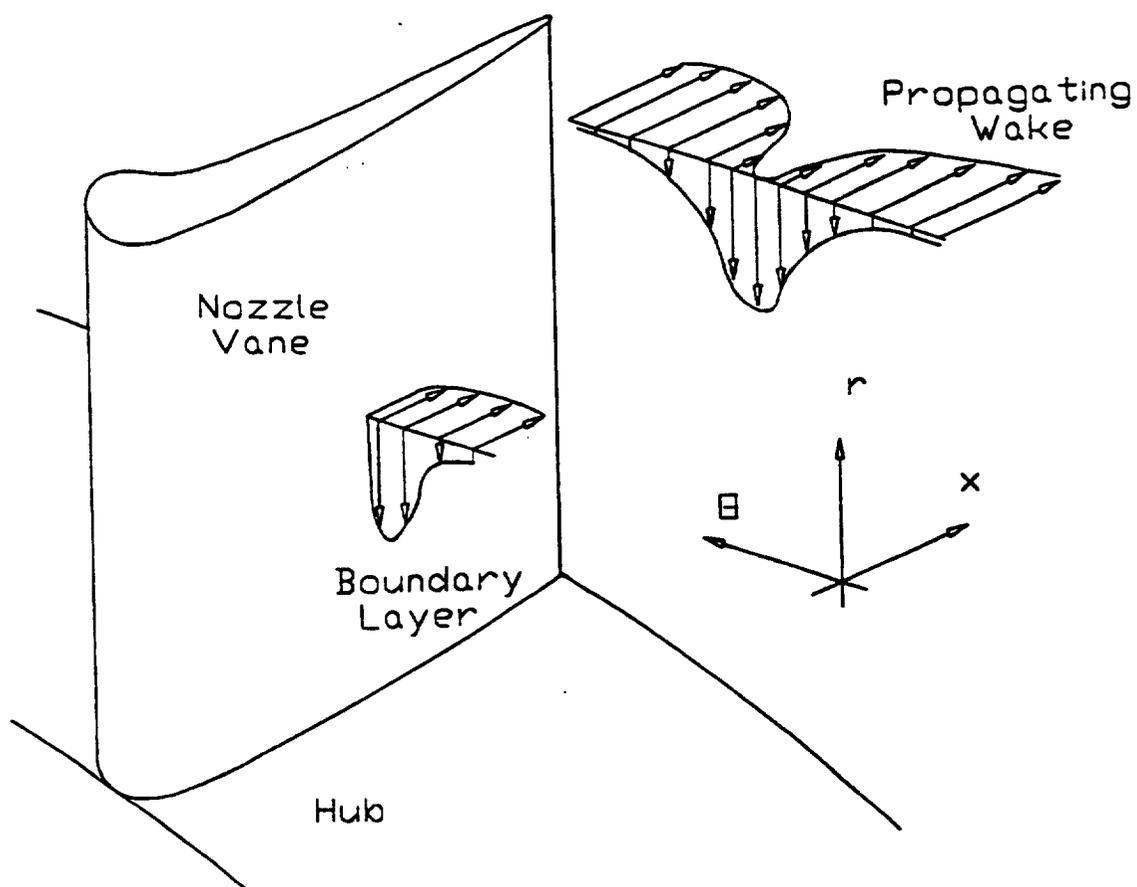
Figure 1.6. Nozzle Wake Development and Propagation

locations. Goldman and Seasholtz (1992) measured the wake in an annular turbine cascade for three axial locations at midspan and Dring et al. (1987) reported wake data at one axial location in a 1 1/2 stage axial flow turbine with a nozzle-rotor spacing of 50% nozzle axial chord. Only one of these (Dring et al., 1987) had a realistic three-dimensional configuration with a rotor downstream. Dring et al.'s rotor was located at 50% nozzle axial chord, which is much higher than usually employed in industry. Furthermore, the wake was measured at only one axial location. The only reported measurement of a wake from a rotating turbine rotor is also from Dring et al. (1987), and the rotor wake was measured at only one axial location, too. Thus, there is a need for a comprehensive survey of the wake at different axial and spanwise locations for a turbine nozzle with a realistic axial distance between the nozzle and the rotor, and also a need for a survey of turbine rotor wakes.

1.1.3 Rotor-Stator Interaction

The understanding of rotor-stator interaction is also important for the efficient design of axial flow turbines. The flow around the blades of a turbine is highly unsteady. This unsteadiness is caused by the aerodynamic interaction of the flow between the nozzle and rotor which is called rotor-stator interaction. Rotor-stator interaction can affect the aerodynamic, structural and thermal performance of a turbine. According to Dring et al. (1982), rotor-stator interaction can be divided into two parts. These are potential flow and wake interactions. The potential flow gradients extend both upstream and downstream of the blade and they decay exponentially with a length scale of the order of the pitch or chord of the blade row. If the axial gap between the blade rows is less than a chord (which it is in a

typical axial flow turbine), then the potential influence can cause unsteadiness in both upstream and downstream of the blades. However, the wake is convected downstream and has a far field rate of decay much lower than that of the potential flow. The wake will still be felt several chords downstream. But in most modern axial flow turbines, which have a rotor-stator spacing close to 20 percent of a blade chord, both the potential and wake effects will occur together. And in the future as gas turbine designers try to reduce weight, and thus the rotor-stator spacing gets smaller, these effects will become more prominent.

Even though unsteady flow plays a major role in axial flow turbines, turbines are designed using three-dimensional steady flow calculation methods (Sharma et al., 1992). Empirical correlations are used to account for the effect of the unsteadiness. Because actual models of the loss generating mechanisms in unsteady flow turbomachinery do not exist, these correlations are based on results from stationary cascade data and do not represent the actual fluid mechanics in the flow field (Sharma et al., 1985). Thus these correlations must be multiplied by some factor to obtain a good estimate of the actual losses that occur in turbines. Although these correlations have worked well in the design of existing turbines, they do not represent the true physics of the flow field and are only useful in the areas from which they were obtained, namely design point predictions and turbines which are similar to existing designs (Hathaway, 1986). Thus, a more thorough knowledge of unsteady flow interactions is needed in order to increase both the design and off-design performance of existing turbines, and to design turbines which are considerably different than existing turbines. To obtain this knowledge, good time accurate data from inside the rotor is needed. This knowledge, in turn, can be used to model the unsteady flow mechanisms that are not currently in existing design codes.

Many researchers have investigated rotor-stator interaction. Greitzer (1985), Gallus (1987) and Sharma et. al. (1992) provide comprehensive surveys of unsteady flows in turbomachinery. Unfortunately, most of these investigations have been in isolated airfoils or axial flow compressors. And there should be significant differences in the unsteady turbine flow field as compared to the unsteady compressor or isolated airfoil flow field (Sharma et al., 1985). This is because the flow field is accelerating in a turbine where as in a compressor the flow field is decelerating and also because the flow turning is much larger in a turbine than in a compressor thus causing stronger secondary flow in a turbine than in a compressor. Also there is the added effect of the horseshoe vortex in a turbine that does not occur in a compressor.

Only four groups have measured the unsteady flow field inside a turbine rotor; the groups at UTRC (Sharma et al., 1985), Cambridge (Hodson, 1984), Allison/Calspan (Rao, Delaney and Dunn, 1992) and at DFVLR (Binder et al. ,1985, Binder, 1985 and Binder et al. ,1987) . The Cambridge group measured the flow field at midspan (nozzle-rotor spacing is 50% of nozzle axial chord), the Allison/Calspan group measured the blade surface pressures at midspan (nozzle-rotor spacing is 22.5% of nozzle axial chord), the UTRC group measured the blade surface pressures and the rotor exit flow field (nozzle-rotor spacing is 65% of nozzle axial chord), and the researchers at DFVLR used a L2F velocimeter to measure two components of velocity and turbulence intensity (axial and circumferential) at four axial planes inside of the rotor (nozzle-rotor spacing is 61% of nozzle axial chord). Three out of the four research groups had a nozzle-rotor spacing of 50% of nozzle axial chord or greater which is not a realistic spacing for modern turbine designs. At this spacing the potential flow interactions will be very small and the nozzle wake will have decayed significantly by the time

it enters the rotor passage. Typically, modern turbines have a nozzle-rotor spacing of around 25% or less nozzle axial chord. The only group to take measurements with a realistic nozzle-rotor spacing (Allison/Calspan), measured only the blade surface pressures at midspan (and did not measure the flow field between the blades). Thus there is a need for flow field measurements in a turbine rotor with a realistic nozzle-rotor spacing that will include both potential flow and wake interactions.

1.2 Objectives

The objectives of this research are as follows:

(1) To understand the three-dimensional flow field in an axial flow turbine nozzle with a focus on secondary flow.

(2) To understand the nozzle wake characteristics and to show how the presence of a rotor in close vicinity affects the decay of a nozzle wake.

(3) To understand the two dimensional unsteady rotor flow field at midspan.

(4) To understand the effects of rotor-stator interaction on the flow field in an axial flow turbine.

(5) To capture the nozzle wake trajectory through the rotor passage.

(6) To determine the influence of the rotor on the decay of the nozzle wake in the rotor passage.

(7) To understand the rotor wake characteristics and to show the decay and profile characteristics.

(8) To understand how the interaction of the nozzle wake with the rotor wake affects the rotor wake decay characteristics

(9) To generate accurate data for CFD code validation.

The ultimate goal of this research is that it will be used to build more efficient turbines.

1.3 Method of Investigation

The axial turbine flow field has been investigated experimentally. The nozzle flow field was measured with a two-dimensional LDV, a five hole probe and a hot wire. The rotor flow field was measured using a two-dimensional LDV. These measurements were performed in a systematic manner. The turbine inlet asymmetry was determined first. Next, the performance of the turbine was measured in order to pick an operating point that was as close to the design point as possible. Then measurements were carried out inside the nozzle flow field. The nozzle surface and endwall static pressure were measured, and the nozzle flow field was investigated at two axial locations. The first location was at midchord using the LDV and the second just upstream of the trailing edge using a five hole probe. The LDV was used provide both the mean velocity and the turbulence intensity, while the five hole probe was used to obtain the total pressure loss in the passage as well as the three component of steady velocity. The data from the five hole probe can also be used to calculate the secondary flow vectors and the streamwise vorticity. Downstream of the nozzle, the flow field was measured also using a five hole probe. Using the measurements in the nozzle passage and nozzle exit, the evolution of the secondary flow vortices, and their importance to the flow field can be determined. The characteristics of the nozzle wake, including its decay rate and the growth of its width can also be determined. The nozzle exit flow field is also used to provide the flow field at the rotor inlet and to compare with the LDV

measurements upstream of the rotor.

The rotor flow field at midspan was measured using a two-component LDV. The LDV was used to measure the steady and unsteady components of the axial and tangential velocity of the rotor flow field. The interaction of the nozzle flow field and the rotor flow field can be measured, including the propagation of the nozzle wake through the rotor passage and its influence on the rotor flow field. The rotor wake was also measured in detail at midspan in order to determine its characteristics, including the decay of the velocity defect and unsteadiness.

CHAPTER 2

EXPERIMENTAL FACILITY AND MEASUREMENT TECHNIQUE

2.1 Facility Description

The Axial Flow Turbine Research Facility (AFTRF) of The Pennsylvania State University is an open circuit facility 91.4 cm in diameter and a hub to tip radius ratio of 0.73, with an advanced axial turbine blading configuration. The facility consists of a large bellmouth inlet, a turbulence generating grid section, followed by a test section with a nozzle vane row and a rotor as shown in Figure 2.1. There are 23 nozzle guide vanes and 29 rotor blades followed by outlet guide vanes. The bellmouth inlet is housed in an enclosure (not shown) covered with wire mesh and a thin layer of rubber foam to filter the air prior to entry to the inlet.

A variable through flow is provided by two auxiliary, adjustable pitch, axial flow fans and an aerodynamically designed throttle. The two fans in the series produce a pressure rise of 74.7 mm Hg (40 " of water) with a mass flow of 10 m^3 per second under nominal operating conditions. The power generated by the experimental turbine rotor assembly is absorbed by an eddy-current brake which is capable of absorbing up to 60.6 kw (90 Hp). The speed of the rotor can be varied between 175 and 1695 rpm with the "dynamic" control system and can be held constant to $\pm$ 1 rpm, with normal fluctuations in line voltage. The eddy current brake is cooled by a closed loop chilled water cooling system.

The rotor and nozzle vane passages are instrumented with fast response instrumentation to measure steady (time averaged), unsteady pressures and wall
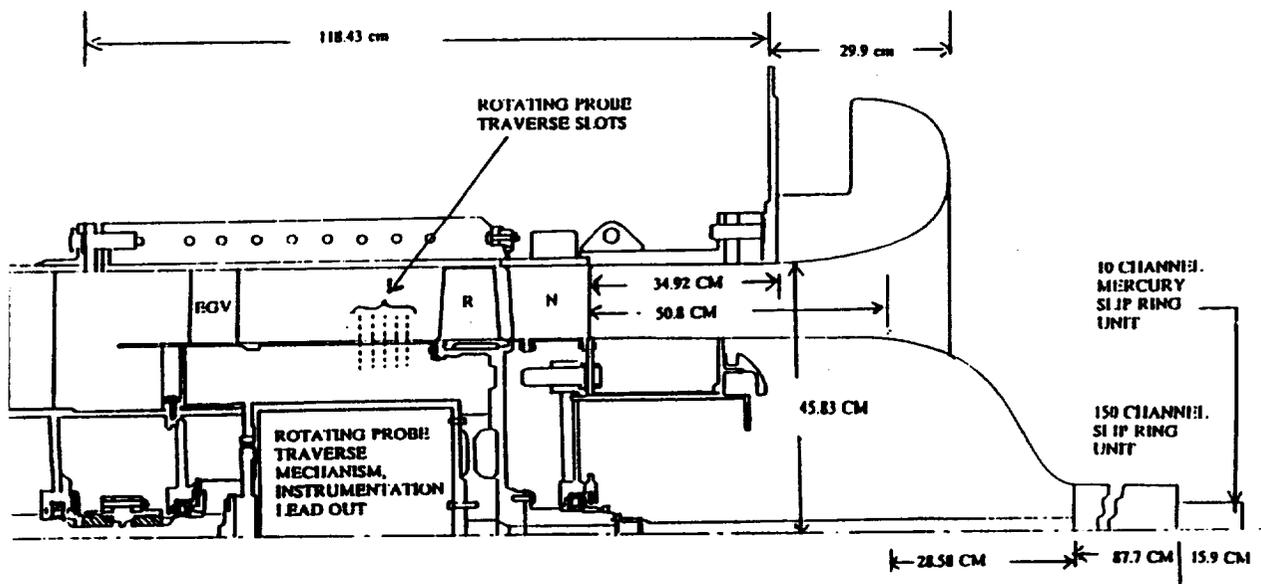
Figure 2.1. Schematic and Flow Path of AFTRF

shear stresses. A window for LDV measurements of the flow field upstream of the nozzle, in the nozzle passage, in the spacing between the rotor and the nozzle, in the rotor passage and downstream of the rotor passage is included.

The facility is equipped with two traversing mechanisms. One of the probe traverse units is mounted directly behind the rotor disk and has provisions for the radial and circumferential traverses in the rotating frame. It is controlled by a stepping motor driven by a computer indexer at tangential increments of 0.019 degrees/step to allow accurate measurements of the rotor passage and downstream flow field. The intra blade radial and tangential surveys are accomplished by a computer controlled indexer and stepping motor in 0.05 mm steps and 0.0234 degree steps in the radial and circumferential directions respectively. The second probe traversing unit is mounted on the outside casing of the turbine, and it provides radial and circumferential traversing at any axial location from one chord upstream of the nozzle to two chords downstream of the rotor. A probe mounted on this traversing unit can be positioned to an accuracy of 0.05 mm in the radial direction, 0.03 degrees in the circumferential direction and 0.5 mm in the axial direction, allowing for very detailed measurements of the absolute flow field in the turbine.

The rotating-to-stationary data transmission system, attached to the rotor shaft ahead of the nose cone, is an integral part of the facility. It consists of a 150 ring mechanical (brush/coin type) slip ring unit, and a specialized ten-channel low noise/signal ratio mercury slip ring unit. A 32 channel electronic pressure scanner unit is located in the rotating drum downstream of the turbine rotor. The electrical signals carrying the pressure information is carried to the stationary frame through the slip ring assembly. The rotor frequency is accurately determined by using an optical shaft encoder.

A completely automated data processing system is built around a computer with a clock rate of 25 MHz. The system consists of a 32 bit computer with 8 Mb random access memory, a disk operating system, 510 Mb hard disk storage space, and a HP laser printer. All the data from both stationary and rotating instrumentation can be processed on line.

2.2 Design Features and Overall Performance Parameters

The overall performance parameters are given in Table 2.1. The principal aerodynamic and geometric design features of the nozzle vane and the rotor blades designed by the General Electric Company (Aircraft Engines Group) personnel are presented in Table 2.2. Provisions exist for changing the vane-blade spacing from 20 percent to 50 percent of nozzle axial chord. All the experiments presented in this thesis were performed at 20% vane-blade spacing. The actual operation conditions of the AFTRF are given in Table 2.3. Isometric views of the nozzle vane and the rotor are shown in Figures 2.2 and 2.3, respectively. A more detailed explanation can be found in Lakshminarayana et al. (1992). The aerodynamic design, while not representing any specific current or future GE product, does embody modern turbine design philosophy. Stage loading flow coefficient, reaction, aspect ratios, and blade turning angles are all within the ranges of current design practice. State-of-the-art quasi-3D design methods were used to design the airfoil shapes. It is felt that the design is fully capable of meeting the intended research applications.

Table 2.1
Design Performance Parameters

	DESIGN
Total temperature at inlet (°K); T_o	289
Total pressure at inlet (kpa); P_o	101.36
Mass flow rate (kg/s); W	11.05
Specific work output (kJ/kg); $\Delta h/W$	5.49
Flow function; $W\sqrt{T}/P$ $(kg\sqrt{°K}\ m^3\ /\ kN\cdot S)$	1.85
Speed function (rpm/$\sqrt{°K}$); $N/\sqrt{T}$	77.69
Rotational speed; N	1300 rpm
Total pressure ratio; $P_{01}\ /\ P_{o3}$	1.0778
Total temperature ratio; $T_{03}\ /\ T_{o1}$	0.981
Pressure drop (mmHg); $P_{o3} - P_{o1}$	56.04
Hub reaction; R	0.181
Pitchline reaction; R	0.3820
Pitchline loading coefficient; Ψ	3.76
Hub loading coefficient; Ψ	5.27
Stator Zweifel coefficient	0.7247
Rotor Zweifel coefficient	0.9759
Power (kw)	60.6
Stator efficiency; η_s	9.9421
Rotor efficiency; η_r	0.8815
Total-to-total Isentropic efficiency; η_{TT}	0.8930

Table 2.2
The Design Features of AFTRF

Hub Tip Ratio	0.7269
Tip Radius	0.4582 m
Blade Height	0.1229 m

Rotor Blade (tip)
rel. mach number	0.240 (max)
number	29
chord	0.1287 m
spacing	0.1028 m
turning angle	95.42 deg (tip), 125.69 deg (hub)
maximum thickness	22 mm
tip clearance	1.27 mm (actual 0.97 mm ave., 1.04 mm max, 0.77 mm min)

Nozzle Guide Vane (tip)
number	23
chord	0.1768 m
spacing	0.1308 m
turning angle	70 deg.
maximum thickness	38.81 mm

Midspan Axial Chord
nozzle	0.1123 m
rotor	0.09294 m

Auxiliary Fan
pressure rise	74.72 mm Hg
mass flow	10.39 m^3 per sec. (22,000.0 cfm)
power	149.1 kw

Vane Reynolds Number
based on inlet vel.	$(3 \sim 4) \times 10^5$
based on exit vel.	$(9 \sim 10) \times 10^5$

Blade Reynolds Number
based on inlet vel.	$(2.5 \sim 4.5) \times 10^5$
based on exit vel.	$(5 \sim 7) \times 10^5$

Table 2.3

Experimental Operating Conditions

Mass flow rate ($\dot{m}$)	10.53 kg/s
Pressure Drop (P_{o1}/P_{o3})	1.078
Rotational Speed	1300 rpm
Nozzle/Rotor gap	
tip	0.18C
midspan	0.226C
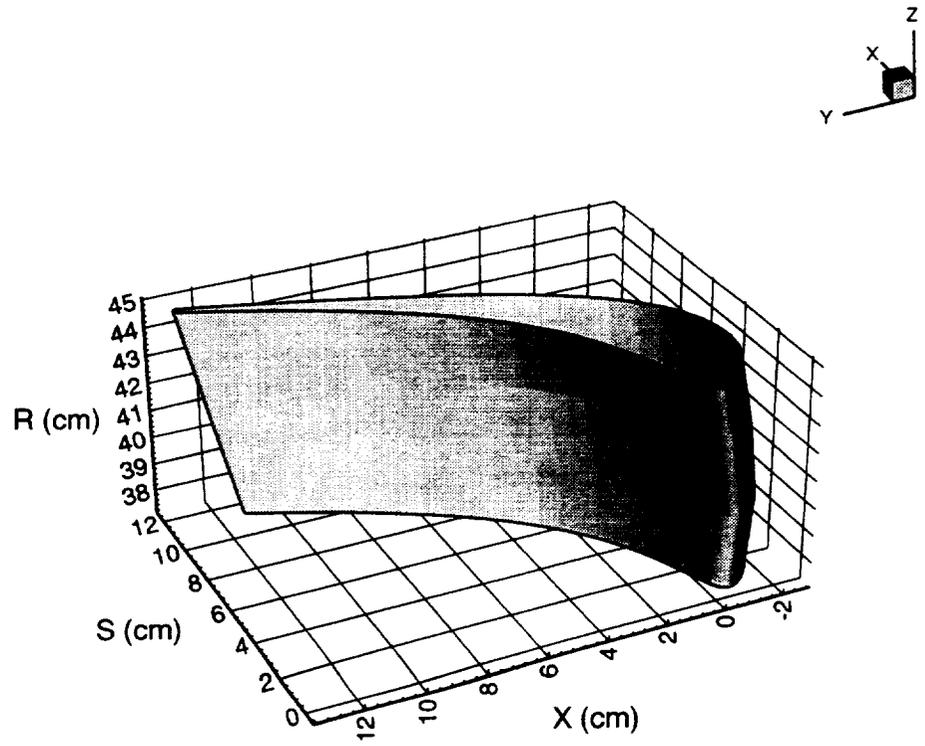
Figure 2.2. Nozzle Vane Profile

TIP

HUB
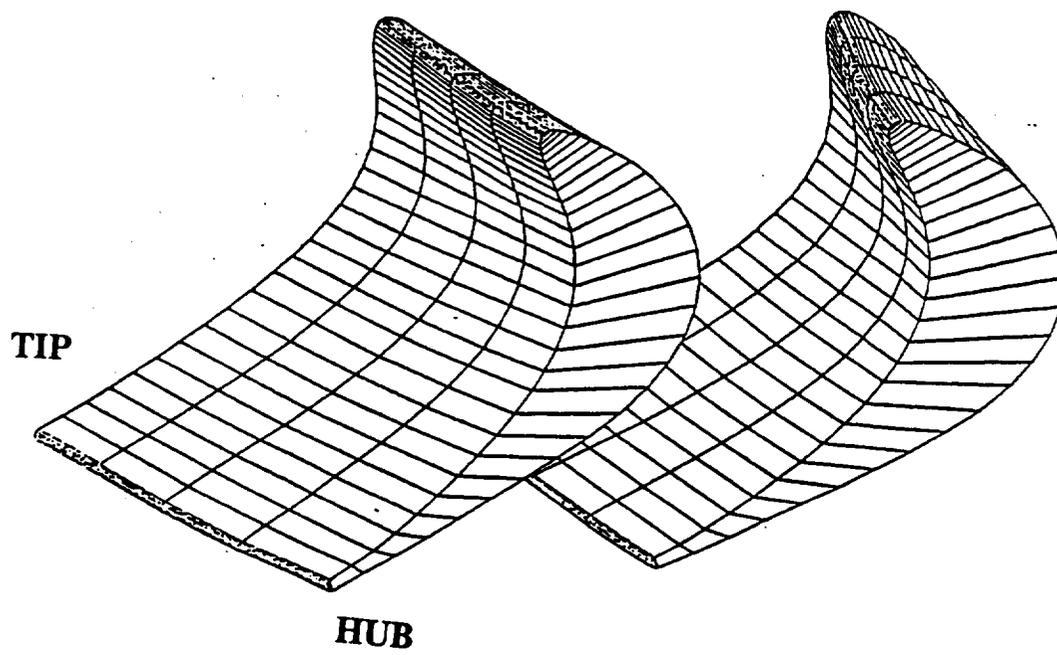
Figure 2.3. Isometric View of the Rotor

2.3 Modifications to the AFTRF

The following is a summary of the modifications made to the AFTRF since its arrival in February 1990.

(1) An intake wooden structure (10' x 10' x 5'), covered with wire mesh and 0.125" thick foam sheet , was designed and built.

(2) An exhaust structure to reduce the noise and recirculate air in the room was designed and built. The exhaust structure uses very dense acoustic absorbing material in a wooden frame to reduce the auxiliary fan noise.

(3) A control system for the eddy current brake has been designed and installed, which is used to monitor the rotor speed and shut down the facility if the rotor speed increases above a predetermined limit.

(4) Slotted windows and a circumferential traverse have been designed and built for circumferential traversing. The aluminum window frame contains a removable Plexiglas window which has a circumferential slot. Three windows have been built with slots at five different axial locations. More windows can be built if needed. The slots contain two strips of rubber foam. As the probe moves between the two strips of rubber foam, the rubber forms a seal around the probe so that air will not leak through the slot.

(5) A computerized data acquisition system has been added to the facility. It consists of a 96 channel scanivalve, an IBM compatible personal computer and a Metrabyte DAS-20 data acquisition board. Software has been written to acquire and reduce the static pressure and five hole data which uses this equipment setup.

(6) The bearing that is located just downstream of the rotor was replaced by a bearing that can withstand higher axial loads. Also, a thermocouple was connected to the bearing and an Omega CN100 six channel monitor was obtained

so that the bearing temperature can be closely monitored.

(7) The six cylindrical struts that hold the slip ring in place have been replaced with three aerodynamically shaped struts. This decreased the turbulence level at the three measuring stations located one chord upstream of the nozzle from 4 percent to 1.5 percent, which is the turbulence level without the struts in place. These measuring stations are directly downstream of the struts.

(8) An optical shaft encoder was connected to the turbine shaft. This encoder enables LDV and hot wire measurements to be made in the rotating frame.

(9) Glass and Plexiglas windows have been designed and built for LDV measurements in both the nozzle and rotor.

2.4 Static Pressure Instrumentation

The Axial Flow Turbine Research Facility is equipped with a large number of static pressure holes (nearly 500) at carefully selected locations. A list of the locations is as follows: (a) Static holes for performance measurements on the outer casing and inner casing of the rig at 4 axial planes. A circumferential average at each plane will be used for performance calculations, (b) 43 static holes on the nozzle (hub) endwall in one passage, (c) 43 static holes on the annulus wall of the same nozzle passage, (d) 154 static pressure holes at several axial and chordwise locations on both surfaces of the nozzle blades (one passage), (e) 52 static holes on the hub surface of one rotor passage, (f) 154 static pressure holes at several radial and chordwise locations of rotor blade on both surfaces (one passage).

2.5 Five Hole Probe

A five hole probe was used to measure the flow field inside of the nozzle. The five hole probe is a miniature one, with a probe head diameter of 1.67 mm. The five hole probe was calibrated so that it could measure flows with a velocity direction oriented ±30 degrees to the probe tip in both the yaw and pitch directions. The estimated errors in the five hole probe measurements are given by Sitaram et al. (1981), and are as follows: wall and blade vicinity effects, Reynolds and Mach number effects, misalignment of probe, probe blockage effect and turbulence effects. A detailed description of the error analysis and the accuracy of the five hole probe is given in Appendix B.

2.6 Hot Wire

A single sensor hot wire was used with a Dantex 55M01 anemometer, to measure the nozzle inlet turbulence intensity. The length of the tungsten sensor was 9.5 mm and its diameter was 5 microns. The probe calibrations were corrected for temperature variations using the method of Kristensen (1973). The hot wire measurement errors are discussed in detail in Appendix C.

2.7 Laser Doppler Velocimeter System

The LDV is a TSI two color, four beam, two-dimensional measuring system. It consists of a seven Watt Argon-Ion laser tuned to the 488 nm (blue) and 514.5 (green) lines. These beams are then split and one beam of each color is passed through a Bragg cell where it is frequency shifted. The beams then pass

through a 3.75 X beam expander and a 190 mm diameter lens which focuses the beams to a probe volume with a length of 0.65 mm based on the $1/e^2$ intensity points. The half angle of the intersecting beams is 4.95 degrees. The green and blue beam pairs travel down the same optical path and are used to measure axial and tangential components of velocity, respectively. Atomized mineral oil or Rosco fog fluid is used to seed the flow. Scattered light from the seed particles passing through the probe volume is collected on-axis, i.e. the receiving optics for the blue-green light is located on the blue-green transmitting optics. On-axis collection was used instead of off-axis to improve access into the rotor blade.

The LDV system is mounted on an optical table which is attached to a mechanical traverse. The traverse can move vertically, parallel and perpendicular to the AFTRF axis (the axial and radial directions, respectively) and also can be tilted. The three linear degrees of freedom plus tilt enables positioning the probe volume very accurately.

The flow in the AFTRF in the nozzle is measured through a curved Plexiglas window, conforming to the inside of the casing and in the rotor through a flat glass window. Both the Plexiglas and the glass are 3.175 mm (1/8 inch) thick. The beams are aligned through the glass by placing a blade solid surface inside the AFTRF at the probe volume, disconnecting the photomultiplier and attaching the eyepiece to the receiving optics to see the probe volume. The photomultipliers are then attached and the Bragg cells turned on. If both probe volumes are aligned correctly a clear sine wave with the downmix frequency set by the frequency shifter will be visible on the oscilloscope.

The nozzle, rotor and endwalls were painted with a high temperature flat black paint to reduce reflections. Both regular flat black and fluorescent orange paint were tried, but the laser beams burnt off these paints.

The LDV system is free to acquire velocity measurements whenever a seed particle crosses the LDV probe volume. In the rotor flow field , this results in the random acquisition of many velocity measurements during every rotor revolution. Thus, an optical shaft encoder has been attached to the turbine shaft. This encoder divides one revolution of the rotor into 6000 counts and since there are 29 rotor blades, this comes to 206.9 counts per rotor passage. One rotor passage is then divided into 50 measurement windows, each which have 4.14 counts and is 1.72 mm in length at midspan. Each velocity measurement is tagged with the angular position of the rotor by means of the optical encoder.

Since a two dimensional LDV is used for measurements in the AFTRF, only the properties in the axial and tangential directions are measured. In order to reduce the reflections of the laser beams from the glass or Plexiglas window on the receiving optics, the LDV system is offset in the tangential directions by 7.6 degrees. This causes the tangential velocity to be in error by a small amount ($< 1\%$) which was considered acceptable.

There are two methods that can be used to acquire the data inside the rotor. The first method is for data to be recorded only when a measurement window is enabled. The advantage of this method is that the data is for only one measurement location which makes post processing easier. The disadvantage is that since LDV data is acquired only at one measurement window at a time, the AFTRF will have to run a long time to complete the measurements in an entire rotor passage.

The second method is to take the data at all the rotor locations at once, tagging each of them with the appropriate rotor location using the encoder. Then after the measurement is done, the data is sorted according to rotor shaft location. The advantage of this method is that the measurements at all the tangential locations in a blade passage will be acquired at once, thus shortening the time it

takes to complete the measurements in the rotor passage. The disadvantage is that more post processing of the data needs to be done (because the data has to sorted according to rotor shaft location). The second method will be used since speed in acquiring the data is more important than speed in post processing the data.

To process the data, two counter-type signal processors (one for each channel) are interfaced with a IBM PC compatible computer. The signal from the photomultiplier tube is fed into the counter through the frequency shifter. In the counter, the signal is passed through a band pass filter to reduce noise (and the pedestal if not frequency shifted). The counter measures the time a particle takes to cross eight fringes with a resolution of one nanosecond. To validate the signal, the transit time for crossing five and eight fringes is compared and when the two agree within a selected percentage, the data is accepted as a valid signal. The signal is then digitized and sent to a buffer where it is held. If a valid burst from the other channel is received within a preselected time interval (typically 50 μsec in the nozzle and 10 μsec in the rotor) the measurement is then sent to the computer and stored. If not the measurement is rejected and the process starts again.

Atomized mineral oil was used as seeding in the nozzle. TSI's six jet seeder is used to atomize the oil. The atomized oil has an aerodynamic mean diameter of 1 μm (TSI, 1987). A 25.4 mm (one inch) diameter tube is connected to the atomizer and is positioned 0.9 m (three feet) upstream of the AFTRF bellmouth intake (1.5 m (five feet) upstream of the nozzle). The seeding tube can be moved radially and circumferentially in order to optimize the data rate each time the LDV probe volume is moved. Atomized mineral oil was tried in the rotor also, but the window became covered with oil very quickly (within 1 minute) and it became impossible to take measurements. A Rosco fog machine was used to seed the flow in the rotor. The seed particles exiting the fog machine have an aerodynamic mean diameter

and standard deviation of 1.1 and 1.9 μm, respectively (Wiedner, 1988). The fog machine produces a high data rate and does not dirty the window so quickly.

2.8 LDV Data Analysis

The data analysis procedure is based on the methods of Strazisar (1985) and Suder et al. (1987). The LDV does not measure the instantaneous velocity V(t) continuously as a hot wire does; instead it measures discrete samples of V(t). For each measurement position, the data at all the rotor shaft locations will be acquired at once, tagging each of them with the appropriate rotor location using the encoder. Then after the measurement is completed, the data are sorted according to rotor shaft location. In the stationary frame of reference, the rotor shaft positions can represent values of time, thus the instantaneous velocity V(t) can be represented by the discretized instantaneous velocity V_i, which is the velocity at one particular rotor shaft position during a given rotor revolution. The instantaneous velocity is than decomposed in the following manner,

$$V(t) = V_i = \overline{\overline{V}} + \tilde{V}_{rev} + \hat{V}_{rev} + V' \qquad (2.1)$$

where $\overline{\overline{V}}$ is the time-average velocity, $\tilde{V}_{rev}$ is the revolution periodic velocity (temporally fluctuating component), $\hat{V}_{rev}$ is the revolution aperiodic velocity (passage to passage average) and V' is the unresolved velocity. The revolution periodic velocity can further be subdivided as follows:

$$\tilde{V}_{rev} = \tilde{V}_b + \hat{V}_{rev} \qquad (2.2)$$

where $\tilde{V}_b$ is the blade periodic velocity and $\hat{V}_b$ is the blade aperiodic velocity. The time averaged value describes a steady-state flow field which is the same in each blade of a blade row. The periodic component is caused by the relative motion between the blade rows. The aperiodic velocity results from different number of nozzle or rotor blades in each stage. In a single stage turbomachine, the aperiodic velocity should be zero (provided there are no differences in each blade passage due to manufacturing tolerances and blade installation).

Since the flow field in turbomachinery is not stationary, ensemble averaging is needed to decouple the periodic unsteady velocity from the unresolved velocity. The ensemble-average of the velocity for each measurement window can be calculated according to the equation

$$\overline{V} = \frac{1}{n} \sum_{i=1}^{n} V_i \qquad (2.3)$$

where $\overline{V}$ is the ensemble-averaged velocity, V_i is the instantaneous velocity measured at a particular measurement window during a given rotor revolution and n is the total number of measurements at that measurement window. The unresolved velocity for each measurement window can also be calculated as

$$V' = V_i - \overline{V} \qquad (2.4)$$

and the corresponding variance as

$$\overline{V'^2} = \frac{\left[\sum_{i=1}^{n} \left(V_i - \overline{V} \right)^2 \right]}{(n-1)} \qquad (2.5)$$

The level of unresolved unsteadiness in each measurement window is

determined by the variance.

The time-averaged velocity $\overline{\overline{V}}$ is obtained by averaging all the ensemble-averaged velocities in each measurement window as follows,

$$\overline{\overline{V}} = \frac{1}{NW} \sum_{j=1}^{NW} \overline{V}$$

(2.6)

where NW is the total number of measurement windows. The time-averaged velocity is a time average of all measurements acquired at a fixed point in space. To find the revolution periodic and aperiodic components, first a time-averaged velocity over one blade passage must be found which is

$$\overline{\overline{V}}_b = \frac{1}{NWB} \sum_{j=1}^{NWB} \overline{V}$$

(2.7)

where NWB is the number of measurement windows in one blade passage. The revolution periodic velocity is then obtained from the equation

$$\tilde{V}_{rev} = \overline{V} - \overline{\overline{V}}_b$$

(2.8)

and the revolution aperiodic velocity is

$$\hat{V}_{rev} = \overline{\overline{V}}_b - \overline{\overline{V}}$$

(2.9)

The blade periodic velocity can then be found by averaging the revolution periodic component for each blade passage over all the blade passages as follows

$$\tilde{V}_b = \frac{1}{NB} \sum_{i=1}^{NB} \tilde{V}_{rev}$$

(2.10)

where NB is the total number of blades. The blade aperiodic component is then calculated as

$$\hat{V}_b = \tilde{V}_{rev} - \tilde{V}_b \qquad (2.11)$$

This velocity decomposition is shown in Figure 2.4 (which is described in more detail below).

A program was written to decompose the velocity into the various components. In order to verify that the program works correctly a sample input was tested. The sample input, S, is composed of

$$S = 0.5 + 0.5\sin 29x + 0.2\sin x \qquad (2.12)$$

where sin 29x has a period of one blade passage and sin x has a period of one revolution. S can be thought of as the ensemble-averaged velocity for each measurement window. The input and output to the program is presented in Figure 2.4. The figure shows that the program successfully decomposed the test input, S, into its various components.

Using this program to decompose the measured data in the rotor, the rms of the total aperiodic unsteadiness is found to be low. The total aperiodic unsteadiness is equal to

$$\hat{V}_T = \hat{V}_{rev} + \hat{V}_b \qquad (2.13)$$

The rms of the total aperiodic unsteadiness is less than 1.0% of the pitchwise averaged relative velocity everywhere in the rotor flow field. This demonstrates the
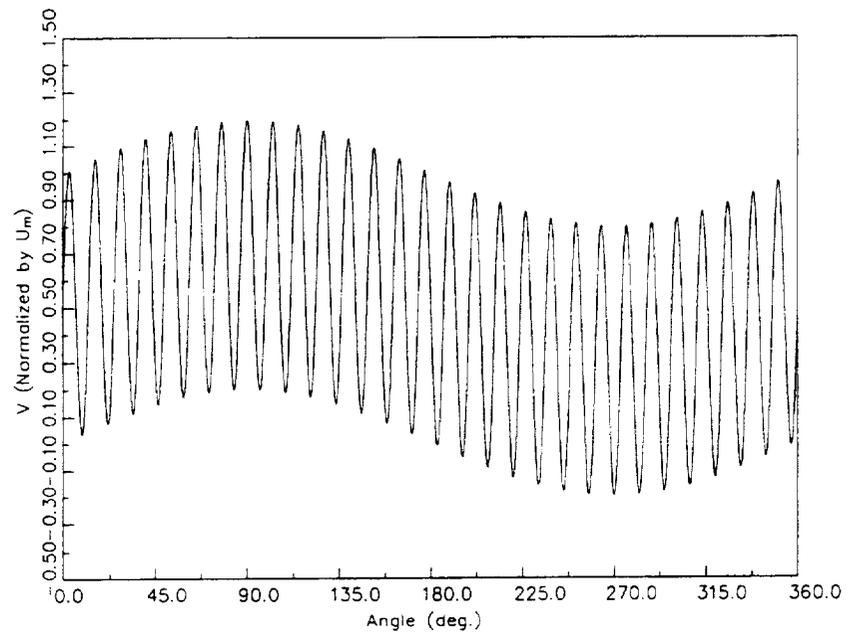
(a)
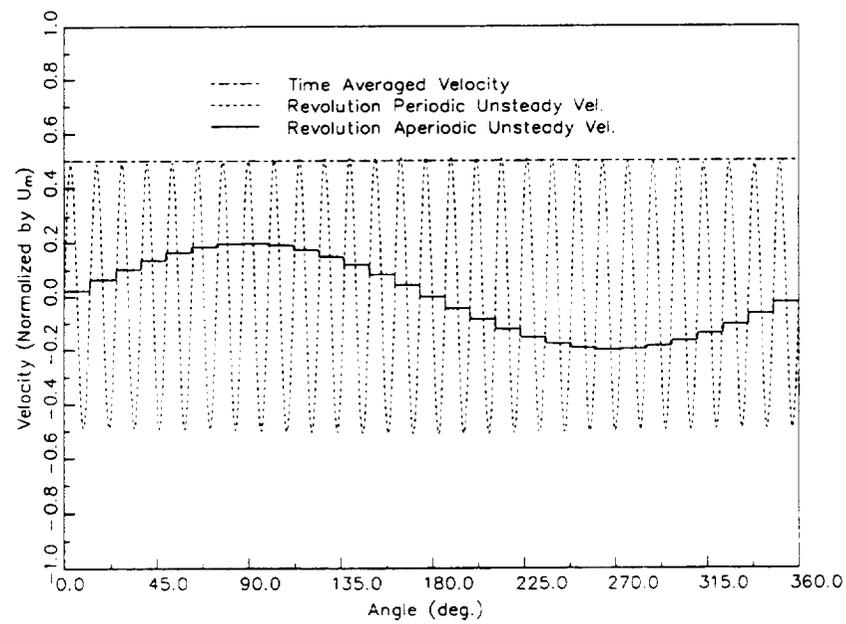
(b)

Figure 2.4. Decomposition of Instantaneous Velocity

(a) Instantaneous Velocity (Test Input)

(b) Decomposed Velocity
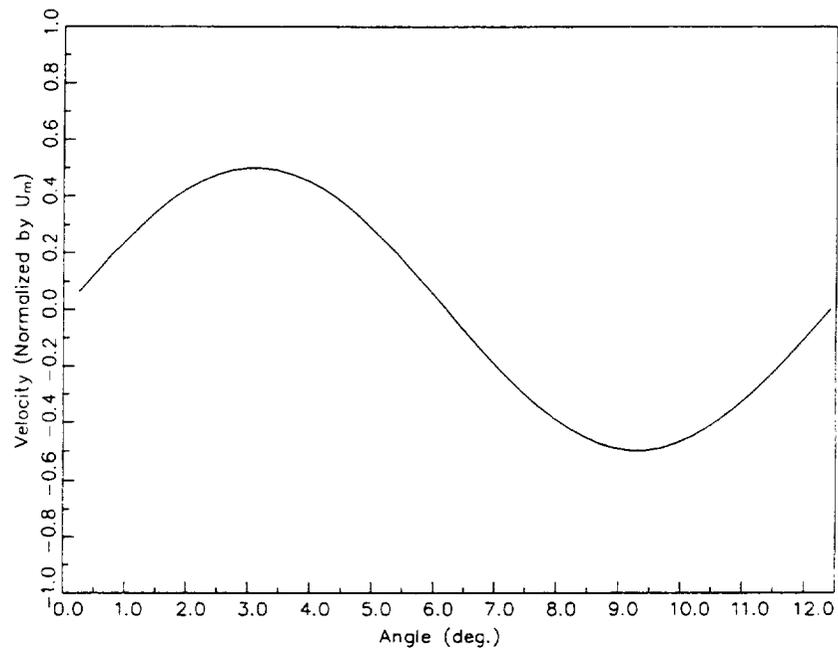
(c)
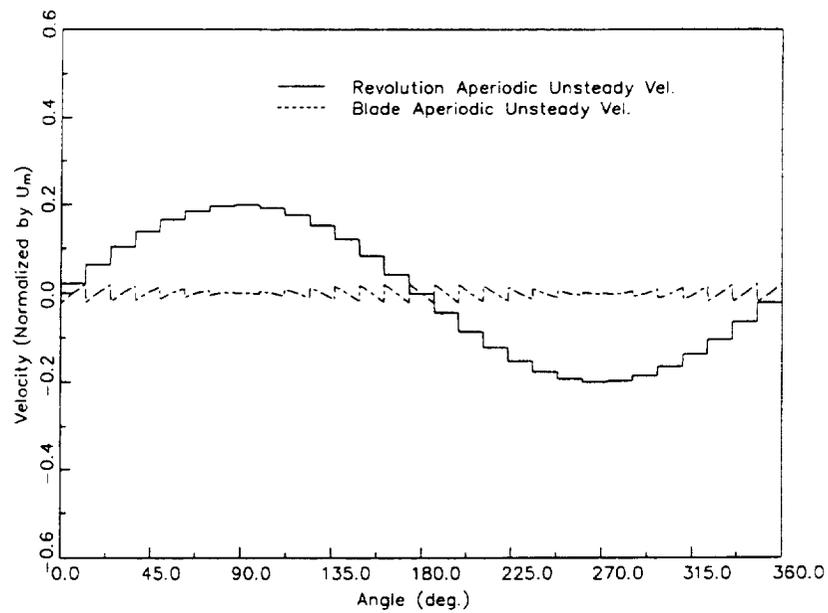
(d)

Figure 2.4 (Cont.). Decomposition of Instantaneous Velocity

    (a) Blade Periodic Component

    (b) Revolution and Blade Aperiodic Components

periodicity of the flow field between the individual rotor passages of this turbine. Thus all ensemble-averaged velocity components can be spatially phase-locked averaged as follows

$$\breve{G}_j = \frac{\sum_{i=1}^{N_{RB}} G_{j,i}}{N_{RB}} \qquad (2.14)$$

where G represents either the ensemble-averaged velocity or variance, the subscript i determines the particular rotor passage and j is the measurement window location relative to the i'th rotor passage and N_{RB} is the number of rotor blades. Since the passage to passage variation in velocity is very small, calculation of the phase-locked average velocity and ensemble averaged velocity are done simultaneously. After the data is acquired, they are placed into the appropriate measurement window. The window from individual blade passages are then overlaid so that an "average" rotor blade passage is obtained. The ensemble-averaged velocity and variance is then calculated for each bin in the "average" blade passage. This is done to increase the number of measurements in each window, since the bin count (number of measurements in each window) is low in certain bins in a few blade passages such as bins in the blade boundary layer and wake center just downstream of the rotor. This increases the number of measurements that the ensemble-averaged velocity and variance is derived from, thus reducing the error. Since all results from now on are phase-locked averaged, the superscript ∪ will be dropped hereafter.

The aperiodic velocity components are small and can be neglected and thus equation 2.1 reduces to

$$V(t) = \overline{\overline{V}} + \tilde{V} + V' \qquad (2.15)$$

where $\overline{\overline{V}}$ is the time-averaged velocity (the subscript b is dropped since $\overline{\overline{V}}_b = \overline{\overline{V}}$ when $\hat{V}_b = 0$) and $\tilde{V}$ is the periodic velocity ($\tilde{V}_b = \tilde{V}_{rev}$ when $\hat{V}_b = 0$). The decomposition for this "average" rotor blade passage is shown in Figure 2.5. From the above velocity decomposition, the axial, tangential and cross velocity correlations (both periodic and unresolved) can be computed, and are discussed in more detail in Chapter 6.

2.9 LDV Measurement Errors

The error in locating the probe volume is +/- 0.03 degrees in the circumferential direction, +/- 0.2 mm in the radial direction and +/- 0.25 mm in the axial direction. Errors in the measurement arise due to fluctuations in the flow field and random noise in the photomultiplier tube signal, statistical or velocity bias and angle bias, among others. The LDV measurement errors are discussed in detail in Appendix D.
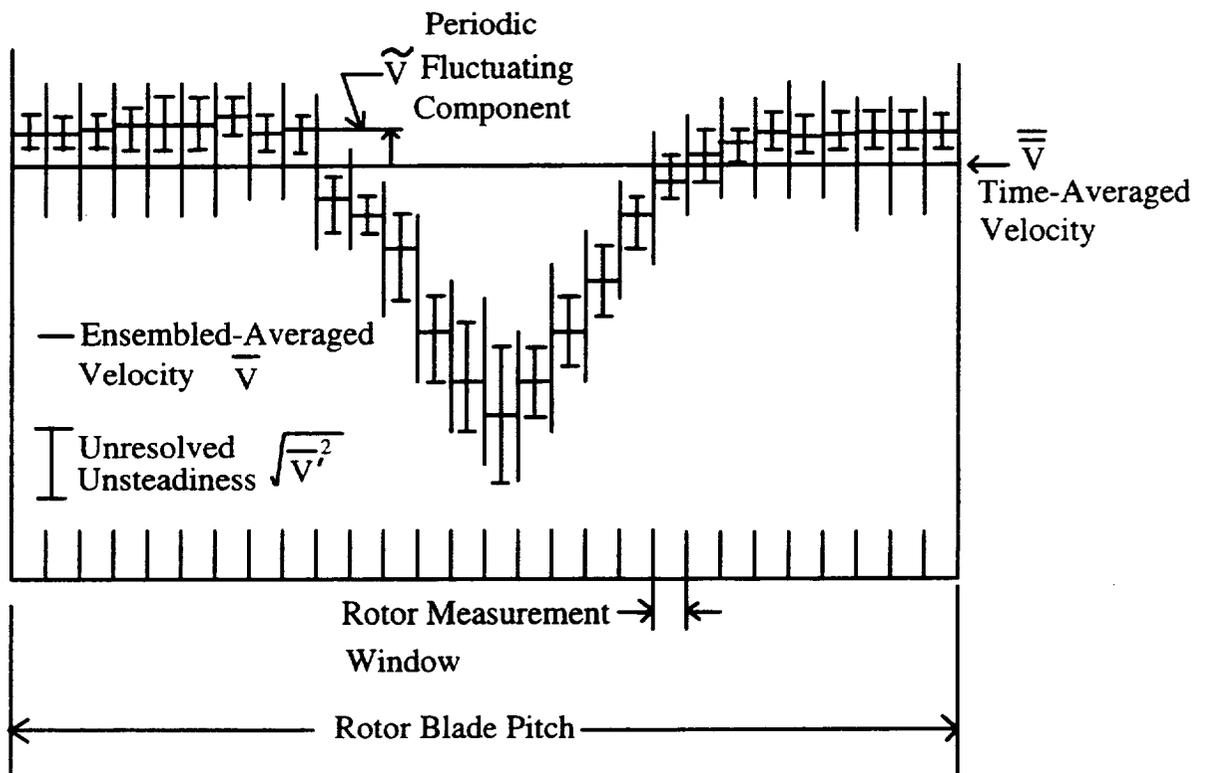
Figure 2.5. Velocity Decomposition for Phase-Locked Averaged Rotor Blade

CHAPTER 3

RADIAL DISTRIBUTION OF FLOW PROPERTIES AT DESIGN AND OFF DESIGN CONDITIONS

The overall performance of the AFTRF is discussed in this chapter. The overall performance consists of determining the pressure drop across the turbine stage at various corrected mass flow rates. These quantities were determined from a radial survey of the flow properties at both upstream of the nozzle and downstream of the rotor. The performance was measured before other measurements in the AFTRF were taken so that the experimental operating point could be selected. The axisymmetry of the inlet flow field of the turbine is also discussed in this chapter. A five hole probe was used for both the performance measurements and to determine the inlet flow velocity profile axisymmetry while a single sensor hot wire was used to measure the inlet turbulence intensity. The performance measurements were obtained using five hole probe radial surveys taken one chord upstream of the nozzle and two chords downstream of the rotor. The inlet flow field axisymmetry was found using radial surveys by both the hot wire and five hole probe taken at three equally spaced circumferential locations one chord upstream of the nozzle.

3.1 Nozzle Inlet Flow Field

In order to check for the flow axisymmetry upstream of the nozzle and to determine the turbulence intensity profile upstream of the nozzle, a single sensor hot wire probe and a miniature five-hole probe were used to measure the radial distribution of axial turbulence intensity and mean velocities at three tangential
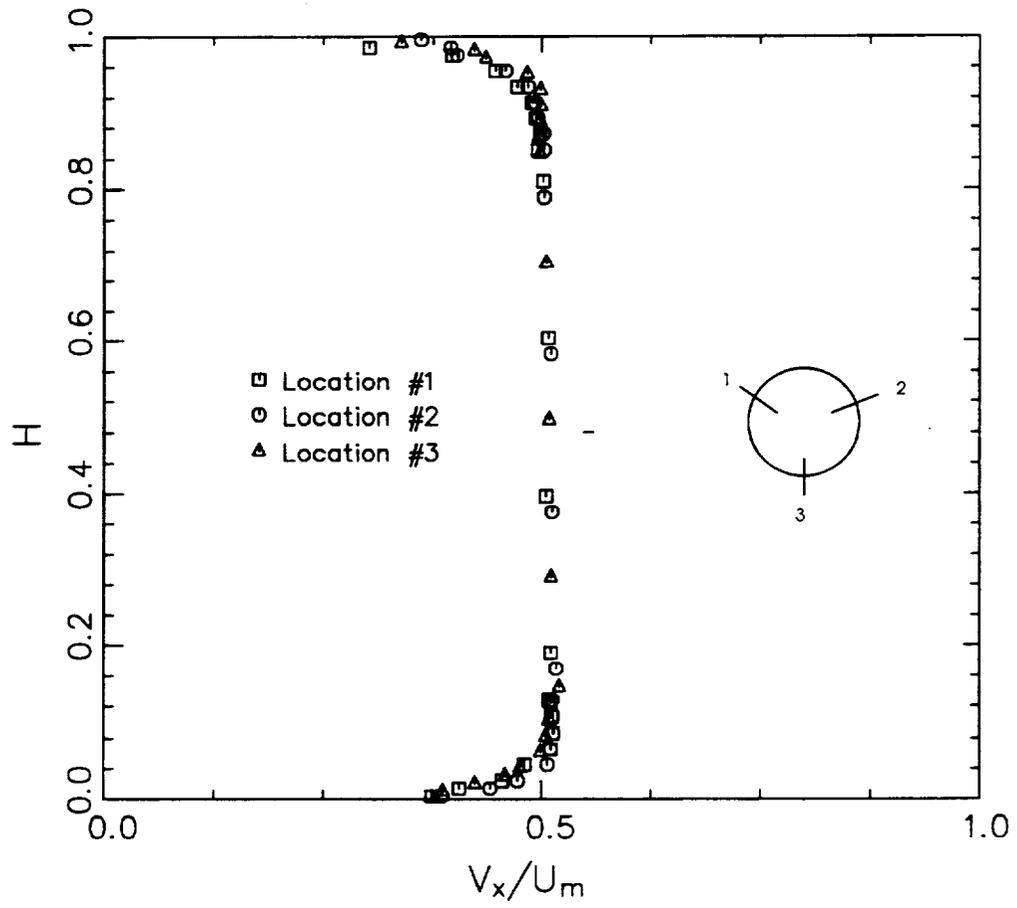
Figure 3.1. Axisymmetric Flow Field 1 Chord Upstream of Nozzle

locations (120 degrees apart) at the inlet. The axial velocity, presented in Figure 3.1, is found to be nearly identical at these locations, being within 0.68% of each other at midspan, thus confirming the axisymmetric nature of the flow. The axial turbulence intensity, shown in Figure 3.2, is nearly constant at around 0.75 to 1.5 percent, except near the hub and casing. The static and stagnation pressure profiles are shown in Figure 3.3. The stagnation pressure was nearly uniform, with the exception of locations inside the wall boundary layer. The static pressure was also uniform radially. The static pressure measured by the five hole probe is compared to the static pressure measured by static pressure taps on the casing and hub endwalls. The agreement is good, which gives confidence in the accuracy of the static pressure measurements by the five hole probe. The axial, tangential and radial velocity profiles are shown in Figure 3.4. The freestream velocity was 29.0 m/s with a Reynolds number of 3.5 x 10^5 based on a basic nozzle vane chord at midspan. The wall boundary layers were turbulent, with a thickness of approximately 5% blade span at the hub and 10% blade span at the tip. (The displacement and momentum thicknesses for the hub wall boundary layer were 0.80 mm and 0.66 mm, respectively, while for the casing boundary layer, the displacement and momentum thicknesses were 1.15 mm and 1.02 mm, respectively.) These figures also show that the radial and tangential velocities are almost negligible upstream of the nozzle.

3.2 Overall Performance

In order to determine the overall performance of the turbine, radial surveys of flow properties were measured one chord upstream of the nozzle and two chords downstream of the rotor. The performance measurements were carried out at five
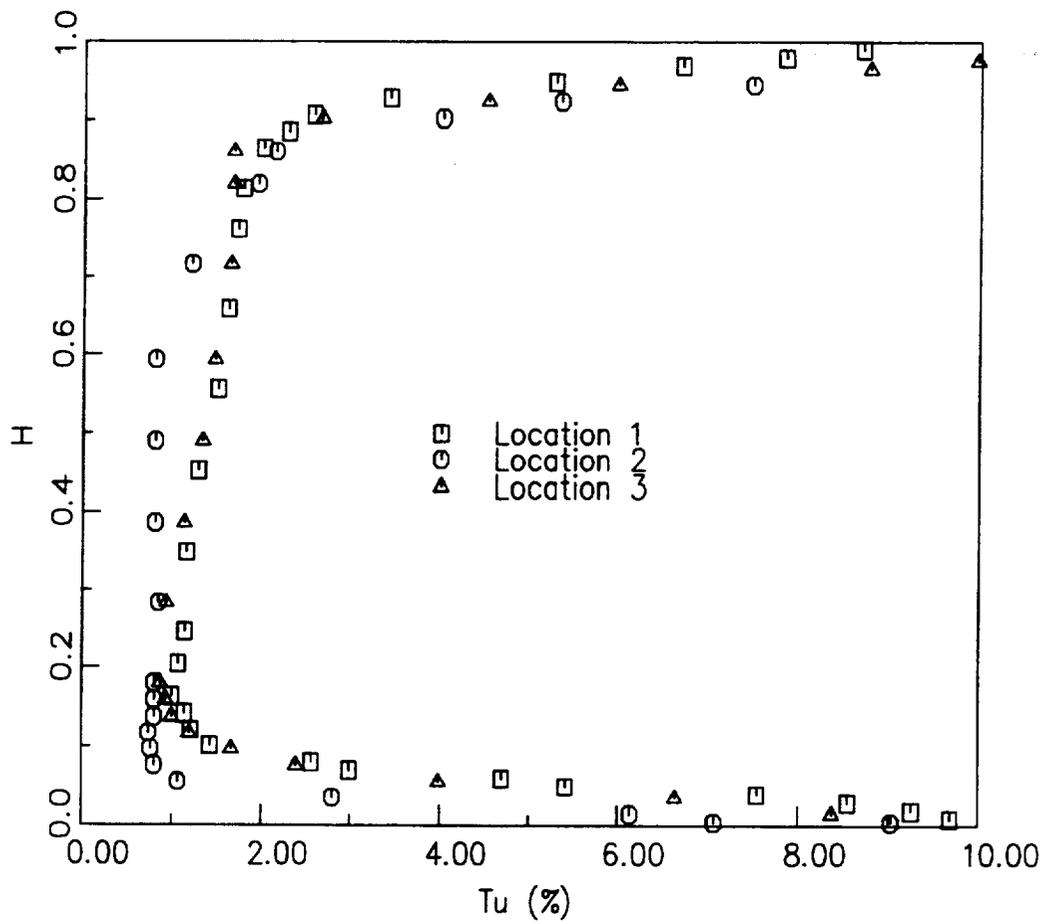
Figure 3.2. Turbulence Intensity 1 Chord Upstream of Nozzle

Operating   Design
Condition   Values
(m=10.5 kg/s)   (m=11.0 kg/s)

Ψ_{LOSS_1} ▫   ------

Ψ_{s_1} ⊙   -----

Endwall Ψ_{s_1} ✱

H

0.0   0.1   0.2   0.3   0.4

Ψ_{LOSS_1} & Ψ_{s_1}
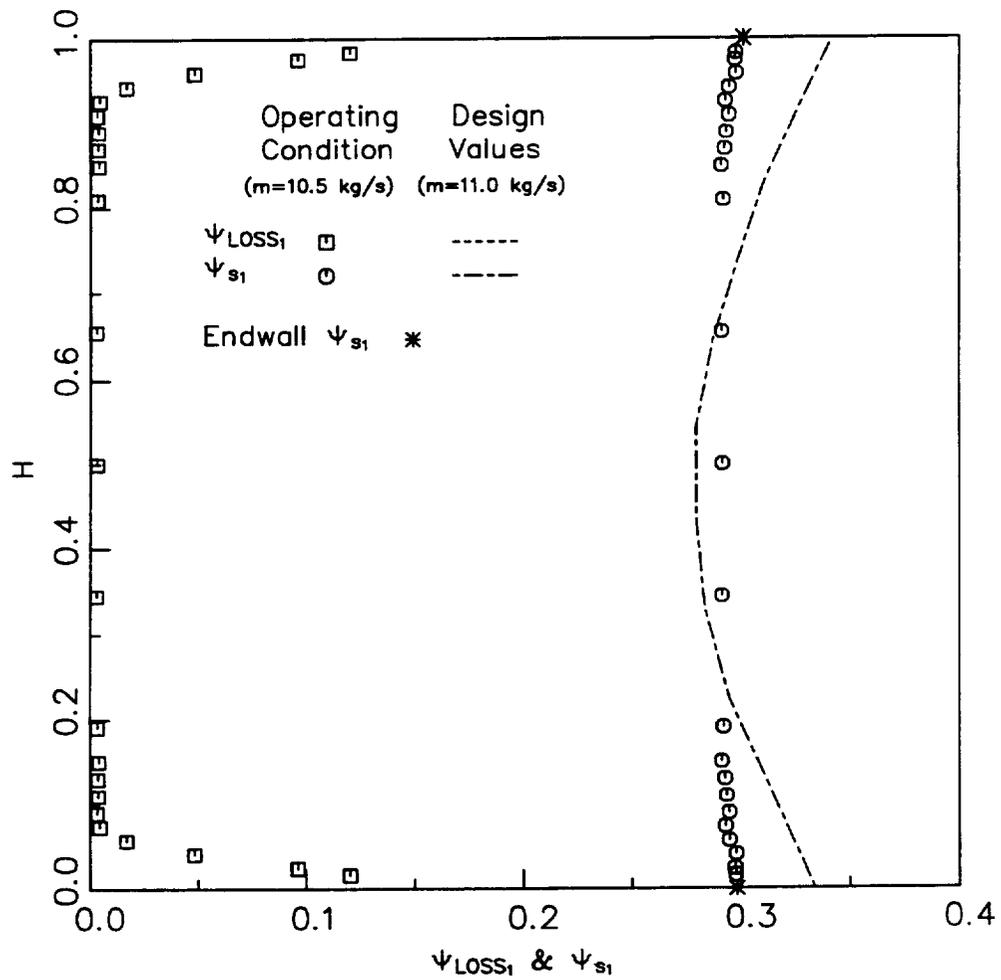
Figure 3.3. Total and Static Pressure Profiles 1 Chord Upstream of Nozzle
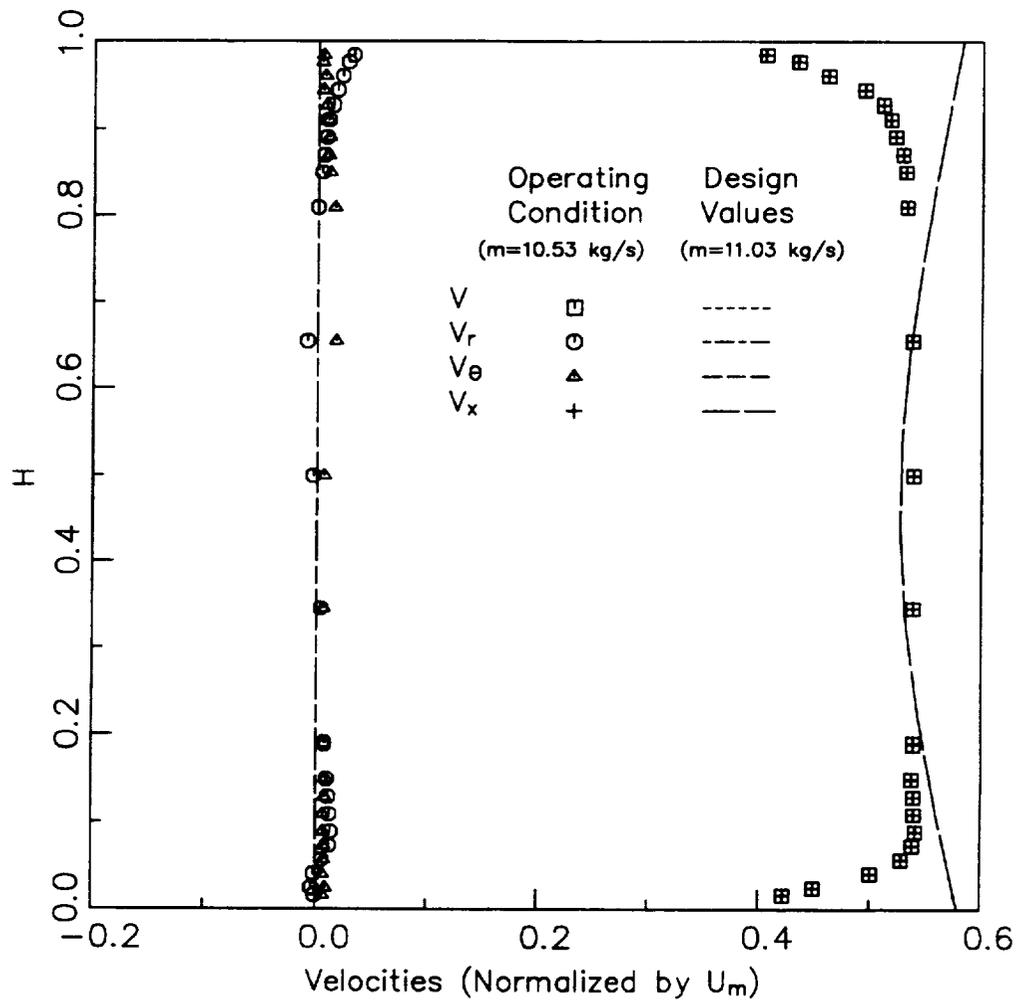
Figure 3.4. Velocity Profiles at 1 Chord Upstream of Nozzle

different mass flows at the corrected design speed of (1300 RPM), using a miniature (1.67 mm) five hole probe. The choice was limited, due to series operation of two downstream axial flow fans. The five-hole probe data included large number of radial stations, with close intervals inside the hub and annulus wall boundary layers. Hence the mass flow calculated includes the blockage due to the annulus and the hub wall boundary layers. The pressure drop coefficient (loading coefficient) is mass-averaged based on the local axial velocity at exit given by

$$\overline{\Psi} = \frac{\int_h^t \Psi V_{x_3} 2\pi r dr}{\int_h^t V_{x_3} 2\pi r dr} \qquad (3.1)$$

The mass-averaged pressure drop coefficient is shown plotted against corrected mass flow in Figure 3.5. As expected, the loading coefficient varies linearly with an increase in the mass flow and the measured loading coefficients near the design mass flow are very close to the design value. The facility will be operated at $\dot{m}$ = 10.5 kg/s during the research phase of the program. The mass-averaged pressure drop coefficient is closely matched at the design and the operating conditions.

3.3 Rotor Exit Measurements

The radial distribution of total and static pressures, total, axial, radial and tangential velocities, and rotor exit flow angle at design conditions were measured two chords downstream of the rotor blade row using a five hole probe. Figures 3.6 through 3.8 show the experimental data measured close to the design point
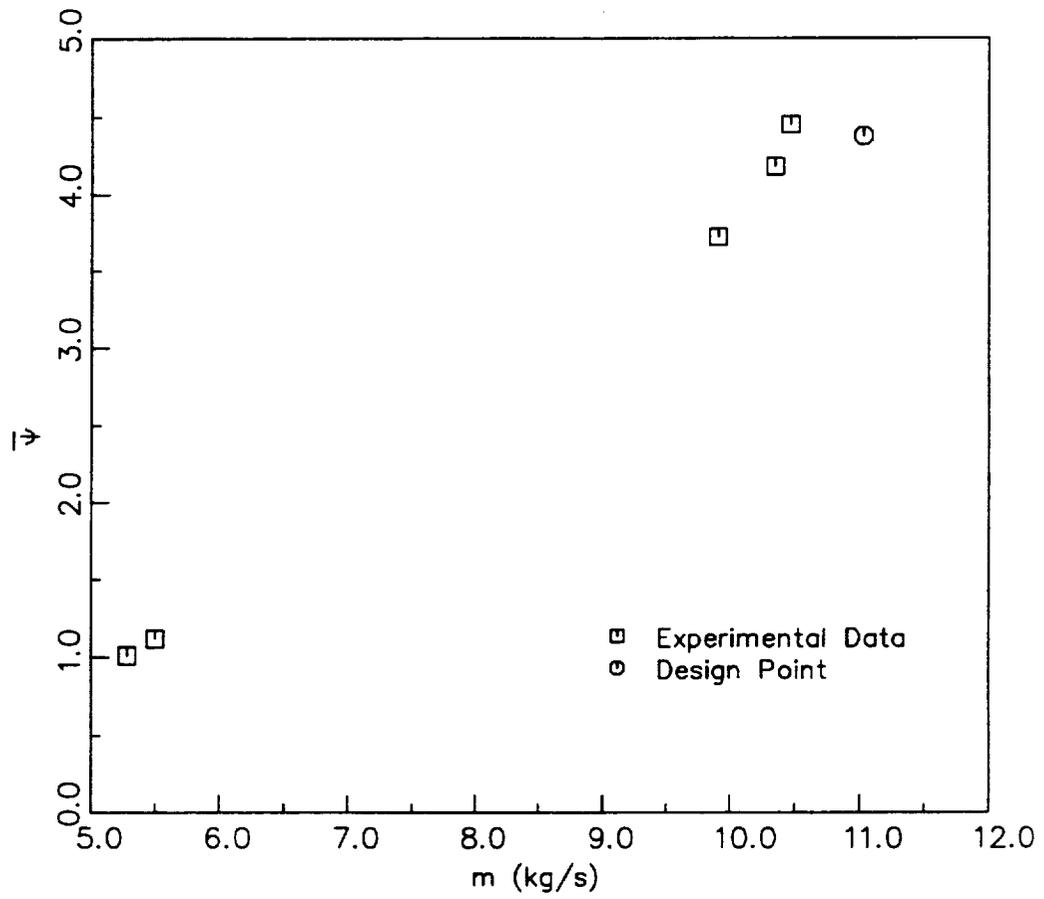
Figure 3.5. Performance Curve

Operating   Design
Condition   Values

(m=10.53 kg/s)   (m=11.03 kg/s)

Ψ □   ----------

Ψ_s ⊙   -·-·-·-

H

1.0   0.8   0.6   0.4   0.2   0.0

4.25   4.50   4.75   5.00   5.25

Ψ & Ψ_s
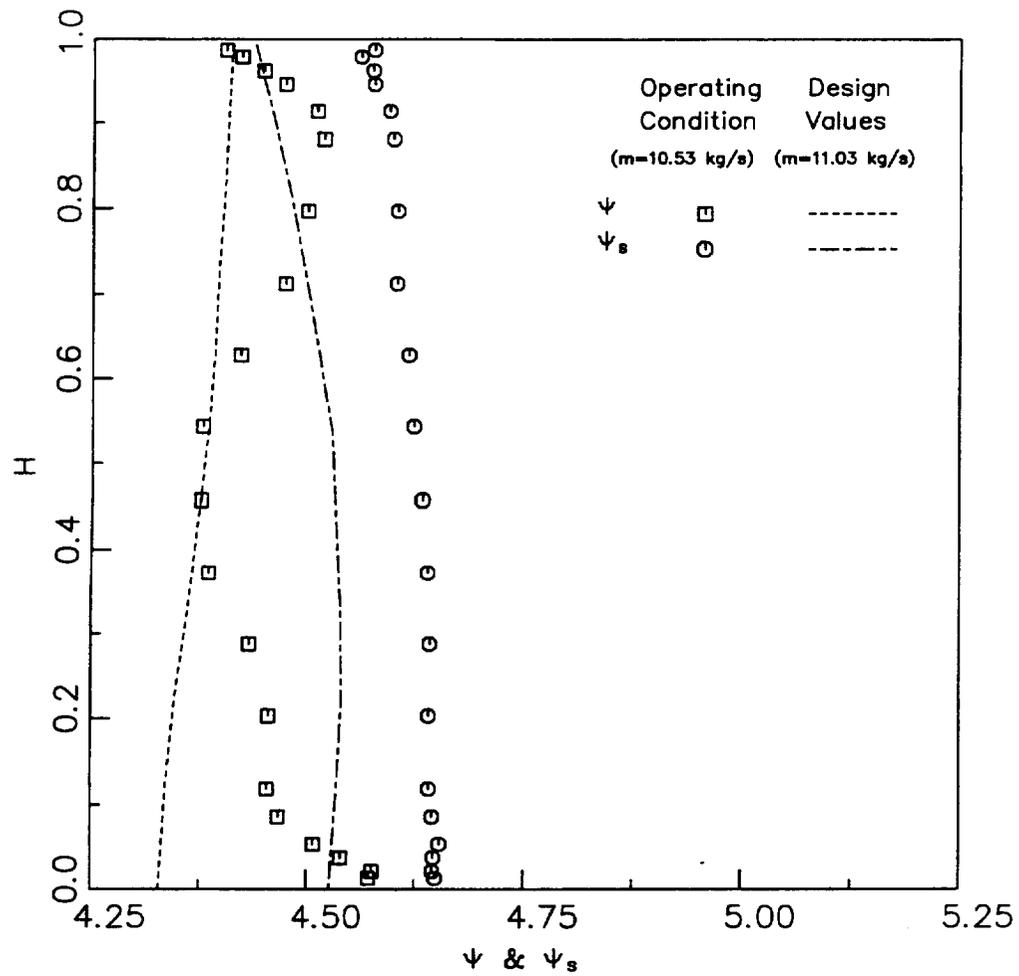
Figure 3.6. Total and Static Pressure Profiles 2 Chords Downstream of Rotor

Operating
Condition
(m=10.5 kg/s)

Design
Values
(m=11.0 kg/s)

V

Vx

Vθ

Vr

H

-0.6   -0.4   -0.2   0.0   0.2   0.4   0.6   0.8

1.0   0.8   0.6   0.4   0.2   0.0

Velocities (Normalized by Um)
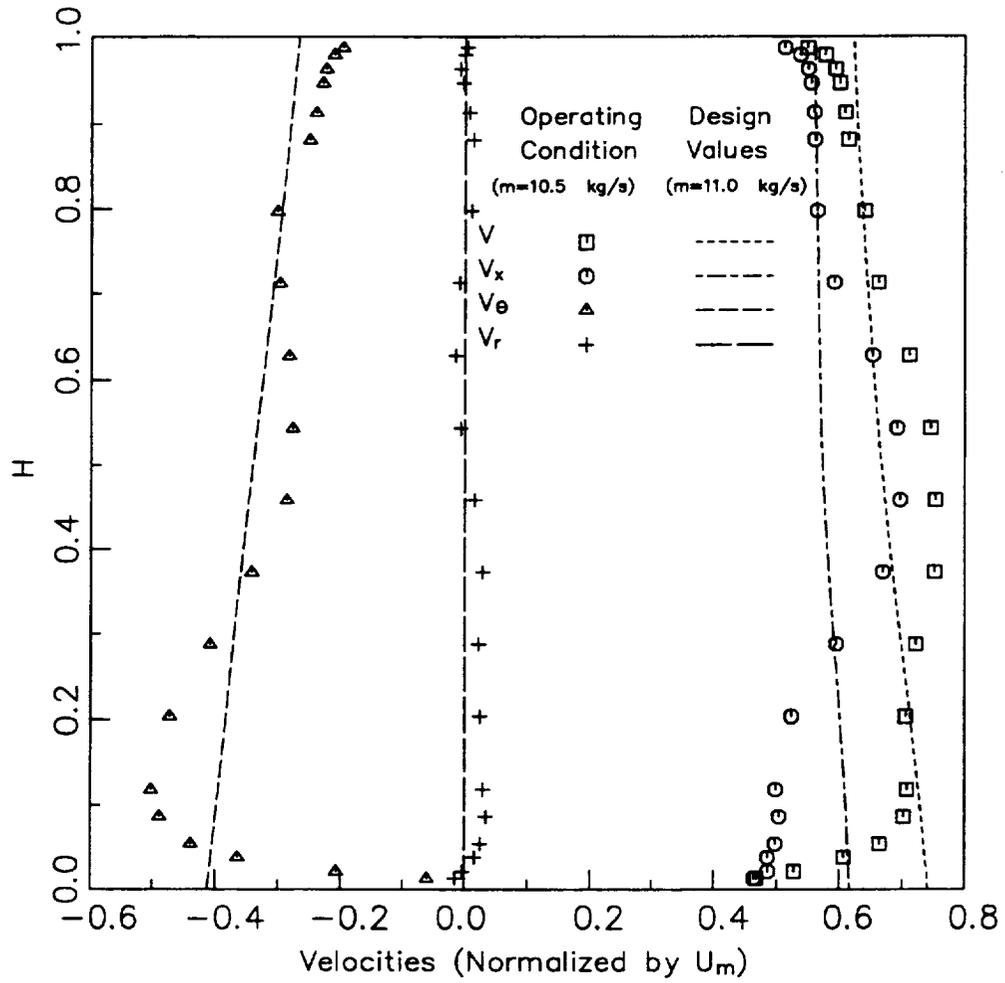
Figure 3.7. Velocity Profiles 2 Chords Downstream of Rotor
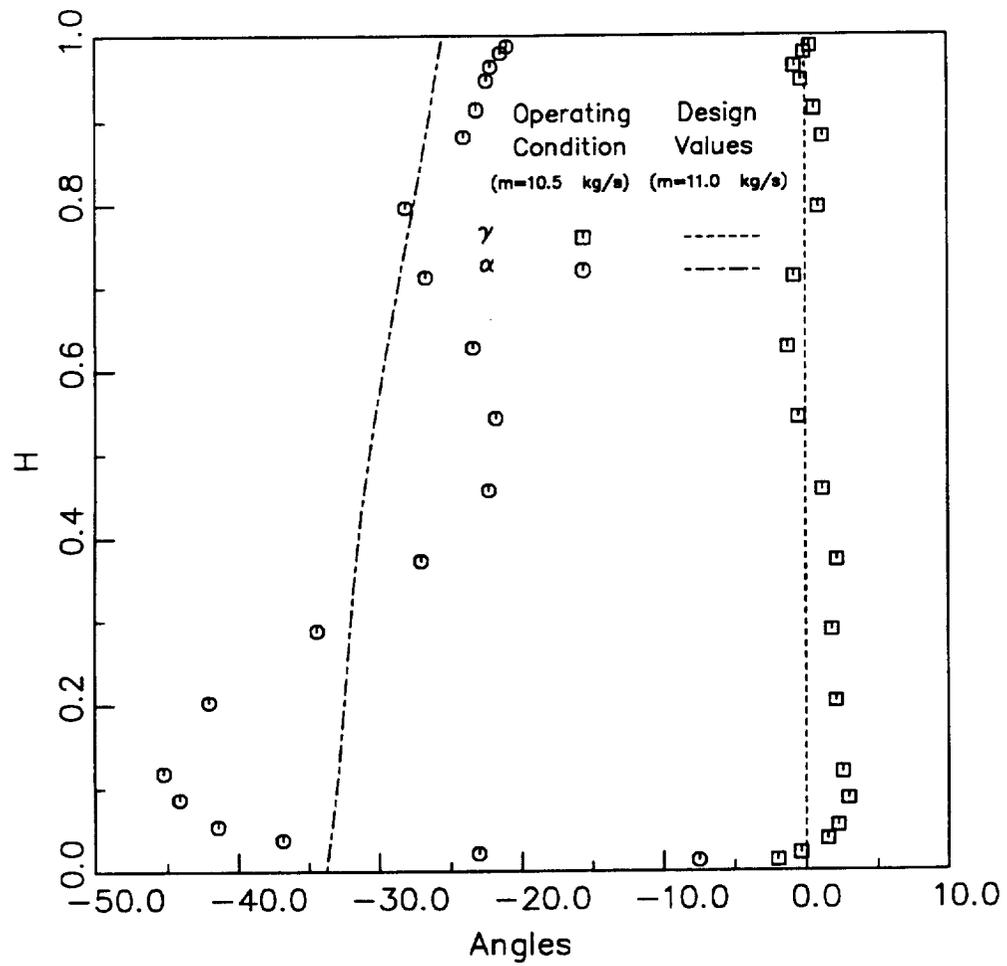
Figure 3.8. Radial and Tangential Flow Angles 2 Chords Downstream of Rotor

$\dot{m}$ = 10.5 kg/s). These results are compared with the design distribution at $\dot{m}$ = 11.0 kg/s, which is close to the operating condition.

The radial distribution of stagnation pressure drop coefficient (loading coefficient, Ψ) and the static pressure drop coefficient (Ψ_s) are shown compared with values at the design point in Figure 3.6. The experimental values are higher design as also is the mass averaged loading coefficient presented in Figure 3.5. The cumulative effect of nozzle and rotor secondary flow near the hub wall results in higher loading coefficient in this region. The leakage flow and the resulting underturning is responsible for lower loading coefficient in the tip region (H > 0.95). The underturning is prevalent in 5% of the span from the tip. The secondary flow, which overturns the fluid, has a major effect in increasing the pressure drop, reaching a maximum value at H = 0.90. The minimum pressure drop occurs near the midspan, while the maximum pressure drop occurs near the hub and the endwall region. Hence, this flow is dominated by the hub and the annulus wall secondary flows and the tip leakage flow. The presence of loss core in the hub region, which moves radially outward results in lower loading coefficient (due to higher losses) away from the hub wall. This is evident from the loading coefficient distribution away from the hub and the annulus walls. The profile boundary layer losses are also substantial in these regions.

The radial variation of axial, absolute tangential and radial velocities are plotted in Figure 3.7. The radial velocities are negligibly small at this far downstream location. The presence of a loss core results in lower axial velocity in the hub region, and flow acceleration in other radial location (e.g. H=0.3 to 0.7). The presence of secondary flow and wall boundary layer result in low velocities in the hub and tip regions. These loss core regions tend to increase flow blockage giving rise to acceleration of the flow near the midspan region. Similar

distributions have been reported by Joslyn and Dring (1990) and Boletis and Sieverding (1991). The tangential velocity distribution shows similar trend. Near the hub wall (from H = 0 to 0.05) the effect of the wall boundary layer is evident. Higher tangential velocities are observed in the region 0.04 < H < 0.4. The tangential velocities are close to design at most other locations, with the exception of the tip regions. The effect leakage flows are clearly in the region H > 0.95, where the tangential velocities are lower.

These distributions are consistent with angle distributions (absolute flow), shown in Figure 3.8. The pitch angles are very small. The overturning of the flow near the hub wall and underturning in regions away from the hub wall is evident from Figures 3.7 and 3.8. The overturning region is confined to 0.04 < H < 0.3 in the hub region. Substantial deviation from the design distribution of yaw angle is evident from Figure 3.8. The yaw angles show substantial overturning in regions 0.04 < H < 0.3, underturning in the middle third of the blade and underturning in regions H > 0.8. Hence, four distinct regions can be recognized.

(1)   0 < H < 0.04: This is the inner region of hub wall boundary layer, where the flow is nearly axial, with boundary layer type of distribution.

(2)   0.04 < H < 0.3: This is the secondary flow and the loss core region, with large overturning (reaching peak value near H = 0.1). The axial velocities are low, tangential velocities are high and the yaw angles are large in this region. The radial velocities are small.

(3)   0.3 > H < 0.7: This is the inviscid core region. The axial velocities are higher, the tangential velocities are closer to the design and the outlet angles are smaller in this region.

(4)   0.7 < H < 0.95: This region seems to be influenced by secondary flow. The changes in outlet angle, axial velocity and tangential velocities are not as

large as those near the hub. But the fact that the flow is overturned with respect to the design indicates the presence of secondary flow in this region.

(5)   H > 0.95: This region is dominated by tip leakage effect, with appreciable underturning, low tangential and axial velocities.

These exit flow distributions are consistent with the measurements by Joslyn and Dring (1990) and Boletis and Sieverding (1991) measured at the exit of a turbine stage.

3.4 Off-Design Measurements

The AFTRF was run at four off-design conditions; one at a mass flow rate of 5.21 kg/s, the second at a mass flow rate of 5.38 kg/s, the third at a mass flow rate of 9.72 kg/s and the last at a mass flow rate of 10.35 kg/s. Figures 3.9 and 3.10 present the radial distribution of the velocities and flow angles two chords downstream of the rotor at the lowest mass flow rate ($\dot{m}$ = 5.21 kg/s). The spanwise distribution of the properties upstream of the nozzle are not presented since they are similar in shape to the design condition except that their magnitude is less. Figures 3.9 and 3.10 show that the flow properties at the off-design condition have a much smoother spanwise variation than those at the design conditions. This results from the decrease in strength of the secondary flow vortices which occurs due to two factors. The first reason is that at this off-design condition the incidence angle entering the rotor is negative, which can be seen in the velocity triangles presented in Figure 3.11 for both the off-design and design conditions at midspan. Since the flow enters the rotor at negative incidence, it experiences less turning as it passes through the rotor, which results in a decreased secondary flow strength. The second factor which causes a decreased secondary
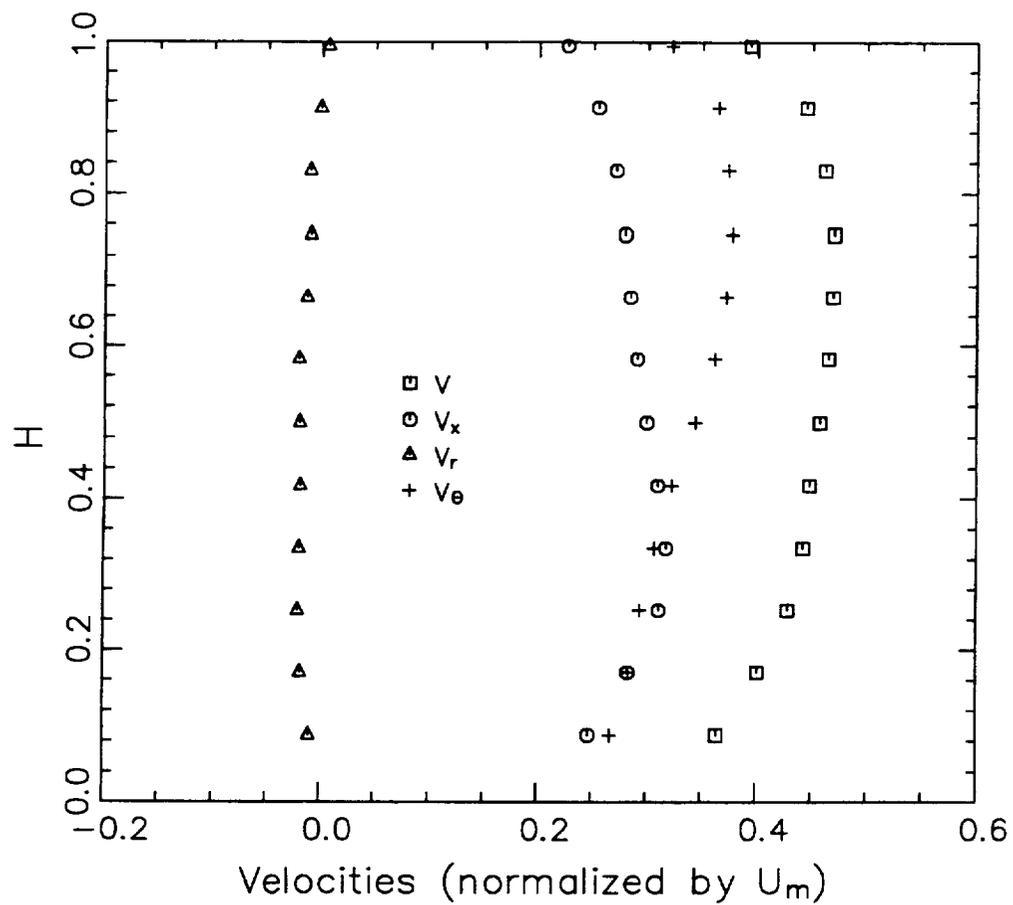
Figure 3.9. Off-Design Velocity Profiles at 2 Chords Downstream of Rotor
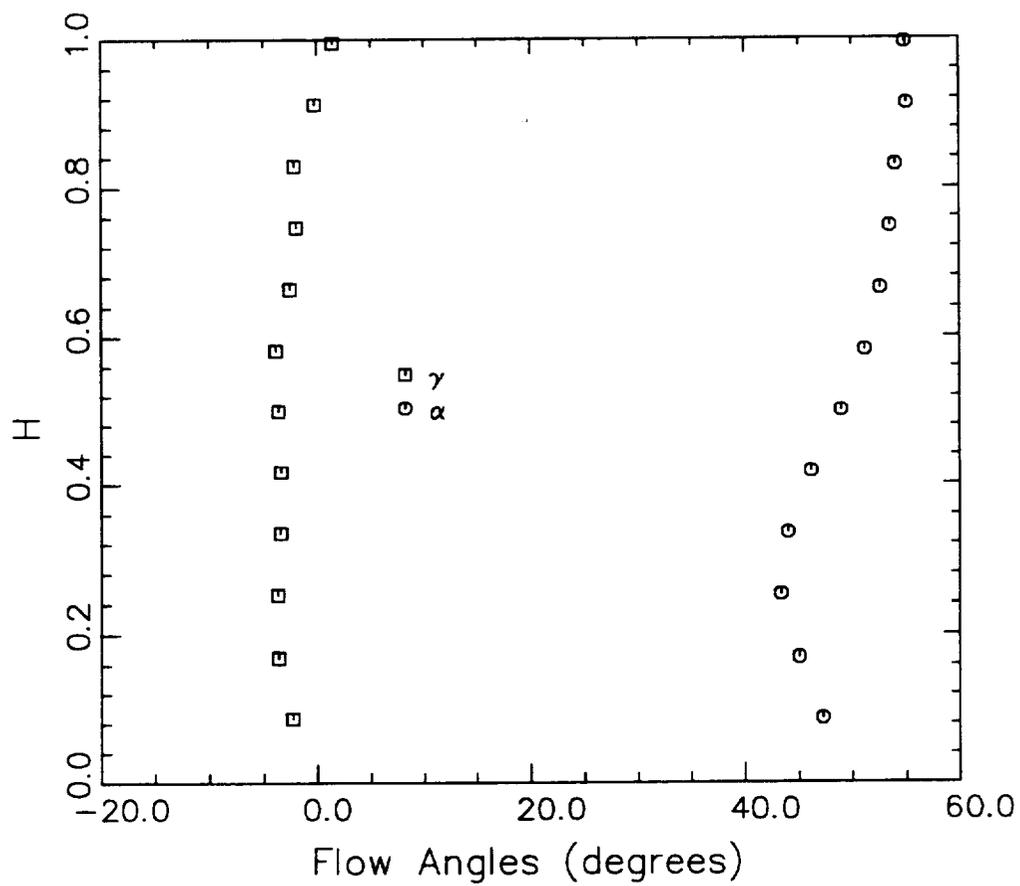
($\dot{m}$ = 5.21 kg/s)

Figure 3.10. Off-Design Radial and Tangential Flow Angle Profiles at 2 Chords

Downstream of Rotor ($\dot{m}$ = 5.21 kg/s)
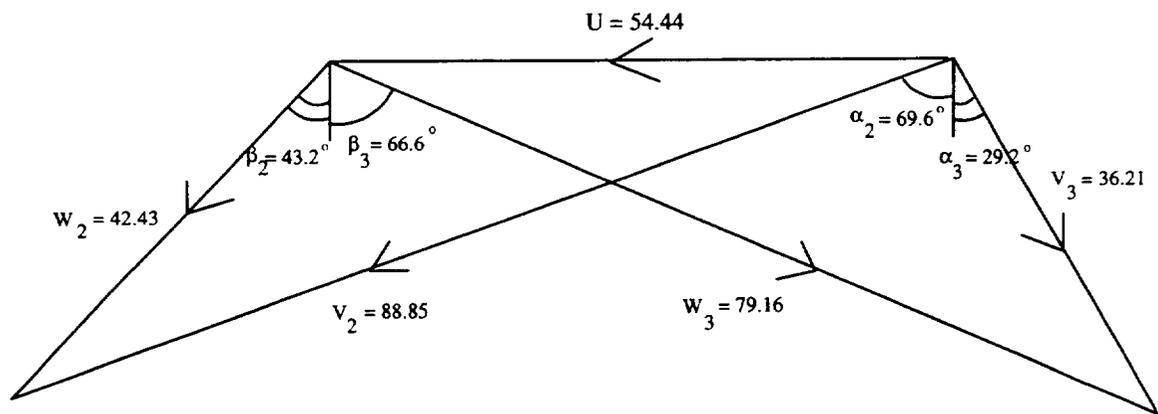
(a)
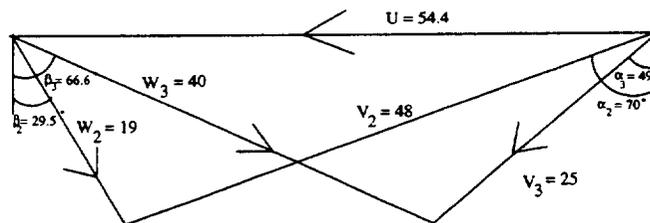
(b)

Figure 3.11. Velocity Triangles (Velocities in m/s)

(a) Design

(b) Off-Design

flow vortex strength is the decrease in Reynolds number compared to that at

design. Hodson and Dominy (1987) state that a decrease in Reynolds number

increases the rate of decay of the secondary flow regions, thus causing the

secondary flow vortices to be smaller at a given distance downstream of the rotor.

CHAPTER 4

NOZZLE PASSAGE FLOW FIELD

The nozzle passage flow field measurements were carried out in order to obtaining a better physical understanding of the evolution of secondary flow inside the blade passage. The flow field in the nozzle was measured using a variety of measuring techniques. The static pressure on the nozzle pressure and suction surface along with the hub and casing endwalls was measured using static pressure taps. The flow field near midchord ($X/C = 0.56$) was measured using a two component LDV in order to capture both the velocity and the turbulence intensity. A miniature five hole probe was used to measure the flow field near the nozzle exit ($X/C = 0.935$), so that the both the losses and secondary flow velocities and streamwise vorticity could be characterized. These measurement locations are shown in Figure 4.1. Measurements at $X/C = -1.0$, 1.025 and 1.09 were also taken and are described in Chapters 3 and 5, respectively.

4.1 Vane Surface and Endwall Static Pressure Distribution

Figure 4.2 shows the vane static pressure distribution at nine spanwise locations on the nozzle pressure and suction surfaces where X_L is the local axial distance from the nozzle leading edge and C_L is the local axial chord. The pressure is normalized by the inlet axial velocity at midspan one chord upstream of the nozzle leading edge. The variation in static pressure from the tip to midspan is much smaller than the variation from midspan to the hub. This is reflected in the

FHP &
HW

LDV

FHP

① ② ③④⑤

Casing

Nozzle

Rotor

Hub

Measurement
Locations
X /C =
①... −1.0
②... 0.56
③... 0.935
④... 1.025
⑤... 1.09

Slot

Hub B.L.

Rotating Hub B.L
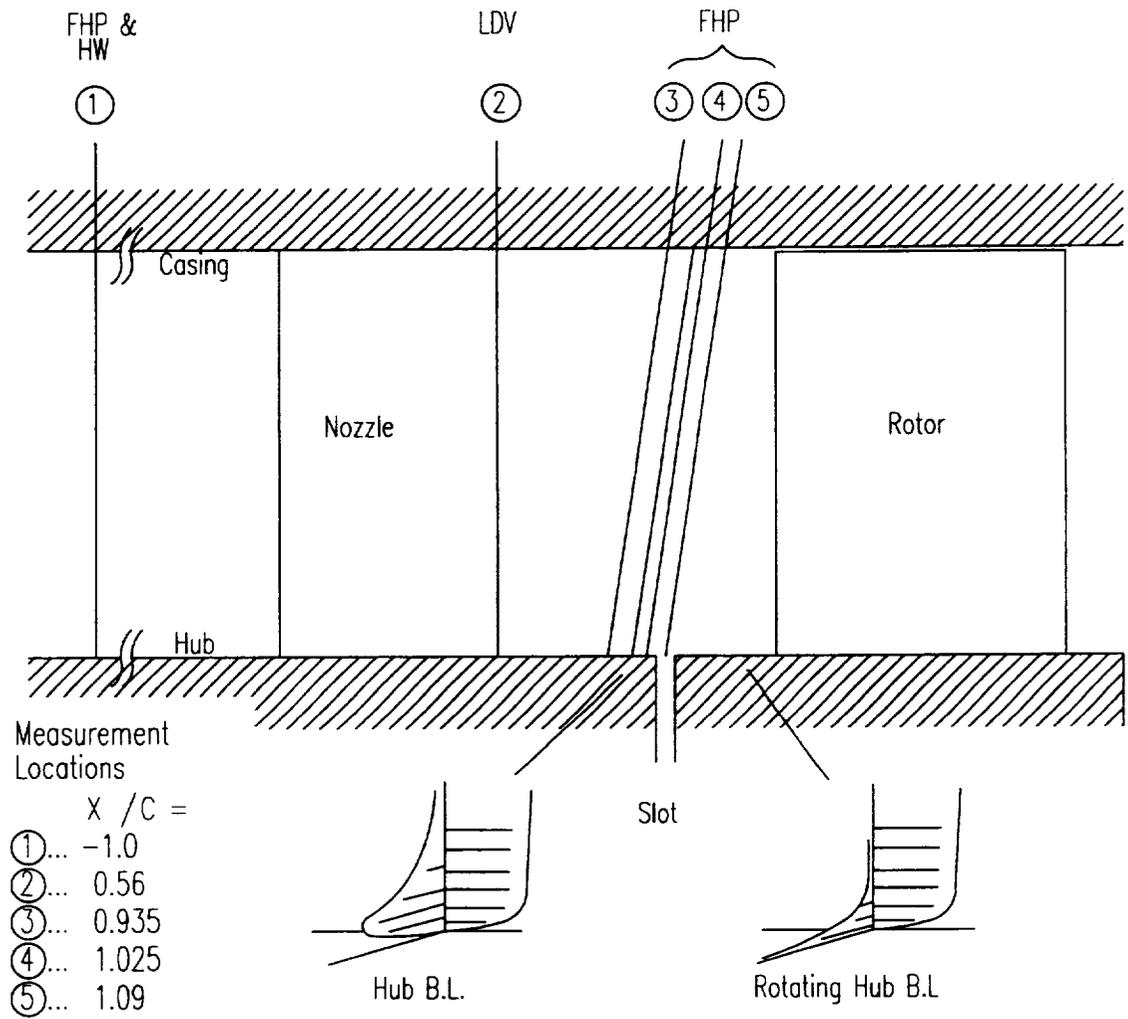
Figure 4.1. Nozzle Flow Field Measurement Locations
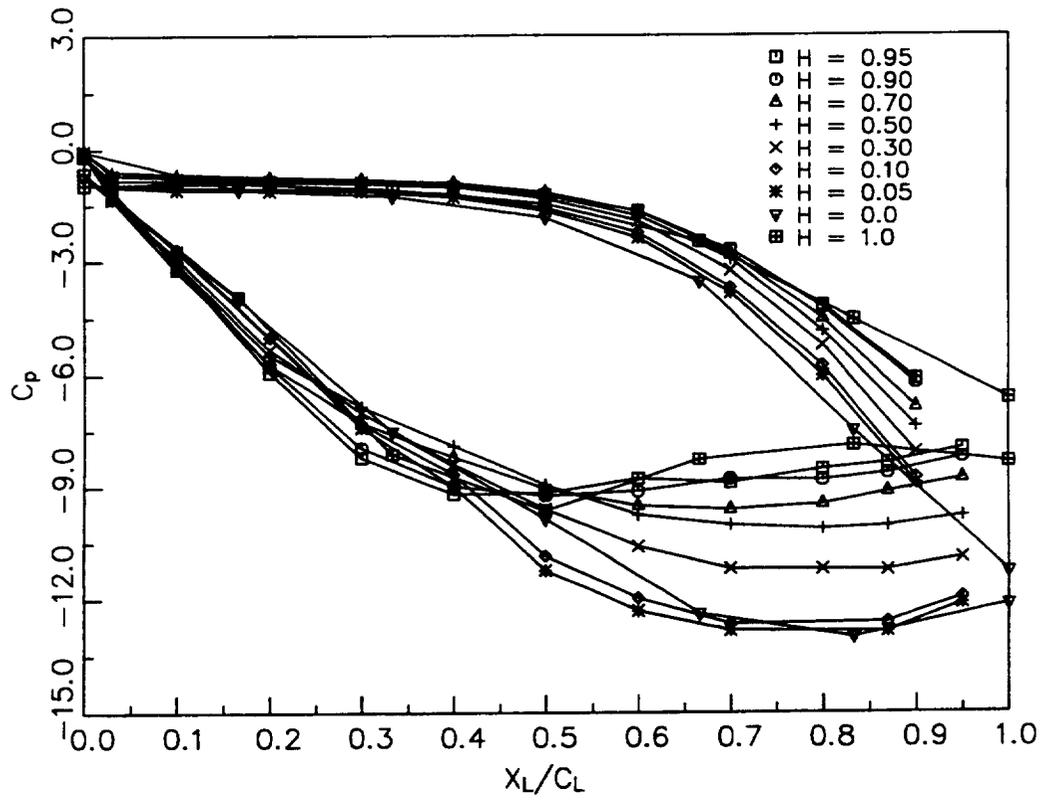
Figure 4.2. Experimental Static Pressure (C_p) Distribution on Nozzle Surface

nozzle vane shape variation presented in Figure 4.3. The variation of the vane shape is small from the tip to midspan of the vane, while it is larger from the midspan to the hub. The pressure distribution away from the endwalls (H=0.10 to H=0.90) is rather well balanced and agrees with the design values (not shown). The pressure distribution near the tip (H = 0.90 to H = 1.0) shows the maximum departure from the design (not shown). The suction peak occurs earlier than design and this is probably caused by the presence of secondary flow and the associated vortex. The distribution on the pressure side is well behaved with very little departure from design. The flow near the pressure surface is mostly inviscid, due to insignificant boundary layer growth. Further interpretation of this data will be given later.

Figure 4.4 compares the experimental static pressure distribution with the static pressure distributions computed using MacFarland's (1981) panel code and the quasi-three-dimensional inviscid code of Katsanis (1977). The panel code matches the experimental data well at H = 0.30 and H = 0.50. At these locations the panel code distribution matches the experimental data exactly on the pressure side but on the suction side the measured flow accelerates less rapidly than the computed flow up to about $X_L/C_L= 0.70$ and H = 0.5. Good correspondence between the computed and experimental distributions at H = 0.3 and 0.5 are to be expected since the turbine nozzle secondary flow does not have a major influence at midspan. At other spanwise locations where the secondary flow affects the flow, the comparison between the computed and the experimental pressure distribution is not so good. The agreement between the data and Katsanis' code is excellent at midspan and at H = 0.10 and 0.30 , while the agreement deteriorates near the outer wall. In general, the three-dimensional inviscid code due to Katsanis shows better agreement with the data than the panel code. Hence, some of the departure between
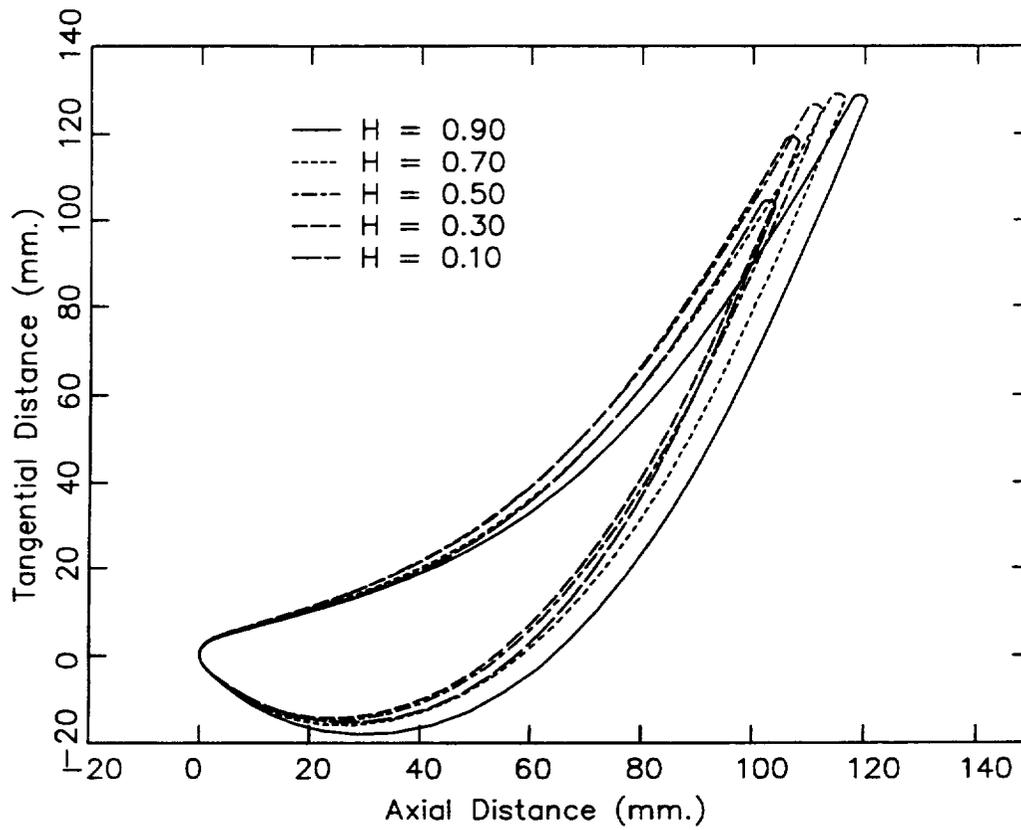
Figure 4.3. Nozzle Vane Profiles at 5 Radial Locations
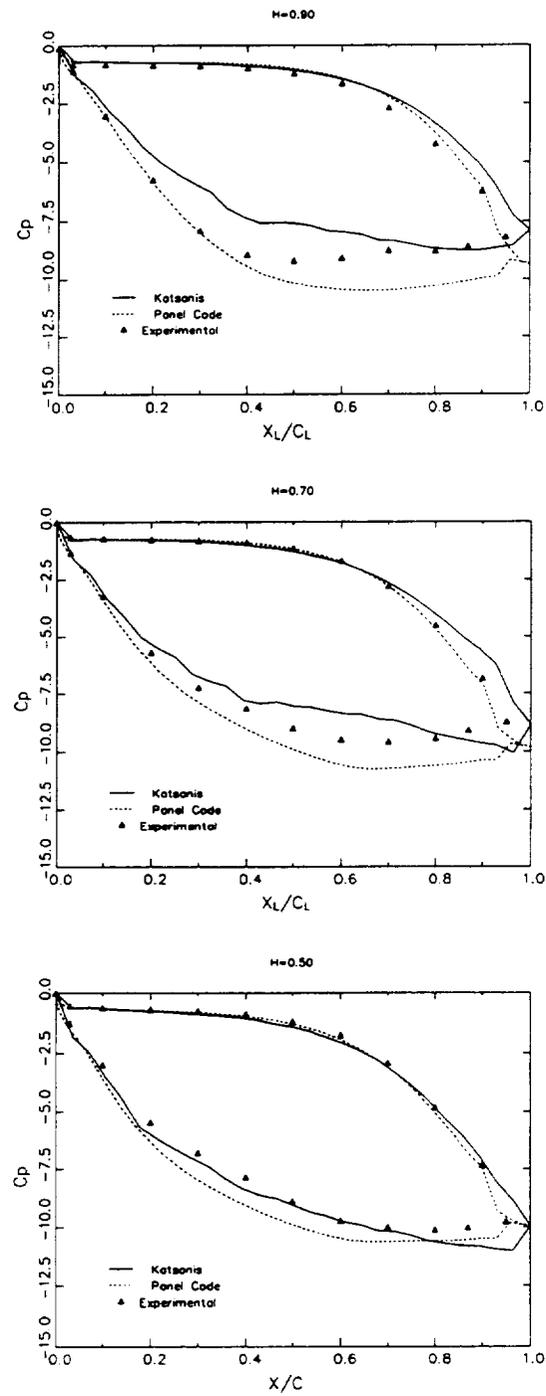
Figure 4.4. Comparison of Predicted and Measured Static Pressure (C_p) Profiles

H=0.30

H=0.10
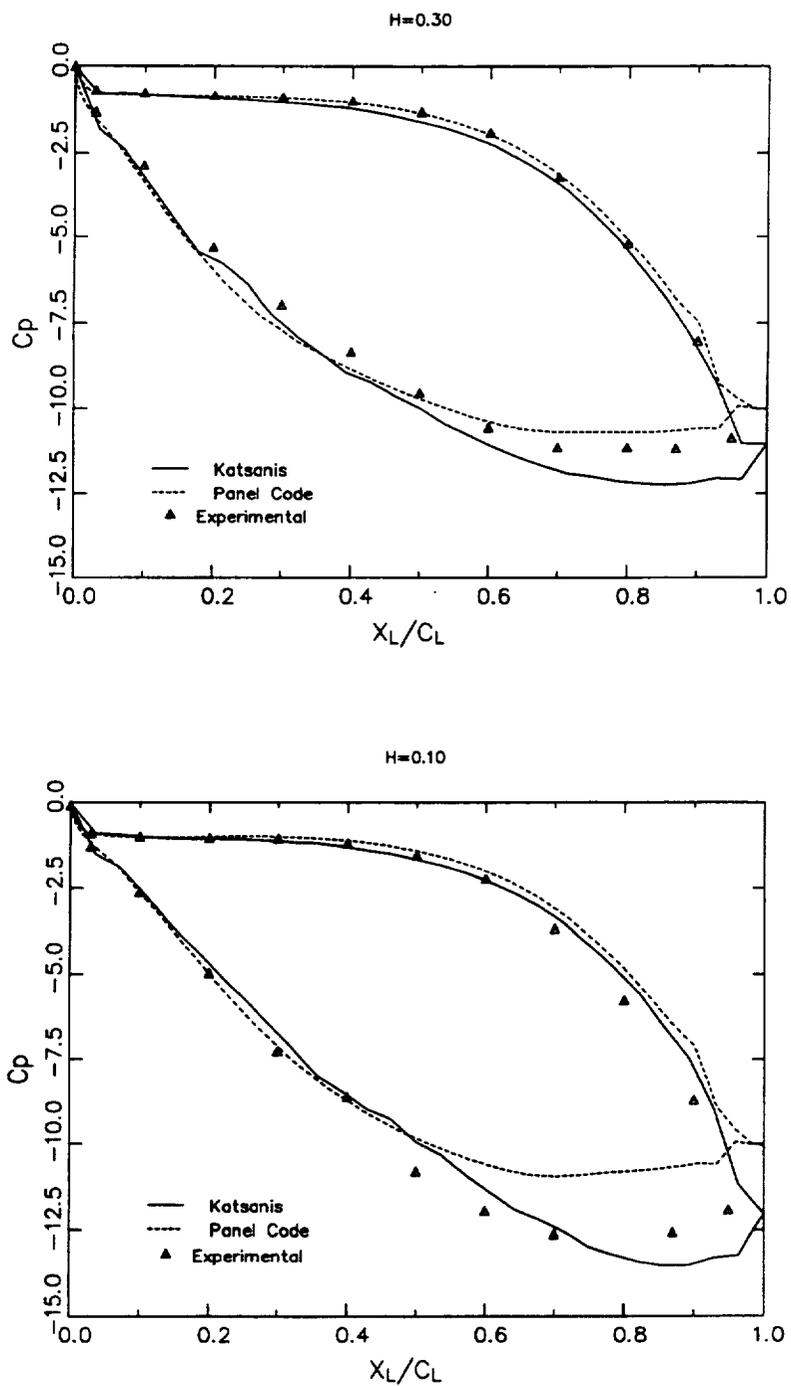
Figure 4.4 (Cont.). Comparison of Predicted and Measured Static Pressure (C_p) Profiles

the design and the measured data is caused by the inviscid effects.

As explained later, the static pressure increases linearly from hub to tip. This increase in static pressure is balanced by a decrease in total velocity (with increasing radius). Later observations indicate that is indeed true. Hence, the static pressure was also normalized by the total velocity at the exit of the nozzle (Figure 4.5). The pressure side distributions collapse to nearly constant values. The suction side shows a spanwise variation from $X_L/C_L = 0.05$ to 0.8. This variation is due to the spanwise differences in loading, the three-dimensional inviscid effects and the secondary flow effects that exist near the endwalls.

Contour plots of the casing and hub wall static pressure coefficients based on inlet dynamic head are shown in Figures 4.6a and 4.6b, respectively. The cross-channel pressure gradients exist over most the endwall for both the hub and casing. Sjolander (1975) found that the shear stress trajectories in the endwall regions were essentially parallel to the pressure gradient, indicating that the energy of the fluid is so small that the inertial effects are unimportant. Thus, the endwall pressure gradient is indicative of the direction of the endwall shear stress and consequently the direction of the flow. Accordingly, the cross passage flow extends over most of the hub and casing walls. The minimum static pressure region on the hub ($C_p = -13$) occurs at $X/C = 0.8$ (downstream of the throat), while the minimum pressure region on the casing ($C_p = -9.5$) occurs at $X/C = 0.5$ (upstream of the throat). (The throat is located at $X/C = 0.71$ along the suction surface for the hub and at $X/C = 0.68$ on the suction surface for the casing.) Graziani et al. (1980) show that this low pressure region is the location where the passage vortex lifts off the endwall surface and begins to grow rapidly when approaching the nozzle suction surface.

Contour plots of static pressure on the nozzle pressure and suction surfaces are presented in Figures 4.7a and 4.7b, respectively. The flow field is two-
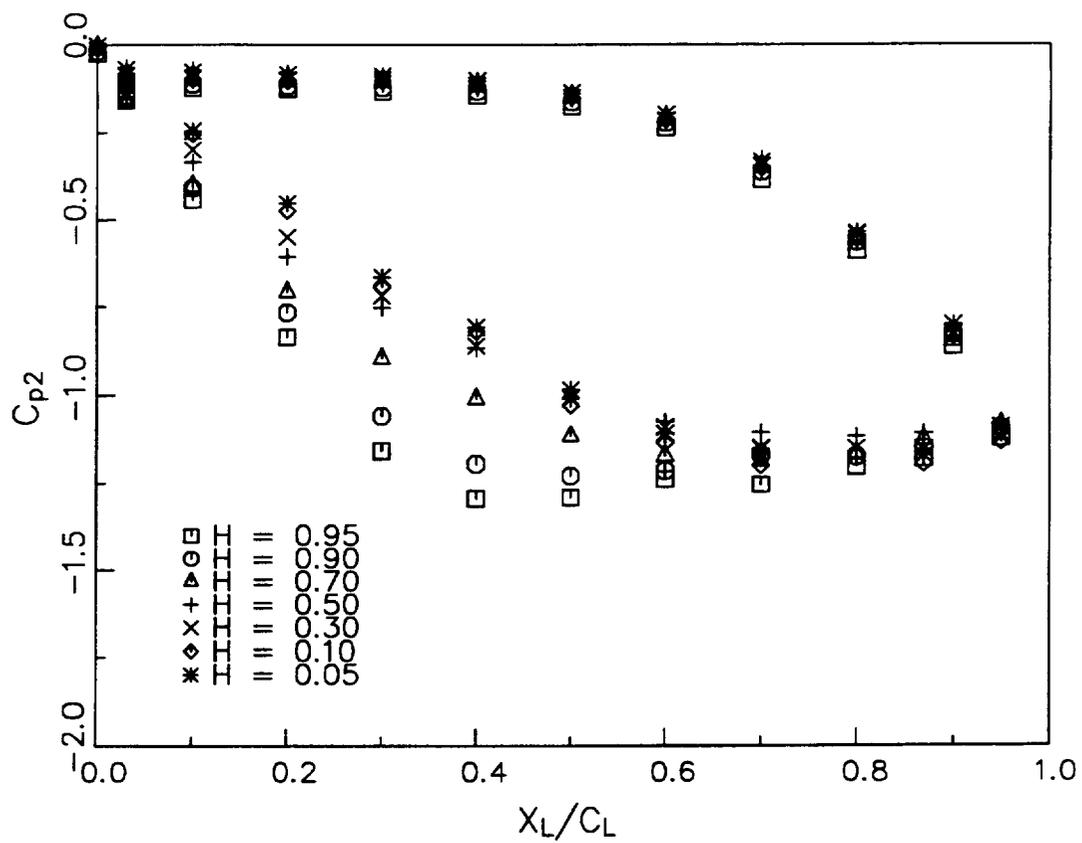
Figure 4.5. Nozzle Pressure Coefficient (C_{p2}) based on Exit Total Velocity
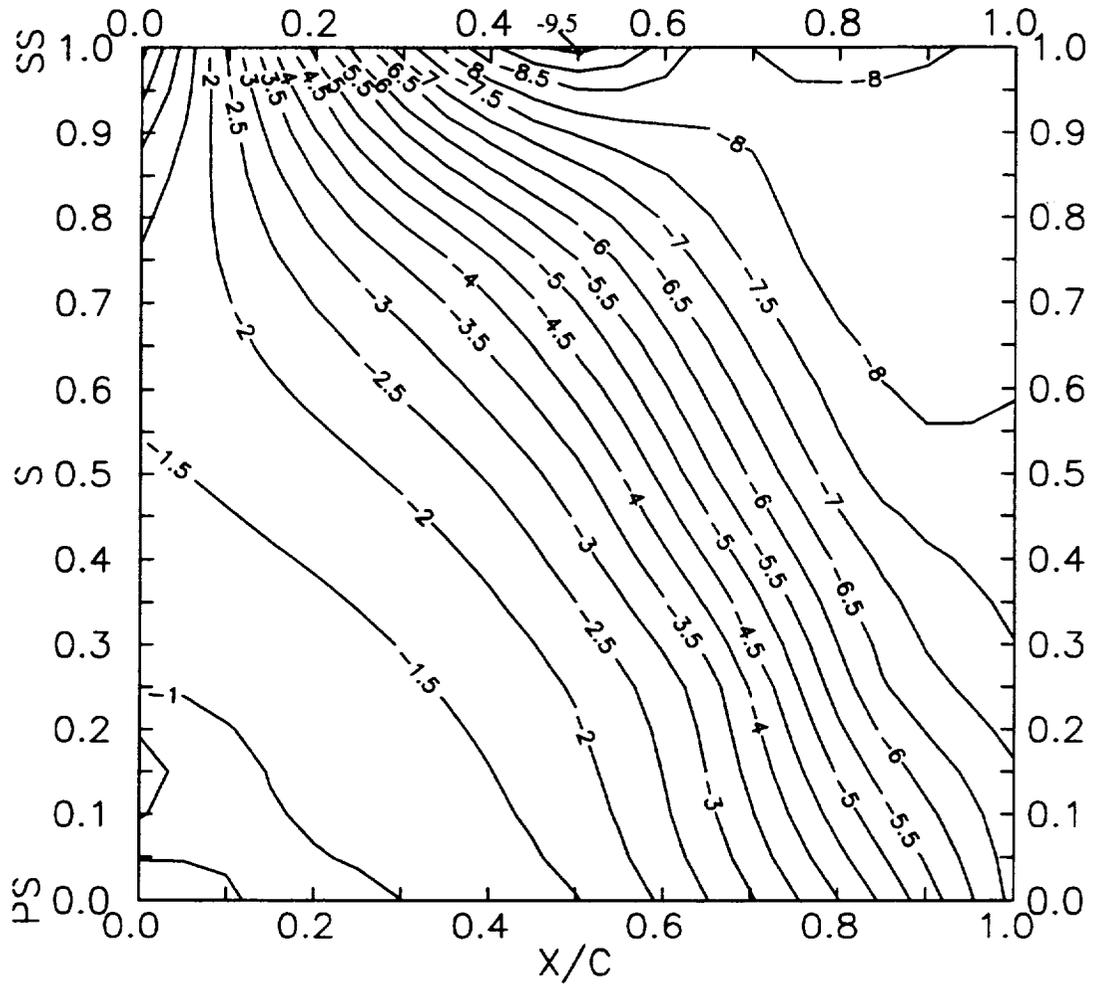
Figure 4.6a. Nozzle Casing Static Pressure Coefficient (C_p)
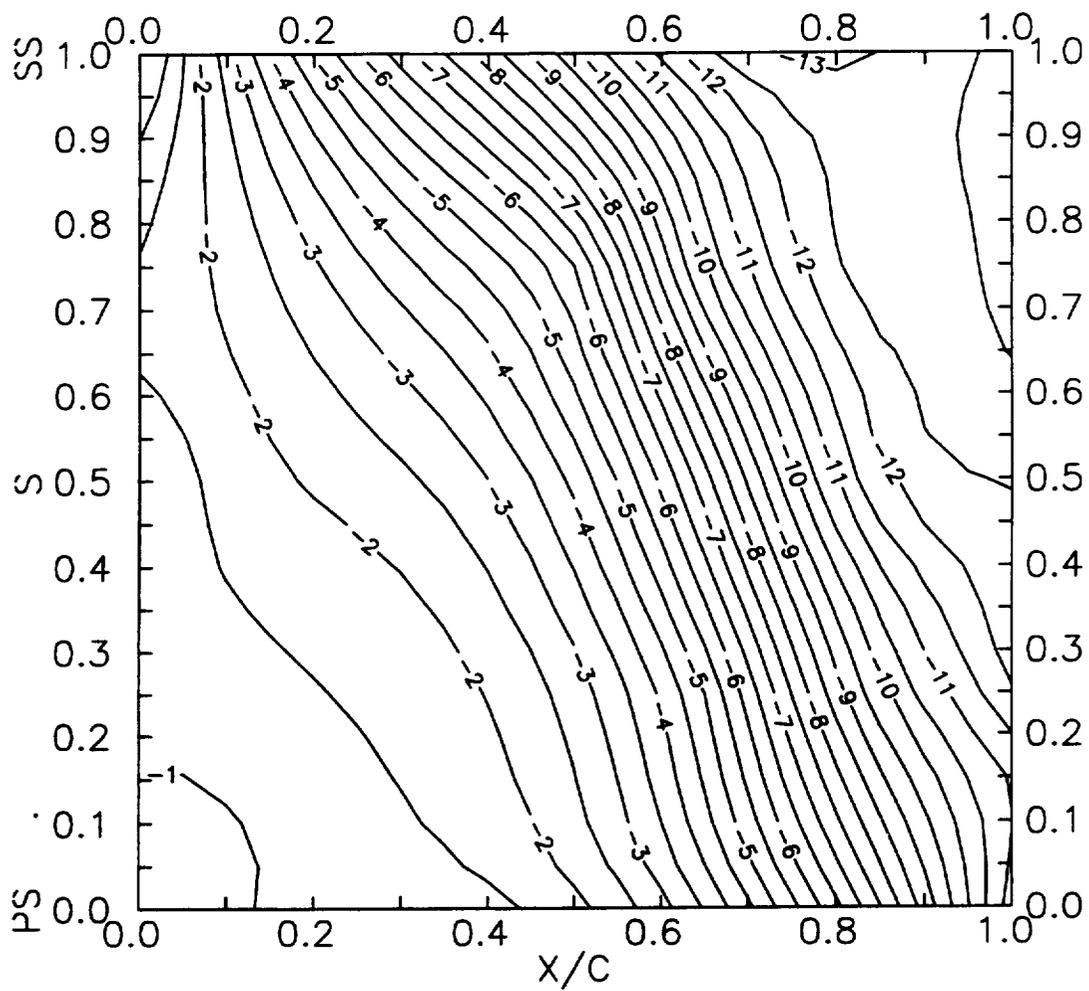
Figure 4.6b. Nozzle Hub Static Pressure Coefficient (C_p)
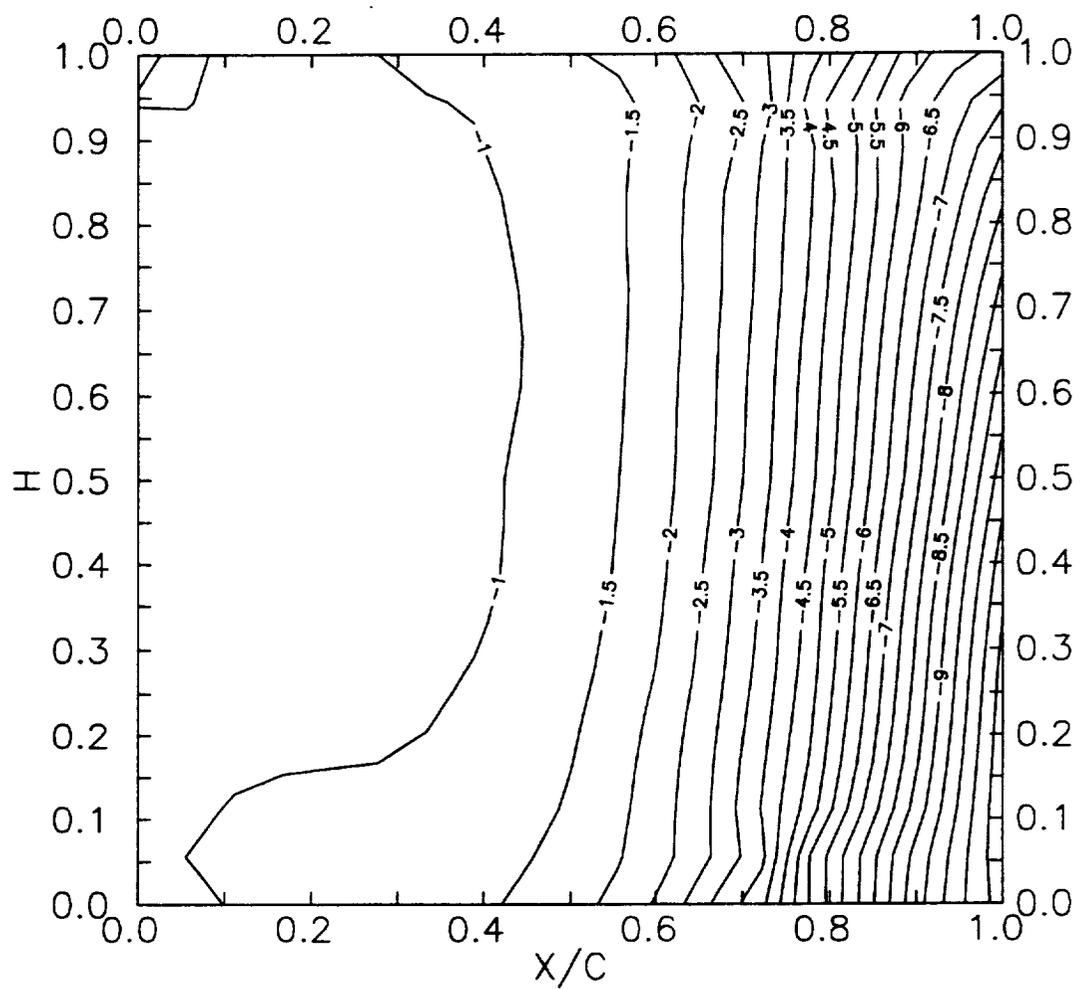
Figure 4.7a. Nozzle Pressure Surface Static Pressure Coefficient (C_p)
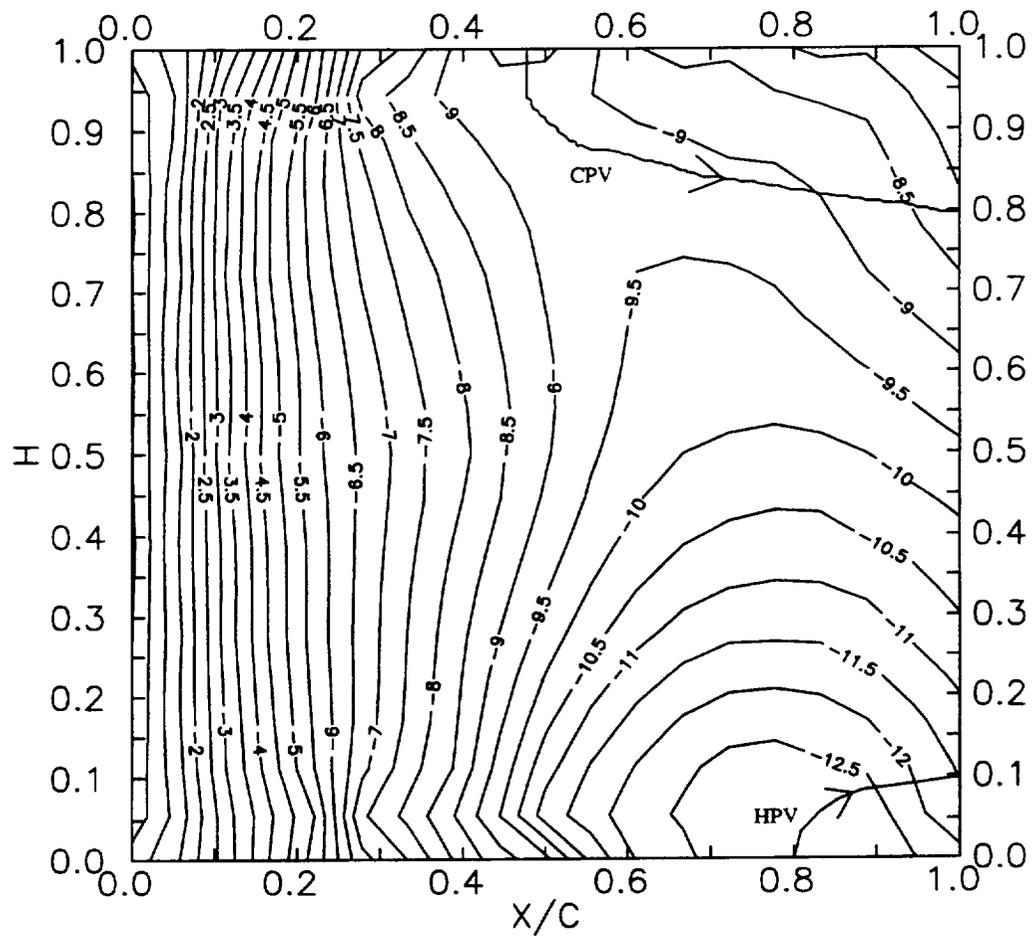
Figure 4.7b. Nozzle Suction Surface Static Pressure Coefficient (C_p)

dimensional over the whole pressure surface which is demonstrated by the relatively constant pressure coefficient values in the spanwise direction. The static pressure varies slightly from the leading edge to midchord. Downstream of midchord, the pressure decreases rapidly and the pressure gradient is perpendicular to the trailing edge over most of the span, with a slight deviation from this direction near the tip. Since the trailing edge is not radial but has a radial lean (see Figure 4.1), the flow moves in a slightly radial direction, but is still two-dimensional. This demonstrates that the flow field is two-dimensional over most of the pressure surface with radial inward flow over most of the span and an increase in radial inward flow at the nozzle trailing edge/casing corner.

The flow field on the suction surface of the nozzle can be divided into three regions. The first region occurs from the leading edge to $X/C = 0.40$. The flow field is two-dimensional over the whole span in this region, with the flow accelerating rapidly from the leading edge to $X/C = 0.40$. The second region is a three-dimensional region and starts at the hub wall at $X/C = 0.80$. As shown in Figure 4.6b, the cross passage pressure gradient drives the flow and thus the passage vortex toward the suction surface. The passage vortex meets the suction surface at $X/C = 0.80$ where the low pressure region occurs ($C_p = -13$) and then travels up the suction surface and toward the trailing edge. The path of the hub wall passage vortex (HPV) along the suction surface is shown in Figure 4.7b. The position of the passage vortex at the trailing edge was determined from the flow field measurements in the trailing edge region discussed later.

The third region on the suction surface is also three-dimensional and begins at $X/C = 0.5$ at the casing wall. The flow behavior is similar to that of the hub wall region with the flow and the casing passage vortex traveling toward the suction surface as shown in Figure 4.6a. The passage vortex meets the suction

surface at the low pressure point ($C_p = -9.5$), which occurs at $X/C = 0.50$ and then the casing passage vortex (CPV) sweeps down the suction surface toward the trailing edge, following the path shown in Figure 4.7b. The position of the passage vortex at the trailing edge was determined from the flow field measurements in the trailing edge region. One interesting feature of this flow field, is that contrary to what occurs in a linear cascade, the casing passage vortex intersects the suction surface farther upstream ($X/C = 0.50$) than the hub passage vortex intersects the suction surface ($X/C = 0.80$). Since the passage vortex grows much more rapidly after it intersects with the suction surface, leaves the endwall and starts moving up the suction surface, this indicates that the casing passage vortex would cover a larger area than the hub passage vortex. This is demonstrated later in this chapter.

4.2 Flow Field Near Midchord (X/C = 0.56)

The flow field near midchord ($X/C = 0.56$) was measured using a two component LDV in order to capture both the velocity and the turbulence intensity. These measurement were taken from hub to tip and blade to blade. Since the nozzle axial chord decreases from hub to tip and the LDV measurement plane is at a constant axial distance downstream of the leading edge of the nozzle, the measuring location as a percent chord decreases from hub to tip ($X_L/C_L = 0.61$ at H = 0.05 and $X_L/C_L = 0.52$ at H = 0.95). $X/C = 0.56$, which is the percentage chord at midspan, will be used to define this axial plane. The third component could not be measured at this location because of limited access.

The LDV measurements at $X/C = 0.56$ are shown in Figures 4.8 through 4.11. The blank areas in the contour plots represent regions where data could not be taken due to limited access in the nozzle. Figure 4.8 shows a comparison of total
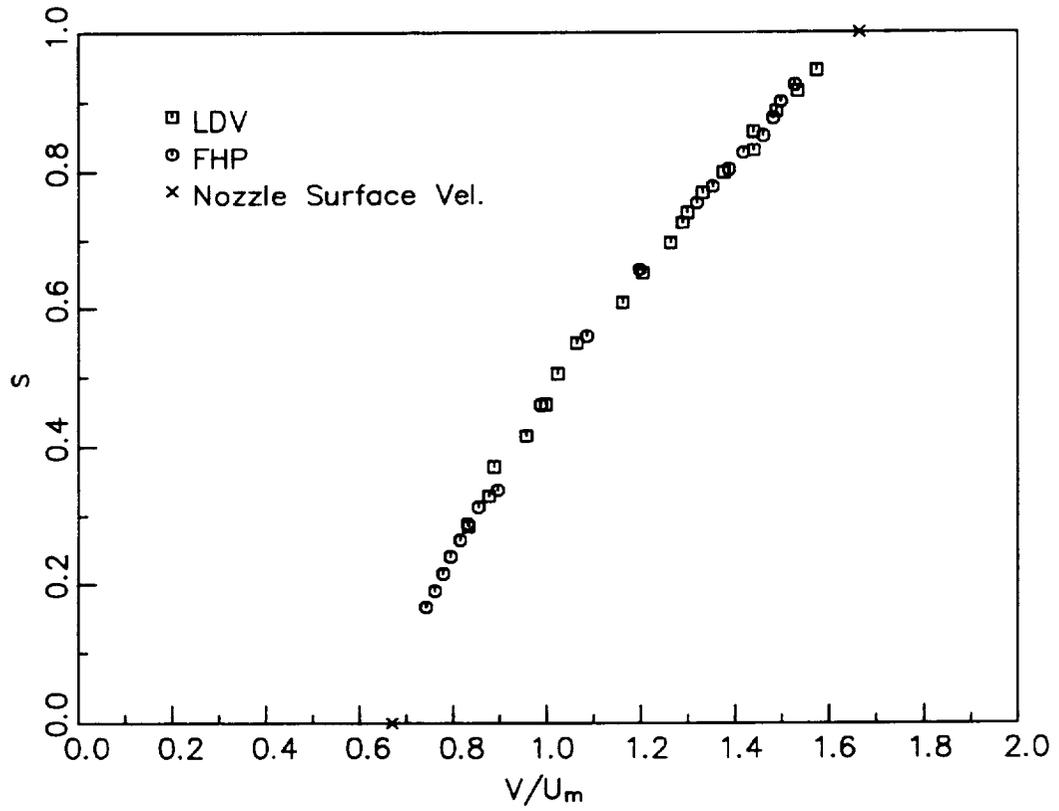
Figure 4.8. Comparison of LDV and FHP Total Velocity Data at X/C = 0.56
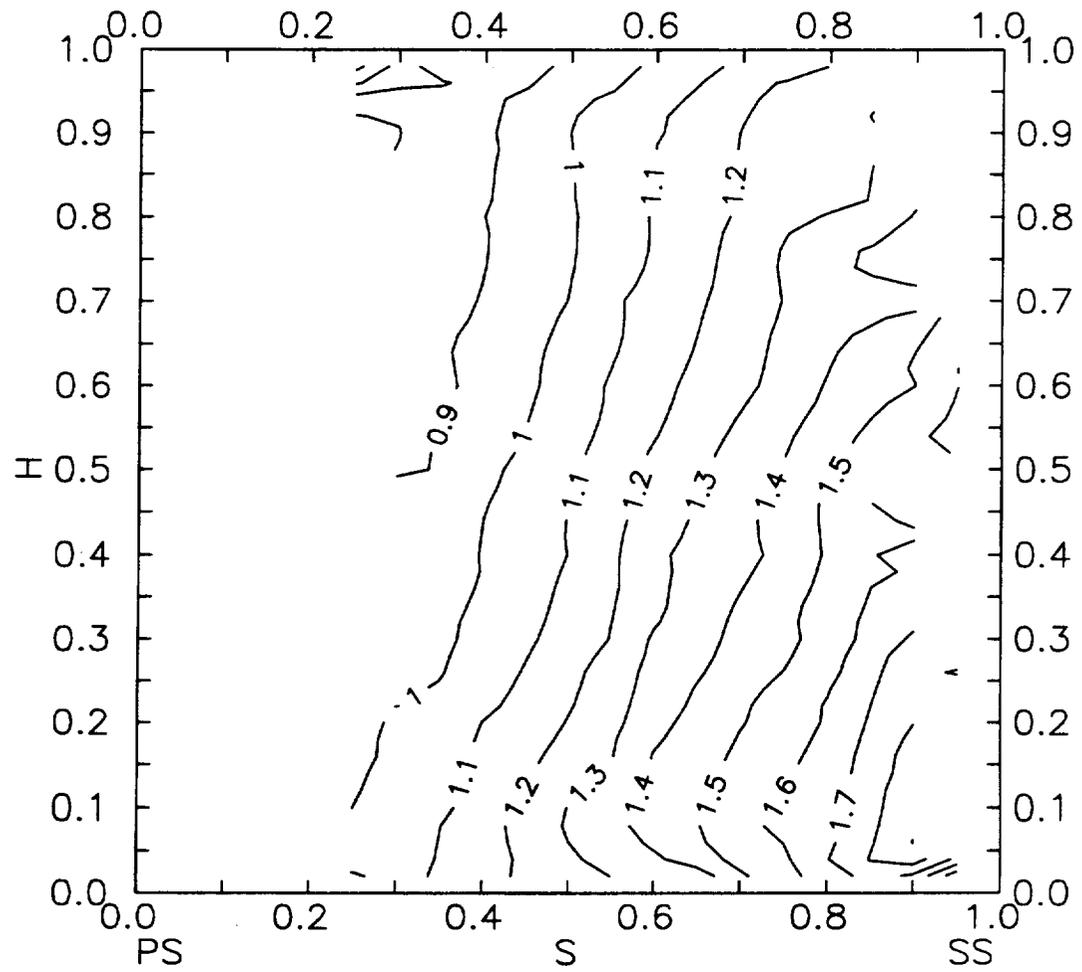
Figure 4.9. Total Velocity (V/U_m) at X/C = 0.56

Figure 4.10. Yaw Angle (α) at X/C = 0.56 (in degrees)

Figure 4.11. Total Turbulence Intensity (Tu) at X/C = 0.56
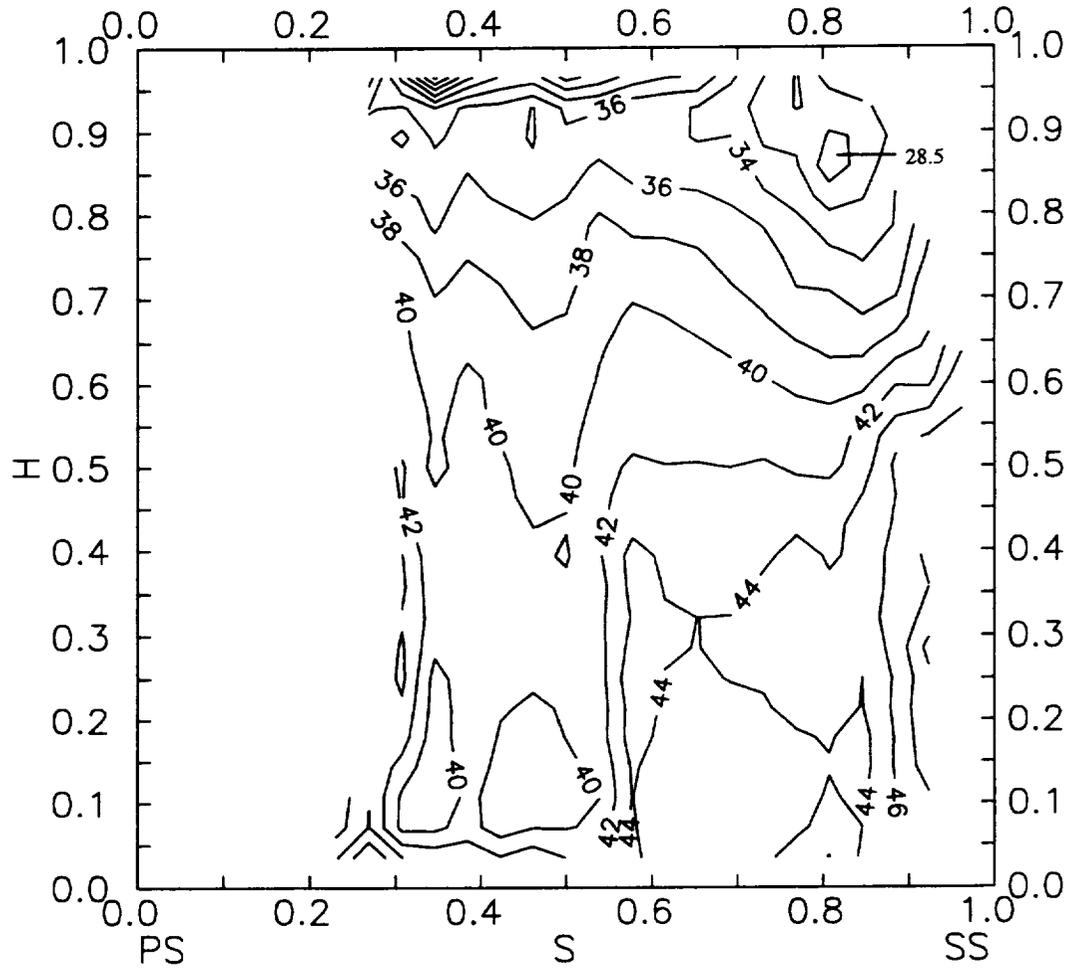
velocity derived from LDV, five hole probe and the vane static pressure at midspan. The tangential distance is normalized by the distance between the pressure and suction sides where S = 0 is the pressure surface and S = 1 is the suction surface. Both the LDV and five hole probe data matches the velocity profile quite well. This data shows a weakly nonlinear variation from pressure to suction surface and is similar to the data presented by Goldman and Seasholtz (1992). This excellent comparison between various types of measurements indicates that error in five hole probe and LDV data is negligibly small.

Total velocity contours are presented in Figure 4.9. The total velocity variation follows the usual inviscid trend and is in agreement with Yamamoto and Yanagi's (1986) data. In addition to the inviscid flow field, one can observe the development of the endwall boundary layers, which are rather thin. This is because, according to Sharma and Butler (1987), all the inlet boundary layer fluid particles have either become part of the passage vortex or been swept toward the suction side, which results in a new endwall boundary layer being formed in the nozzle passage downstream of the separation line defined by the passage vortex (see Figure 1.5) .

The yaw angle contours, presented in Figure 4.10, show a rather well behaved flow with a ±2 degree variation at most locations. (The design mean flow angle is 40 degrees at this axial location.) As expected in inviscid flow, the turning angle near the suction surface is higher than that near the pressure surface. There is a region of high underturning in the corner formed by the casing and suction side. The angle in that location is 28.5 degrees. This is due to the passage vortex. The overturning region associated with this vortex could not be observed due to constraints imposed by the LDV measurement limitations. The secondary flow seems to be rather weak and it is in the early stages of development. This is also

confirmed by the turbulence intensity contours (Figure 4.11) which show that the maximum turbulence intensity in this region is about three-fold compared to one percent at the inlet. No evidence of secondary flow is seen at the hub. This also corresponds to the nozzle endwall and surface static pressure contours presented earlier (Figures 4.6a, 4.6b and 4.7b). These static pressure contours showed that while the casing passage vortex has traveled across the passage and met the suction surface at midchord (where it begins to grow rapidly), the hub passage vortex is still being convected across the passage and does not intersect with the suction surface until farther downstream. Thus the hub passage vortex should still be rather weak and hard to detect. In addition to the secondary flow phenomenon, one can observe the increased turbulence intensity both in the hub and in the tip endwall boundary layer regions in Figure 4.11.

4.3 Flow Field Near Trailing Edge (X/C = 0.935)

Near the trailing edge, the flow field was surveyed with a five hole probe. A five hole probe was employed to facilitate stagnation pressure loss evaluation as well as to measure the blade endwall flows more thoroughly. The axial plane position is parallel to the trailing edge and ranges from $X_L/C_L = 0.93$ at the hub to 0.94 at the tip. The axial plane position will be defined by the axial distance at midspan, X/C=0.935. Data were taken at 23 spanwise locations, clustered near the endwalls, and 40 to 55 tangential locations clustered near the vane surfaces.

4.3.1 Stagnation and Static Pressures

Figure 4.12 shows the stagnation pressure loss coefficient Ψ_{LOSS}. The two

high loss regions located in the corner formed by the suction surface and the

annulus wall as well as the suction surface and the hub wall show that the

secondary flow is fairly well developed here. These high loss regions are

associated with the passage vortex caused by the secondary flow. High losses occur

in the core region and the maximum loss coefficient observed is 1.33 near the tip

and 1.86 near the hub. The tip loss core is located farther from the casing than the

hub loss core is from the hub, which results from the radial inward velocities that

exist in both the freestream and the vane boundary layer. This is also the cause for

the loss core near the hub to have a higher loss coefficient than the loss core near

the tip. This is consistent with the measurements made slightly downstream of the

trailing edge (Chapter 5) at $X/C = 1.025$. A comparison of the losses in the two

axial planes show that the loss contours are very similar in the tip and the hub

regions, indicating no major redistribution of the losses as the flow progresses from

$X/C = 0.935$ to $X/C = 1.025$.

Another noticeable feature of this flow field is that the casing passage

vortex covers more area than the hub passage vortex. This results from three

reasons. The first is the radial inward velocities cause the hub passage vortex to be

pushed against the hub, which causes it to be compressed, while the casing passage

vortex moves away from the casing. The second reason can be found in the

discussion of the nozzle endwall and surface static pressure contours presented

earlier (Figures 4.6a, 4.6b and 4.7b). These static pressure contours showed that the

casing passage vortex travels across the passage and meets the suction surface

farther upstream than the hub passage vortex does. Since the passage vortex begins
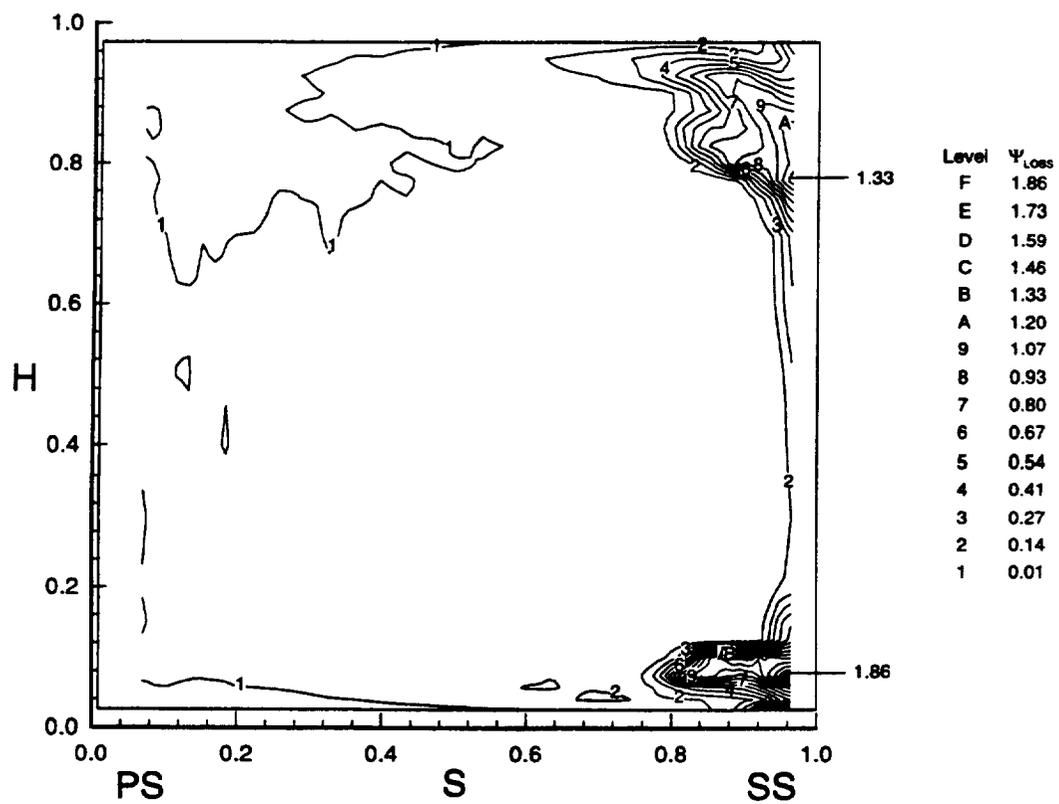
Figure 4.12. Total Pressure Loss Coefficient (Ψ_{Loss}) at X/C = 0.935

to grow rapidly after it intersects with the suction surface, the casing passage vortex has a larger area due to the longer distance it has traveled between the endwall/suction surface intersection point and this measuring location. The third reason is that the casing inlet boundary layer is larger than the hub wall boundary layer, which also results in the larger extent of the casing passage vortex.

The static pressure contours at this location are given in Figure 4.13. The most striking feature is the strong radial pressure gradient that exists over the whole span. In the corner formed by the annulus wall and the suction surface there is a low pressure region (static pressure coefficient is 2.2) indicating the presence of the secondary flow vortex. A similar patch can be seen near the hub surface as well.

4.3.2 Velocity and Flow Angles

Figure 4.14 shows the total velocity contours. The total velocity increases from the tip to the hub due to the existence of the radial pressure gradient discussed earlier. A low velocity region is observed near the corner formed by the suction surface and hub and casing walls. This is the region of intense mixing of secondary flow and wall and blade boundary layers.

One of the more interesting features of this flow field is the yaw angle shown in Figure 4.15. Most of the total flow turning has taken place by this location and the maximum overturning of about eight degrees occurs at H = 0.85 close to the suction side. The maximum underturning region is about four degrees. This is observed slightly below (H = 0.80) and a little farther from the suction side than the overturning region. This over and underturning of the flow is characteristic
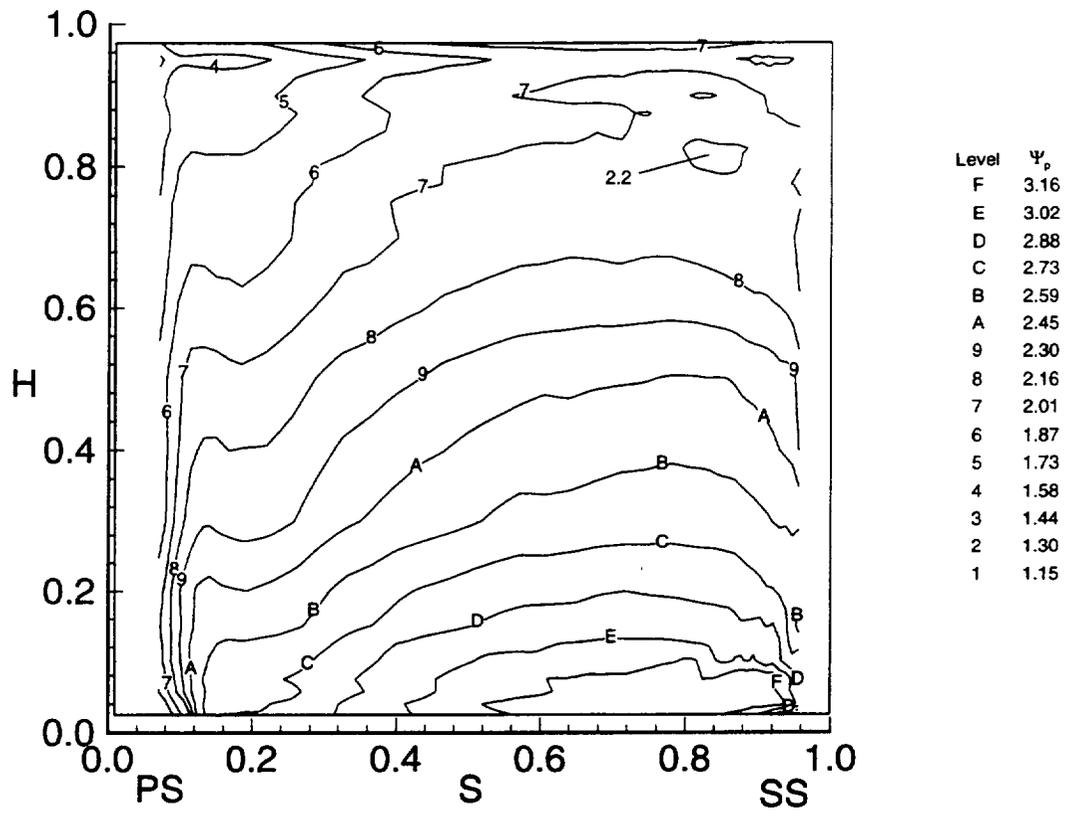
Figure 4.13. Static Pressure Coefficient (Ψ_s) at X/C = 0.935
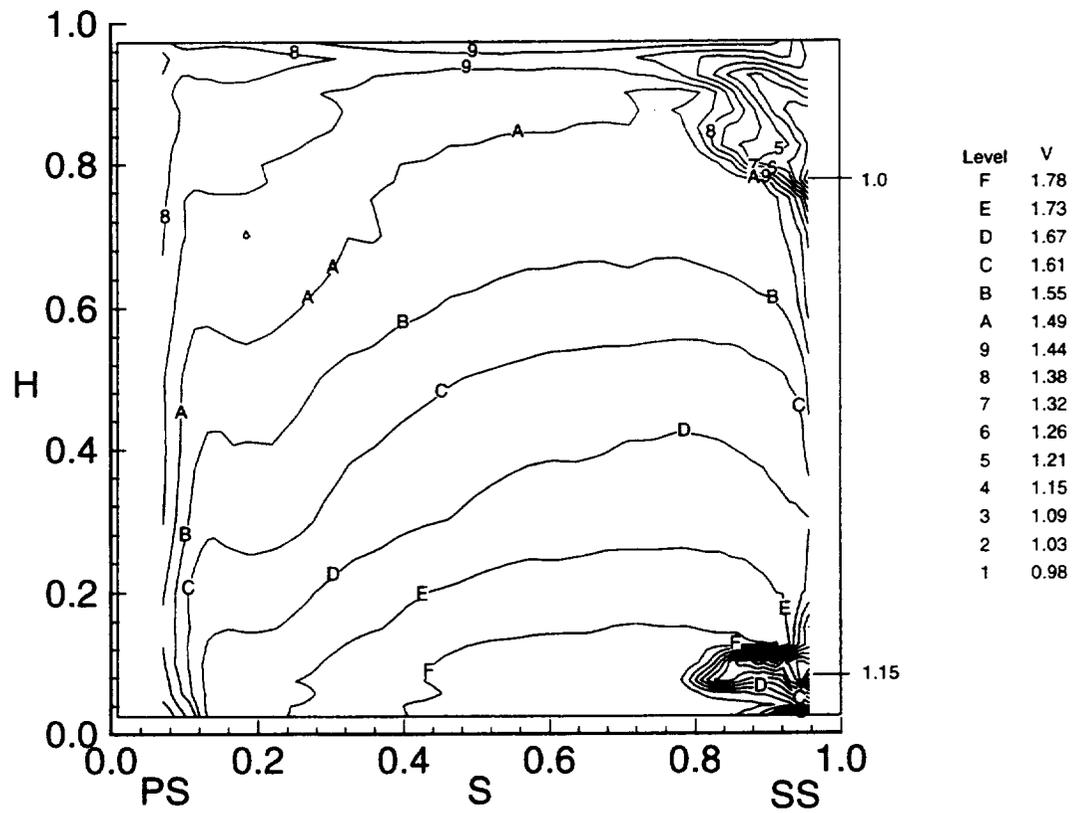
Figure 4.14. Total Velocity (V/U_m) at X/C = 0.935
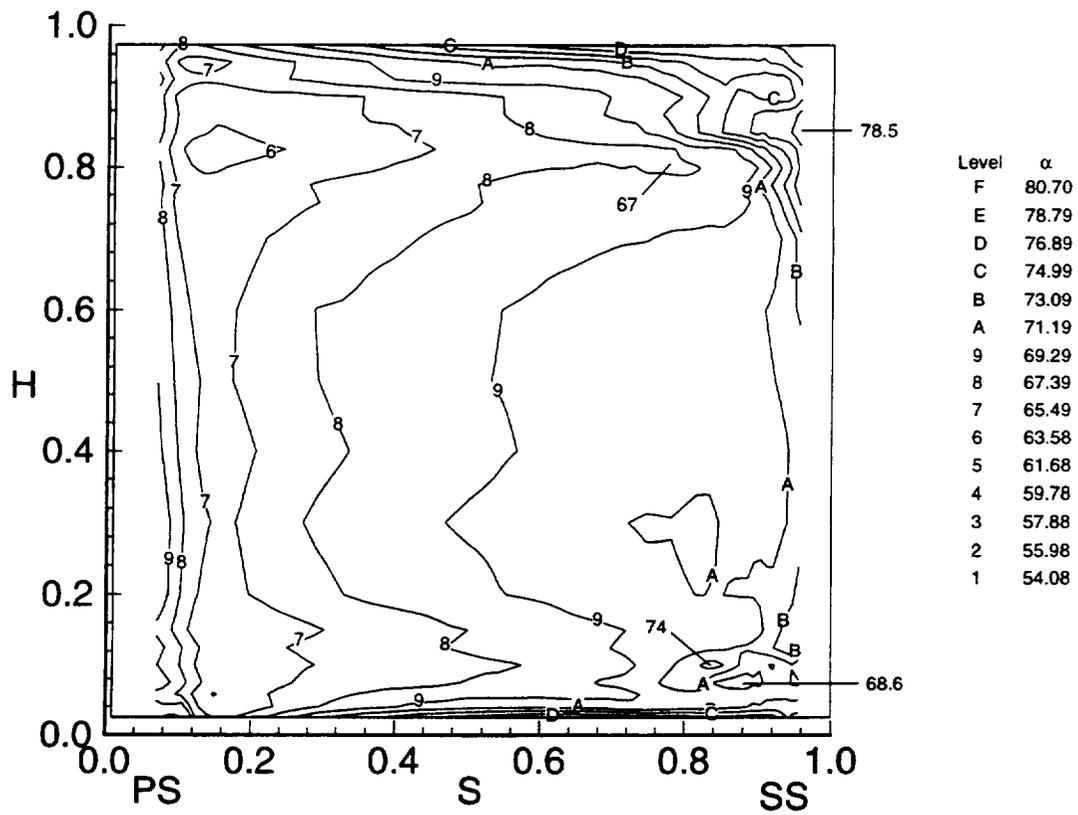
Figure 4.15. Yaw Angle (α) at X/C = 0.935 (in degrees)

of a vortex. Otherwise, the flow is well behaved with an angle variation of four degrees across the entire passage at midspan. A similar secondary flow region is observed near the hub. The maximum overturning of about three degrees and a similar magnitude of underturning close to the suction side can by seen. This seems to indicate a conventional secondary flow pattern both in the hub and tip region. In addition, the flow very close to the walls, across the entire passage is overturned slightly.

The magnitude of radial velocity can be discerned from the radial flow angle distribution shown in Figure 4.16. Negative values of radial flow angle indicate that flow is toward the hub over most of the passage. There are two regions with much higher and much lower radial flow angles than the rest of the flow. They are located in the suction surface hub and casing wall corners. Near the casing the maximum radial flow angle is -68 degrees and the minimum is one degree, while near the hub the maximum radial flow angle is -37 degrees and the minimum is six degrees. These high and low radial flow angles are another indication of the presence of secondary flow vortices.

4.3.3 Secondary Flow Vectors

The secondary flow velocity vectors in the r-θ plane, shown in Figure 4.17, are derived from the measured data. The primary flow angle at X/C = 0.935 was taken from the measured flow angle at the midspan at the respective tangential position, since the flow at midspan was not affected by the secondary flow, while downstream of the nozzle the primary flow angle was set equal to the design exit angle (70.0 degrees). Using this procedure, the secondary velocities were derived

Level	γ
F	3.23
E	-1.86
D	-6.96
C	-12.05
B	-17.15
A	-22.24
9	-27.33
8	-32.43
7	-37.52
6	-42.62
5	-47.71
4	-52.81
3	-57.90
2	-62.99
1	-68.09
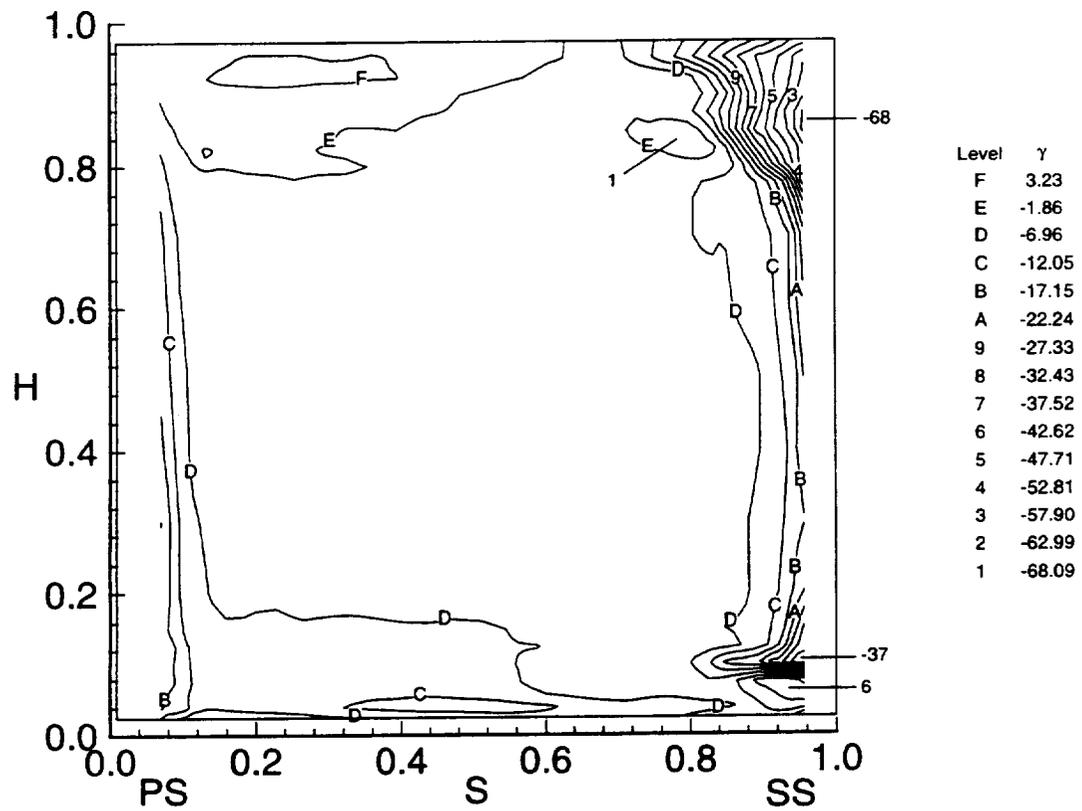
Figure 4.16. Radial Flow Angle (γ) at X/C = 0.935 (in degrees)
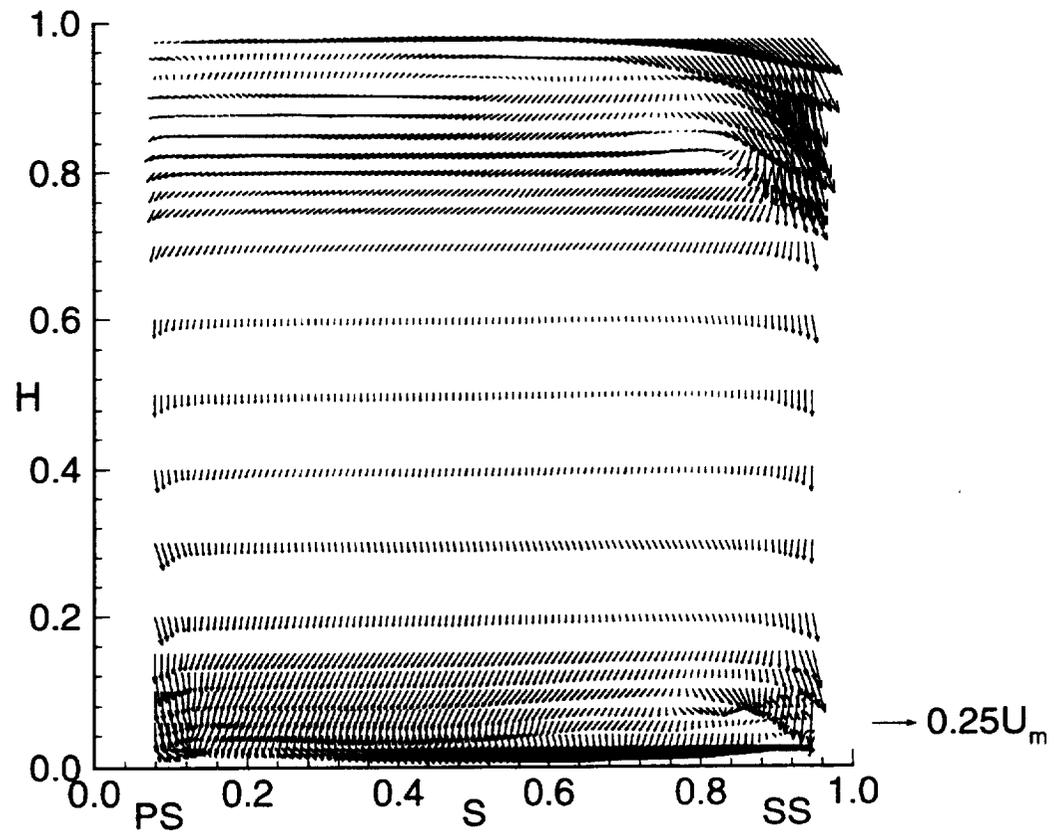
Figure 4.17. Secondary Flow Velocity Vectors at X/C = 0.935

from

$$\bar{V}_{sec} = \bar{r}V_r + \bar{n}V_n$$

$$= (\bar{V})_{measured} - (\bar{V})_{design}$$

(4.1)

where V_r is the radial velocity and V_n is the velocity normal to the streamwise

direction (estimated as indicated above). Strong radial inward flow can be seen to

occur over most of the passage at X/C = 0.935 (Figure 4.17). Since there is radial

inward flow over most of the passage, the secondary flow phenomena is obscured.

In order to perceive the secondary flow more clearly, the radial velocity at midspan

and at midpitch $\left((V_r)_{ref}\right)$ is subtracted from the velocity vectors. Figures 4.18a and

b show the secondary flow vectors with $(V_r)_{ref}$ subtracted from them. At

X/C=0.935 (Figure 4.18a), the passage vortex (clockwise) can be clearly seen near

the suction surface/casing corner. Since the pressure side leg of the horseshoe

vortex has the same direction of rotation as the passage vortex, this vortex could be

a combination of the passage vortex and the pressure side leg of the horseshoe

vortex. Other researchers such as Langston (1977) and Sieverding (1985b) believe

that the pressure side leg of the horseshoe vortex merges with the passage vortex

and the results here do not show otherwise. There is no evidence of the suction side

leg of the horseshoe vortex near the casing (which would rotate opposite to the

passage vortex).

Radial inward flow exists in the vane boundary layers caused by the

imbalance of the centrifugal force and the pressure gradient inside the boundary

layer. The tangential velocity decreases as the surface of the blade is approached,

and thus the centrifugal force decreases, while the radial pressure gradient remains

constant. This imbalance between the centrifugal and the pressure forces sets up

radial inward flow, which continues even in the wake. This radial inward flow is in
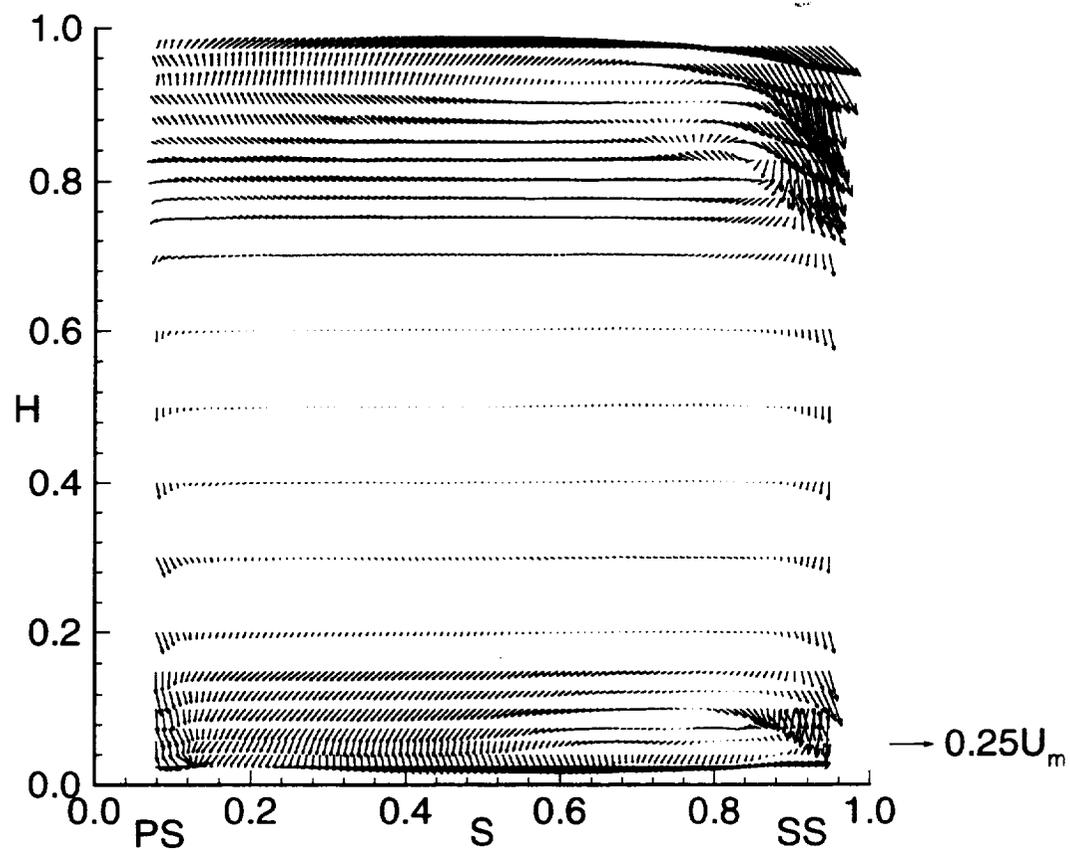
Figure 4.18a. Secondary Flow Velocity Vectors at $X/C = 0.935$, $\left(V_r\right)_{ref}$ subtracted
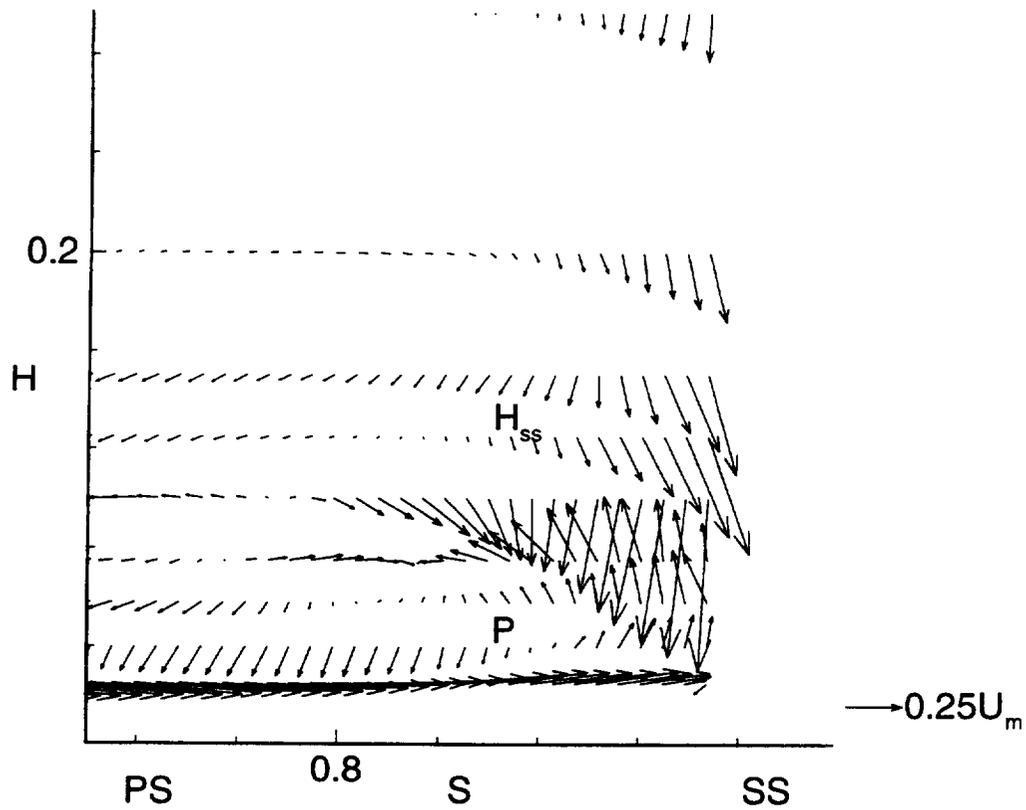
Figure 4.18b. Secondary Flow Velocity Vectors at X/C = 0.935, $\left(V_r\right)_{ref}$ subtracted

the same direction as those induced by the casing passage vortex close to the suction side and thus it augments the passage vortex. At the hub, on the other hand, there is evidence of a passage vortex, but it is much weaker than the vortex near the casing. The radial inward flow in the suction surface boundary layer near the hub is in the opposite direction to those caused by the passage vortex, and thus the radial inward flow seems to overshadow those induced by the passage vortex. This is shown more clearly in Figure 4.18b which is an enlargement of the secondary velocity vectors near the hub/suction side corner. The passage vortex in this figure is labeled P. Above the passage vortex, there seems to be a weak vortex rotating in the opposite direction. This could be the suction side leg of the horseshoe vortex and it is labeled H_{SS} in this figure.

4.3.4 Streamwise Vorticity

The components of vorticity in the axial, tangential and radial directions are given by:

$$\omega_x = \frac{\partial V_r}{r\partial\theta} - \frac{\partial(rV_\theta)}{r\partial r} \tag{4.2}$$

$$\omega_\theta = \frac{\partial V_x}{\partial r} - \frac{\partial V_r}{\partial x} \tag{4.3}$$

$$\omega_r = \frac{\partial V_\theta}{\partial x} - \frac{\partial V_x}{r\partial\theta} \tag{4.4}$$

The streamwise vorticity is then given by:

$$\omega_s = \omega_x \cos\alpha_p + \omega_\theta \sin\alpha_p + \omega_r \sin\gamma \tag{4.5}$$

where α_p is the primary flow angle and γ is the radial flow angle. The streamwise

vorticity is normalized by C/V_{x1}. The primary flow angle is determined as

indicated above. The streamwise vorticity derived from the data at X/C = 0.935 is

shown in Figure 4.19. The tangential and radial components of the vorticity

involve axial gradients and since at X/C = 0.935, measurements were not made at

an axial plane inside the vane close enough to this location to determine the axial

gradients, another method had to be used to estimate the axial gradients. Gregory-

Smith et al. (1988) have developed a method, which was extended for

compressible flow by Niehuis et al. (1990), to estimate the axial gradients. Using

their method, the axial gradients can be estimated as follows. Consider the Navier-

Stokes equation for a compressible fluid with constant viscosity, which is

$$\rho \frac{D\bar{V}}{Dt} = -\nabla p + \nabla \cdot \left(\mu \left[\nabla \bar{V} + \left(\nabla \bar{V} \right)^T \right] \right) + \nabla \left[\lambda \left(\nabla \cdot \bar{V} \right) \right] \qquad (4.6)$$

Nondimensionalizing this equation gives

$$\rho^* \frac{D\bar{V}^*}{Dt^*} = -\nabla p^* + \frac{1}{Re} \left\{ \nabla \cdot \left(\mu^* \left[\nabla \bar{V}^* + \left(\nabla \bar{V}^* \right)^T \right] \right) + \nabla \left[\lambda^* \left(\nabla \cdot \bar{V}^* \right) \right] \right\} \qquad (4.7)$$

where the superscript * represents the nondimensional variables. Assuming high

Reynolds number flow, the viscous terms become very small and can be neglected.

Converting back to dimensional form yields
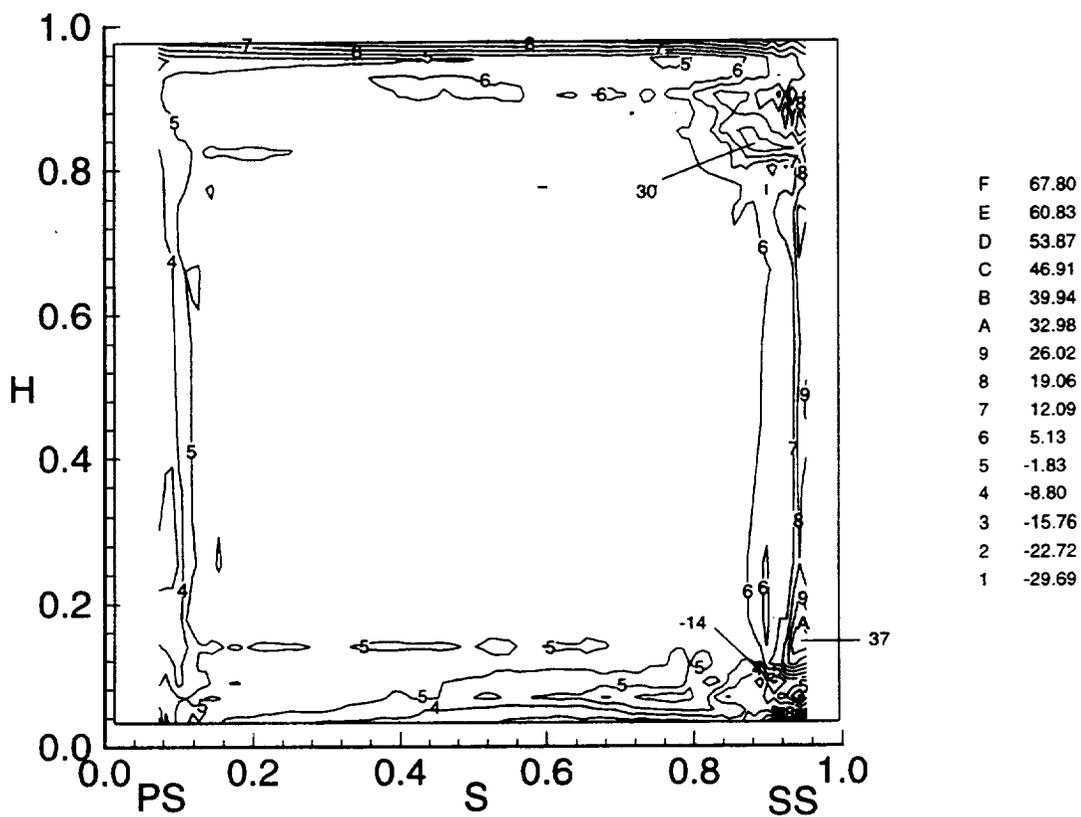
Figure 4.19. Streamwise Vorticity $\left(\omega C/V_{x1}\right)$ at X/C = 0.935

$$\rho\frac{D\vec{V}}{Dt} = \rho\left[\frac{\partial\vec{V}}{\partial t} + (\vec{V}\cdot\nabla)\vec{V}\right] = \nabla p \tag{4.8}$$

$$= \rho\left[\frac{\partial\vec{V}}{\partial t} + \frac{\nabla V^2}{2} - \vec{V}\times(\nabla\times\vec{V})\right] = -\nabla p \tag{4.9}$$

Substituting the definition of vorticity which is

$$\vec{\omega} = \nabla\times\vec{V} \tag{4.10}$$

into equation (4.9) and assuming steady flow yields

$$\rho\left[\frac{\nabla V^2}{2} - \vec{V}\times\vec{\omega}\right] = -\nabla p \tag{4.11}$$

Solving equation (4.11) for the components of vorticity in the radial and tangential directions yields

$$\omega_r = \frac{1}{V_x}\left[\frac{1}{\rho r}\frac{\partial p}{\partial\theta} + \frac{1}{2r}\frac{\partial V^2}{\partial\theta} + V_r\omega_x\right] \tag{4.12}$$

$$\omega_\theta = -\frac{1}{V_x}\left[\frac{1}{\rho}\frac{\partial p}{\partial r} + \frac{1}{2}\frac{\partial V^2}{\partial r} + V_\theta\omega_x\right] \tag{4.13}$$

Thus, with the radial and tangential vorticity now known, the streamwise vorticity can now be solved. The streamwise vorticity is normalized with respect to inlet axial velocity and vane chord at midspan. Since to derive equations (4.12) and (4.13), the viscous terms of the Navier-Stokes equations were dropped, the

streamwise vorticity presented in Figure 4.19 should be looked at qualitatively, not quantitatively.

The passage vortex near the casing at X/C = 0.935 is shown clearly in Figure 4.19. The large positive vorticity (magnitude of 30.0) in the suction surface/casing corner corresponds to the passage vortex. Near the hub wall/suction surface corner, a large negative vorticity region (magnitude of -14.1) corresponds to the passage vortex also. The large positive vorticity region above the passage vortex could possibly correspond to the suction side leg of the horseshoe vortex. The vorticity is zero in the freestream giving confidence in this method to calculate vorticity correctly.

Six criteria are used to determine the existence of a vortex in a flow field. These are high total pressure loss, low static pressure, high vorticity, over and underturning of the yaw angle, positive and negative radial flow angles and vortical motion in the secondary flow vectors. A vortex exists when these six flow phenomena occur at the same position in the flow field. The existence of the passage vortices at both the hub and the casing of X/C = 0.935 is confirmed since they both meet all six of the criteria. On the other hand, the existence of the suction side leg of the horseshoe vortex is more doubtful. There is no evidence of its existence in the casing/suction side corner. While in the hub/suction side corner there is a region of high positive vorticity which could correspond to the suction side leg of the horseshoe vortex, the other criteria are not met. Thus, its existence cannot be proven conclusively.

CHAPTER 5

NOZZLE EXIT FLOW FIELD

The nozzle exit flow field measurements were carried out with the following objectives:

(1) To obtain a better physical understanding of the evolution of secondary flow downstream of the blade passage.

(2) To determine the characteristics of the nozzle wake, including its decay rate and the growth of its wake width.

(3) Measurement of the flow field upstream of the rotor was needed for the analysis of the rotor flow field measurements presented in Chapters 6 and 7.

The flow field downstream of the nozzle was measured using a miniature five-hole probe, with a probe head diameter of 1.67 mm. The exit flow is measured at 50 to 80 tangential locations across the one passage and at 21 radial locations at $X/C = 1.025$ and 1.09, and at midspan at $X/C = 1.007$, 1.01, 1.12 and 1.16. Figure 4.1 shows the measurement planes at $X/C = 1.025$ and 1.09. For the following plots, the tangential distance is normalized by the nozzle pitch, where $S = 0$ is the wake center at midspan at $X/C = 1.025$. The positive values of S are on the pressure side of the wake and the negative values of S are on the suction side. The pitchwise extent of the plots is a little less than one blade pitch for both $X/C = 1.025$ and $X/C = 1.09$.

5.1 Total Pressure Loss and Static Pressure Drop

The contours of total pressure loss coefficient (Ψ_{LOSS}) are shown for X/C = 1.025 and X/C = 1.09 in Figures 5.1 and 5.2. There are two high loss regions, one near H = 0.10 and the other near H = 0.80 for both axial locations. These two high loss regions are caused by secondary flow vortices and their dissipation. The maximum loss regions occur close to the suction surface. Furthermore, the tip loss core is located further from the casing than the loss core near the hub wall, which results from the radial inward velocities that exist in the wake and in the free stream region. Comparing the loss at both the tip and hub between these two axial locations and X/C = 0 935, one can see that the peak loss coefficient increases slightly between X/C = 0.935 and X/C = 1.025 and then decreases dramatically at X/C = 1.09. This can be seen more clearly in Figure 5.3, which presents the peak total pressure loss coefficient (($\Psi_{LOSS})_{max}$) in both the hub and tip secondary flow regions as a function of axial distance. The dramatic decrease between X/C = 1.025 and X/C = 1.09 results from the interaction of the passage vortex and the wake, the interaction of the passage vortex and the freestream flow and also the decay of the passage vortex as it travels downstream of the nozzle.

On the other hand, the size of the passage vortex remains basically the same between X/C = 0.935 and 1.09. Figure 5.4, which presents the maximum width of the hub and casing passage vortices as a function of axial distance, shows this more clearly. The maximum width of the passage vortex, L_s, is defined as the maximum pitchwise width of the passage vortex from the wake center (for the data downstream of the nozzle) or the nozzle surface (for X/C = 0.935) to the edge of the passage vortex (where Ψ_{LOSS}= 0.2). In contrast, while the width (pitchwise extent) of the secondary flow loss regions has not changed between the two axial
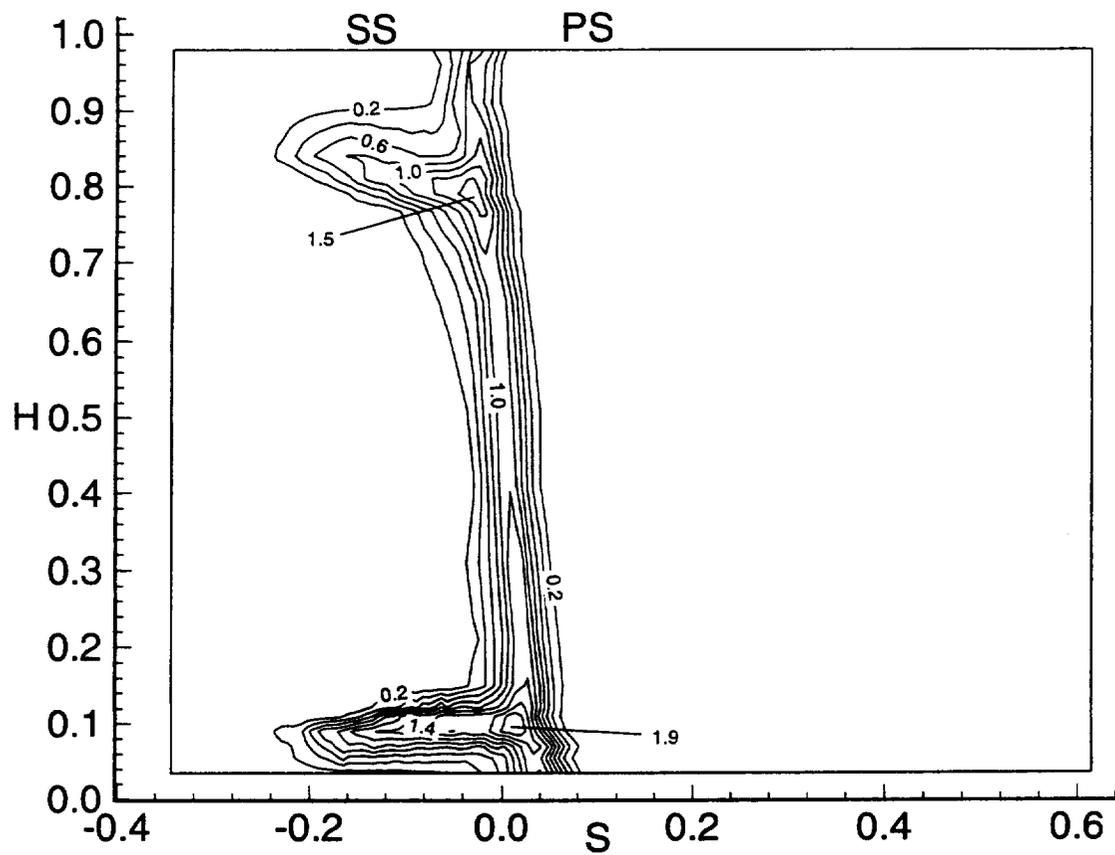
Figure 5.1. Total Pressure Coefficient $\left(\Psi_{LOSS}\right)$ at 1.025
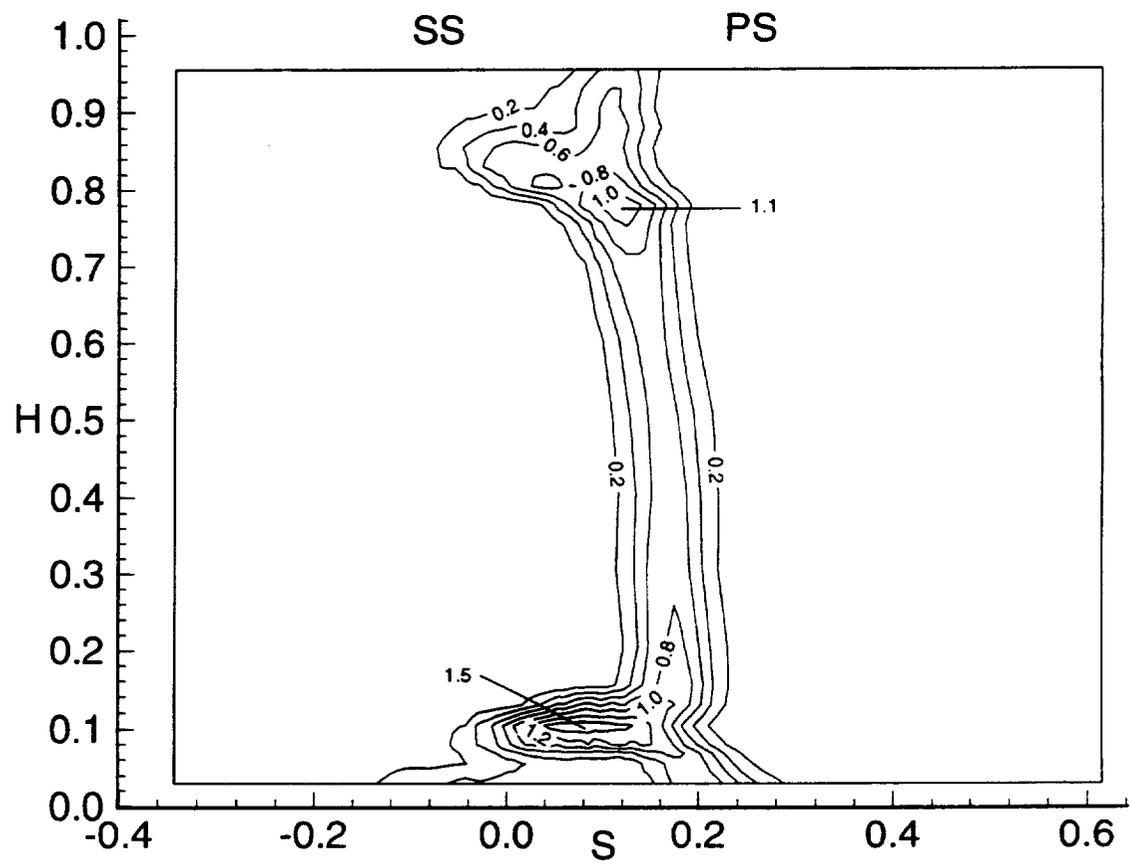
Figure 5.2. Total Pressure Coefficient $\left(\Psi_{\text{Loss}}\right)$ at 1.09
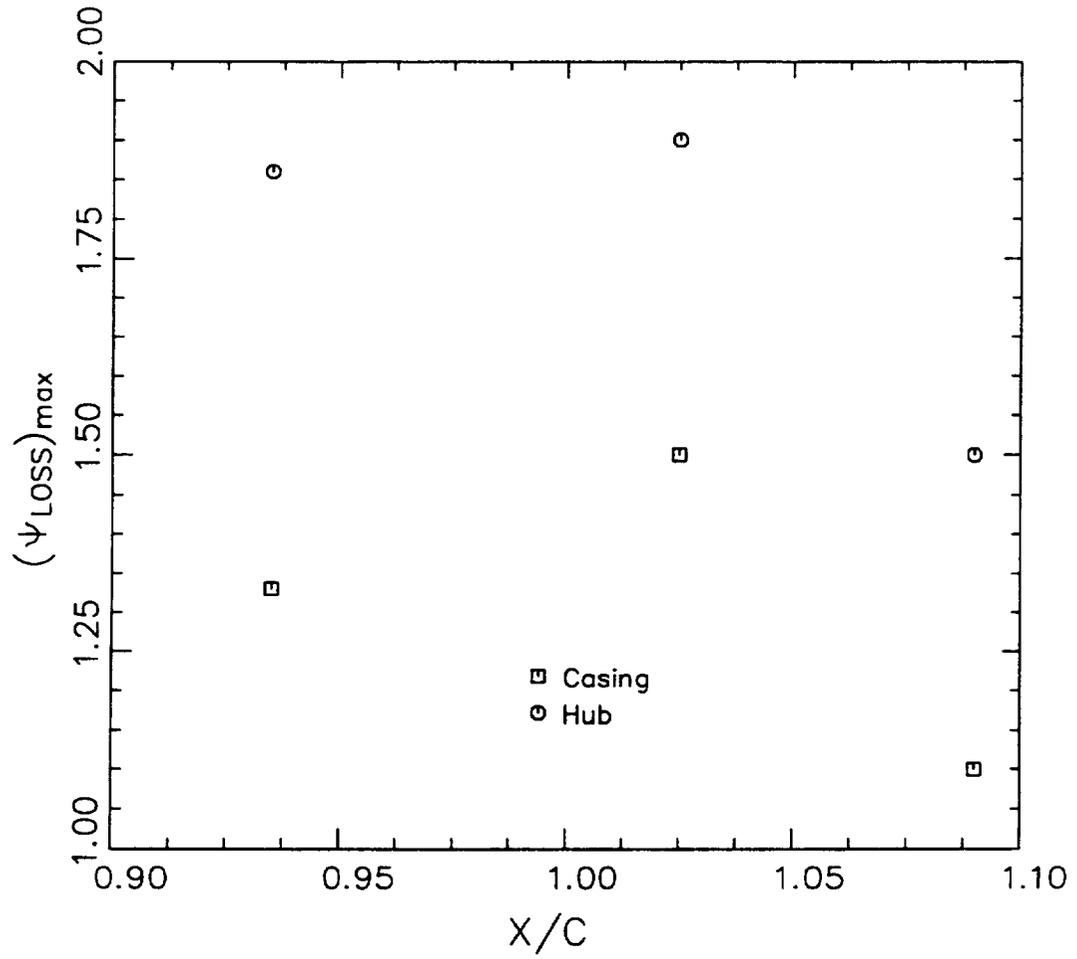
Figure 5.3. Maximum Total Pressure Loss $\left(\Psi_{LOSS}\right)_{max}$ For Hub and Casing
Secondary Flow Regions
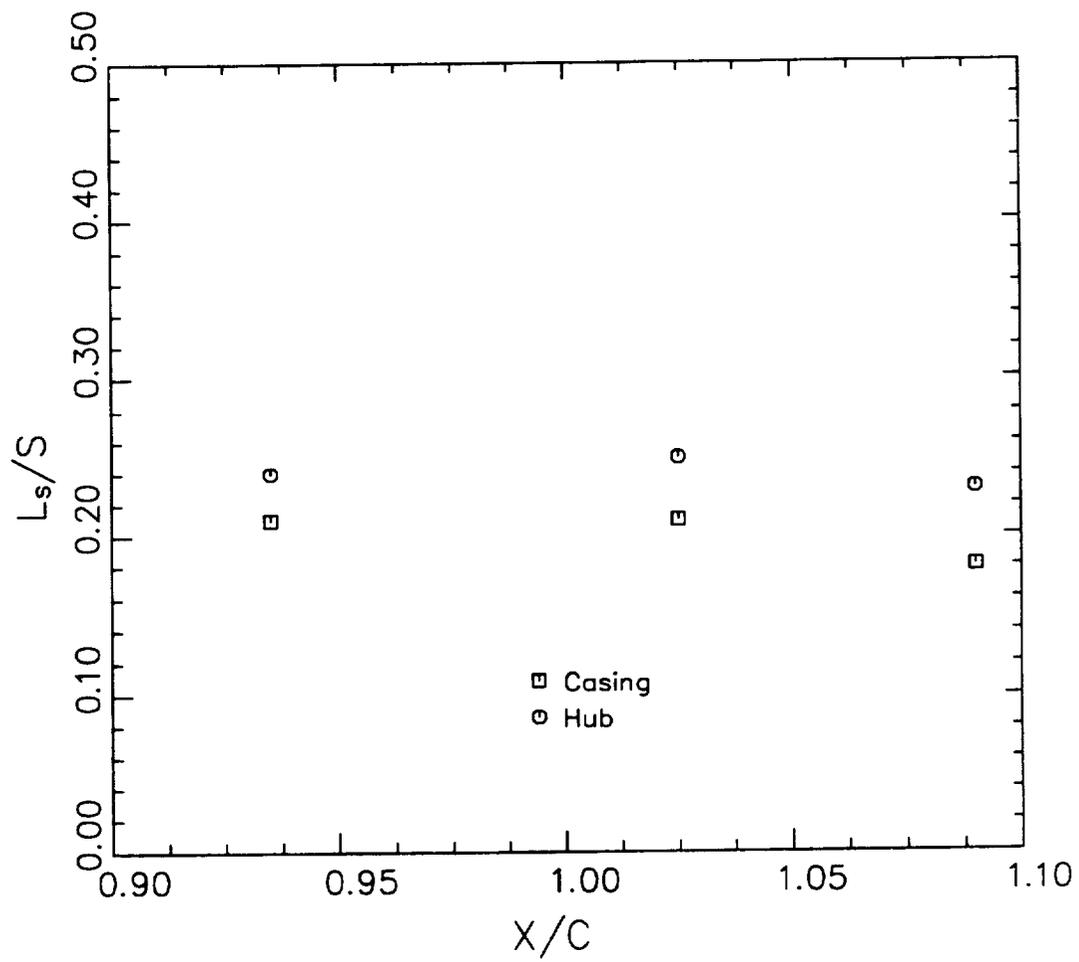
Figure 5.4. Maximum Width of Hub and Casing Secondary Flow Regions

locations, the width of the loss region outside of the secondary flow loss region has increased. The circumferentially mass-averaged total pressure loss coefficient for X/C = 1.025 is given in Figure 5.5. The two loss peaks can be seen clearly in this figure. The peak near the hub is larger in magnitude but smaller in radial extent than the one near the casing. The reasons for the larger extent of the loss region at the casing was discussed in section 4.3.1 of this thesis. The larger magnitude of the hub loss region is a result of the radial inward flow inside the wake which causes the low momentum fluid in the wake to move toward the hub. Both Yamamoto and Yanagi (1986) and Hunter (1982) report similar distributions in their annular nozzle cascades.

At midspan, the secondary flow effects are absent and the mass averaged loss coefficient is the profile loss coefficient for the vane, which is 0.05. This is close to the value of 0.06 predicted from the correlation by Kacker and Okapuu (1982) which is shown in Figure 5.5. The area averaged total pressure loss coefficient ($\overline{\overline{\Psi}}$) is calculated to be 0.077 at X/C=1.025 and 0.0818 at X/C=1.09. The losses increase as flow travels downstream of the rotor due to mixing of the wake, the decay of the vortices and the growth of the endwall boundary layer. The secondary flow loss is the loss calculated by the subtracting profile loss from the total loss. The mass averaged secondary flow loss coefficient measured in this nozzle is equal to 0.0262. This is less than the value of secondary flow loss coefficient predicted from the correlation by Dunham (1970) which is 0.0503. There are two main reasons for this difference. The first is that Dunham's formula overestimates the secondary loss parameter for low-aspect ratio blades. Kacker and Okapuu (1982) have derived a correlation for low aspect ratio blades to include the dependence on aspect ratio. Substituting Kacker and Okapuu's aspect ratio dependence formula into Dunham's secondary loss prediction yields a value of
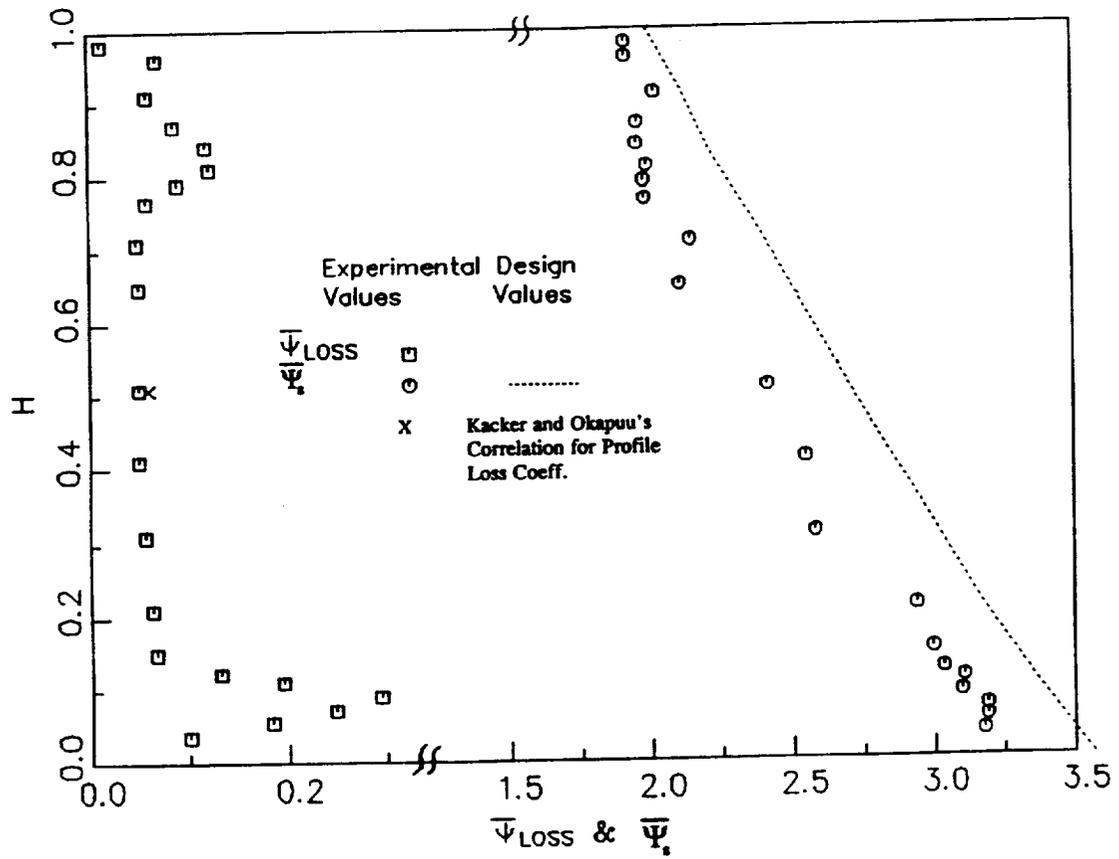
Figure 5.5. Circumferentially Mass-Averaged Pressures at X/C = 1.025

0.0361 for the secondary loss coefficient which is much closer, but still higher than the measured value. The second reason for this difference is that the secondary flow loss correlations were developed from cascade loss data taken between 0.7 and 1.0 chord downstream of the blade, and thus include the additional losses due to mixing, decay of the secondary vortices and boundary layer growth. Moore and Adhye (1985) measured the losses at three axial planes (from X/C=1.1 to X/C=1.4) downstream of a turbine cascade. Extrapolating their data, the nozzle secondary flow losses are found to increase by 30% from trailing edge to 0.70 chord downstream. Applying this correction to Dunham's correlation results in a value of 0.0253 which is within 2% of the measured secondary flow loss coefficient (0.0262).

Contours of static pressure loss coefficient for X/C = 1.025 and 1.09 are given in Figures 5.6 and 5.7 and the mass average distribution of static pressure loss coefficient is given in Figure 5.5. The mass averaged experimental values are compared to the design values that were calculated using a two-dimensional throughflow analysis that solved the circumferentially-averaged equations of motion in the meridional plane using a streamline curvature technique (see Lakshminarayana et al., 1992). The presence of strong radial pressure gradient is evident in these figures. The static pressures are generally lower in secondary vortex regions and higher in the wake regions. (Higher static pressure coefficient indicates lower static pressure.) While the radial variation in static pressure is similar for both X/C = 1.025 and X/C = 1.09, the pitchwise variation is not. The pitchwise variation of static pressure is much smaller and smoother at X/C = 1.09 than at X/C = 1.025, due to the rapid decay of the wake static pressure. Detailed interpretation of the static pressure across the wake is discussed later in this chapter.
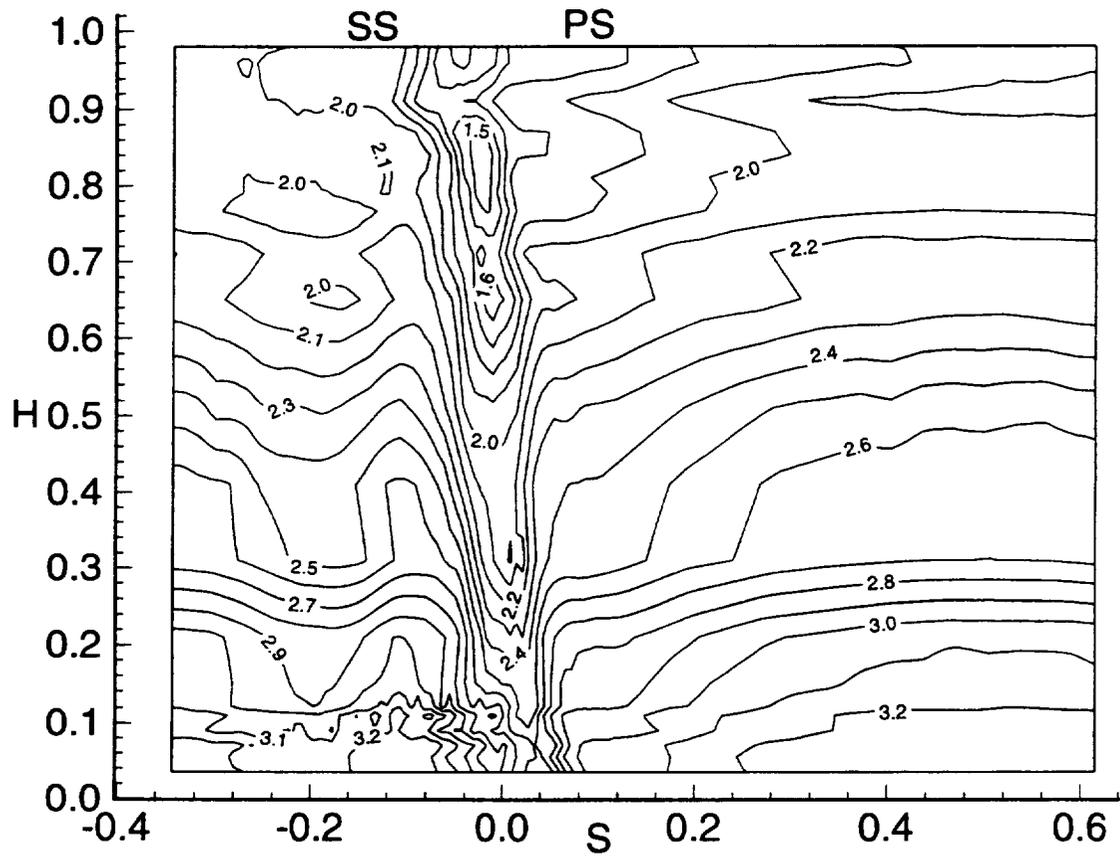
Figure 5.6. Static Pressure Drop Coefficient (Ψ_s) at X/C = 1.025
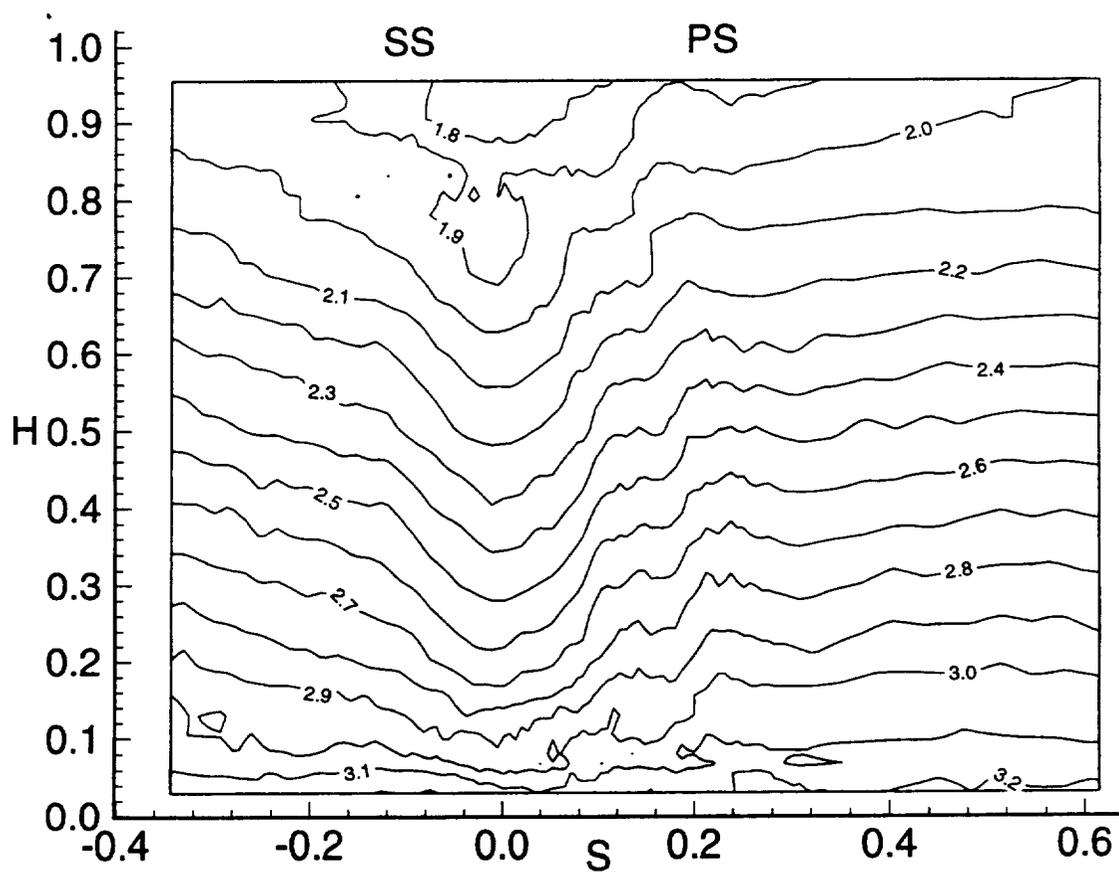
Figure 5.7. Static Pressure Drop Coefficient (Ψ_s) at X/C = 1.09

5.2 Velocity and Flow Angles

The circumferentially mass-averaged velocities at X/C = 1.025 are shown plotted in Figure 5.8. The total and tangential velocity plots show a decrease in velocity near H=0.1 and 0.8, which is due to the hub and tip wall secondary flows. The axial velocity profiles show a decrease near the endwalls, due to the presence of the wall boundary layers. The total, axial and tangential velocities are in agreement with the design values near midspan region, while deviating from the design values in the secondary flow regions near the endwalls.

Contour plots of the yaw angles (α) at X/C = 1.025 and 1.09 are shown in Figure 5.9 and 5.10, respectively. The flow is underturned on the pressure side of the wake and overturned on the suction side of the wake away from the endwalls. This is because the suction surface blade angle is higher than the design exit flow angle (70 degrees) and the pressure side blade angle is lower than the design exit flow angle at the trailing edge. This over and underturning of the flow decreases as the flow travels downstream of the trailing edge from a value of 6 degrees of both over and underturning at X/C = 1.025 (midspan) to 2 degrees of both over and underturning at X/C = 1.09 (midspan), which is a result of mixing of the wake. The maximum underturning occurs near H = 0.1 and H = 0.8. This local underturning of the flow is caused by secondary flow vortices. In the core region of these vortices at X/C = 1.025, underturning as high as 25 degrees is observed at H = 0.80 while near the hub the maximum underturning is 15 degrees. There is an overturning of 11 degrees near the suction side of the wake at H=0.80 and of 8 degrees near the hub wall also at this axial location. This phenomena is as expected from secondary flow theories and this overturning and underturning of the flow located next to each other is another indication of the presence of vortices at these
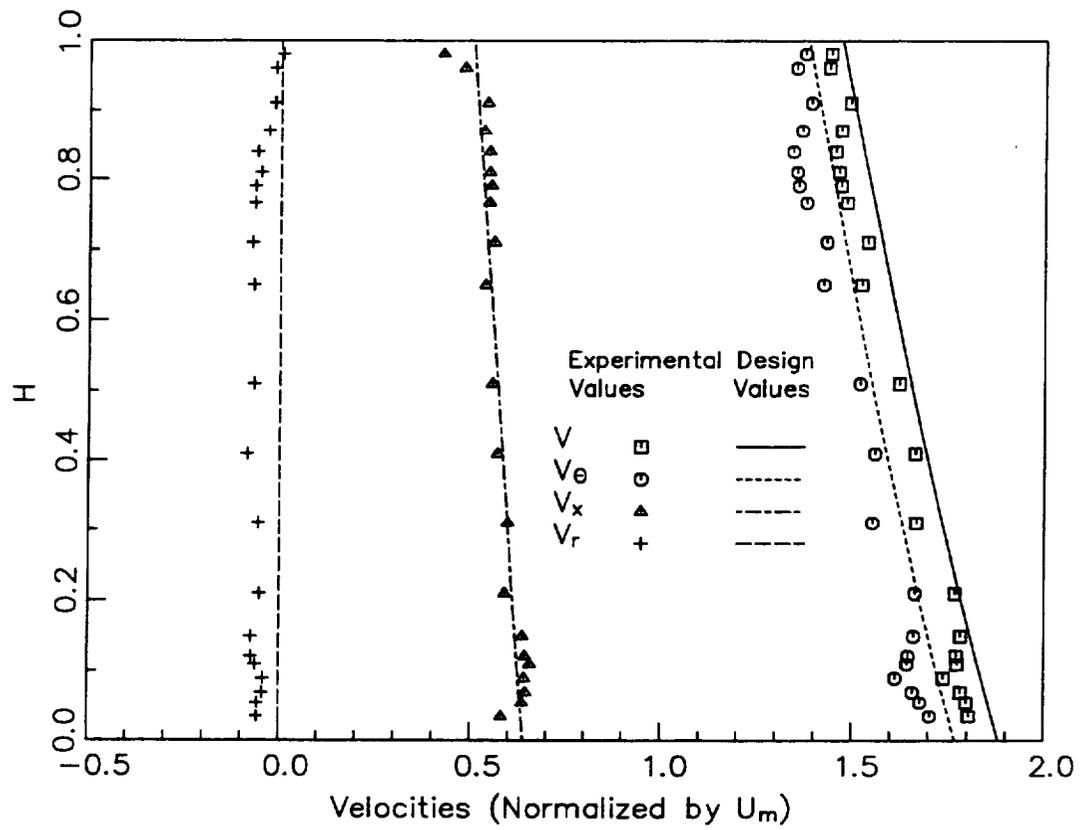
Figure 5.8. Circumferentially Mass-Averaged Velocities at X/C = 1.025
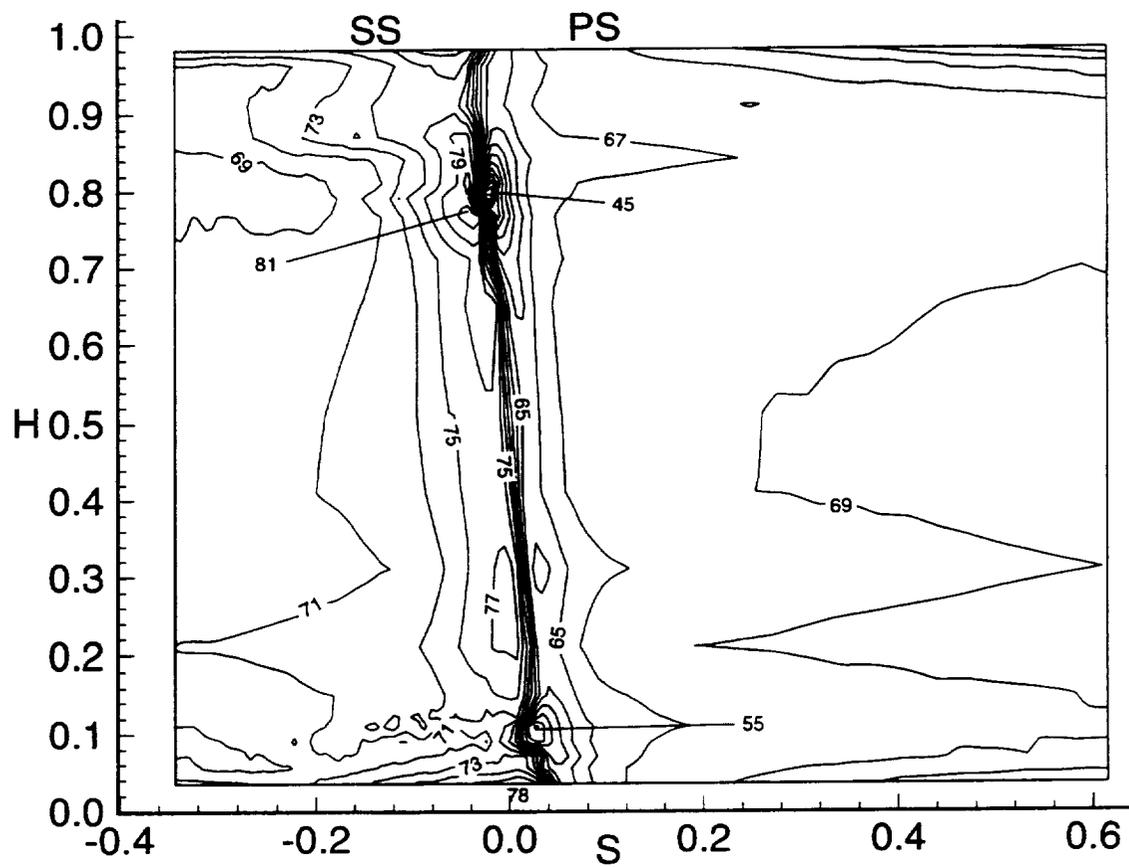
Figure 5.9. Yaw Angle (α) at X/C = 1.025 (in degrees)
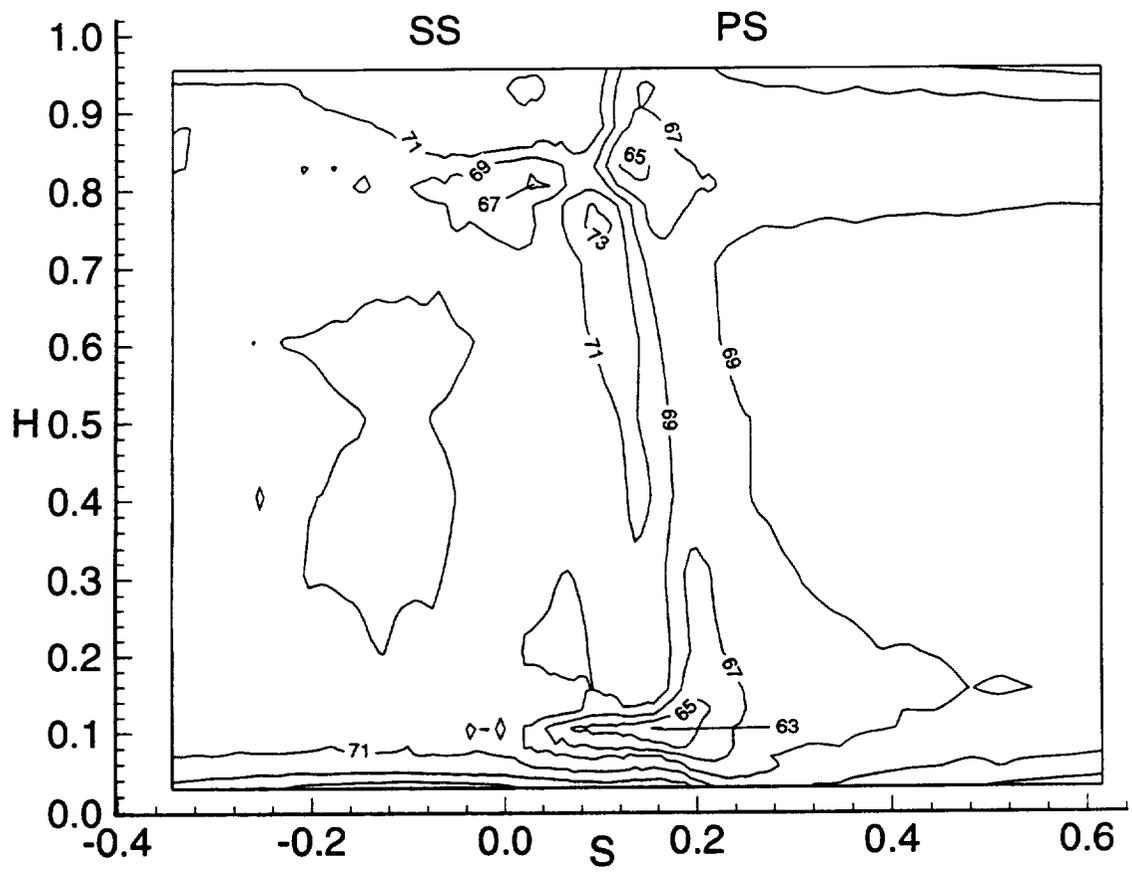
Figure 5.10. Yaw Angle (α) at X/C = 1.09 (in degrees)

locations. Between X/C = 1.025 and 1.09, there is a dramatic decrease in maximum over and underturning in the secondary flow regions. The maximum over and underturning in the casing secondary flow region decreases by 8 and 20 degrees, respectively, between X/C = 1.025 and 1.09, while at the hub the peak values of over and underturning decrease by 3 and 8 degrees, respectively. This results from the secondary flow vortex decay which is caused by the interaction of the secondary flow vortices with the nozzle wake and freestream flow. The mass-averaged yaw angles, presented in Figure 5.11, shows the overturning near the casing and near the hub endwall due to secondary flow and vortices. The closest measurement at the casing endwall is 4.5% of the span from the casing, while the closest measurement to the hub is 3.0% from the hub. As one moves away from the endwalls the flow becomes underturned achieving design flow near 20% of span from the hub and 30% of span from the casing. The larger underturned region near the casing is due to the larger secondary flow region near the casing. This is consistent with predictions from secondary flow theories and measurement by others. The experimental values of yaw angle match the design values well near the midspan, while deviating from design in the secondary flow regions, which is expected, since the design code is two-dimensional.

The contours of radial flow angles (γ) at both downstream locations are shown in Figures 5.12 and 5.13, respectively. The flow is directed toward the hub over most of the passage in the inviscid region. This is due to the radially inward lean of the nozzle trailing edge (see Figure 2.2). Binder and Romey (1982), who have a radially inward lean of their nozzle trailing edge, also see radially inward flow over most of the span just downstream of the trailing edge of their annular nozzle cascade. At X/C = 1.025, very high negative radial flow angles or pitch angles (-66 degrees) occur at H=0.83 near the suction side of the wake, while
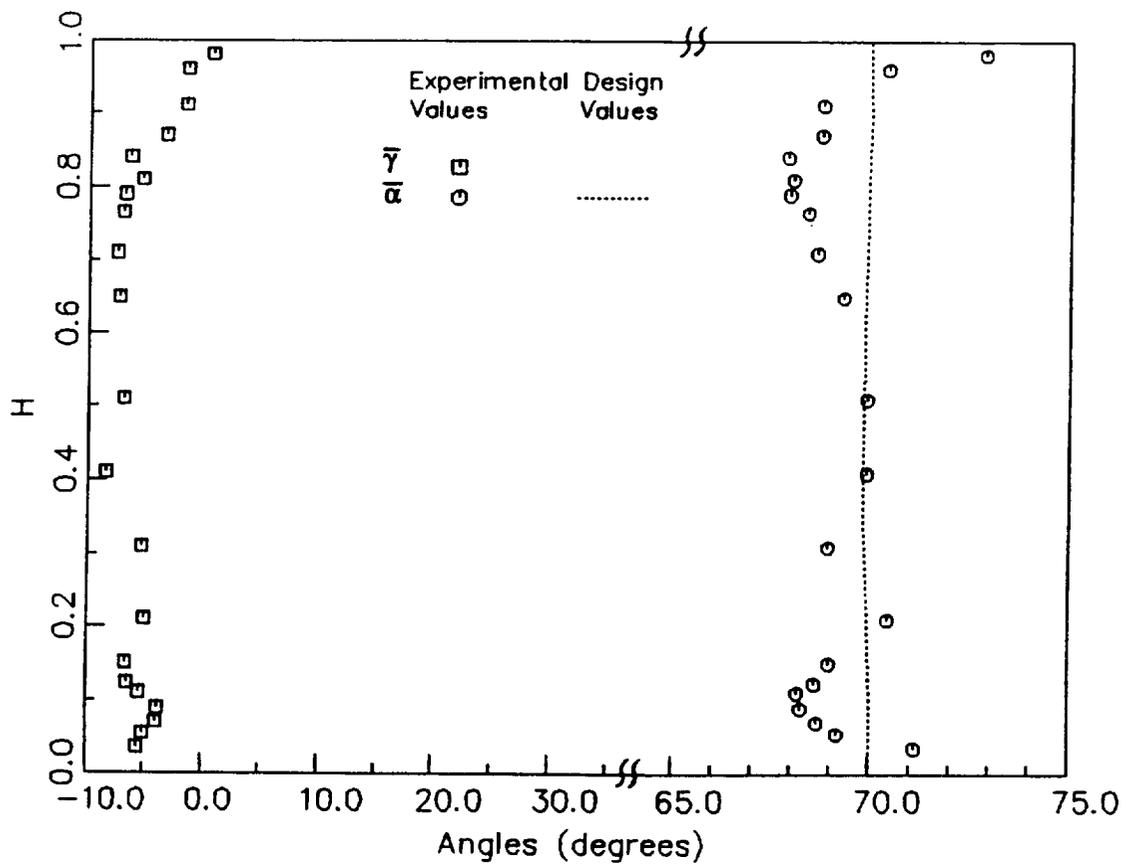
Figure 5.11. Circumferentially Mass-Averaged Angles at X/C = 1.025
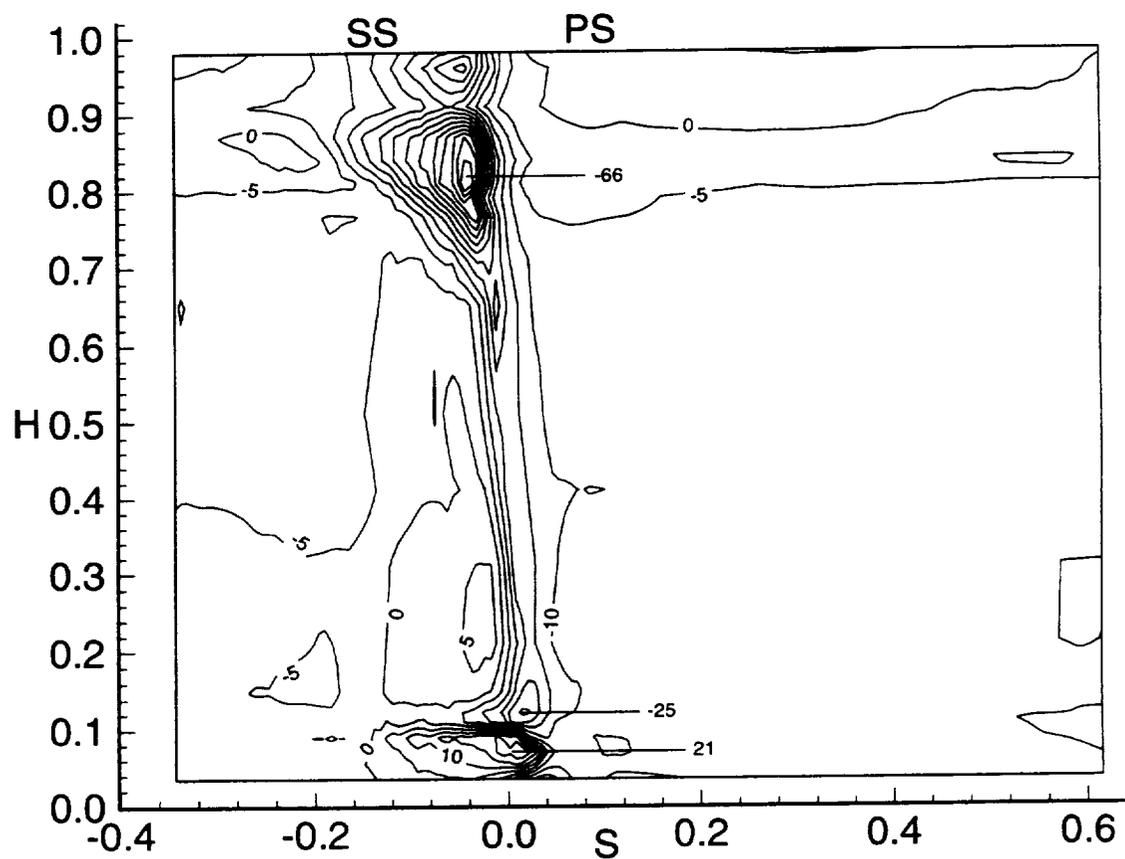
Figure 5.12. Radial Flow Angle (γ) at X/C = 1.025 (in degrees)
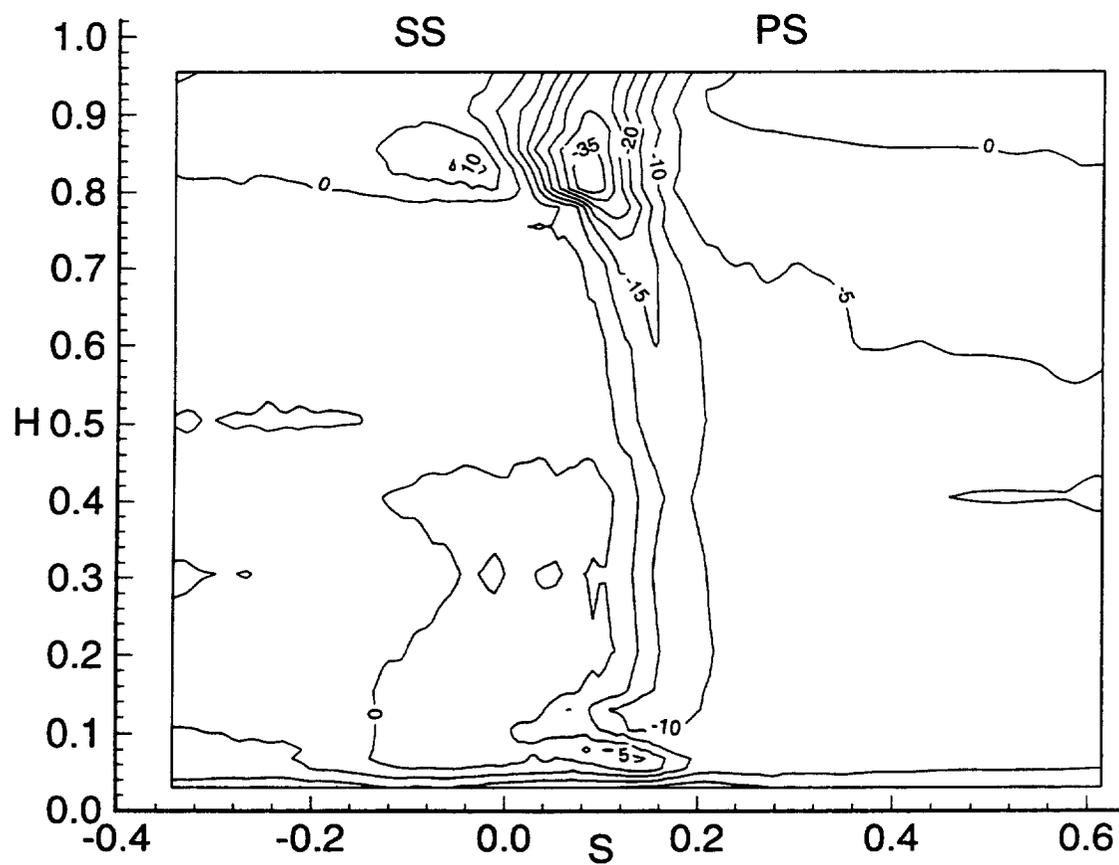
Figure 5.13. Radial Flow Angles (γ) at X/C = 1.09 (in degrees)

positive angles occur at S= -0.25, at the same radial location. Also at the same axial location, high negative radial flow angles (-25 degrees) occur at H=0.13 and S=0 degrees while positive angles (21 degrees) occur closer to the hub. This is another indication of the presence of vortices, since local high and low radial flow angles occur across a vortex. Just as in the yaw angle, the difference between the maximum and minimum radial flow angle decreases between X/C = 1.025 and 1.09 by 21 degrees in both the hub and casing secondary flow regions. This results from the secondary flow vortex decay. The mass-averaged radial flow angles at X/C = 1.025 are shown in Figure 5.11. The radial flow angles are negative over most of the span, reaching zero at the casing. The negative radial flow angles at the hub are due to the slot which separates the rotating hub from the stationary hub, which is located just downstream of this location.

5.3 Secondary Flow Velocity

The secondary flow velocity vectors are shown in Figures 5.14 and 5.15, for X/C=1.025 and 1.09, respectively. The secondary flow vectors in the r-θ plane are derived from the measured data and the design flow angle (70 degrees) using equation (4.1), as described previously. The presence of strong radial inward flow in the wake can be seen. Strong radial inward flow at the wake center near the casing is caused by the passage vortex (clockwise) which augments the radial inward flow of the wake. The passage vortex can be seen clearly, near H=0.8 at X/C=1.09, while at X/C=1.025 the radial inward flow is so strong that the vortical motion cannot be seen. Since the pressure side leg of the horseshoe vortex has the same direction of rotation as the passage vortex, this vortex could be a combination of the passage vortex and the pressure side leg of the horseshoe vortex as discussed
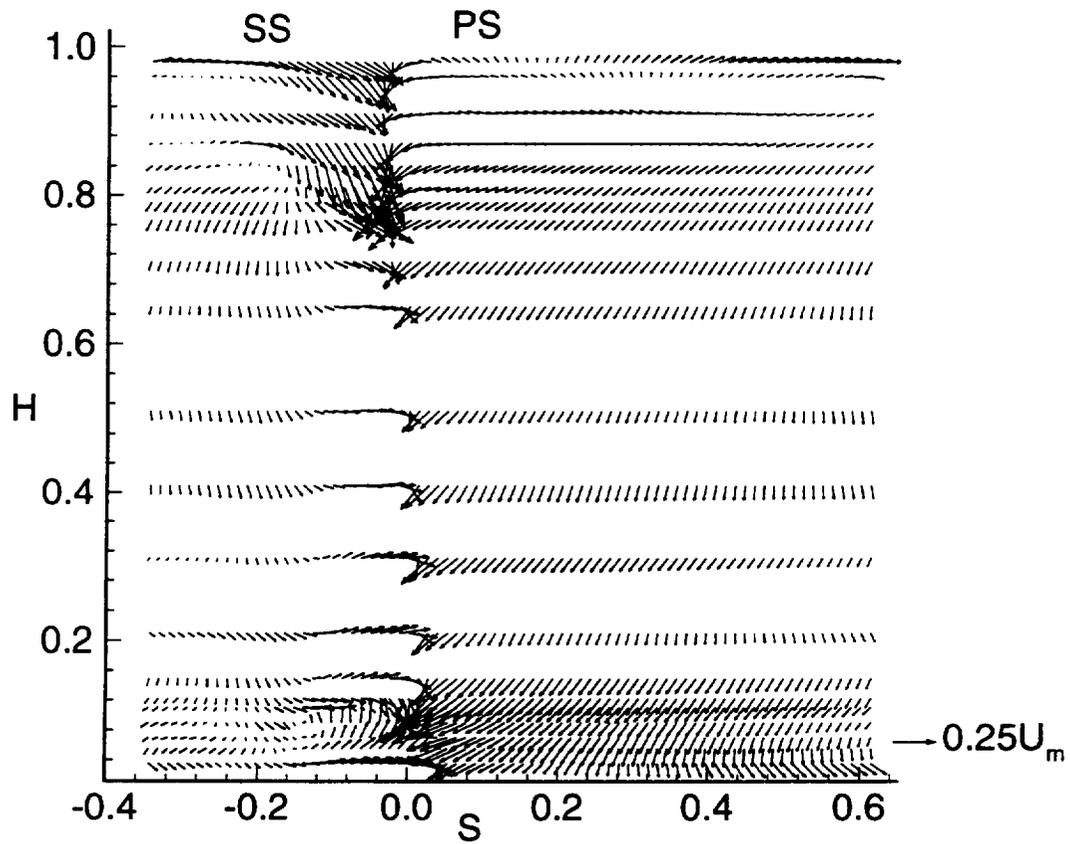
Figure 5.14. Secondary Flow Velocity Vectors at X/C = 1.025
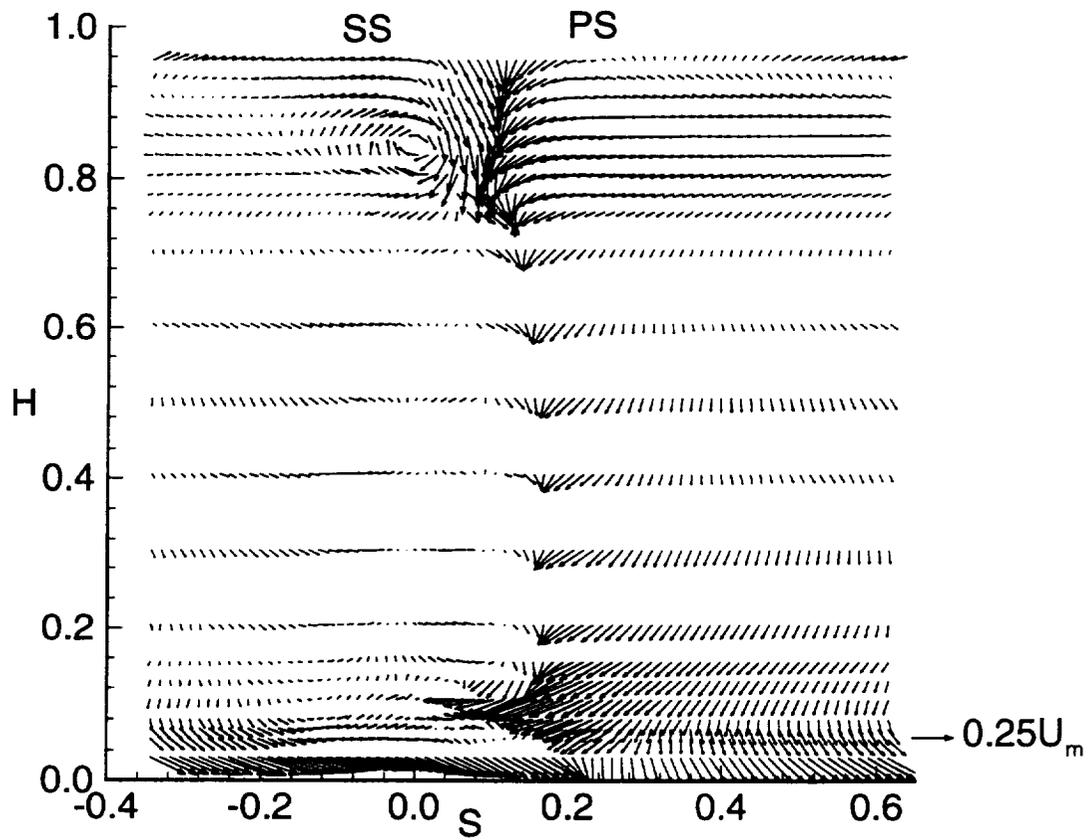
Figure 5.15. Secondary Flow Velocity Vectors at X/C = 1.09

earlier. There is no evidence of the suction side leg of the horseshoe vortex near the casing (which would rotate opposite to the passage vortex). Very close to the passage vortex, there is a vortical motion in the counterclockwise direction on the pressure side of the wake (This will be called the counter-rotating vortex). This is formed by the interaction of the passage vortex with the wake.

The radial flow is directed inward over almost the whole inviscid flow field. This is because of the radial inward lean of the nozzle trailing edge, discussed earlier, which causes this flow movement toward the hub. The overturning on the suction side and the underturning on the pressure side can be clearly seen at the wake center. The radial inward flow is stronger in the wake than in the freestream, resulting from an imbalance of the centrifugal force and the pressure gradient close to the surface of the blade, which was described earlier. This radial inward flow is in the same direction as those induced by the casing passage vortex and thus it augments the casing passage vortex. At the hub there is also evidence of the passage vortex at X/C=1.025. But the radial inward flow in the wake near the hub is in the opposite direction to those caused by the passage vortex, and thus the radial inward flow seems to counteract those induced by the hub passage vortex. This is similar to interaction of the radial inward flow of the suction surface boundary layer at X/C = 0.935 and the passage vortices. The strong radial inward flow of the suction surface boundary layer, observed at X/C = 0.935 (Figure 4.18) seems to have disappeared at X/C = 1.025. In fact, the flow on the suction side of the wake near the hub has reversed direction and is moving radially outward. This is a result of the rotating hub that is located just downstream of this location. The rotation of the hub is toward increasing S in this figure. The hub wall boundary layer is highly skewed and undergoes sudden perturbation as shown in Figure 4.1. At X/C=1.09 the hub passage vortex seems to have dissipated while the casing

passage vortex remains strong. This is also a result of the interaction of the hub passage vortex with the rotating hub which is located just downstream of this location (see Figure 4.1). This interaction causes the hub passage vortex to dissipate. The radial inward flow at the hub is due to the gap between the stationary and rotating hub which is at this location.

Comparing the secondary flow vectors at X/C = 0.935 (Figure 4.18) with those at X/C = 1.025, no dramatic change in secondary flow is observed at the tip. The pitchwise and spanwise position of the passage vortex relative to the wake center remains the same as one travels from X/C = 0.935 to X/C = 1.09. This is in contrast to the results of Moore and Adhye (1985) where the passage vortex in their turbine cascade migrates toward midspan and toward the middle of the passage as it progresses downstream. The secondary flow at the hub, however, undergoes a dramatic change going from X/C = 0.935 to X/C = 1.09. This is a result of the rotating hub which interacts with the secondary flow at the hub.

The diameter of the passage vortices in the AFTRF nozzle are much smaller than the diameter of the passage vortices in other turbine cascades. The maximum pitchwise distance of the AFTRF passage vortices downstream of the nozzle are 25% of the nozzle pitch (0.25S). This is in constrast to the rotor cascades of others such as Langson et al. (1977), Moore and Adhye (1985), and Gregory-Smith et al. (1988) whose maximum pitchwise width of the passage vortices are 100% of the blade pitch. This is also in constrast to the nozzles of Hunter (1982) and Sieverding et al. (1984) whose maximum pitchwise width of the passage vortices are 100% of the blade width, also. The rotor cascade's passage vortices are larger because the rotors have a much larger turning (120 degrees) compared to the AFTRF nozzle (70 degrees). The other researcher's nozzles have larger passage vortices due to the larger nozzle inlet boundary layers.

5.4 Streamwise Vorticity

Even though the isocline angle plots and the secondary flow vector plots are useful in identifying vortices, they have their limitations. The isoclinal angle plots cannot determine the sign of the vortex, while the secondary flow vectors can change depending on what the primary flow is defined to be. A more logical approach in identifying both the vortices and their sign is to examine the strength of the streamwise vorticity. But this method has its problems, too. The scatter in experimental data can cause unrealistic gradients and thus false levels of vorticity. But, usually the biggest problem is that the axial distance between the data points is much larger than the radial and tangential distances between the data points, thus, the streamwise vorticity cannot be found explicitly since it would involve gradients of velocity in the axial direction. But in this experiment the axial distance between the measurement planes is small (7 mm) and comparable to the tangential distance (1 mm) and average radial distance (5 mm) between the data points.

The components of vorticity in the axial, tangential and radial directions are given by equations 4.2 through 4.4 and the streamwise vorticity is calculated from equation 4.6 The primary flow angle is set equal to the design exit flow angle (70.0 degrees).

The contour plots of streamwise vorticity ($\omega_s C/V_{x_1}$) at X/C = 1.025 and X/C = 1.09 are given in Figures 5.16 and 5.17, respectively. The existence of a strong casing passage vortex is clearly seen in these figures. The large positive vorticity (peak magnitude of $\omega_s C/V_{x_1} = 17$ at X/C = 1.025 and $\omega_s C/V_{x_1} = 18$ at X/C = 1.09) near the casing corresponds to the passage vortex. At the hub, the passage vortex is revealed by the presence of large negative vorticity. The magnitude of peak
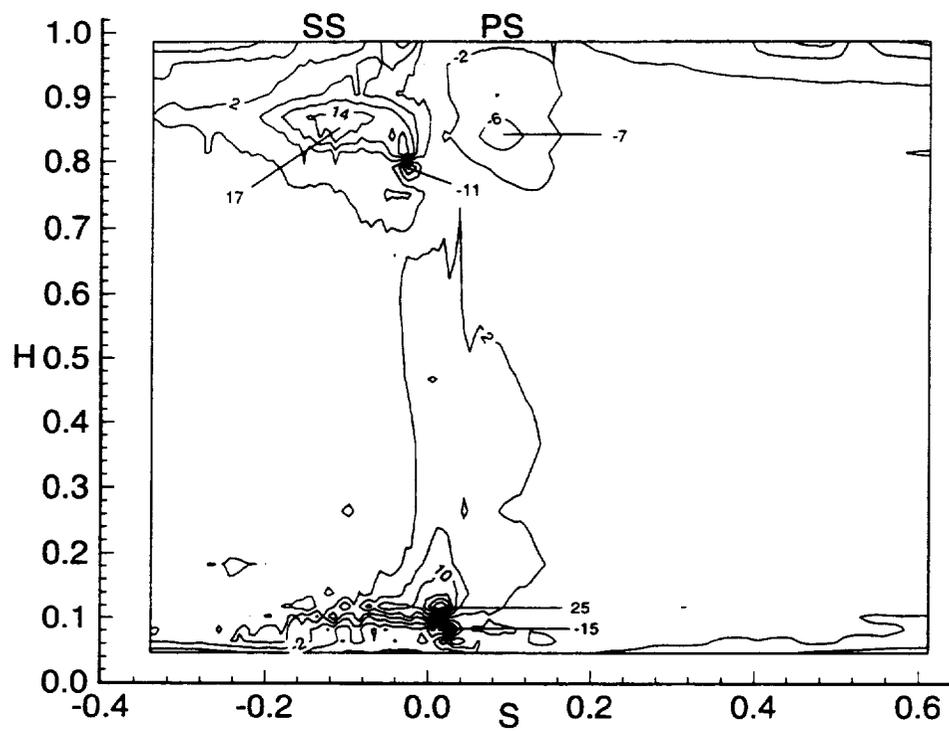
Figure 5.16. Secondary Vorticity $\left(\omega C/V_{x1}\right)$ at X/C = 1.025
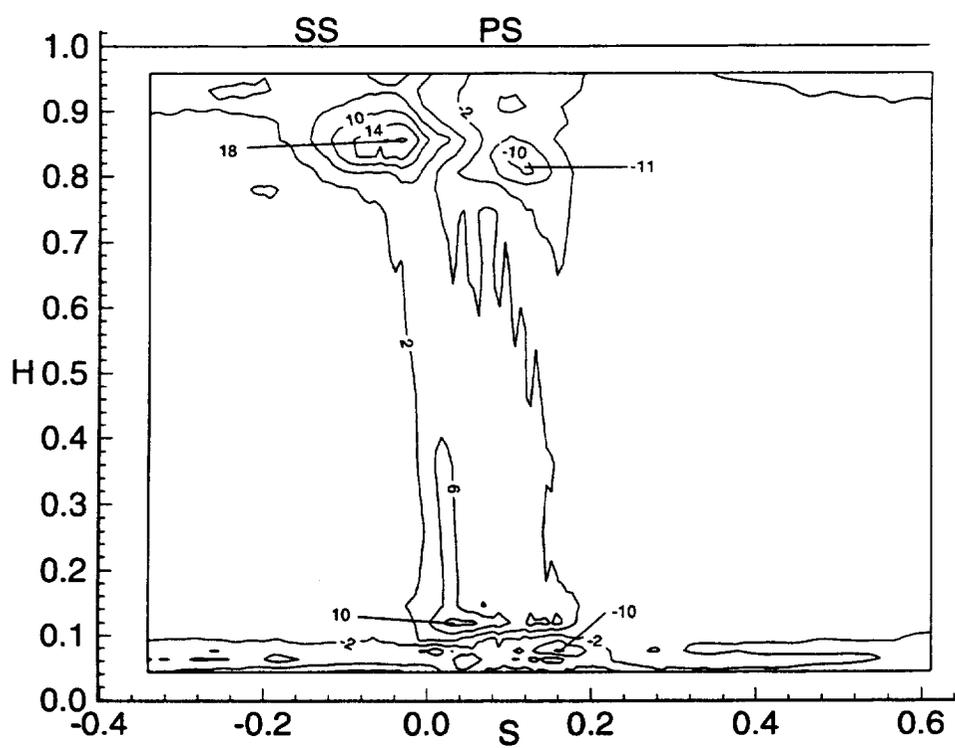
Figure 5.17. Secondary Vorticity $\left(\omega C/V_{x1}\right)$ at X/C = 1.09

vorticity at the center of the vortex at X/C = 1.025 ($\omega_s C/V_{x_1}$ = -15) is similar in magnitude to the peak vorticity at the casing, which demonstrates that the hub passage vortex is similar in strength to the casing passage vortex at X/C = 1.025. The magnitude of peak negative vorticity at the hub decreases by 33% from X/C=1.025 to X/C=1.09 which agrees with the secondary flow vectors that the hub passage vortex is decreasing in strength as it moves downstream of the nozzle trailing edge.

At X/C = 1.025, there are two negative vorticity regions near the casing. The larger (in area) of the two (peak magnitude of $\omega_s C/V_{x_1}$ = -7) is due to the counter-rotating vortex (which is caused by the interaction of the passage vortex and the wake). The smaller negative vorticity region (peak magnitude of $\omega_s C/V_{x_1}$ = -11) located just below the casing passage vortex, possibly could be the suction side leg of the horseshoe vortex. At X/C = 1.09, there is only one negative vorticity region near the casing. This vortex is also due to the interaction of the passage vortex with the wake. The small negative vorticity region seen at X/C = 1.025, seems to have disappeared. It is possible that this vortex has either merged with the large negative vorticity region between the two axial planes or has been dissipated by its contact with the casing passage vortex.

Near the wake center from H=0.7 to H=0.1, there is a positive vorticity region which corresponds to the over and underturning regions in the wake. There is a positive vorticity peak at H = 0.1, which is caused by the interaction of the passage vortex and the wake. The peak magnitude of this positive vorticity decreases from $\omega_s C/V_{x_1}$ = 25 at X/C = 1.025 to $\omega_s C/V_{x_1}$ = 11 at X/C = 1.09. This is a also a result of the interaction of the flow near the hub with the rotating hub.

Comparing the streamwise vorticity upstream of the trailing edge (X/C = 0.935) which is presented in Figure 4.20 with the vorticity at X/C = 1.025, the

magnitude of the casing passage vortex has decreased by half (from $\omega_s C/V_{x_1} = 30$

to 17). This is due to the interaction of the passage vortex and the wake, the

interaction of the passage vortex and the freestream flow and also the decay of the

passage vortex as it travels downstream of the nozzle. On the other hand, the

negative vorticity region associated with the hub passage vortex has not changed

very much in strength between X/C = 0.935 ($\omega_s C/V_{x_1} = -14$) and X/C = 1.025

($\omega_s C/V_{x_1} = -15$). Whereas at X/C = 0.935, the negative vorticity region corresponds

to only the hub passage vortex, at X/C = 1.025 the negative vorticity region results

from both the hub passage vortex and the interaction of the endwall flow with the

rotating hub.

The streamwise vorticity was also calculated using the method of Gregory-

Smith (1988), discussed in Chapter 4, which approximates the axial velocity

gradients with an inviscid form of the Navier-Stokes equations.

The pitch-averaged vorticity ($\overline{\omega}_s C/V_{x_1}$) plots are shown in Figure 5.18 for

X/C=1.025 and 1.09. Outside of the secondary flow regions the pitch-averaged

vorticity is positive due to the over- and under-turning regions in the wake. A large

positive vorticity region occurs at H=0.1, which is a result of the vortex formed by

the interaction of the passage vortex and the wake. Moving closer to the hub, the

vorticity becomes negative due to the existence of the passage vortex. The

maximum negative vorticity occurs next to the hub and is a result of the interaction

of the flow with the rotating hub. The variation in vorticity is not as large near the

casing as it is near the hub, because the passage vortex and the counter-rotating

vortex are side by side (at the same radial location) near the casing instead of at

different radial locations as they are near the hub. The high positive vorticity at

H=0.85 is due to the passage vortex.

The experimentally derived pitch-averaged secondary vorticity is compared
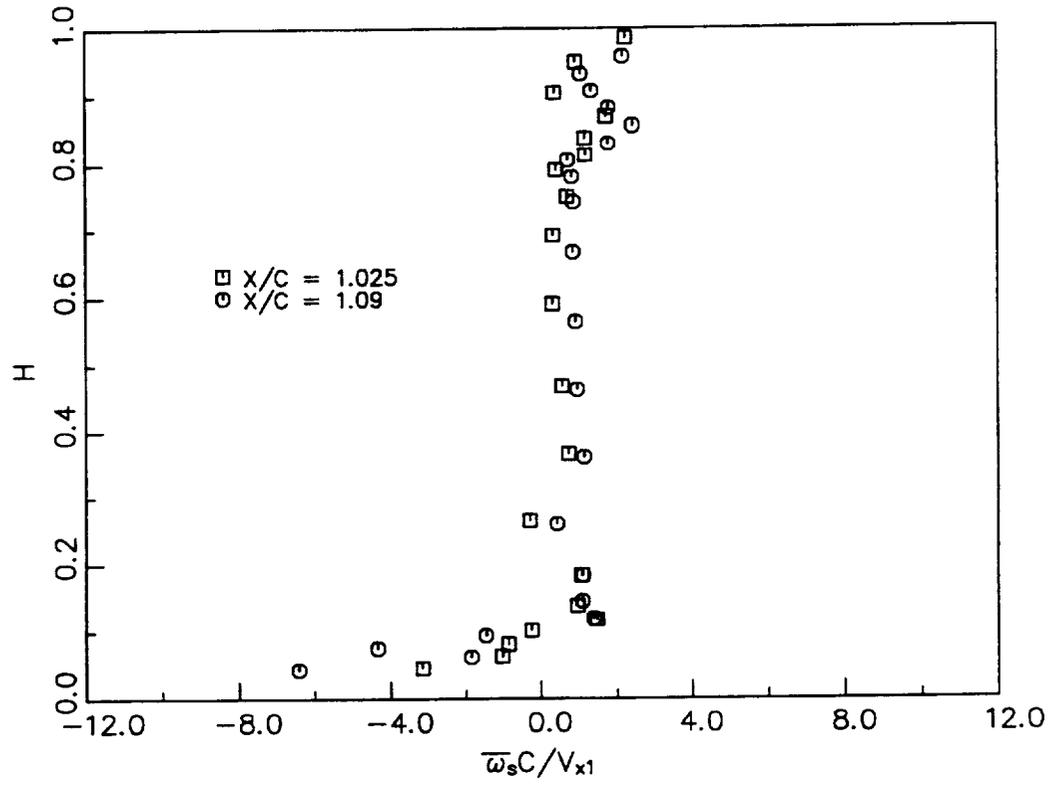
Figure 5.18. Pitchwise Averaged $\left(\overline{\omega}C/V_{x1}\right)$ Distribution at X/C = 1.025 and 1.09

to the theoretical secondary vorticity of Squire and Winter (1951) (derived using classical secondary flow theory) in Figure 5.19. The experimental pitch-averaged secondary vorticity $\overline{\omega}_{sec}$ is defined as

$$\overline{\omega}_{sec} = \overline{\omega}_s - \overline{\omega}_{s_m} \tag{5.1}$$

where $\overline{\omega}_s$ is the pitch-averaged streamwise vorticity at each radii and $\overline{\omega}_{s_m}$ is the pitch-averaged streamwise vorticity at midspan. The secondary vorticity of Squire and Winter ($\omega_{sec_{sw}}$) is calculated as follows:

$$\omega_{sec_{sw}} = 2\omega_{n_1}(\alpha_2 - \alpha_1) \tag{5.2}$$

where ω_{n_1} is the vorticity at the nozzle inlet, α_1 is the inlet flow angle and α_2 is the mass-averaged exit flow angle. The agreement between the theoretical vorticity and the experimentally derived vorticity is good at the hub, while at the casing Squire and Winter's formula over predicts the secondary vorticity. This is somewhat unexpected, since the experimental secondary vorticity $\overline{\omega}_{sec}$ at the casing only contains the vorticity due to the secondary flow, while at the hub $\overline{\omega}_{sec}$ contains both the vorticity due to secondary flow and due to the rotating hub. Therefore it must be just fortuitous that the prediction of the secondary vorticity matches the experimental secondary vorticity at the hub. Thus one can conclude that the theoretical secondary vorticity does not correctly predict the actual secondary flow vorticity in a turbine cascade. This is expected, since one of the assumptions in deriving Squire and Winter's secondary vorticity is that the turning angle ($\alpha_2 - \alpha_1$) is small and this is violated in turbine cascades. The experimentally derived secondary vorticity was also compared to the secondary vorticity derived by Came
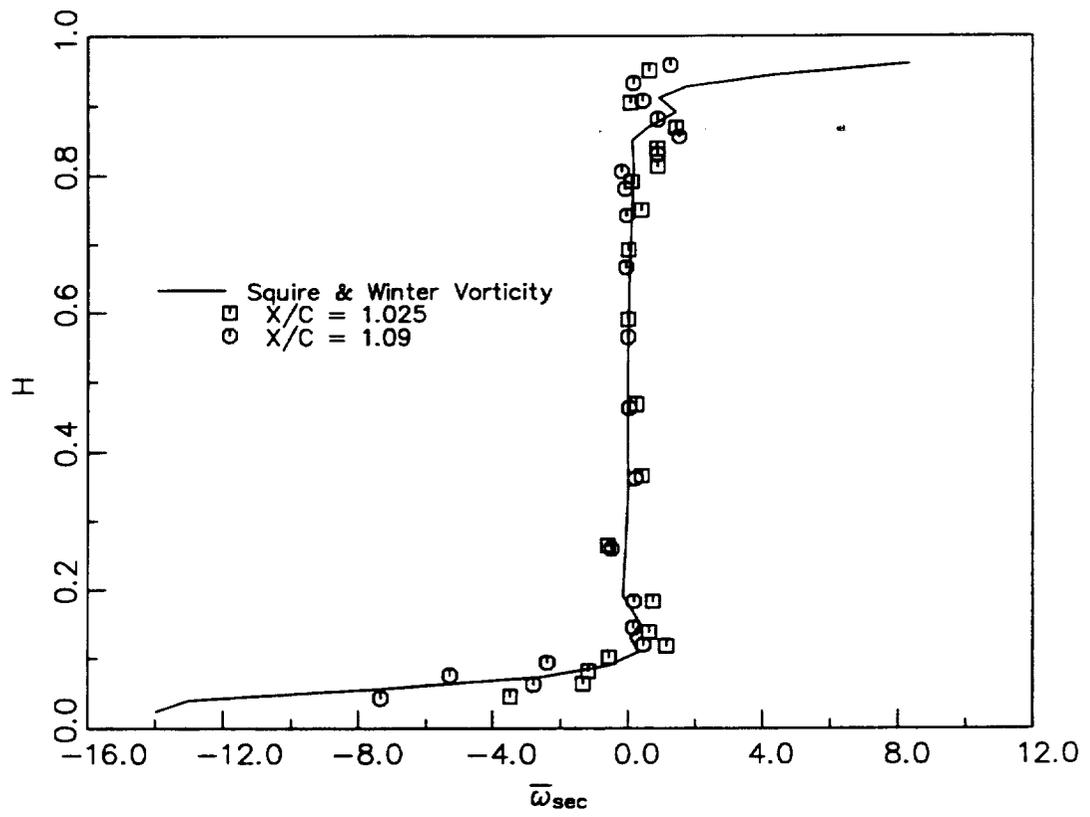
Figure 5.19. Nozzle Exit Secondary Flow Vorticity

and Marsh (1974), but this vorticity is similar to that of Squire and Winter's and thus it is not shown.

Comparison of the peaks in streamwise vorticity with the total pressure loss contours (Figures 5.1 and 5.2) shows that the peak total pressure loss does not occur at the peak vorticity location, but occurs somewhere between the positive and negative vorticity peaks. This is contrary to the results of linear cascades where the loss peaks coincide with the vorticity peaks (vortex centers), (see Gregory-Smith et al. (1988), and Hodson and Dominy (1987)). The interaction between the secondary flow vortices and the wake causes the accumulation of the low momentum and energy endwall boundary layer fluid into these two locations.

The six criteria that are used to determine the existence of a vortex in the flow field were described in Chapter 4. A vortex exists when these six flow phenomena occur at the same position in the flow field. The existence of the passage vortices at both the hub and the casing are confirmed since they meet all six criteria. On the other hand, the existence of the suction side leg of the horseshoe vortex is more doubtful. There is no evidence for its existence at the hub. While at the casing there is a region of high negative vorticity at $X/C=1.025$ that could correspond to the suction side leg of the horseshoe vortex, the other criteria are not met. Thus its existence cannot be proven conclusively, and has probably decayed by the time it has reached the nozzle trailing edge. This is in agreement with the findings of other researchers, both experimental (Gregory-Smith et al., 1988) and computational (Ho and Lakshminarayana, 1994), who found that the suction side leg of the horseshoe vortex had decayed by the time it had reached the trailing edge.

5.5 Nozzle Wake Characteristics

An understanding of turbine nozzle wakes are important for the efficient design of axial flow turbomachinery. A major cause of noise and vibration characteristics of turbomachinery is caused by wakes. Turbine wakes represent a source of loss in efficiency, since the mixing of the wakes with the freestream dissipates energy. The three-dimensional characteristics of the wake, the decay characteristics and the path that it follows is important in the design of the following blade rows. This information is essential for both the prediction of the aerodynamic and mechanical performance of a turbine and for building quieter turbomachines. An understanding of the wake development and its decay is also essential because of the role it plays in the rotor-stator interaction .

5.5.1 Nozzle Wake Static Pressure

The static pressure variation across the wake for different radii at X/C = 1.025 is shown plotted in Figure 5.20. Starting from the pressure side, the static pressure coefficient decreases sharply until the wake center, after which it increases rapidly across the suction side of the wake. A decrease in static pressure coefficient Ψ_s indicates an increase in static pressure as this is an accelerating flow. A hump at the suction side wake edge (A) has been caused by the over-turning on the suction side, while the dip in static pressure coefficient on the pressure side wake edge (B) is caused by the under-turning on the pressure side of the wake.

The strong radial pressure gradient is evident with the static pressure decreasing more than 35% as one goes from the tip to the hub. The static pressure variation across the wake is as high as 20-25% of the value in the freestream. This
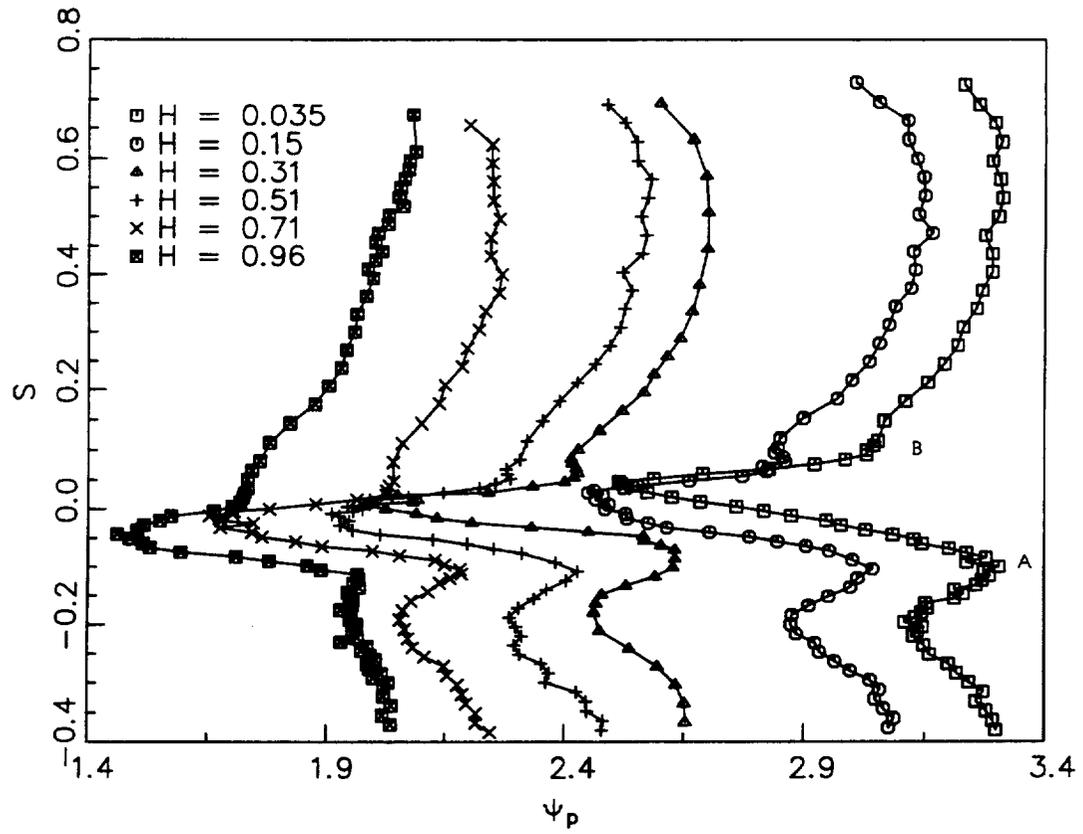
Figure 5.20. Static Pressure (Ψ_s) Variation at X/C = 1.025

is consistent with the measurements of Lakshminarayana and Davino (1980) who found similar static pressure gradients across the wake of a compressor inlet guide vane.

The existence of pressure gradients across the wake has been explained for a compressor rotor blade by Ravindranath and Lakshminarayana (1980), and can be comprehended by examining the equation of motion in a streamwise (s) and normal (n) coordinate system. The equation can be approximately written as

$$\frac{1}{\rho}\frac{\partial p}{\partial n} \approx \frac{V_s^2}{R_c} + \frac{\partial}{\partial n}\left(\overline{v_n'^2}\right) \tag{5.3}$$

where n is the direction normal to the streamline, V_s is the streamwise velocity, R_c is the radius of curvature of the streamline and (v_n') is the turbulent fluctuation in the n direction. It is clear from the above equation that in addition to the centrifugal force, the gradient of turbulent intensity in the n direction has a major influence on the pressure gradient $\partial p / \partial n$. The static pressure gradient is caused by the flow curvature, velocity change, turbulence intensity and possibly separated flow in the trailing edge region.

5.5.2 Total Velocity

Figures 5.21 and 5.22 show the total velocity profiles for X/C=1.025. The plot indicates that the suction surface boundary layer is thicker than the pressure surface boundary layer. Several interesting observations can be made. The wake at H=0.98 is well behaved. The influence of interaction between the wake and the secondary flow can be seen in the wake data at H=0.870 to H=0.810. The two distinct troughs from H=0.870 and 0.840 indicate that the wake and secondary
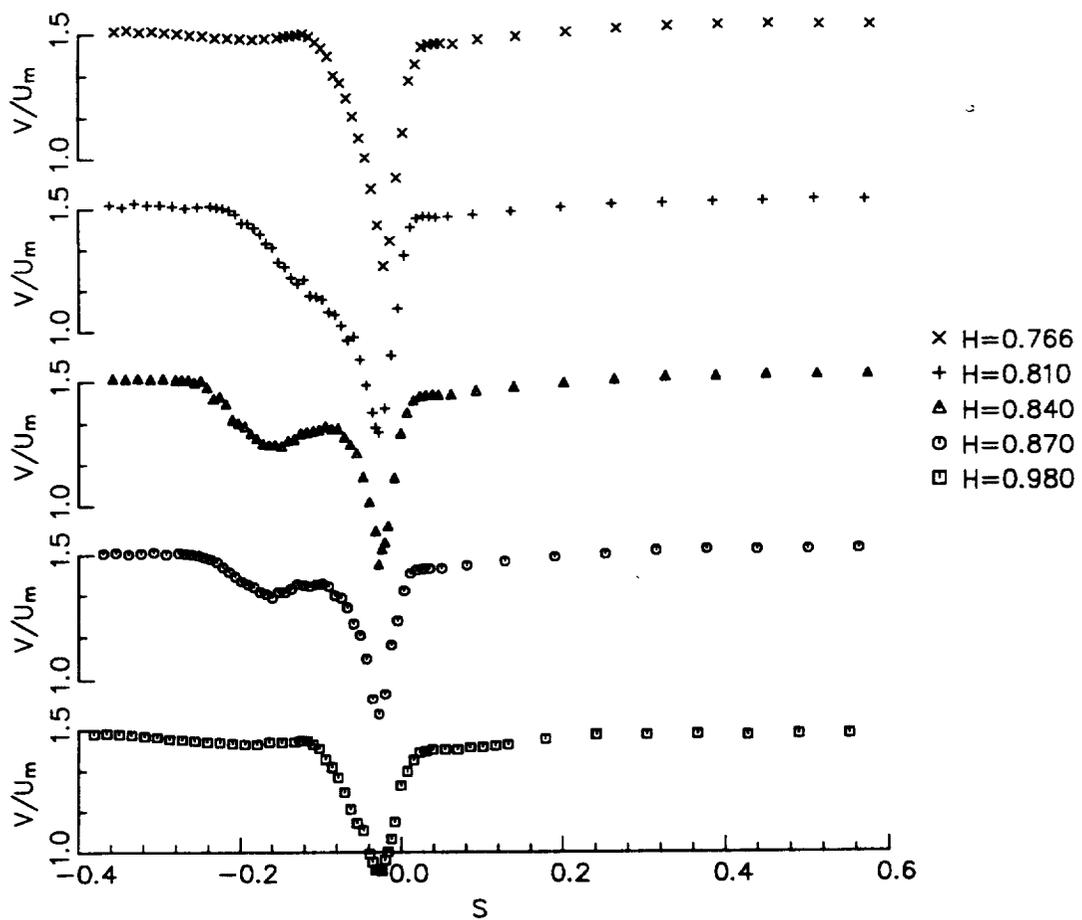
Figure 5.21. Total Velocity (V/U_m) Profiles at X/C = 1.025
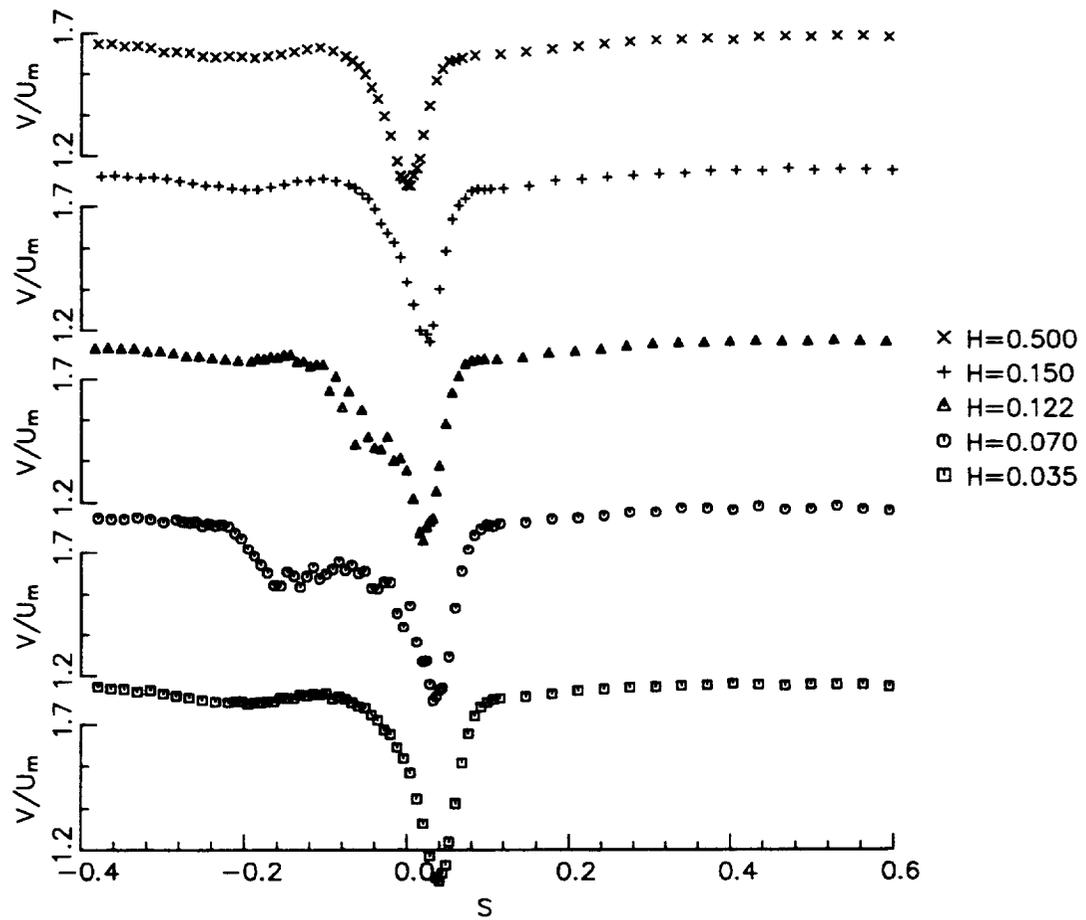
Figure 5.22. Total Velocity (V/U_m) Profiles at X/C = 1.025

flows are still distinct and they are likely to merge as the flow progresses downstream. The region near H=0.810 is the location of the strongest secondary flow/vorticity and here, there is clear evidence of interaction between the wake and vortex resulting in a thick shear layer on the suction side. The region from H=0.766 to 0.150 has a well behaved wake and the secondary flow/vortex interaction with the wake is again evident below this region. In general, the wake defect is higher in the secondary flow regions.

5.5.3 Nozzle Wake Decay Characteristics

A knowledge of the rate of decay for the wake defect is necessary for an understanding of the rotor-stator interaction. The decay of the velocity defect is influenced by many phenomena, including the pressure gradient, turbulence intensity, curvature and viscous effects. The endwall secondary flow and passage vortices also have an effect on the wake decay. The velocity defect plotted in Figure 5.23, is based on the maximum and minimum velocity in the wake, plotted against $Z/\cos\alpha_o$, where α_o is the local value of the vane outlet angle. This corresponds approximately to the streamwise distance downstream of the nozzle.

The authors' data at midspan is compared with data from other sources. Goldman and Seasholtz (1982), (1992) did their measurements in an annular cascade, while Dring et al. (1987) measured the wake behind the nozzle with a rotor-stator spacing of 50% of nozzle axial chord. Sitaram and Govardhan (1986) did their measurements in a linear turbine rotor cascade. Ho and Lakshminarayana (1994) computed the flow field in a linear turbine rotor cascade. Raj and Lakshminarayana (1973) measured the wake behind a linear cascade of compressor blades and developed a correlation. They found that the wake from a compressor
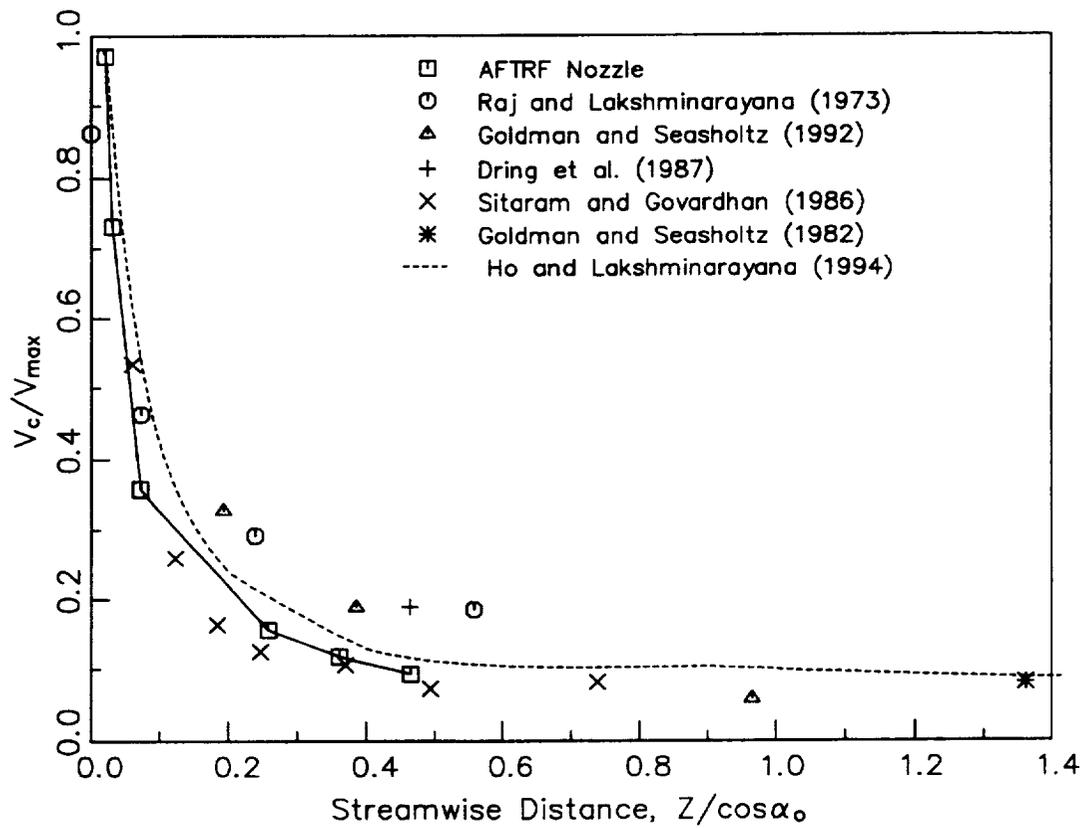
Figure 5.23. Decay of Total Velocity Defect with Streamwise Distance (Midspan)

cascade decays slower than that of a flat plate, cylinder or a symmetrical airfoil. They attributed this to the fact that the wake edge velocity decelerates in a compressor cascade, thus causing an adverse pressure gradient, which causes the wake to decay slower.

The nozzle wake decays rapidly close to the trailing edge and less rapidly farther downstream. This can be seen more clearly in Figure 5.24, which shows the nozzle wake at midspan for several axial locations downstream of the nozzle. Lakshminarayana and Davino (1980) state that the rapid decay rate close to the trailing edge is due to pressure gradients, high turbulence intensities and wake centerline curvature. The wake data from Dring's cascade and Goldman's cascade decay slightly faster than Raj's cascade. This is because the wake edge velocity decay is almost zero for the turbine nozzle and rotor cascades (Figure 5.25), hence, the streamwise pressure gradient in the edge of the wake is zero. And according to Hill et al. (1963), wakes in an adverse pressure gradient will decay slower than wakes in the presence of zero pressure gradient. In addition, the wake in the presence of favorable pressure gradient is found to decay faster. Also, the increased loading on the nozzle vanes compared to Raj and Lakshminarayana's compressor cascade could cause an increase in the wake decay rate.

The data from the AFTRF nozzle, on the other hand, have a much more rapid decay rate than the compressor cascade wake or Goldman and Seasholtz's turbine nozzle cascade. This is due to the presence of the rotor downstream at a very small rotor-stator axial spacing (rotor-stator spacing is 20% of the nozzle axial chord). The relative motion between the rotor and the stator causes periodic variations in the potential flow field around the blades. This unsteadiness causes the wake to decay faster than the wake of a cascade with no rotor behind it. The nozzle wake is also affected by the favorable pressure gradient in the rotor, which
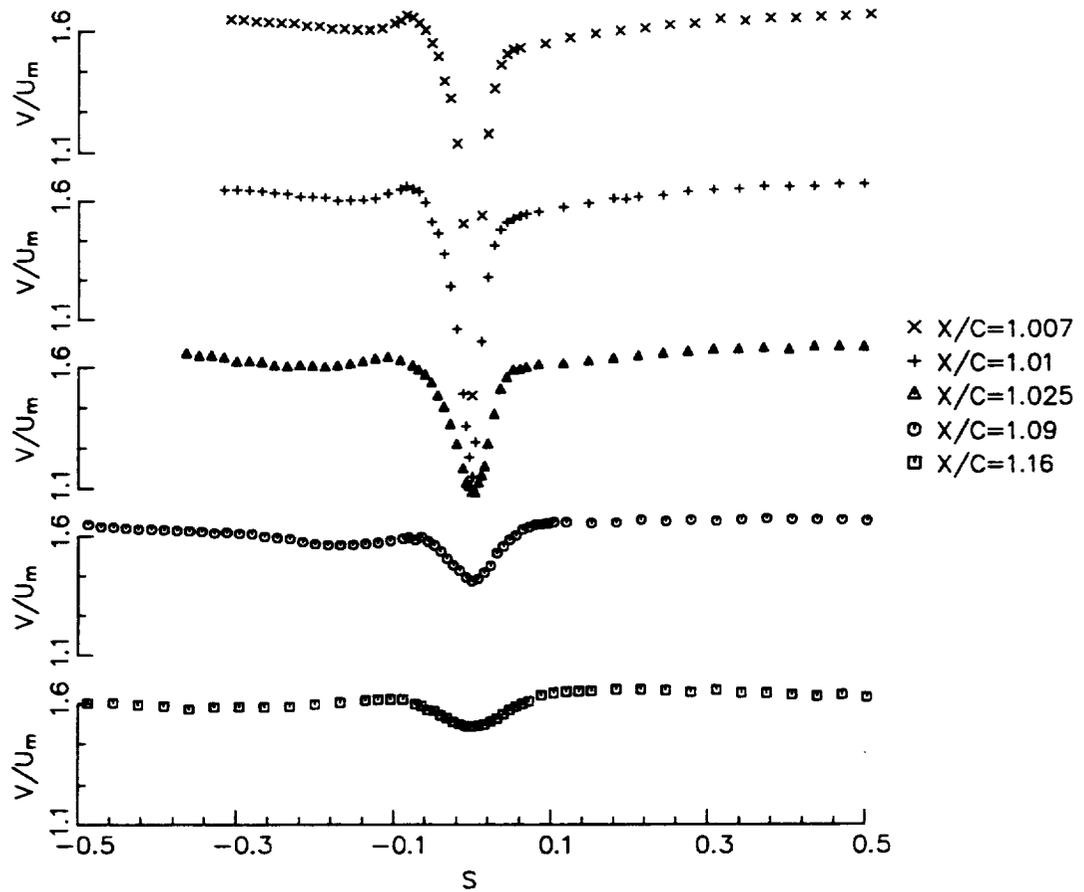
Figure 5.24. Total Velocity Profiles at Midspan
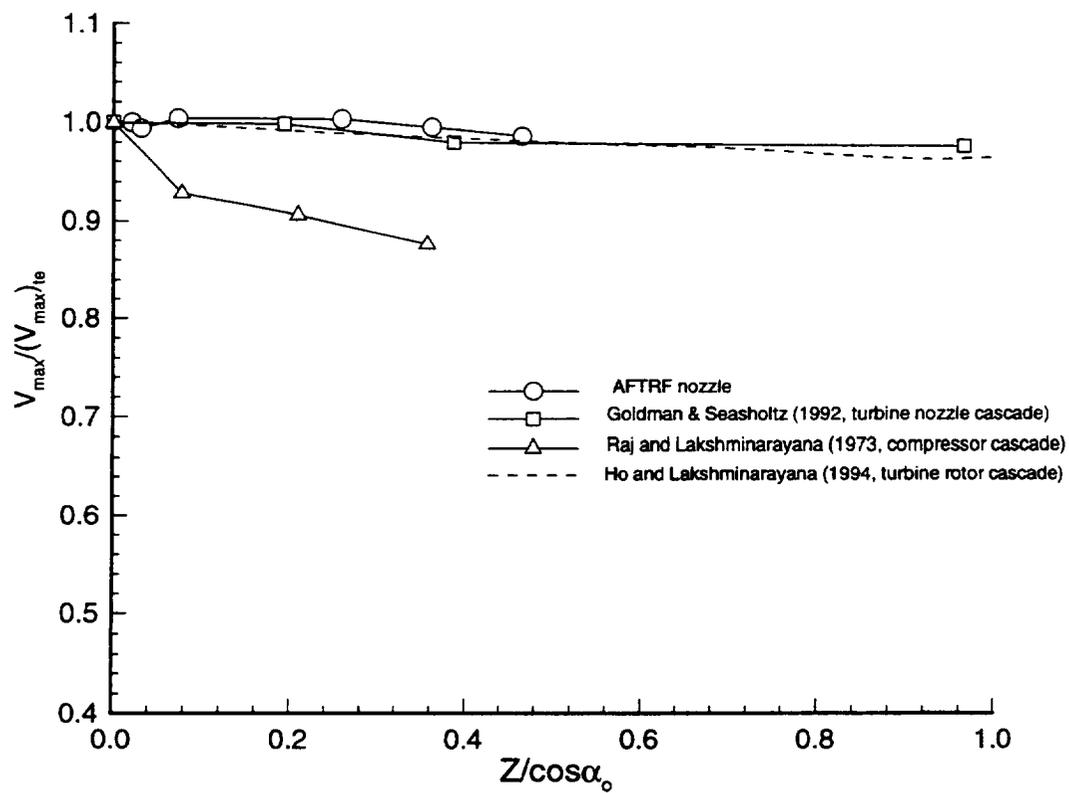
Figure 5.25. Variation of Wake Edge Velocity with Downstream Distance

causes it to decay faster. Even though the nozzle of Dring et al. (1987) has a rotor downstream, the rotor-stator spacing is much larger (50% nozzle axial chord) than that of the AFTRF nozzle. Thus the potential flow interaction will have less effect on the nozzle wake in Dring's et al. (1987) case. Ho and Lakshminarayana's turbine rotor cascade (computed) also decays faster than the compressor wake or Dring's or Goldman's nozzles. This is due to the fact that the loading on the rotor was much higher than on the nozzles, since the rotor turning is 110 degrees while the turning is around 70 degrees for all the nozzle data shown in Figure 5.23. Sitaram and Govardhan's turbine rotor wake decays a little faster than Ho and Lakshminarayana's rotor cascade since their loading is higher (rotor turning is 120 degrees for Sitaram and Govardhan's cascade).

The decay of maximum (absolute) radial velocity (Figure 5.26) normalized by the maximum velocity in the wake is constant from the trailing edge until $Z/\cos\alpha_o = 0.30$, and then decreases slightly. The magnitude is similar to the radial velocity decay of a compressor stator reported by Lakshminarayana and Davino (1980). Figure 5.27 shows the radial variation of total velocity defect at the centerline at $X/C = 1.025$ and $X/C = 1.09$. Caution should be used in interpreting this data. Since the wake belongs to different blade sections with varying in boundary layer growth, the variation of defect in the radial direction should not be interpreted as the decay rate. The variation of wake defect with spanwise distance is clearly seen from this plot. There are two regions where the wake defect is larger than the others, one centered around H=0.1 and the other centered around H=0.8. This is the region where the secondary flow vortices are located, and the interaction of these with the wake results in deeper and wider wakes. Thus the wake defect will be larger at these locations. The wake decay between X/C=1.025 to 1.09 is almost constant from the hub to H=0.6 and then increases until the
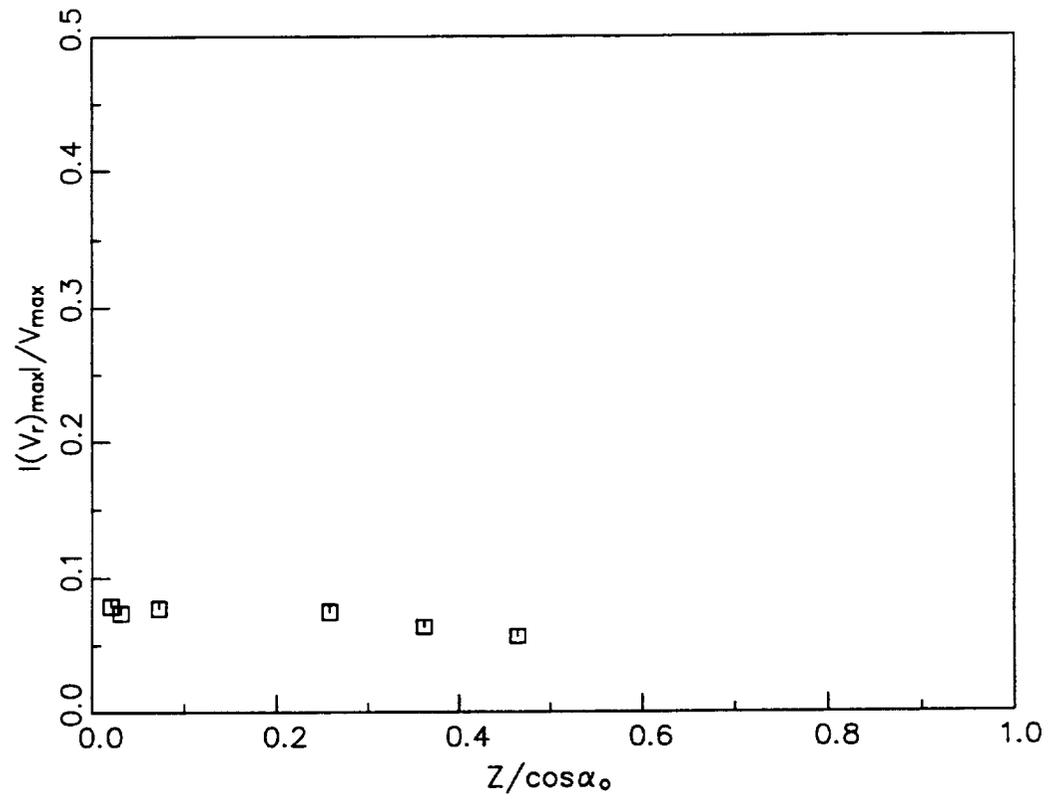
Figure 5.26. Decay of Radial Velocity
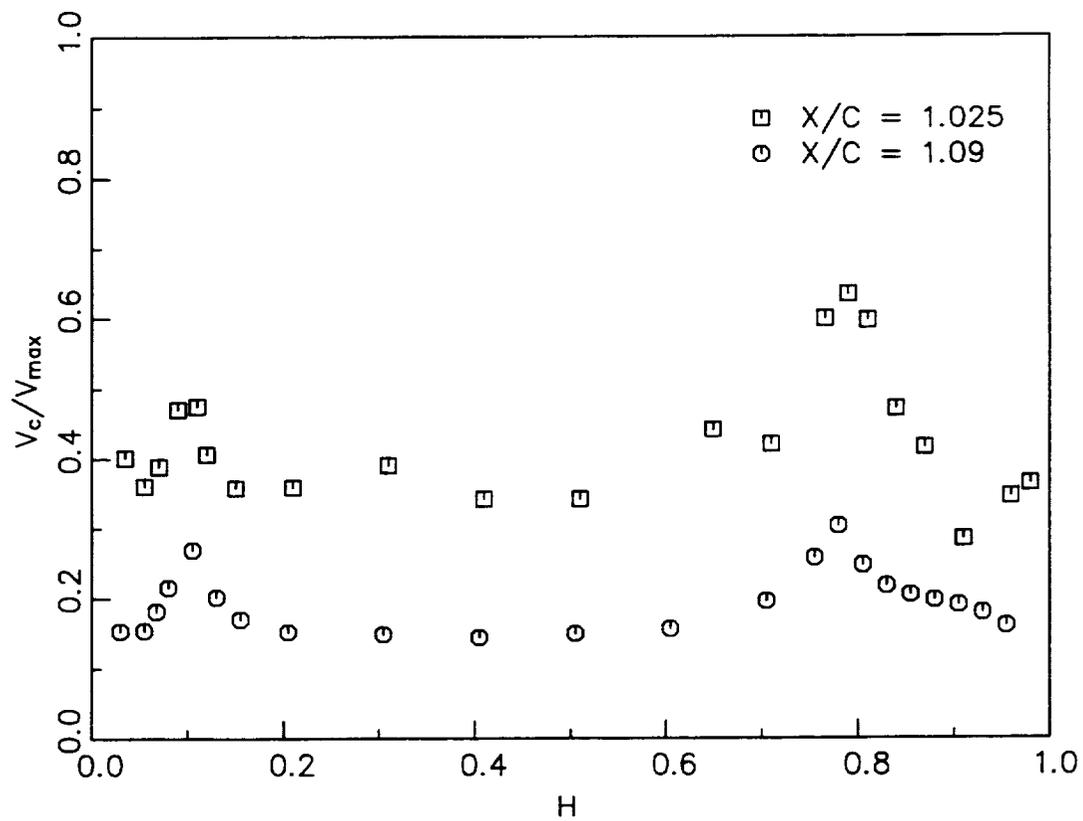
Figure 5.27. Radial Variation of Total Velocity Defect

maximum decay rate is reached at H=0.8. This is due to effect of the two counter-rotating vortices at this location.

The variation of the semi-wake width at midspan with streamwise distance is shown in Figure 5.28. The semi-wake width is defined as the width of the wake at half the defect of total velocity. The semi-wake width grows rapidly close to the trailing edge and more gradually farther downstream. This growth is due to the exchange of momentum, mass and energy on both sides of the wake. The variation of the maximum static pressure difference (Ψ_d) across the wake at midspan is shown vs. streamwise distance in Figure 5.28. The value of Ψ_d decays to 50 percent its value within a streamwise distance of 10 percent chord. This rapid decay is caused by the intense mixing and high turbulence intensities that occur close to the trailing edge (see Ravindranath and Lakshminarayana (1980)). The decay rate levels off as the wake moves downstream of the trailing edge reaching a value of 28 percent of its value at the trailing edge within a streamwise distance of 40 percent of chord. Most researchers assume that the static pressure is uniform at the trailing edge, both inside the wake and in the free stream. This assumption is not valid in view of the data shown in Figures 5.28 and 5.20.

5.6 Mass-Averaged Properties

The circumferentially mass-averaged total pressure loss profiles at various locations from upstream of the nozzle to downstream of the nozzle are shown in Figure 5.29 (The properties upstream of the nozzle inlet for all the following figures are a single radial traverse). The stagnation pressure profile at the nozzle inlet shows the boundary layer thickness to be approximately 10% at the hub and 15% at the tip. At X/C=0.935, 1.025 and 1.09, the upstream boundary layer profile
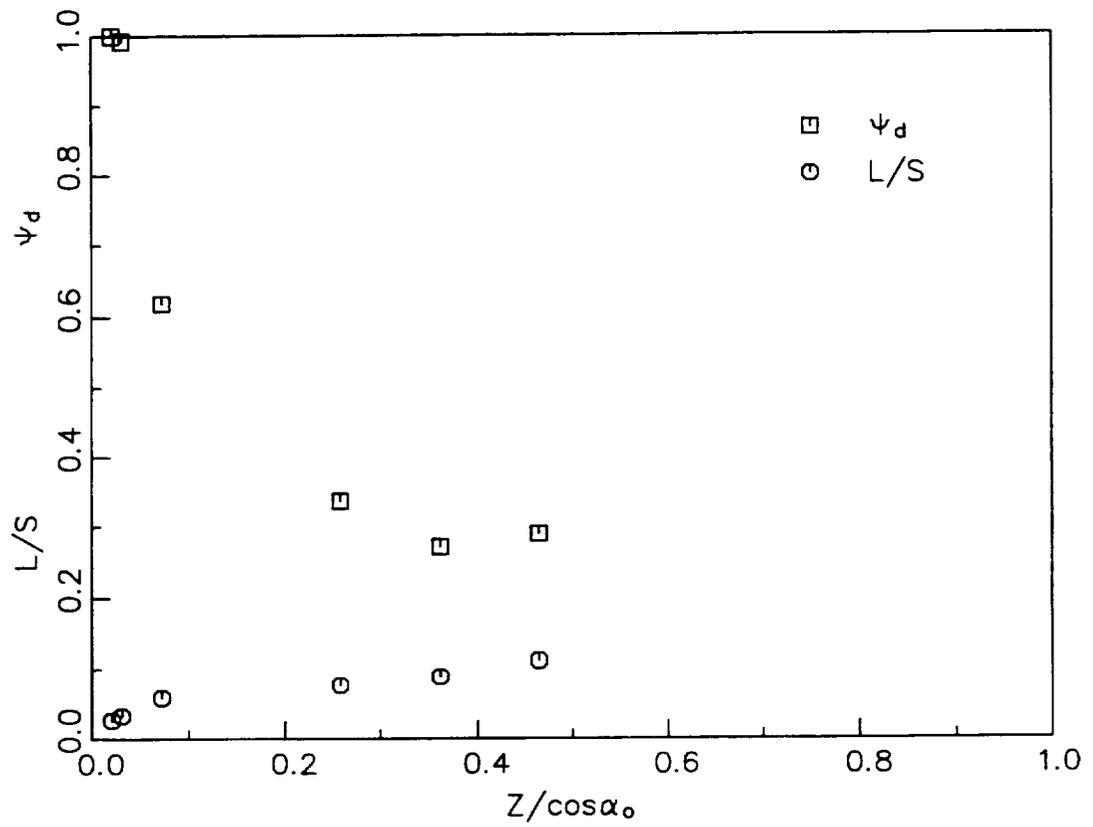
Figure 5.28. Variation of Static Pressure and Semi-Wake Width with Streamwise Distance
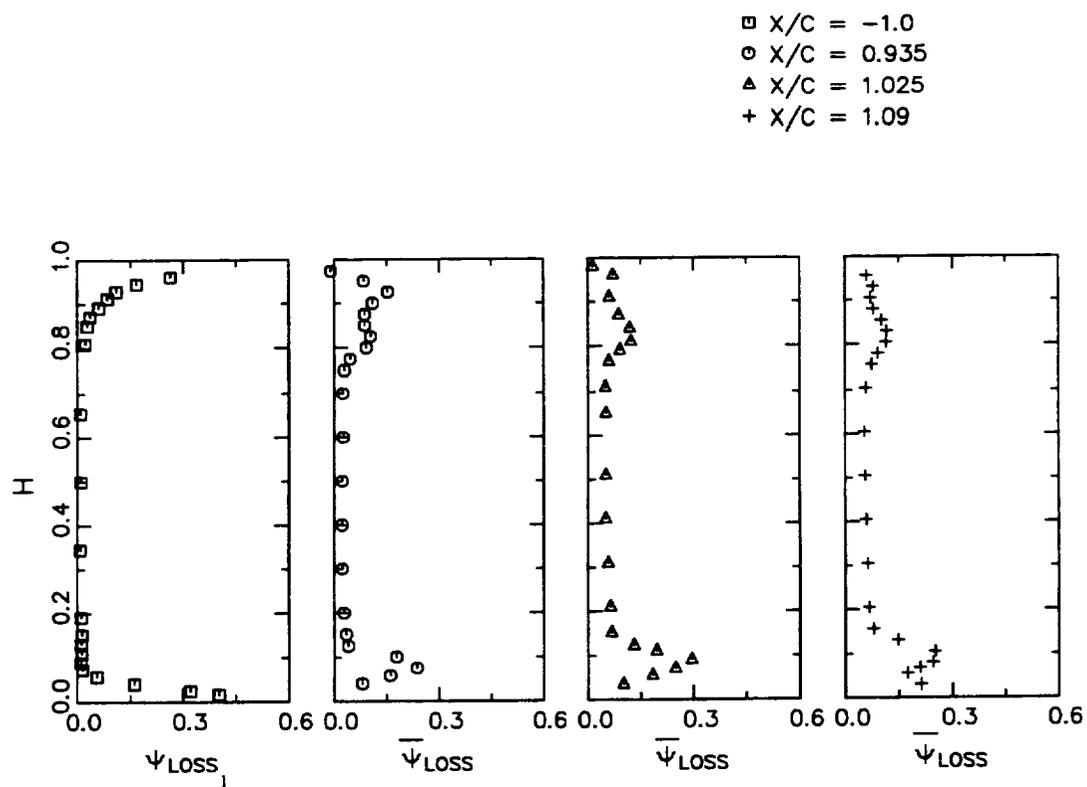
Figure 5.29. Mass-Averaged Total Pressure Loss $\left(\overline{\Psi}_{LOSS}\right)$

losses have been subtracted, hence, those represent the losses occurring within the nozzle passage. At all three axial locations, there are two loss peaks. The peak near the hub is larger in magnitude but smaller in radial extent than the one near the casing. The larger inlet casing boundary layer results in the larger extent of the secondary flow region near the casing. The larger magnitude of the hub loss region is a result of the radial inward flow of the boundary layer and wake which cause the low momentum fluid in the boundary layer and wake to move toward the hub.

The mass-averaged static pressure coefficient is shown in Figure 5.30. The radial static pressure gradient at the locations X/C = 0.935 to X/C = 1.09 is nearly constant from hub to tip and is consistent with the velocity distributions shown later.

The mass-averaged total velocity is shown in Figures 5.31. The boundary layer profile is clearly visible upstream of the nozzle inlet. At X/C = 0.935 to X/C = 1.09, the total velocity profiles show a sharp decrease in velocity near H = 0.10 and a more gradual decrease in velocity near H = 0.80, which is due to the hub and tip wall secondary flow. The total velocity predicted by Katsanis' code is compared with the total velocity measured at X/C = 0.935 and X/C = 1.025. The agreement is excellent.

The mass-averaged yaw angle is given in Figure 5.32. The yaw is derived from the mass averaged tangential velocity and the mass averaged axial velocity. At the nozzle inlet (X/C = -1.0), the yaw angle is about zero everywhere. The yaw angles at X/C = 0.56 show the presence of weak secondary flow. From X/C = 0.935 to X/C = 1.09, the yaw angle shows overturning at the casing and hub endwalls. As one moves away from the endwalls, the flow becomes underturned, achieving design flow near 30% span. This is consistent with the predictions from secondary flow theories and measurements by others. The largest overturning is
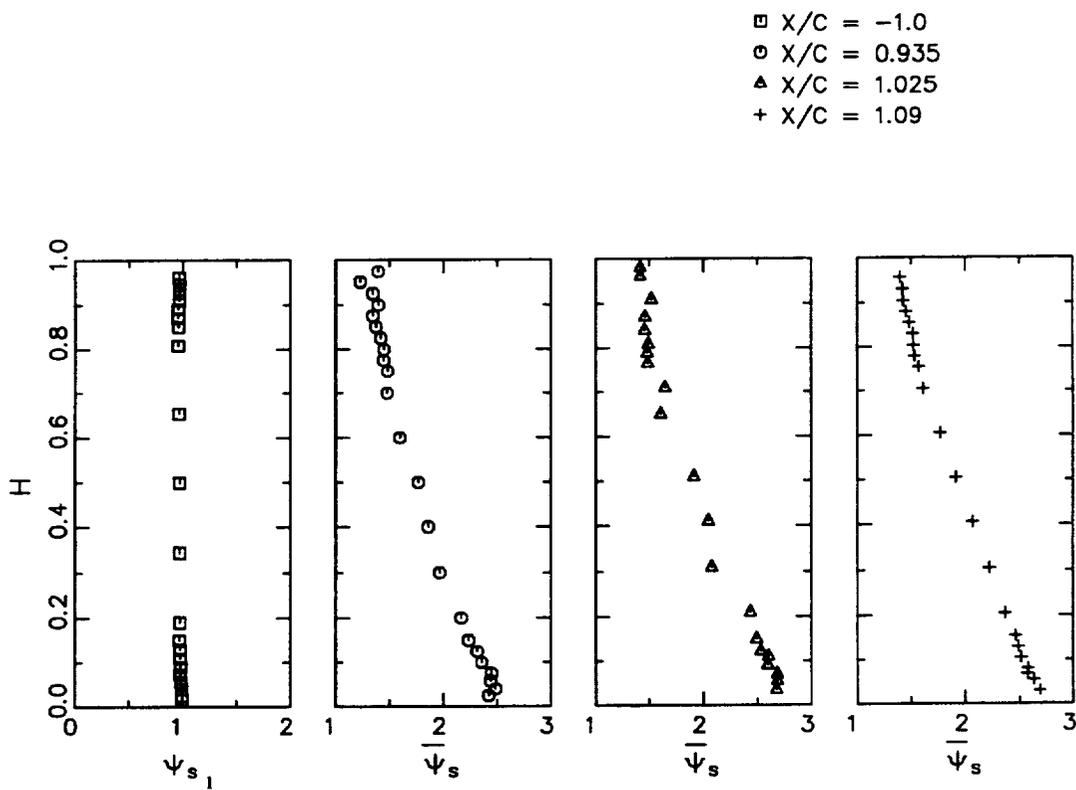
Figure 5.30 Mass-Averaged Static Pressure Coefficient ($\overline{\Psi_s}$)
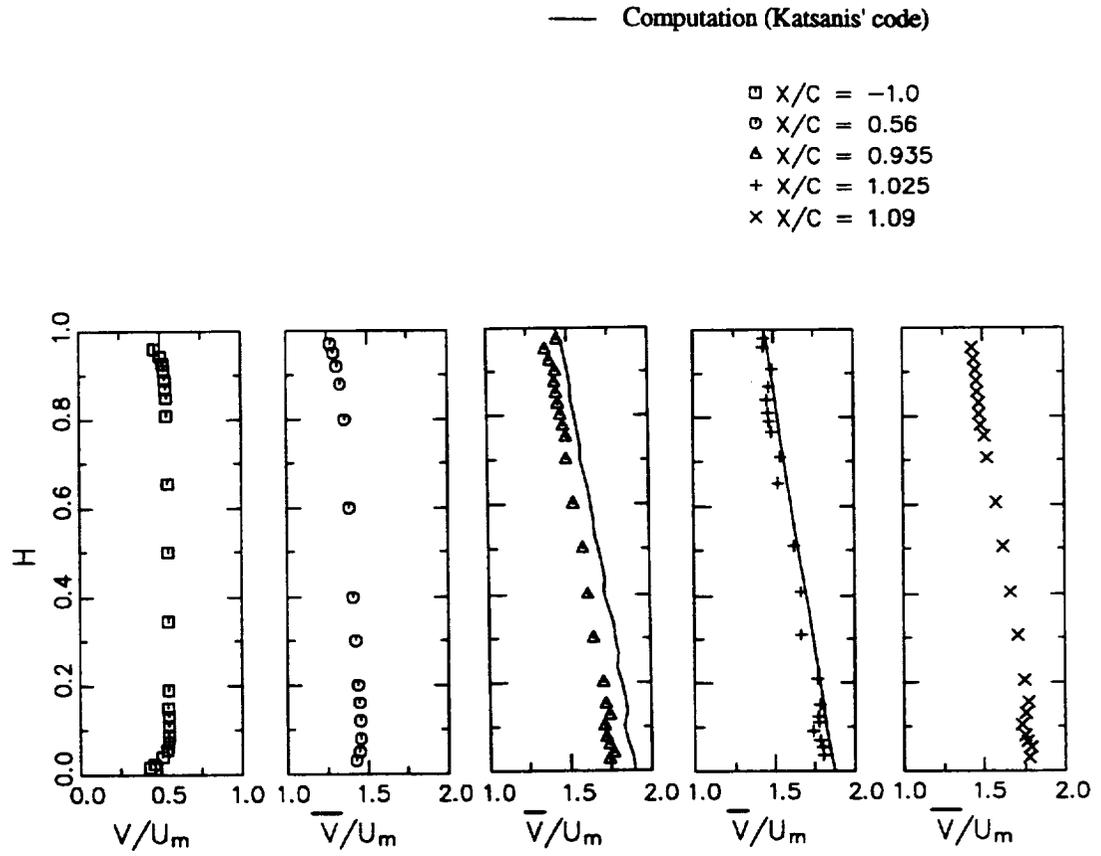
Figure 5.31. Predicted and Measured Mass-Averaged Total Velocity $(\overline{V}/U_m)$

——— Computation (Katsanis' code)

□ X/C = -1.0
○ X/C = 0.56
△ X/C = 0.935
+ X/C = 1.025
× X/C = 1.09
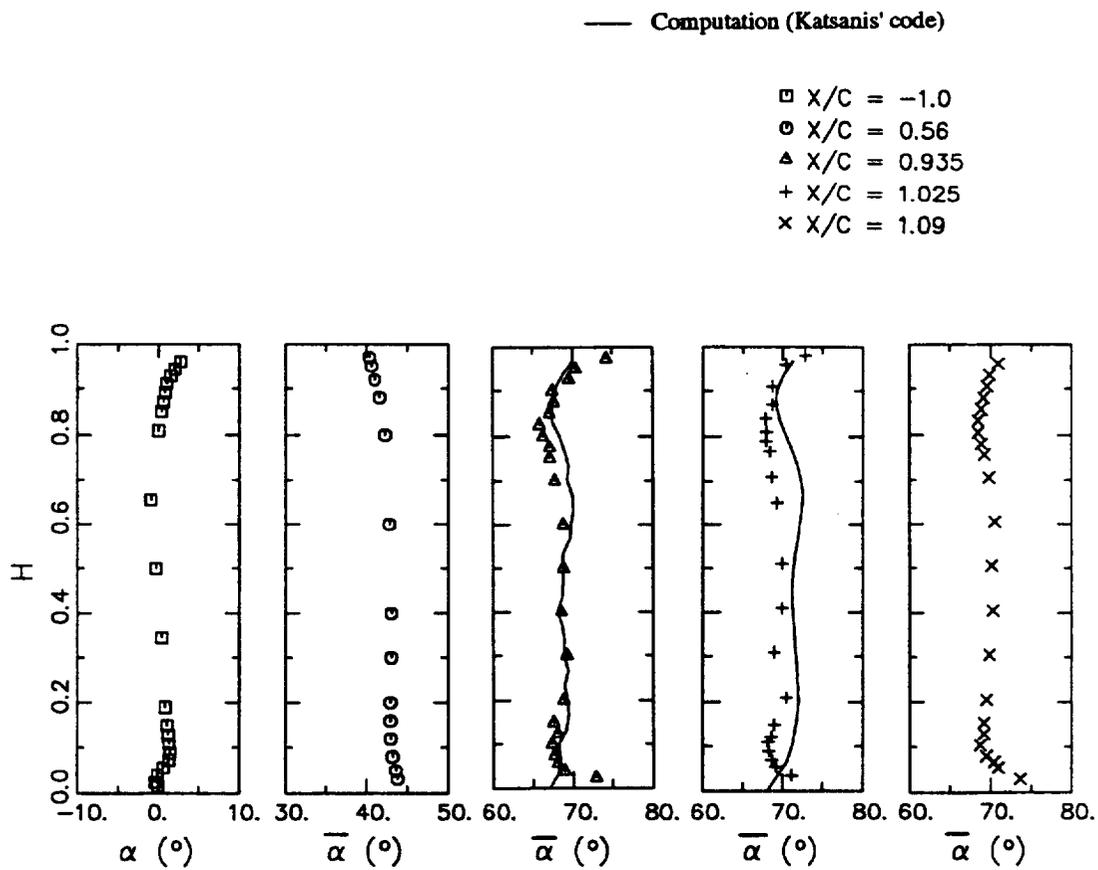
Figure 5.32. Predicted and Measured Mass-Averaged Yaw Angles ($\overline{\alpha}$)

about five degrees, and this is much smaller than those reported by others for rotor cascades. The yaw angle at X/C = 0.935 and 1.025 is compared to Katsanis' inviscid code predictions. The agreement is very good everywhere except very close to the hub. The prediction even captures the overturning at the casing. This demonstrates the usefulness of using an inviscid code in turbomachinery design.

Figure 5.33 shows the area-averaged stagnation pressure loss for the PSU AFTRF and two other turbine cascades. In order to compare the losses between the three turbine blades, the stagnation pressure loss for all three are normalized by the inlet dynamic head. The AFTRF nozzle follows the same trend as the other turbine blades, increasing as one moves downstream. The large increase in losses going from X/C = 0.935 to X/C = 1.025 is partly due to separation that occurs at the vane's trailing edge and partly to the fact that the vane surface boundary layer could not be completely measured close to the wall (thus giving a lower area averaged loss), while downstream of the nozzle the losses in the entire wake could be measured. The loss growth downstream of the nozzle trailing edge is caused by the mixing of the flow downstream of the vane and by turbulence mixing.
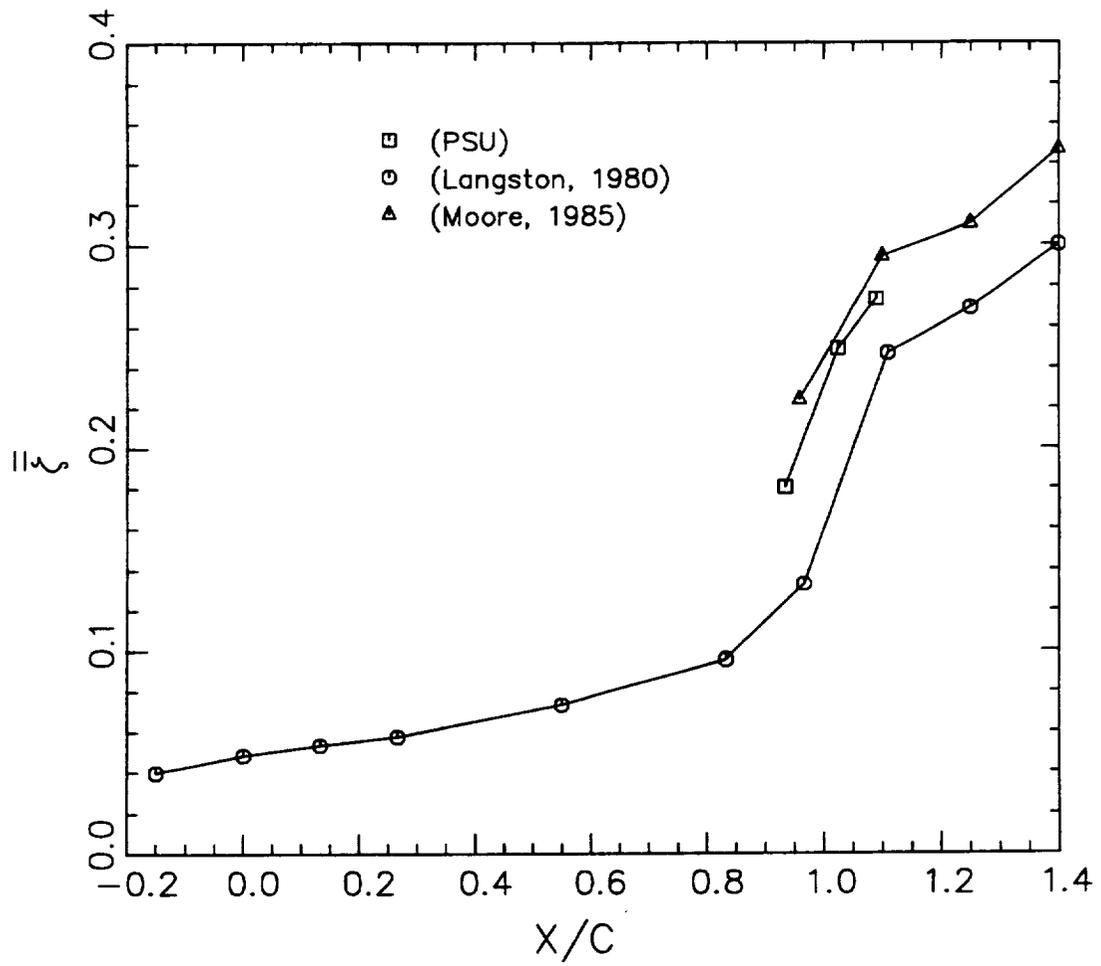
Figure 5.33. Area-Averaged Total Pressure Loss ($\overline{\overline{\zeta}}$)

CHAPTER 6

STEADY AND UNSTEADY FLOW FIELD AT ROTOR MIDSPAN

The flow around turbine blades is highly unsteady. This unsteadiness is caused by the aerodynamic interaction of the nozzle and rotor flow fields and is called rotor-stator interaction. Rotor-stator interaction can affect the aerodynamic, structural, thermal and acoustic performance of a turbine and is important for the efficient design of axial flow turbines. According to Dring et al. (1982), rotor-stator interaction can be divided into two parts. These are potential flow and wake interactions. The potential flow gradients extend both upstream and downstream of the blade and they decay exponentially with a length scale of the order of the pitch or chord of the blade row. If the axial gap between the blade rows is less than a chord (which it is in a typical axial flow turbine), then the potential influence can cause unsteadiness in both upstream and downstream of the blades.

However, the wake is convected downstream and has a far field rate of decay much lower than that of the potential flow. The wake will still be felt several chords downstream. But in most modern axial flow turbines, which have a rotor-stator spacing close to 20 percent of a blade chord, both the potential and wake effects will occur together. And in the future as gas turbine designers try to reduce weight, and thus the rotor-stator spacing gets smaller, these effects will become more prominent.

Even though unsteady flow plays a major role in axial flow turbines, turbines are designed using three-dimensional steady flow calculation methods (Sharma et al., 1992). Empirical correlations are used to account for the effect of the unsteadiness. Because actual models of the loss generating mechanisms in unsteady flow turbomachinery do not exist, these correlations are based on results from stationary cascade data and do not represent the actual fluid mechanics in the

flow field (Sharma et al., 1985). Thus these correlations must be multiplied by some factor to obtain a good estimate of the actual losses that occur in turbines. Although these correlations have worked well in the design of existing turbines, they do not represent the true physics of the flow field and are only useful in the areas from which they were obtained, namely design point predictions and turbines which are similar to existing designs (Hathaway, 1986). Thus, a more thorough knowledge of unsteady flow interactions is needed in order to increase both the design and off-design performance of existing turbines, and to design turbines which are considerably different than existing turbines. To obtain this knowledge, good time accurate data from inside the rotor is needed. This knowledge, in turn, can be used to model the unsteady flow mechanisms that are not currently in existing design codes. Thus, a better understanding of unsteady flow interactions can lead to an improvement in the ability to predict the performance of turbines and to corresponding improvements in the actual performance of turbines.

6.1 Measurement Procedure

Figure 6.1 shows the LDV measurement locations in the rotor. Measurements have been acquired at 37 axial measurement locations from just upstream of the rotor ($X_r/C_r = -0.088$) to one chord downstream of the rotor. Table 6.1 lists these locations. Each measurement location is at midspan. Since a two-dimensional LDV was used for measurements in the rotor, only the velocities in the axial and tangential directions are measured. To account for the nonuniformity of the rotor absolute inlet flow field, measurements were made at six tangential locations in the absolute frame equally spaced over one nozzle pitch. These six tangential locations represent six different relative positions between the nozzle
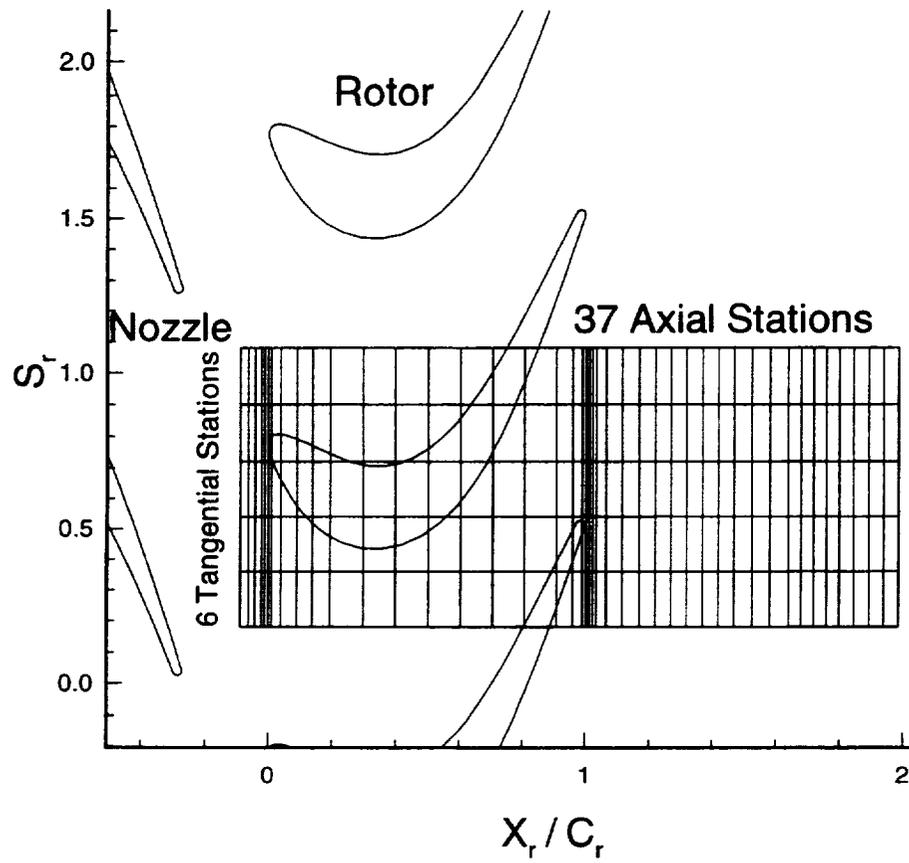
Figure 6.1. Rotor LDV Measurement Locations

Table 6.1

Axial Measurement Locations in the Rotor

X_r/C_r	X_r/C_r
-0.088	0.992
-0.063	1.004
-0.042	1.014
-0.021	1.024
-0.011	1.035
0.000	1.066
0.010	1.116
0.040	1.170
0.091	1.220
0.142	1.270
0.194	1.320
0.297	1.370
0.398	1.420
0.502	1.470
0.604	1.527
0.706	1.640
0.808	1.800
0.911	1.987
0.962	

and the rotor (labeled nozzle/rotor locations 1 through 6) or if viewed from the nozzle frame of reference, six different time resolved positions of the rotor in relation to the nozzle.

As discussed in the LDV data analysis section (section 2.6), each rotor passage is divided into 50 measurement windows, which means that there are measurements at 50 circumferential locations across the rotor pitch. The velocity is then ensemble averaged at each measurement window according to the following equation

$$\overline{V} = \frac{1}{n} \sum_{i=1}^{n} V_i \qquad (6.1)$$

where $\overline{V}$ is the ensemble averaged velocity, V_i is the instantaneous velocity measured at a particular rotor measurement window and n is the total number of measurements in that measurement window. The unresolved velocity for each measurement window can also be calculated as

$$V' = V_i - \overline{V} \qquad (6.2)$$

and the corresponding variance as

$$\overline{V'^2} = \frac{\left[\sum_{i=1}^{n} \left(V_i - \overline{V} \right)^2 \right]}{(n-1)} \qquad (6.3)$$

The level of unresolved unsteadiness in each measurement window is determined by the variance.

Since the flow field between the rotor passages was demonstrated to be periodic (see section 2.6 in this thesis), all the ensemble average velocity

components were spatially phase-locked averaged as follows

$$\breve{G}_j = \frac{\sum\limits_{m=1}^{N_{RB}} G_{j,m}}{N_{RB}}$$ (6.4)

where G represents either the ensemble averaged velocity or variance, the subscript m determines the particular rotor passage and j is the measurement window location relative to the m'th rotor passage and N_{RB} is the number of rotor blades. The successive application of equation (6.4) results in a description of the flow field at 50 equally spaced shaft positions across a representative rotor passage (Figure 2.10). Since all results presented from now on are spatially phase-locked averaged, the superscript $\cup$ will be dropped hereafter.

For the LDV measurements in the rotor, the instantaneous velocity, V_i, is decomposed as follows

$$V_i = \overline{\overline{V}} + \tilde{V} + V'$$ (6.5)

where $\overline{\overline{V}}$ is the time averaged velocity, $\tilde{V}$ is the periodic velocity and V' is the unresolved velocity component as calculated in equation (6.2). The decomposition for the phase-locked averaged rotor blade passage is shown in Figure 2.10. The time averaged velocity $\overline{\overline{V}}$ is obtained by averaging all the ensemble averaged velocities in each measurement window as follows,

$$\overline{\overline{V}} = \frac{1}{NW} \sum\limits_{j=1}^{NW} \overline{V}$$ (6.6)

where NW is the total number of measurement windows. The time averaged

velocity is a time average of all measurements acquired at a fixed point in space. The periodic velocity is then obtained from the equation,

$$\tilde{V} = \overline{V} - \overline{\overline{V}} \qquad (6.7)$$

From the above velocity decomposition, the axial, tangential and cross velocity correlations (both periodic and unresolved) can be computed, also.

Figure 6.2 shows the rotor inlet velocity triangles. The velocity defect in the nozzle wake produces a slip velocity in the relative frame towards the rotor suction surface. A more detailed discussion of this phenomenon is provided later in this chapter.

6.2 Cycle Average Properties

The cycle averaged values are obtained by averaging the ensemble averaged properties in each rotor measurement window for one nozzle/rotor location over the six nozzle/rotor locations as follows:

$$\overset{...}{G}_j = \frac{1}{N_{NRP}} \sum_{k=1}^{N_{NRP}} \overline{G}_{j,k} \qquad (6.8)$$

where G represents any flow parameter (such as velocity or unresolved unsteadiness), the superscript ... stands for cycle averaged property, N_{NRP} is the number of nozzle/rotor positions (6), the subscript j represents the individual measurement window location in the rotor passage, and the subscript k = 1 to 6 denotes a particular nozzle/rotor position. All the rotor flow field contour plots presented in this thesis are for one ensemble averaged rotor blade pitch which is
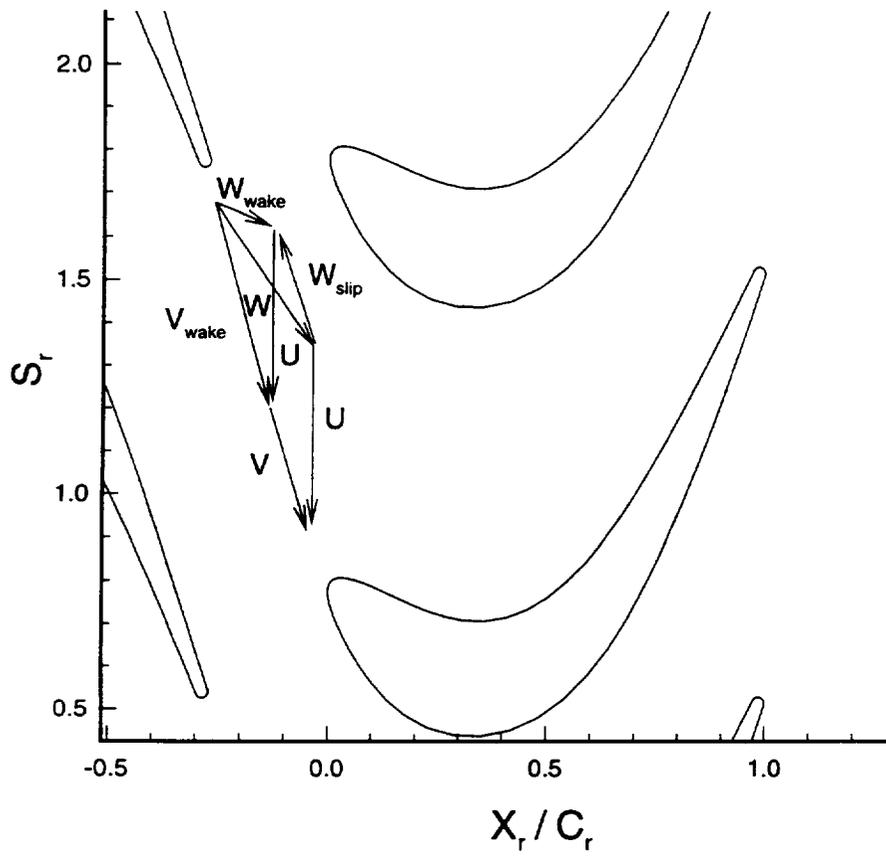
Figure 6.2. Rotor Inlet Velocity Triangles

doubled so that two rotor pitches are shown in the contour plots. Since the LDV was oriented at 7.6 degrees to the circumferential direction (in order to reduce reflections from the laser beam on the casing window from saturating the photomultipliers), there is a shadow region on the blade suction side where no measurements could be obtained.

The cycle averaged LDV data at the farthest measurement location upstream of the rotor ($X_r/C_r = -0.088$) was mass averaged over one rotor pitch and compared the mass averaged five hole probe data closest to this location ($X_r/C_r = -0.080$ or $X/C = 1.16$). The agreement is excellent with the absolute total velocity being 0.98% of each other ($\hat{V}/U_m = 1.6119$ for the five hole probe and $\hat{V}/U_m = 1.6278$ for the LDV) and the absolute flow angles being within 0.30% of each other ($\bar{\alpha} = 70.42$ degrees for the five hole probe and $\bar{\bar{\alpha}} = 70.63$ degrees for the LDV). In Chapter 6, the superscript $\frown$ represents mass-averaged properties, in order to differentiate mass-averaged from ensemble averaged properties. (The comparison of LDV and five hole probe data is presented in section 6.4 of this thesis.)

6.2.1 Relative Total Velocity and Total Unresolved Unsteadiness

The cycle averaged relative total velocity normalized by mean rotor speed (U_m) is presented in Figure 6.3a. (The bar over the velocity and angle notation in the figures in Chapters 6 and 7 represents ensemble averaging.) This figure shows the flow acceleration from the pressure to the suction surface of the blade. The velocity accelerates gradually on the suction side from the leading edge to $X_r/C_r = 0.80$, after which it levels off and becomes fairly uniform until the trailing edge. On the pressure side the velocity change is fairly gradual from the leading edge to the trailing edge. The effect of the leading edge on the flow field is clearly shown with

Level	W/U_m
F	1.56
E	1.45
D	1.35
C	1.25
B	1.14
A	1.04
9	0.94
8	0.83
7	0.73
6	0.62
5	0.52
4	0.42
3	0.31
2	0.21
1	0.10

(a)

Level	W/U_m
F	1.558
E	1.455
D	1.351
C	1.247
B	1.143
A	1.039
9	0.935
8	0.831
7	0.727
6	0.623
5	0.519
4	0.416
3	0.312
2	0.208
1	0.104

(b)
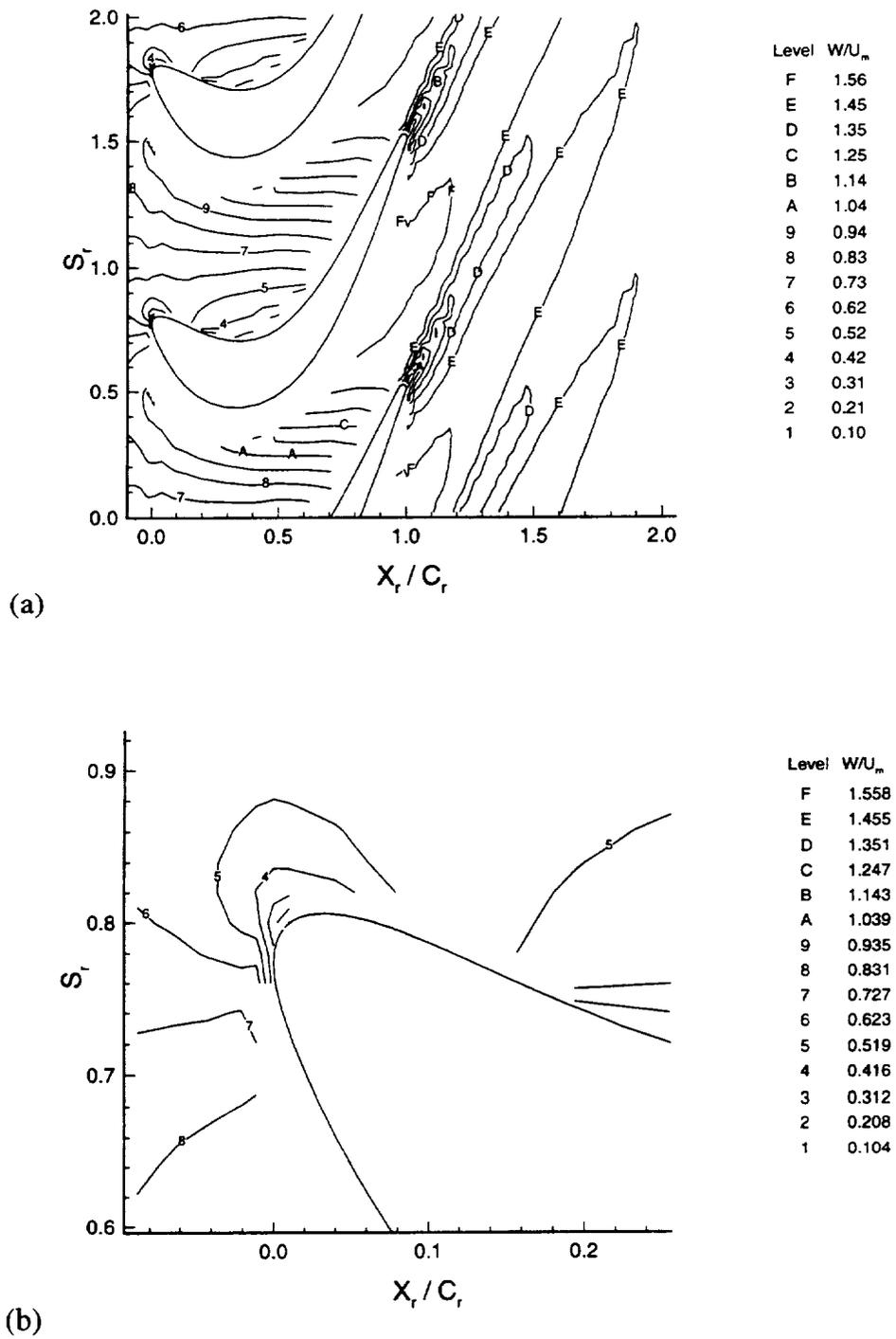
Figure 6.3. Cycle-Averaged Relative Total Velocity $\left(\overline{\overline{W}}/U_m\right)$

the flow decelerating as the leading edge is approached. The relative total velocity decelerates to a value of $\overline{\overline{W}}/U_m = 0.2$ just upstream of the leading edge. This can be seen more clearly in Figure 6.3b which presents an enlargement of the flow field near the rotor leading edge. Downstream of the blade, the rotor wake decays to negligible values within half a chord length downstream of the blade. The rotor wake thickness is small. The rotor wake is discussed in more detail in Chapter 7 of this thesis. Figures 6.4a, b and c show the blade-to-blade cycle averaged velocity profiles at three axial locations inside the rotor passage compared to the design blade surface velocity. Extrapolating the measured velocity to the blade surfaces, the design velocity matches the measured velocity well near the rotor leading edge. At midchord and near the trailing edge the match is not as good due to the boundary layer on the blade surfaces, which causes the measured velocity to be lower near the blade surface than the design velocity (The design velocity was calculated using an inviscid code.)

The cycle averaged relative total velocity vectors are presented in Figure 6.5. The measured velocity vectors follow the rotor blade contour almost everywhere, except near the leading and trailing edge. The potential effect can clearly be seen at the leading edge, while the over and underturning of the flow field on the suction and pressure side, respectively, at the trailing edge can also be seen clearly.

The cycle averaged relative total unresolved unsteadiness is shown in Figure 6.6. The total relative unresolved unsteadiness is defined as follows:

$$Tu_r = \frac{\sqrt{\left(\overline{u'^2} + \overline{v'^2}\right)/2}}{W} \times 100\% \qquad (6.9)$$

where

(a)

(b)

(c)
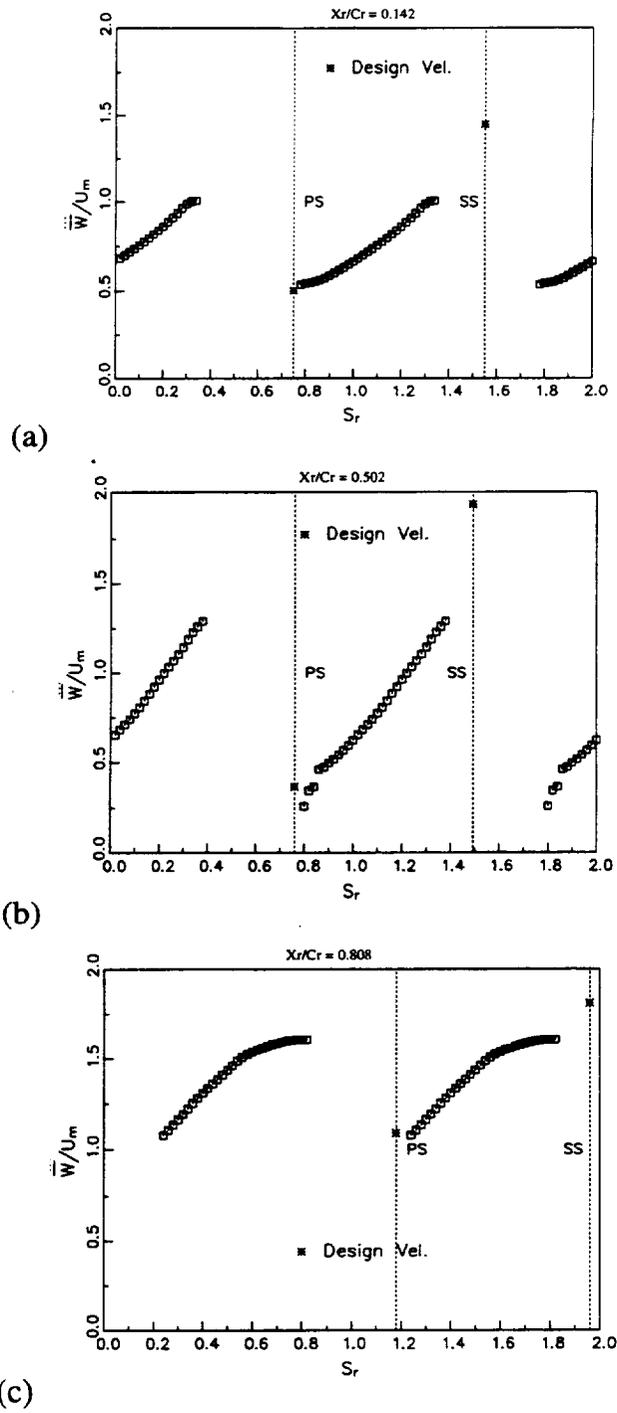
Figure 6.4. Cycle-Averaged Relative Total Velocity $\left(\overline{\overline{\overline{W}}}/U_m\right)$
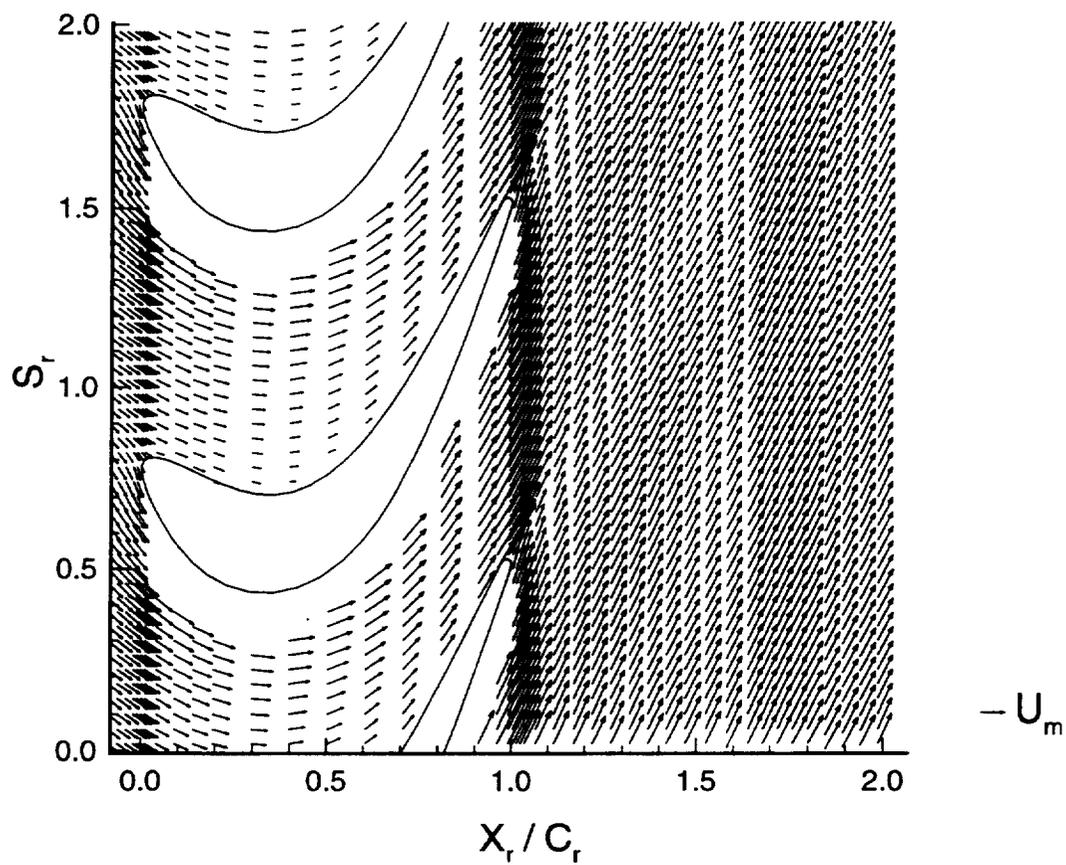
Figure 6.5. Cycle-Averaged Relative Total Velocity Vectors

Level	Tu_r (%)
D	100.00
C	50.00
B	30.00
A	20.00
9	18.00
8	16.00
7	14.00
6	12.00
5	10.00
4	8.00
3	6.00
2	4.00
1	2.00
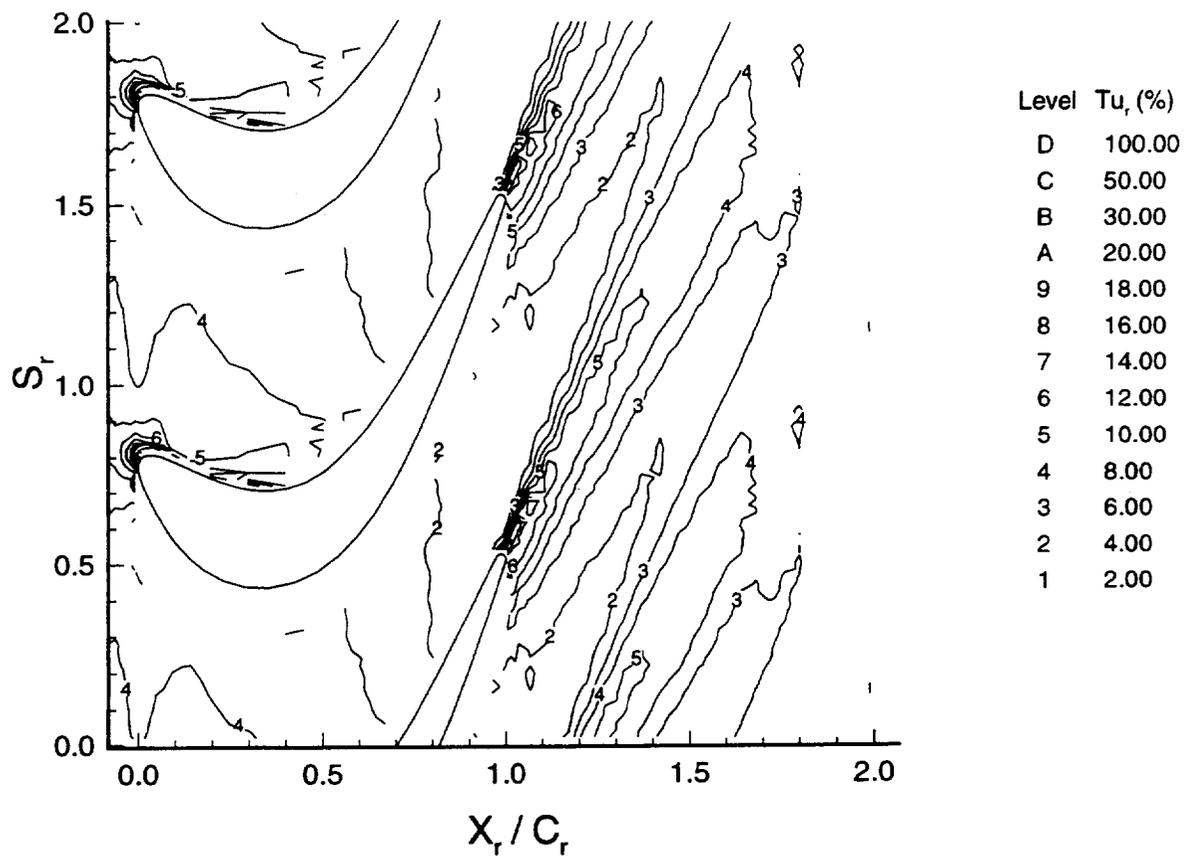
Figure 6.6. Cycle-Averaged Relative Total Unresolved Unsteadiness $\left(\overset{\bullet\bullet\bullet}{Tu}_r\right)$

$$\overline{u'^2} = \frac{\left[\sum_{i=1}^{n}\left(V_{x_i} - \overline{V}_x\right)^2\right]}{(n-1)} \qquad (6.10)$$

and

$$\overline{v'^2} = \frac{\left[\sum_{i=1}^{n}\left(V_{\theta_i} - \overline{V}_\theta\right)^2\right]}{(n-1)} \qquad (6.11)$$

where $\overline{V}$ is the ensemble averaged velocity, V_i is the instantaneous velocity measured at a particular rotor measurement window and n is the total number of measurements at that measurement window. The relative total unresolved unsteadiness is then cycle averaged using equation (6.8). The relative unresolved unsteadiness is low inside the rotor passage and high in the rotor wake. The highest level is observed at the leading edge. This is demonstrated more clearly in Figure 6.7 which is a blade-to-blade profile of cycle average total relative unresolved unsteadiness just upstream of the rotor leading edge. Figure 6.8 shows the total cycle-averaged unresolved unsteadiness at the leading edge with the total unresolved unsteadiness (Tu_t) normalized by the mean rotor speed instead of the local relative velocity. The total unresolved unsteadiness is defined as follows:

$$Tu_t = \frac{\sqrt{\left(\overline{u'^2} + \overline{v'^2}\right)/2}}{U_m} \times 100\% \qquad (6.12)$$

The total unresolved unsteadiness is then cycle averaged using equation (6.8).The high levels of total unresolved unsteadiness are still visible at the leading edge. This demonstrates that the increase in relative total unresolved unsteadiness at the rotor leading edge shown in Figures 6.6 and 6.7 is not only due to low relative velocities, but also due to an increase in the absolute magnitude of the velocity fluctuations. This is in contrast to measurements made at the leading edge of a
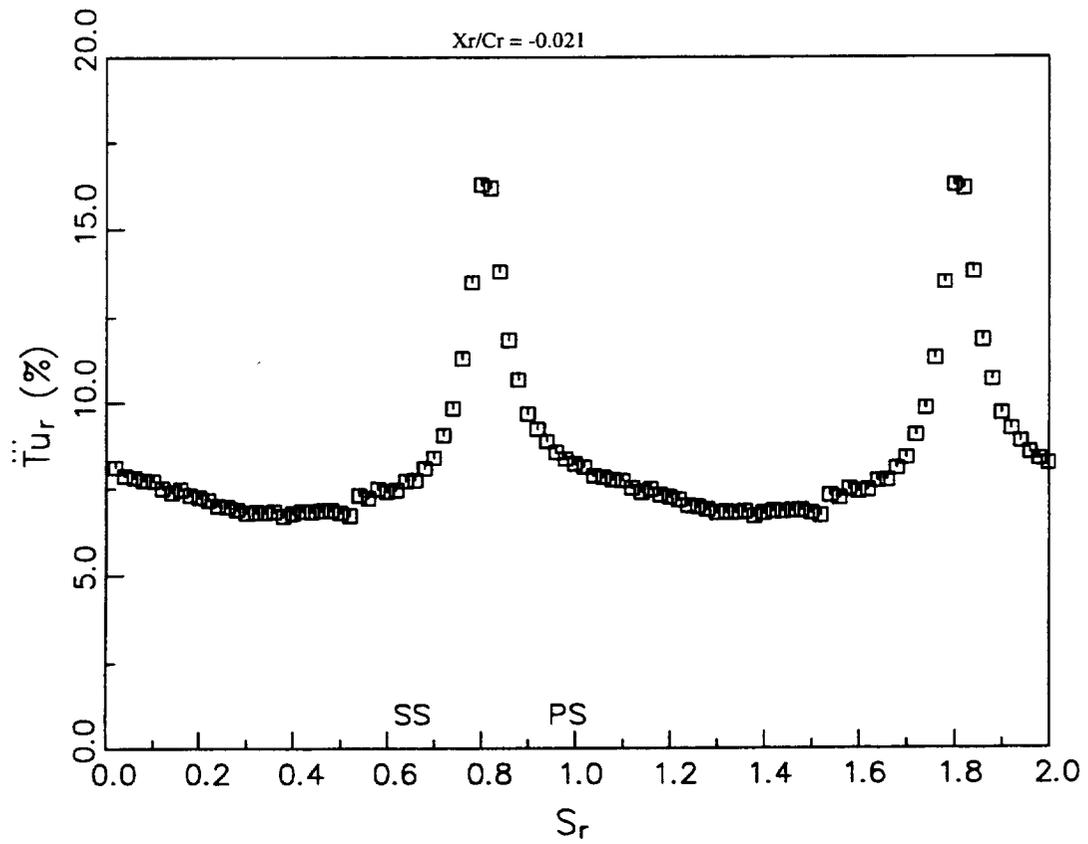
Figure 6.7. Cycle-Averaged Relative Total Unresolved Unsteadiness $\left(\overset{\cdots}{\text{Tu}}_r\right)$
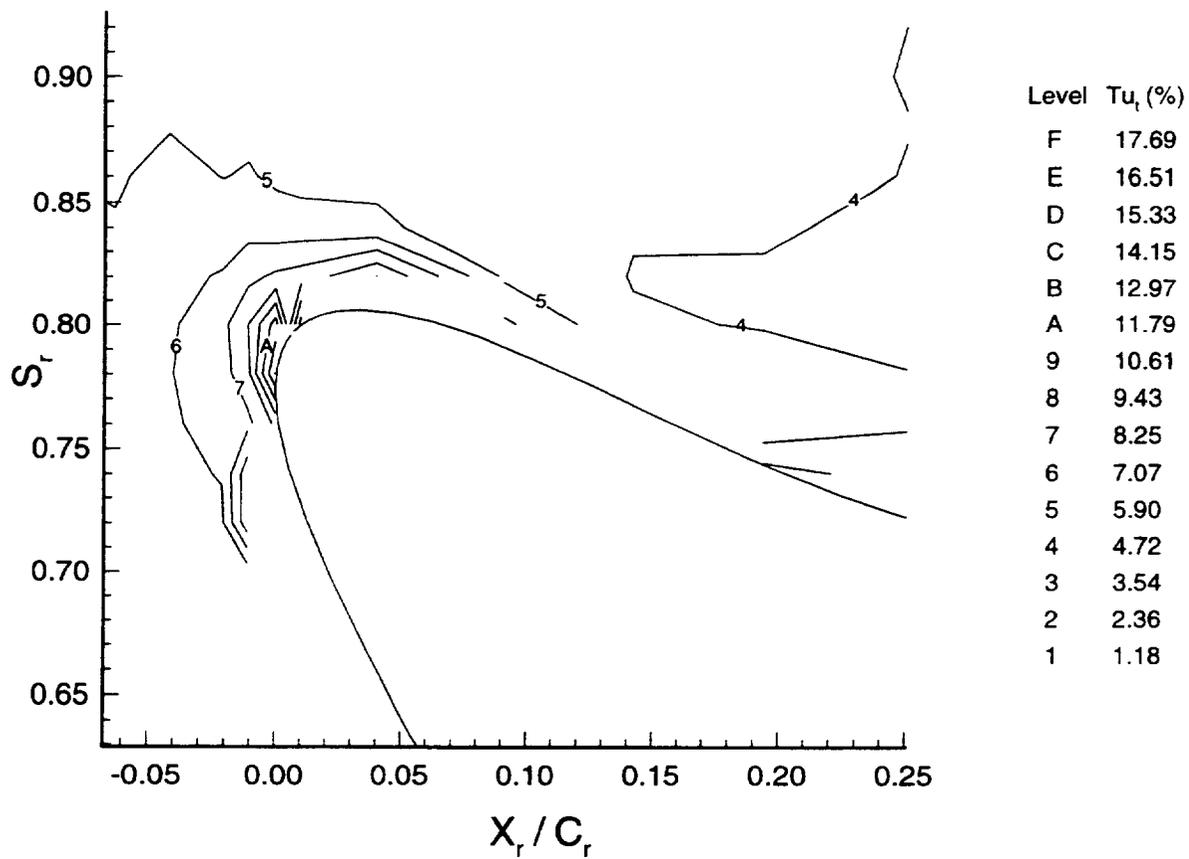
Figure 6.8. Cycle-Averaged Total Unresolved Unsteadiness $\left(\overset{\bullet\bullet\bullet}{Tu_t}\right)$

rotor cascade by Priddy and Bayley (1988), who showed that the absolute

magnitude of the velocity fluctuations slightly decreased as the leading edge was

approached. But it agrees with the results of Hobson and Shreeve (1991), who

measured an increase in the absolute magnitude of the velocity fluctuations at the

leading edge of a compressor cascade. This can be explained by examining the

turbulent kinetic energy equation, which is,

$$\frac{\partial k}{\partial t} + U_i \frac{\partial k}{\partial x_i} = \frac{\partial}{\partial x_i}\left(\frac{v_t}{\sigma_k}\frac{\partial k}{\partial x_i}\right) - \overline{u_i u_j}\frac{\partial U_i}{\partial x_j} - \varepsilon$$

$$\text{I} \qquad \text{II} \qquad\qquad \text{III} \qquad\quad \text{IV} \quad \text{V}$$

(6.13)

where term I is the rate of change of kinetic energy (k), term II is the convection

term , III is the diffusion term, IV is the production term and V is the dissipation.

The kinetic energy is a measure of the intensity of the velocity fluctuations. As the

leading edge is approached, the large increase in mean flow velocity gradients

cause an increase in production term which overshadows the dissipation, diffusion

and convection terms. Thus, the total unresolved unsteadiness should increase as

the leading edge of the blade is approached. In addition, the total unresolved

unsteadiness is observed to be higher near the pressure side. This is because the

unresolved unsteadiness in thin shear layers is highly sensitive to streamline

curvature in the plane of the mean shear. The unresolved shear stress and

unsteadiness are increased due to curvature when the angular momentum of the

flow decreases in the direction of the radius of curvature.

6.2.2 Axial Velocity and Relative Flow Angle

Figure 6.9 and 6.10 show the cycle averaged axial velocity and relative flow angle contours, respectively. The potential effect of the blade is seen to have a large effect on the axial velocity upstream of the leading edge, which is shown more clearly in Figure 6.11, which is a blade-to-blade cycle averaged axial velocity profile just upstream of the leading edge. The deceleration of the flow field in the presence of the stagnation point at the rotor leading edge and the acceleration away from it are dramatically illustrated in this figure. The axial velocity in the stagnation region is 30% of the free stream value at this location. Inside the passage, the axial velocity increases almost linearly from the pressure to the suction side. The relative flow angle shows the characteristic large change in flow angle for a turbine rotor, with the flow being turned around 110 degrees in the rotor passage. The effect of the leading edge on the flow field is also evident by the large change of flow angle at the leading edge. The blade-to-blade profiles of the cycle averaged relative flow angle presented in Figures 6.12a and b show that the rotor leading edge has a significant effect on the flow field even 9% of the rotor axial chord upstream of the leading edge, with the change in flow angle being 18 degrees across the passage at this location. This effect increases as the rotor leading edge is approached with the change in angle increasing 35 degrees just upstream of the rotor leading edge.

6.2.3 Unresolved and Periodic Unsteady Velocity Correlations

Figures 6.13 and 6.14 show the cycle averaged unresolved unsteady velocity cross correlations for both the turbine coordinate system ($\overline{u'v'}$) and streamwise-normal coordinate system ($\overline{u'_s v'_n}$). The unresolved velocity correlations

Level	V_x/U_m
F	1.18
E	1.10
D	1.03
C	0.95
B	0.87
A	0.79
9	0.71
8	0.63
7	0.55
6	0.47
5	0.39
4	0.32
3	0.24
2	0.16
1	0.08
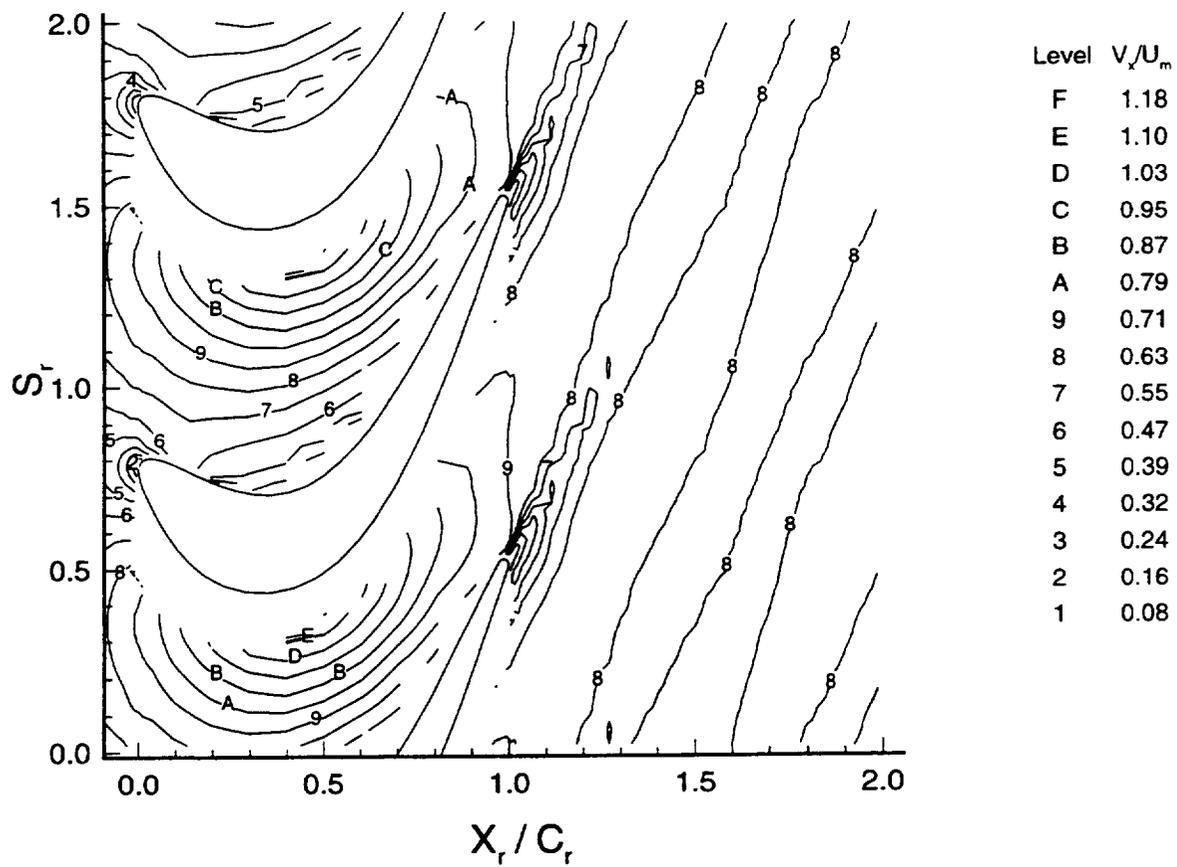
Figure 6.9. Cycle-Averaged Axial Velocity $\left(\overline{\overline{V}}_x/U_m\right)$
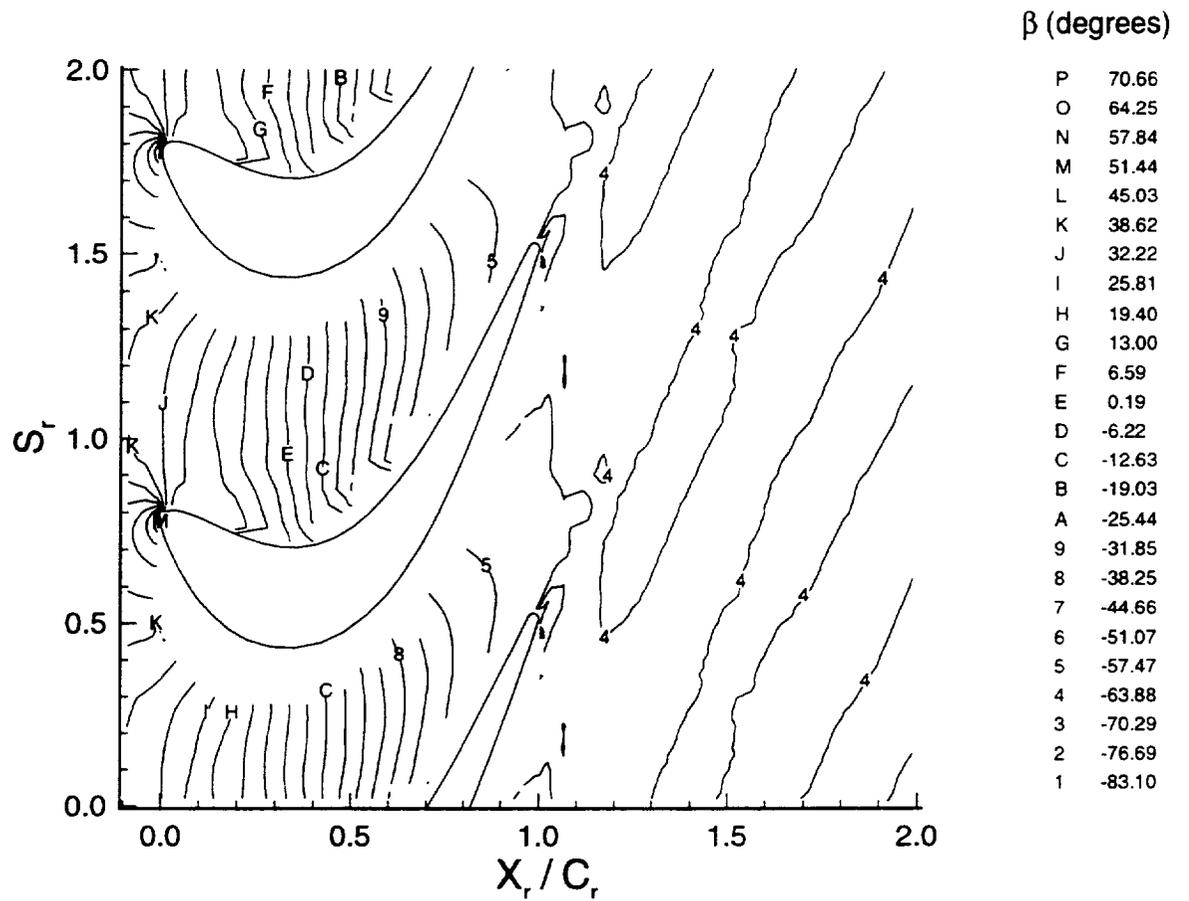
Figure 6.10. Cycle-Averaged Relative Flow Angle $\left(\overline{\overline{\beta}}\right)$
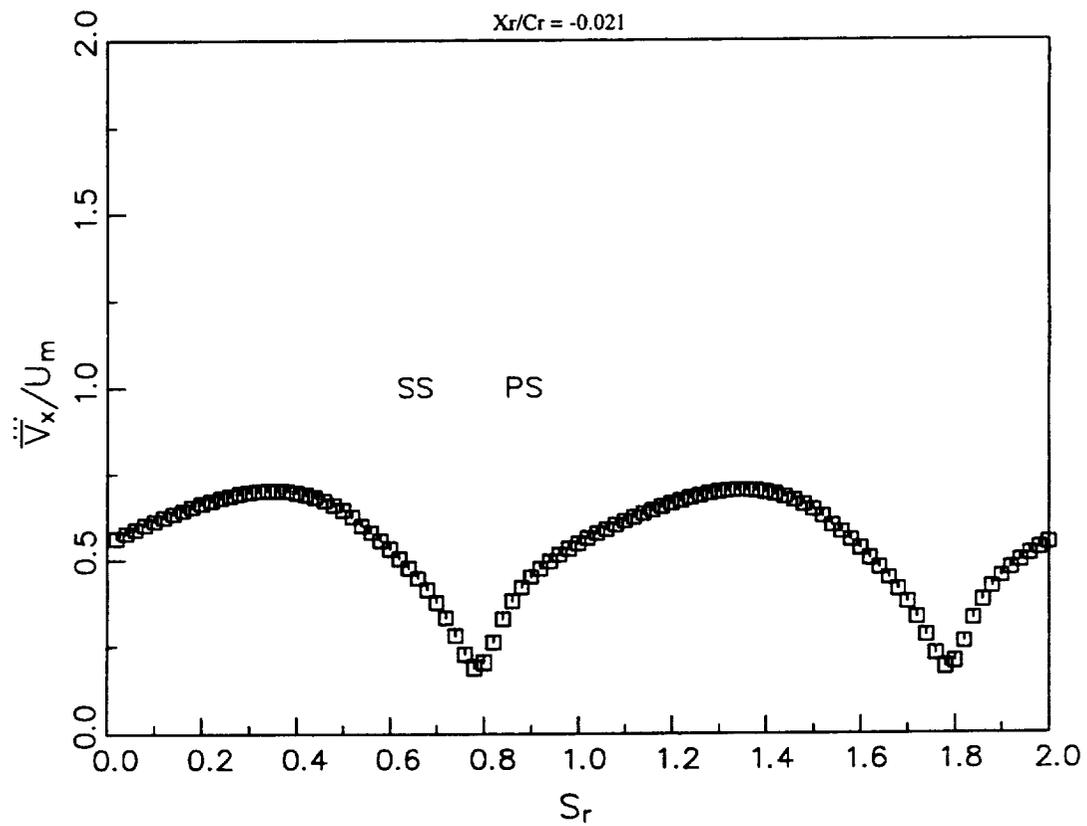
Figure 6.11. Cycle Averaged Axial Velocity $\left(\overset{\ldots}{\overline{V}}_x / U_m\right)$
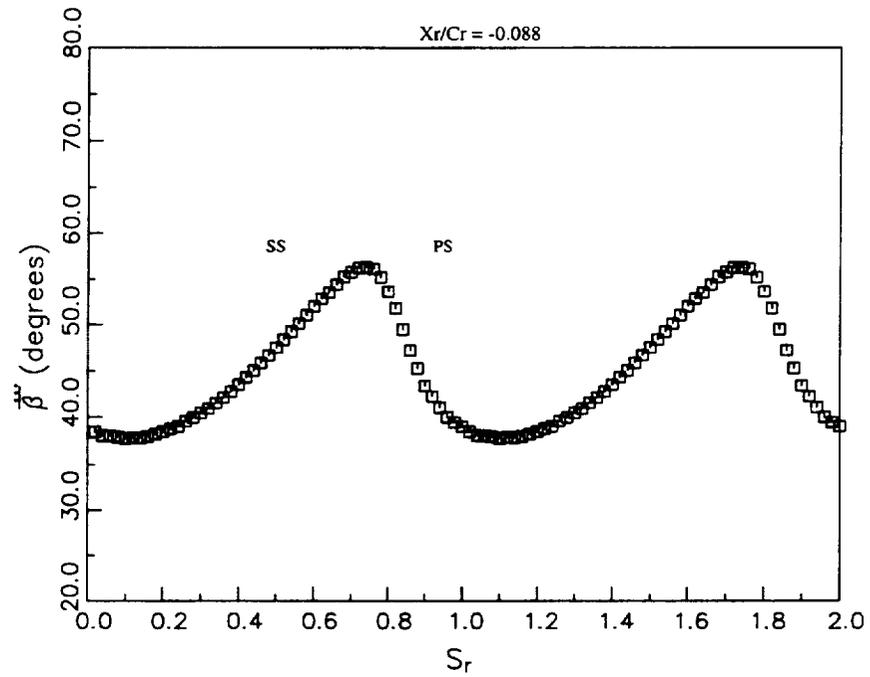
(a)
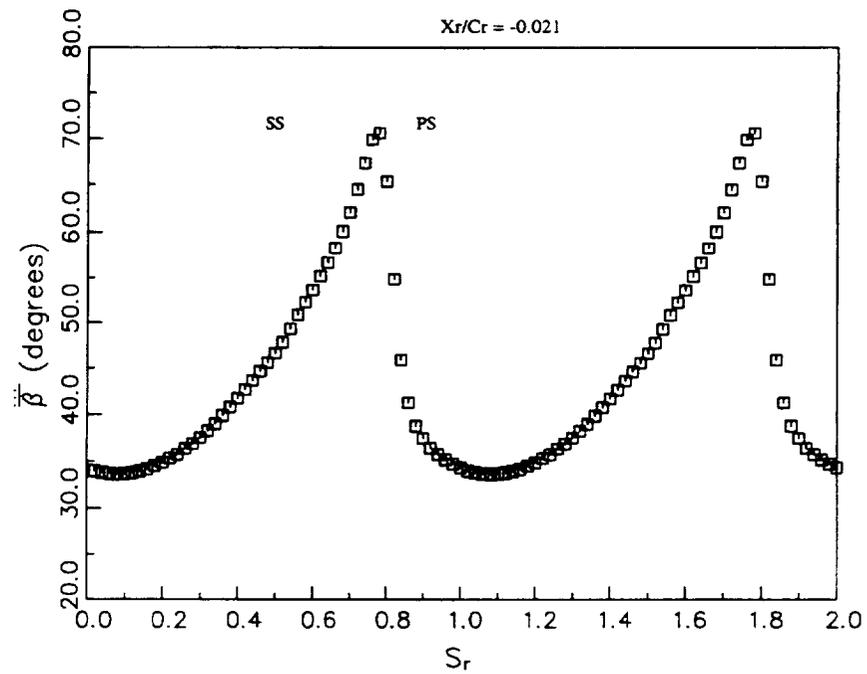
(b)

Figure 6.12. Cycle-Averaged Relative Flow Angles $\left(\bar{\bar{\beta}}\right)$

Level	$\overline{u'v'}$ (%)
H	1.00
G	0.80
F	0.60
E	0.40
D	0.20
C	0.10
B	-0.10
A	-0.20
9	-0.40
8	-0.60
7	-0.80
6	-1.00
5	-1.20
4	-1.40
3	-1.60
2	-1.80
1	-2.00
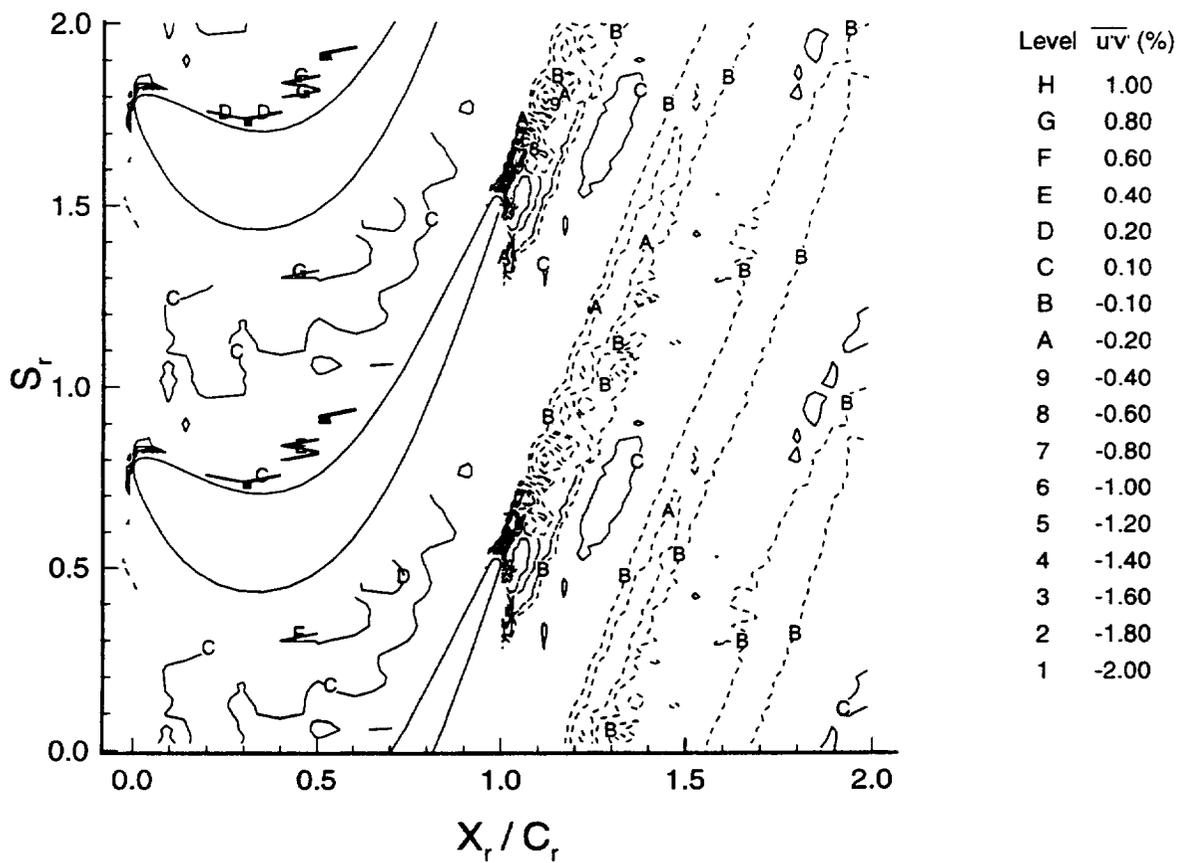
Figure 6.13. Cycle-Averaged Unresolved Velocity Correlation $\left(\overline{u'v'} \right)$

Level	$\overline{u_s' v_n'}$ (%)
M	2.00
L	1.80
K	1.60
J	1.40
I	1.20
H	1.00
G	0.80
F	0.60
E	0.40
D	0.20
C	0.10
B	-0.10
A	-0.20
9	-0.40
8	-0.60
7	-0.80
6	-1.00
5	-1.20
4	-1.40
3	-1.60
2	-1.80
1	-2.00
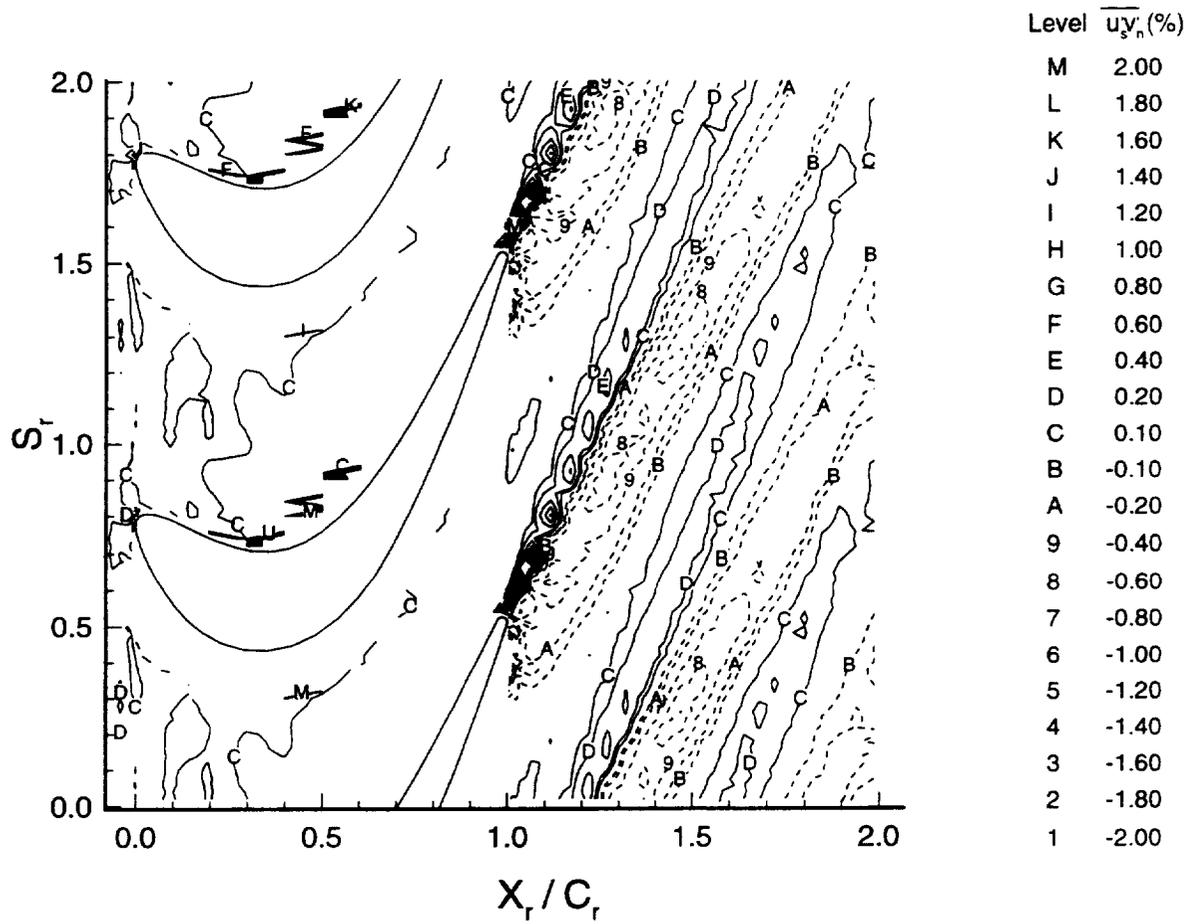
Figure 6.14. Cycle-Averaged Unresolved Velocity Correlation $\left(\overline{u_s' v_n'} \right)$

are defined as follows:

$$\overline{u'v'} = \frac{\overline{\left(V_{x_i} - \overline{V}_x\right)\left(V_{\theta_i} - \overline{V}_\theta\right)}}{U_m^2} \times 100\%$$ (6.14)

$$\overline{u'_s v'_n} = \frac{\overline{v'_x v'_\theta}\left(\cos^2\beta - \sin^2\beta\right) + \left(\overline{u'^2} - \overline{v'^2}\right)\cos\beta\sin\beta}{U_m^2} \times 100\%$$ (6.15)

where

$$\overline{v'_x v'_\theta} = \overline{\left(V_{x_i} - \overline{V}_x\right)\left(V_{\theta_i} - \overline{V}_\theta\right)}$$

and the subscript i represents instantaneous velocity, the superscript — represents the ensemble averaged velocity in each rotor measurement window and β is the relative flow angle. The unresolved unsteady velocity cross correlations for both the turbine coordinate system $(\overline{u'v'})$ and streamwise-normal coordinate system $(\overline{u'_s v'_n})$. are then cycle averaged using equation (6.8). The unresolved cross correlations are zero almost everywhere except at the leading edge and near the pressure surface of the rotor and in the rotor wake. This trend is expected since the production of the unresolved velocity cross correlations is brought about by velocity and turbulence intensity gradients. While the axial-tangential unresolved cross correlation is negative in the rotor wake, the streamwise-normal unresolved cross correlation is positive on the pressure side of the wake and negative on the suction side of the wake. The positive and negative streamwise-normal velocity cross correlation distribution about the wake center results from opposite gradients of streamwise mean velocity about the wake center.

The cycle averaged periodic velocity correlations are presented in Figures 6.15, 6.16 and 6.17. The periodic velocity correlations are defined as follows:

Level	$\overline{\tilde{u}\,\tilde{u}}$ (%)
F	24.34
E	22.72
D	21.10
C	19.47
B	17.85
A	16.23
9	14.60
8	12.98
7	11.36
6	9.74
5	8.11
4	6.49
3	4.87
2	3.25
1	1.62
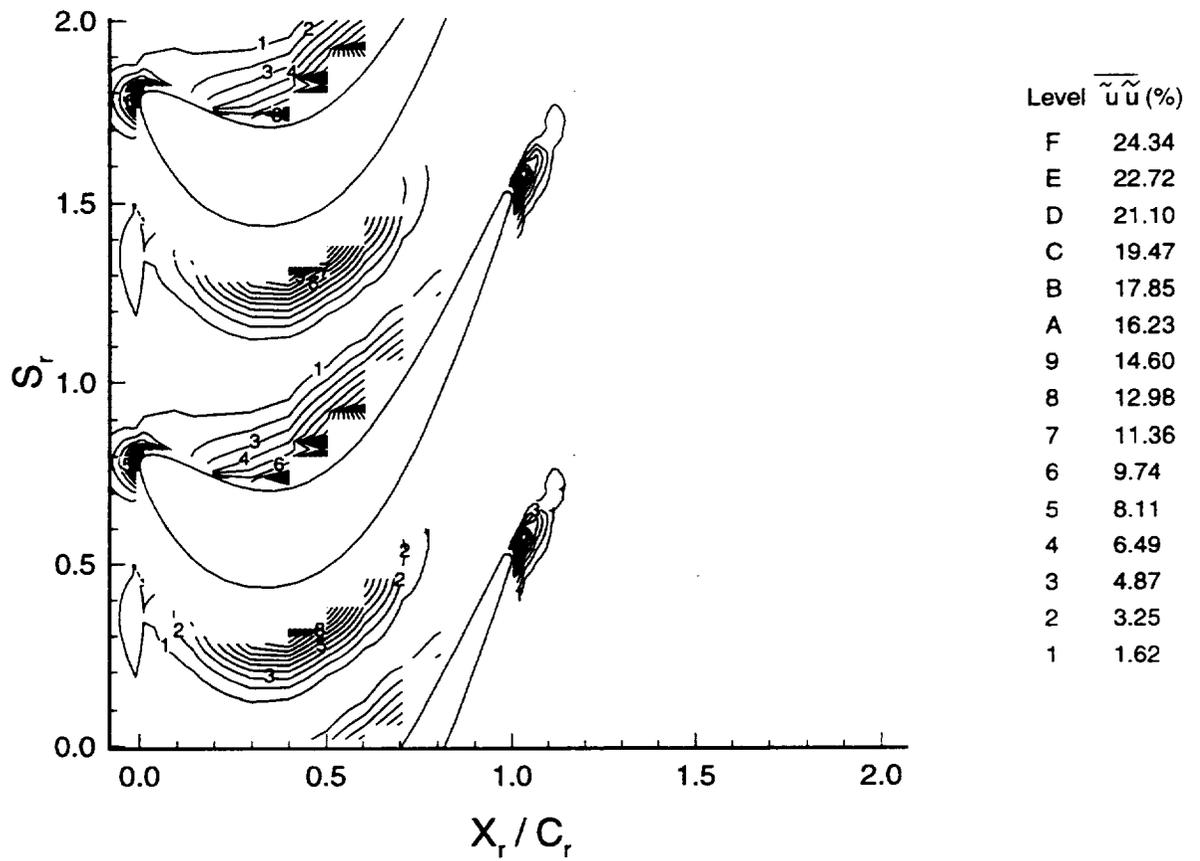
Figure 6.15. Cycle-Averaged Periodic Velocity Correlation $\left(\dfrac{\overline{\cdots}}{\tilde{u}\tilde{u}}\right)$
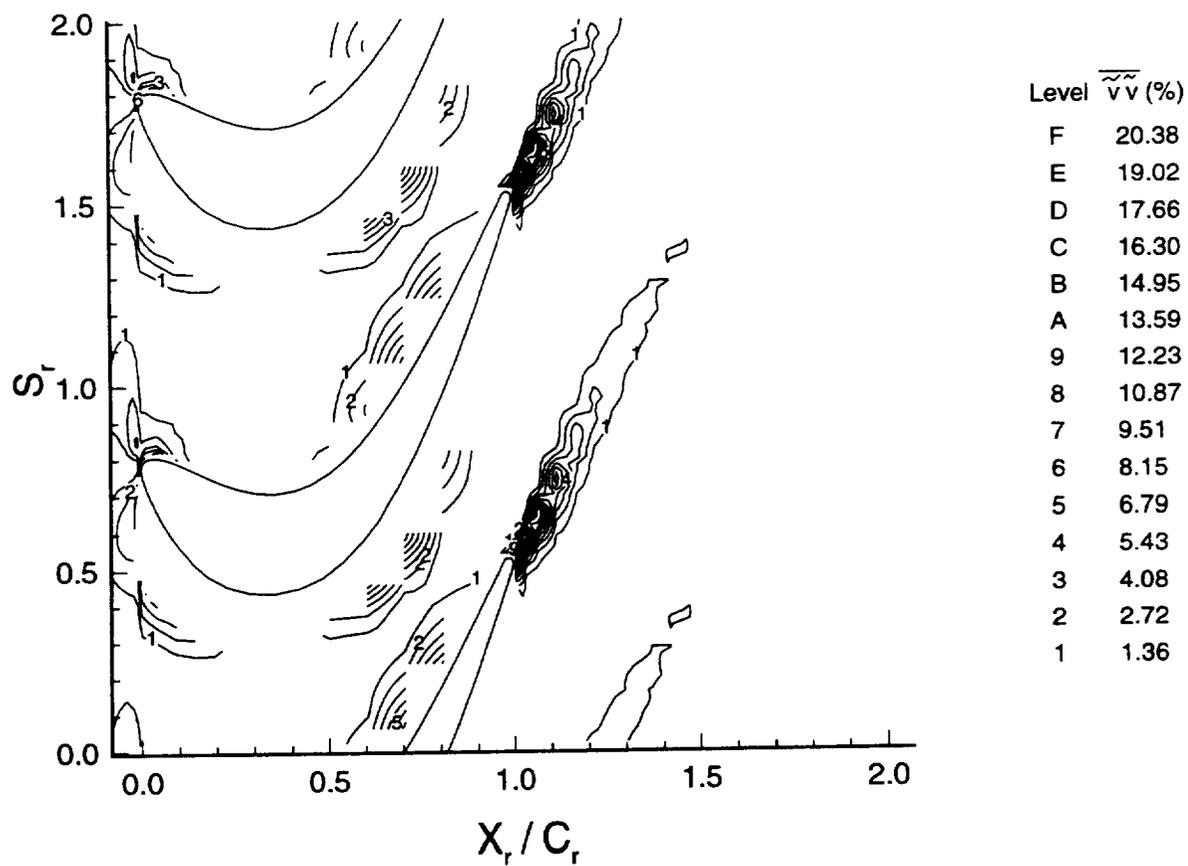
Figure 6.16. Cycle-Averaged Unresolved Velocity Correlation $\left(\overline{\widetilde{v}\,\widetilde{v}}\right)$
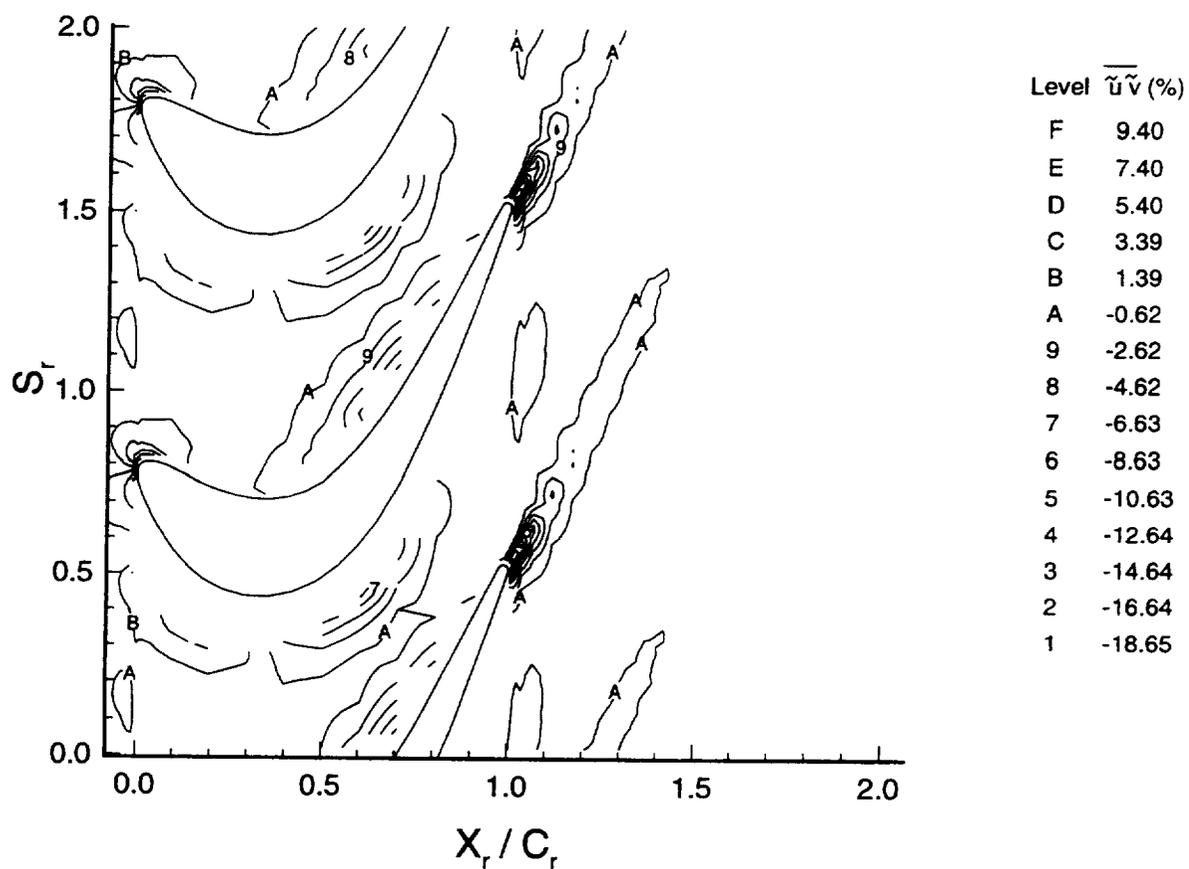
Figure 6.17. Cycle-Averaged Unresolved Velocity Correlation $\left(\overline{\widetilde{u}\,\widetilde{v}}\right)$

$$\overline{\tilde{V}_p \tilde{V}_q} = \frac{\overline{\left(\overline{V} - \overline{\overline{V}}\right)_p \left(\overline{V} - \overline{\overline{V}}\right)_q}}{U_m^2} \times 100\% \qquad (6.16)$$

where the subscripts p and q correspond to the axial and /or tangential velocity components. The periodic velocity correlations are then cycle averaged using equation (6.8). All three show high levels of periodic unsteadiness at the rotor leading edge, near the pressure and suction surfaces and in the rotor wake. The high level of periodic unsteadiness at the leading edge is a result of the large potential effect of the rotor blade on the flow field, while the high levels near the blade surfaces is a result of the large velocity change across the rotor pitch. The rotor wake periodic unsteadiness decays fairly rapidly, decaying to negligible values within one half chord downstream of the rotor.

6.3 Rotor Time Resolved Flow Field Including Nozzle Wake Propagation through the Rotor

To understand the propagation of the nozzle wake through the rotor, one needs to look at the flow field in the rotor at different relative positions of the rotor with respect to the nozzle. This will show of the chopping the nozzle wake and its transport through the rotor, and is accomplished by looking at the rotor flow field at the six different nozzle/rotor blade locations measured (as shown in Figure 6.1).

There are several criteria that can be used to identify the nozzle wake in the rotor passage. Compared to the free stream flow field outside of the wake, the wake has a velocity defect, higher unresolved unsteadiness, a variation in flow angle across the nozzle wake, and higher shear stress. These criteria will be used in this section to determine the presence and propagation of the nozzle wake through the

rotor passage.

The level of the interaction between the nozzle and rotor flow field can be determined by examining the ratio of the time it takes the rotor to traverse one nozzle pitch versus the time it takes for fluid particles to travel through the rotor. blade passage. This is called the reduced frequency and it is given by

$$\Omega = \frac{C_r/V_x}{S/U_m} \qquad (6.\ 17)$$

where Ω is the reduced frequency, C_r is the rotor axial chord, V_x is the axial velocity at theinlet to the rotor and S is the nozzle pitch. This ratio determines the number of nozzle wakes in each rotor passage at any instant in time. For the turbine in this investigation, the reduced frequency is 1.5, which means that there should be one and a half nozzle wakes in each rotor passage for each nozzle/rotor blade location, which is demonstrated in the following paragraphs.

6.3.1 Relative Total Unresolved Unsteadiness

Figures 6.18a through 6.18f show the relative total unresolved unsteadiness at the six different nozzle/rotor locations. They represent six different "snapshots" of the rotor flow field, and since these six different locations are equally spaced over one nozzle pitch, they can be viewed sequentially from nozzle/rotor location one to location six and then back to one again. Examining position 2 first,a region of increased unresolved unsteadiness upstream of the rotor leading edge can be seen as compared to the cycle averaged relative total unsteadiness upstream of the rotor presented in Figure 6.5. This is the nozzle wake. Moving to position 3, the nozzle wake enters the rotor passage, and is subsequently chopped into individual

Position #2

Level	Tu$_r$ (%)
E	100
D	75
C	50
B	25
A	20
9	18
8	16
7	14
6	12
5	10
4	8
3	6
2	4
1	2

(a)

Position #3

Level	Tu$_r$ (%)
D	100
C	50
B	25
A	20
9	18
8	16
7	14
6	12
5	10
4	8
3	6
2	4
1	2

(b)
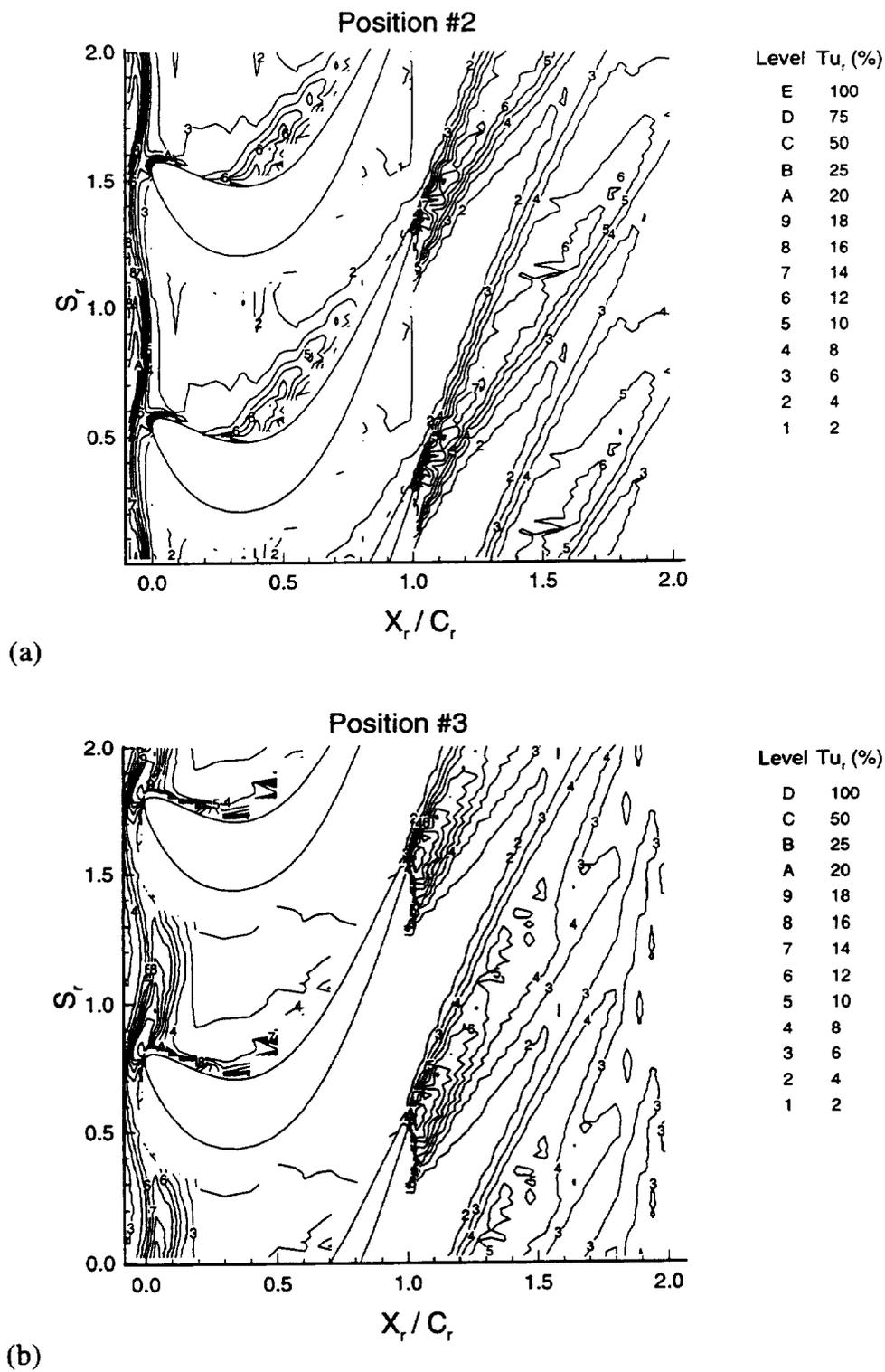
Figure 6.18. Relative Total Unresolved Unsteadiness (Tu_r) at the Six Nozzle/Rotor Positions
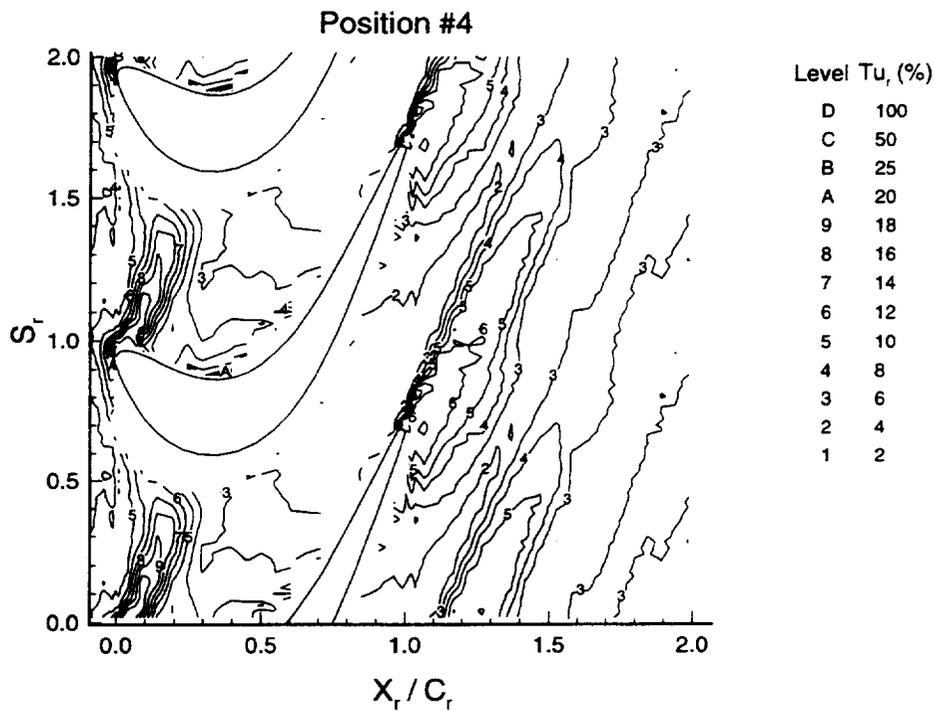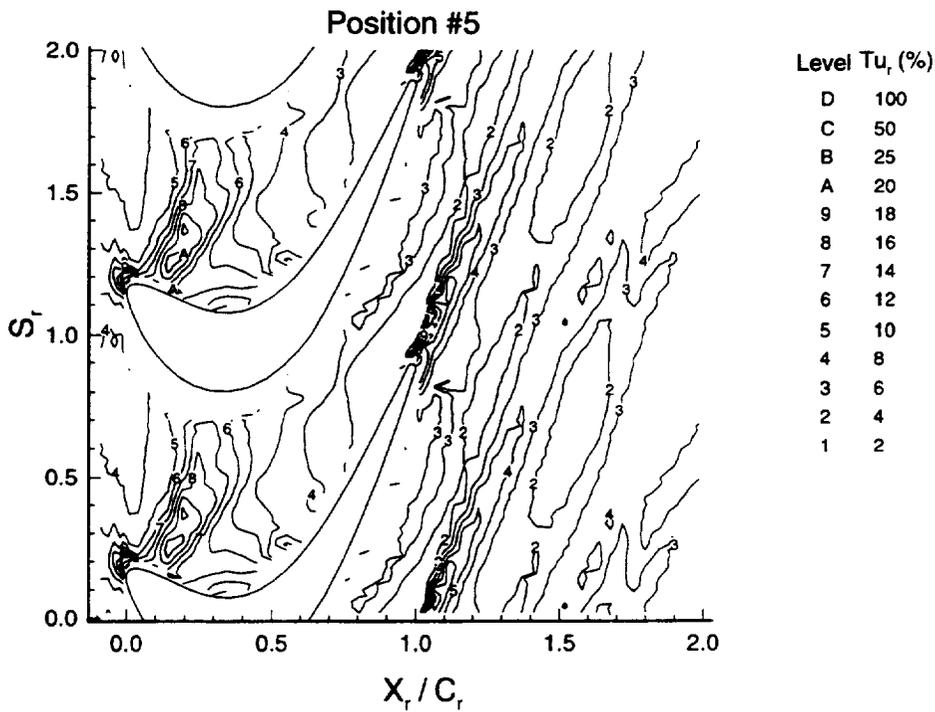
Position #4

Level	Tu_r (%)
D	100
C	50
B	25
A	20
9	18
8	16
7	14
6	12
5	10
4	8
3	6
2	4
1	2

(c)

Position #5

Level	Tu_r (%)
D	100
C	50
B	25
A	20
9	18
8	16
7	14
6	12
5	10
4	8
3	6
2	4
1	2

(d)

Figure 6.18 (Cont.). Relative Total Unresolved Unsteadiness $\left(Tu_r\right)$ at the Six Nozzle/Rotor Positions

Position #6

Level	Tu_r (%)
D	100
C	50
B	25
A	20
9	18
8	16
7	14
6	12
5	10
4	8
3	6
2	4
1	2

(e)

Position #1

Level	Tu_r (%)
E	100
D	75
C	50
B	25
A	20
9	18
8	16
7	14
6	12
5	10
4	8
3	6
2	4
1	2
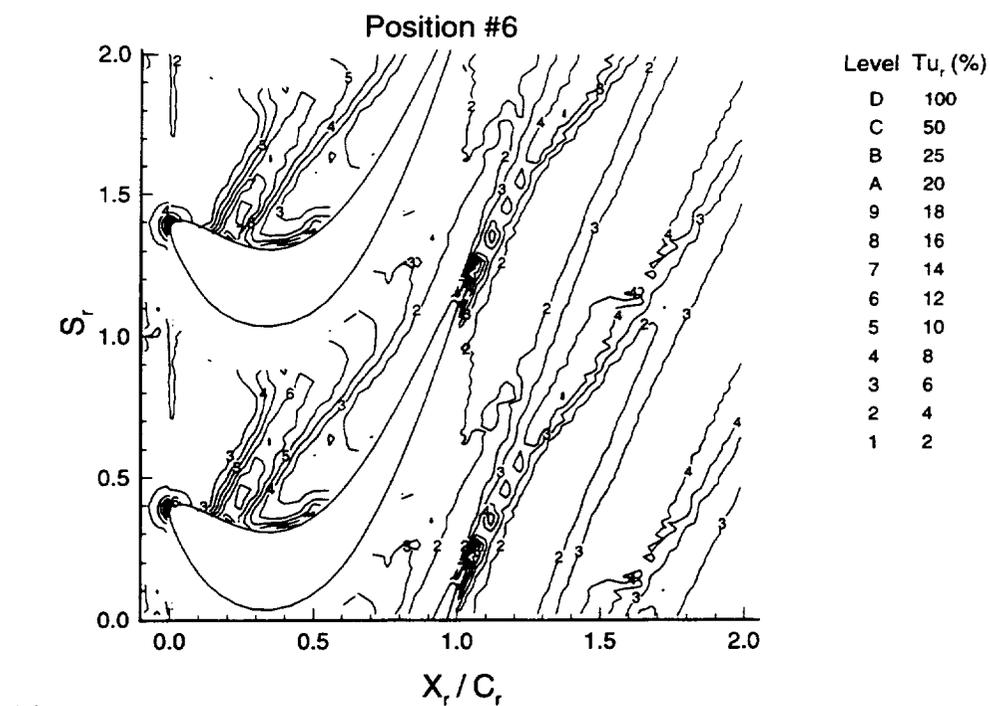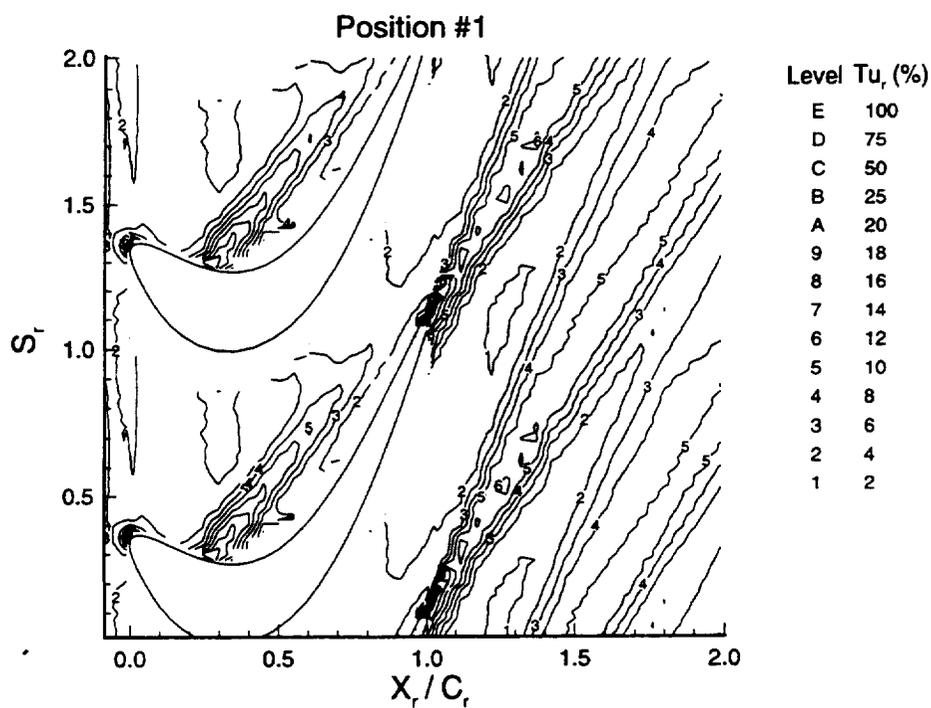
(f)

Figure 6.18 (Cont.). Relative Total Unresolved Unsteadiness $\left(Tu_r\right)$ at the Six

Nozzle/Rotor Positions

segments by the rotor blades. The nozzle wake is bowed because the convection velocity at midpitch is higher than at the rotor leading edge. These individual segments of the nozzle wake can now move independently of each other resulting in a mismatch between segments that were originally part of the same nozzle wake by the time they reach the rotor exit. There is also increased unresolved unsteadiness near the pressure surface of the rotor blade, just downstream of the point where the nozzle wake interacts with the rotor pressure surface. This increase in unresolved unsteadiness is a result of the interaction of the nozzle wake with the rotor pressure surface boundary layer which, along with the concave curvature effects discussed earlier, destabilizes the flow.

At position 4, the nozzle wake is becoming distorted as it travels through the rotor passage, with the region of the nozzle wake near the rotor suction surface moving faster than the region near the pressure side. This distortion of the nozzle wake is due to the large differential in the convection velocity between the pressure and suction surface, especially at the leading edge. Moving to positions 5 and 6, the distortion of the nozzle wake is continuing with the nozzle wake turning clockwise in the rotor passage. Continuing onto positions 1 and 2, the nozzle wake has turned more than 30 degrees from its orientation at the rotor leading edge and it is now parallel to the rotor pressure surface. At position 3, the nozzle wake is stretched along the rotor pressure surface. Thus, it can not be easily identified in the rotor passage since it is close to the rotor pressure surface where is cannot be measured by the LDV. This is in contrast to other measurements of the nozzle wake in the rotor passage (Hodson, 1984 and Binder et al., 1985) and computations (Hodson, 1985 and Korakianitis, 1992) who show that at the rotor trailing edge, the nozzle wake stills spans the rotor passage from the pressure to suction surfaces. The reason for this can be found by looking at the blade surface velocity distributions. In both Hodson's and Binder's turbine rotors the difference between the pressure

and suction surface velocities is much less than the difference between the pressure and suction surface velocities for the AFTRF rotor. (Korakianitis (1992) calculates the flow in Binder's turbine rotor, while Hodson (1985) calculates the flow in his own turbine rotor.) At midchord, the suction surface to pressure surface velocity ratio of the AFTRF turbine rotor is twice that of Hodson's and Binder's turbine rotors suction to pressure surface velocity ratios. This large difference between the pressure and suction surface velocities in the AFTRF turbine rotor causes the region of the nozzle wake near the rotor suction surface to travel much more rapidly than the region of the nozzle wake near the pressure surface. Thus by the time the region nozzle wake near the rotor suction surface has reached the rotor trailing edge, it has rotated so that it hugs the pressure surface. In Hodson and Binder's turbine rotors, the difference between the pressure surface and suction surface velocities is not as great, thus the nozzle wake does not turn as much and by the time it reaches the rotor trailing edge it still spans the rotor passage from the pressure to suction surface.

Using an averaged convection velocity along the AFTRF rotor pressure surface between X/C=0.50 and X/C=1.0 (where the nozzle wake is located at position 2) to calculate the distance the nozzle wake moves between each position, the nozzle wake should be completely inside the rotor wake after six nozzle/rotor locations. Thus six nozzle/rotor locations from position 2 is position 2.

This is confirmed by examining the flow field downstream of the rotor. It can be seen that the flow field is not the same at every nozzle/rotor position, but changes from one position to another. Sharma et al. (1985) also noticed this phenomena downstream of their rotor. Measuring the flow field at 10% axial chord downstream of a rotor with a three sensor hot wire, they showed that there are two distinct flow fields downstream of the rotor which they called the minimum and maximum interaction between the nozzle and rotor wakes. The maximum

interaction occurs when the nozzle wake is directly inside of the rotor wake while the region outside the wake shows low total unsteadiness. The minimum interaction occurs when the upstream nozzle wakes are in between the rotor wakes, which is shown by the high total unsteadiness in this region. A similar feature can be seen in the AFTRF rotor flow field just downstream of the rotor (from the trailing edge to one half chord downstream). The maximum interaction occurs at position 2 with high relative total unsteadiness in the rotor wake (maximum relative total unsteadiness of 16% at $X_r/C_r = 1.12$) and low total unsteadiness in the region between the wakes (relative total unsteadiness of 4% at $X_r/C_r = 1.12$). This low relative total unsteadiness region occupies more than 60% of the rotor pitch at 10% axial chord downstream of the rotor trailing edge.

The minimum interaction occurs at position 5 with the low relative total unsteadiness region between the wakes ($Tu_r = 4\%$) occupying only 15% of the rotor pitch at $X_r/C_r = 1.10$. At this location the maximum relative total unsteadiness in the rotor wake is 12% as compared to 16% at the maximum interaction. This is because the nozzle wake is located in between the rotor wakes at position 5, causing higher relative total unsteadiness in between the rotor wakes while at position 2 the nozzle wake is located in the rotor wake, thus causing higher relative total unsteadiness in the rotor wake.

Blade to blade profiles of total unresolved unsteadiness for nozzle/rotor positions 4 and 1 are presented in Figures 6.19a and 6.19b, respectively, at five typical axial locations in the rotor passage. The total unresolved unsteadiness is normalized by U_m here, so that the magnitude of the unsteadiness at different axial locations can be compared. While near the leading edge ($X_r/C_r = 0.01$ and 0.04) the unresolved unsteadiness increases from 6% outside the nozzle wake ($S_r = 1.2$) to 10% inside the nozzle wake ($S_r = 1.0$), near the trailing edge ($X_r/C_r = 0.706$) the unresolved unsteadiness increases from 2.5% outside the nozzle wake ($S_r = 0.7$) to

Position #4

X_r/C_r=0.194
+ X_r/C_r=0.142
▲ X_r/C_r=0.091
⊙ X_r/C_r=0.040
▣ X_r/C_r=0.010

(a)

Position #1

× X_r/C_r=0.706
+ X_r/C_r=0.604
▲ X_r/C_r=0.502
⊙ X_r/C_r=0.398
▣ X_r/C_r=0.297
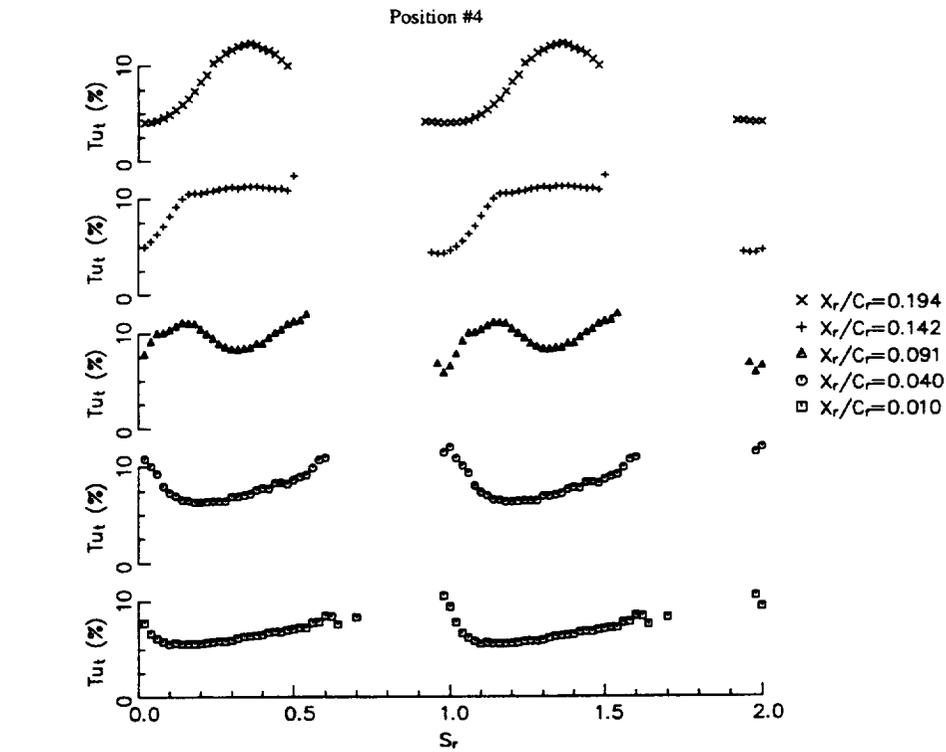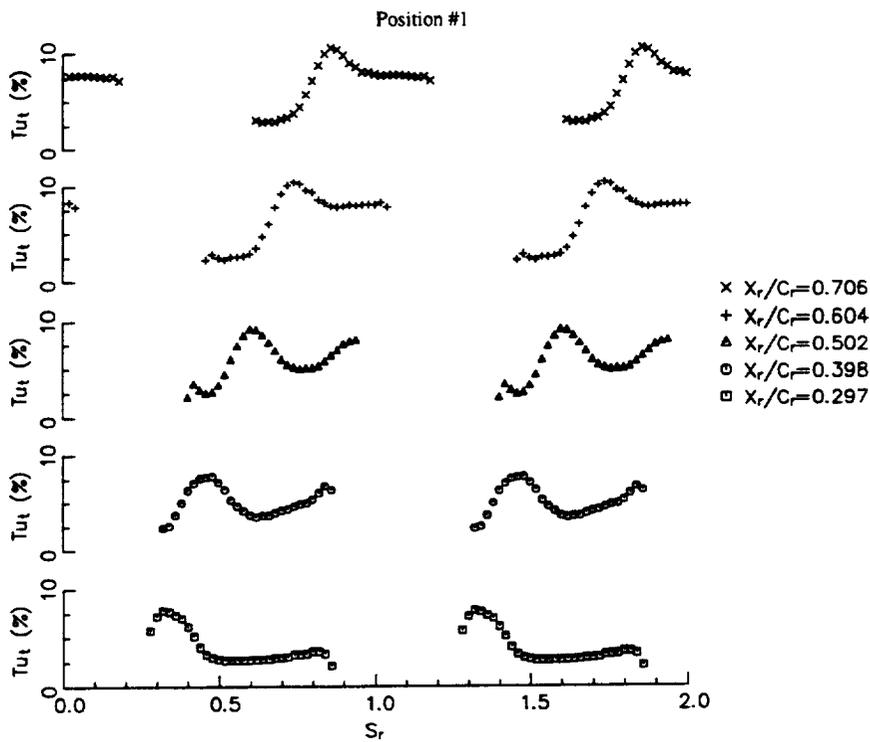
(b)

Figure 6.19. Blade to Blade Profiles of Total Unresolved Unsteadiness $\left(Tu_t\right)$

10% inside the nozzle wake (S_r= 0.9). This demonstrates that the unresolved

unsteadiness in the nozzle wake does not decay significantly in the rotor passage.

This is discussed in more detail in Chapter 7.

6.3.2 Relative and Absolute Total Velocity

Figures 6.20a through 6.20f show the relative total velocity in the rotor at

the six nozzle/rotor positions. The location of the nozzle wake in the rotor can be

identified by the region that has a lower total velocity than the cycle averaged total

velocity shown in Figure 6.3. Using this criteria the nozzle wake can be identified

at nozzle/rotor position 2, upstream of the rotor leading edge at the same location

as the increased relative total unsteadiness shown in Figure 6.18. Examining the

successive nozzle/rotor locations, this velocity defect is located at the same

location as the higher relative total unsteadiness. This gives added confirmation

that the nozzle wake is located at these positions. Downstream of the rotor trailing

edge, one can see the flow field is not the same at every nozzle/rotor position, but

changes from one position to another, similar to the total unsteadiness plots. At the

maximum interaction position (position 2), the free stream flow field outside of the

rotor wakes has a uniform velocity over almost 70% of the rotor pitch at

X_r/C_r=1.10. At this position the nozzle wake is located in the rotor wake (in the

region from the rotor trailing edge to one half chord downstream). On the other

hand, at the minimum interaction position (position 5), the free stream flow field at

X_r/C_r = 1.10 covers only 28% of the rotor pitch. At this position the nozzle wake

is in between the rotor wakes. Also, the free stream velocity is lower at the

minimum interaction position (from the trailing edge to X_r/C_r = 1.50) than at the

maximum interaction position thus providing added evidence that the nozzle wake

is located between the rotor wake at the minimum interaction position.

Position #2

Level	W/U_m
F	1.56
E	1.45
D	1.35
C	1.25
B	1.14
A	1.04
9	0.94
8	0.83
7	0.73
6	0.62
5	0.52
4	0.42
3	0.31
2	0.21
1	0.10

(a)

Position #3

Level	W/U_m
F	1.56
E	1.45
D	1.35
C	1.25
B	1.14
A	1.04
9	0.94
8	0.83
7	0.73
6	0.62
5	0.52
4	0.42
3	0.31
2	0.21
1	0.10

(b)
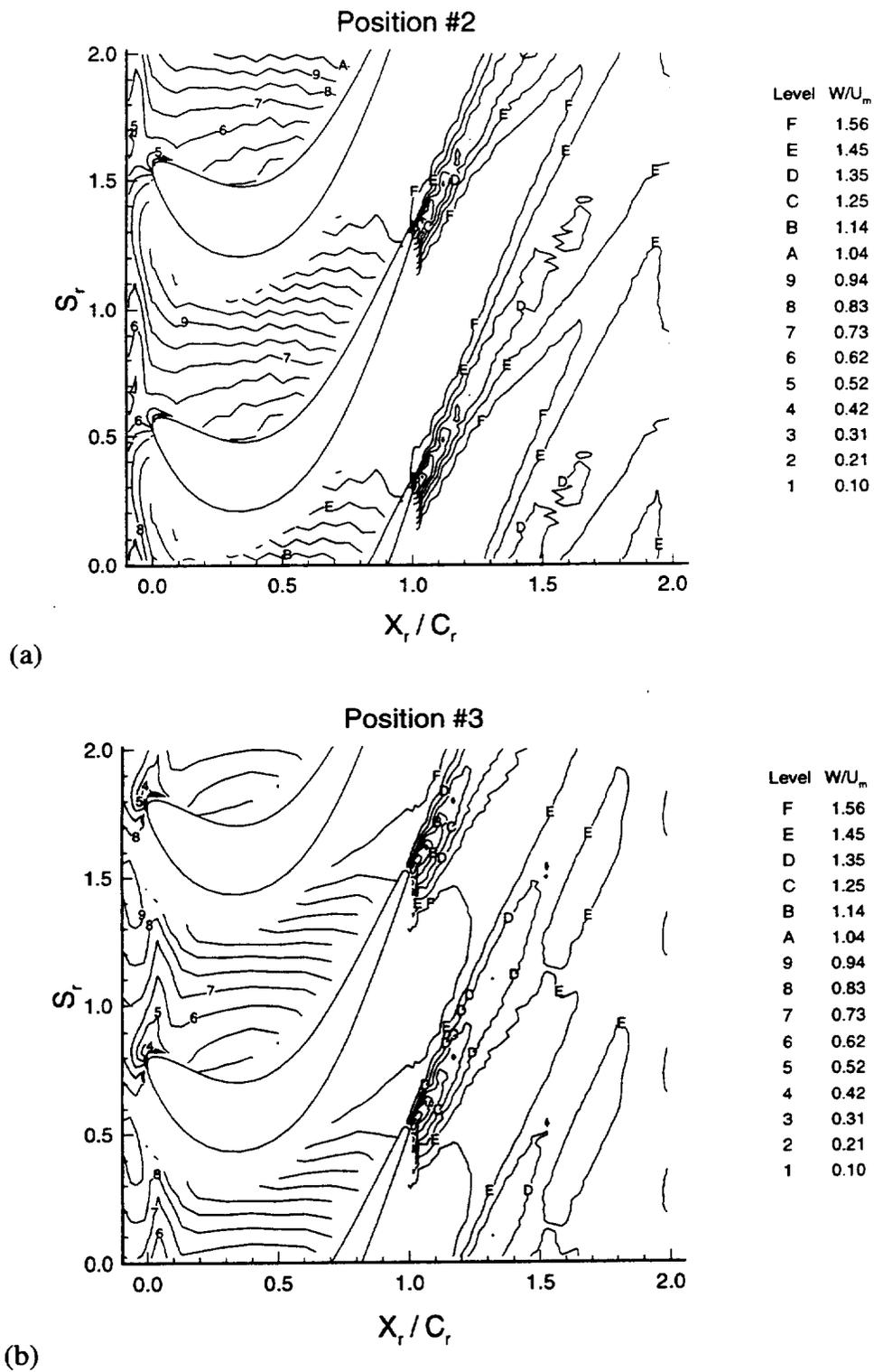
Figure 6.20. Relative Total Velocity $\left(\overline{W}/U_m\right)$ at the Six Nozzle/Rotor Locations
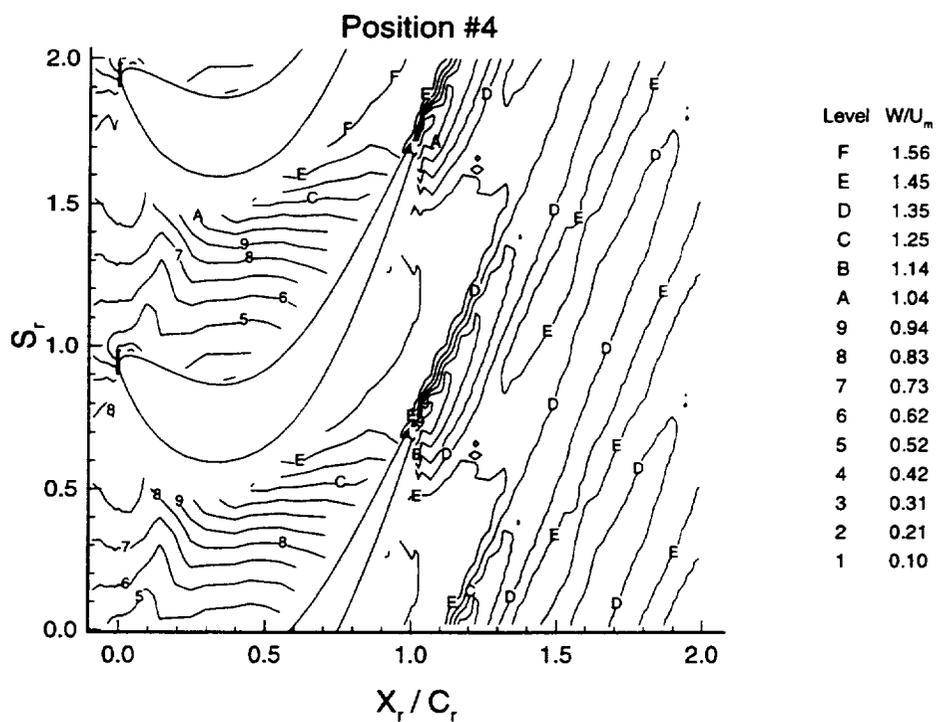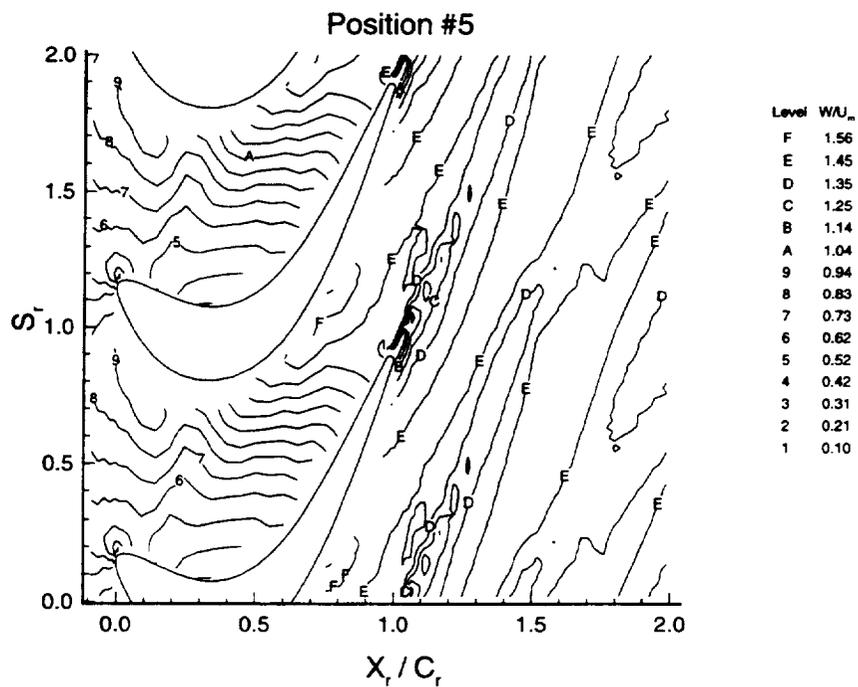
Position #4

(c)

Position #5

(d)

Figure 6.20 (Cont.). Relative Total Velocity $\left(\overline{W}/U_m\right)$ at the Six Nozzle/Rotor Positions

Position #6

Level	W/U_m
F	1.56
E	1.45
D	1.35
C	1.25
B	1.14
A	1.04
9	0.94
8	0.83
7	0.73
6	0.62
5	0.52
4	0.42
3	0.31
2	0.21
1	0.10

(e)

Position #1

Level	W/U_m
F	1.55
E	1.45
D	1.35
C	1.24
B	1.14
A	1.04
9	0.93
8	0.83
7	0.73
6	0.62
5	0.52
4	0.41
3	0.31
2	0.21
1	0.10

(f)
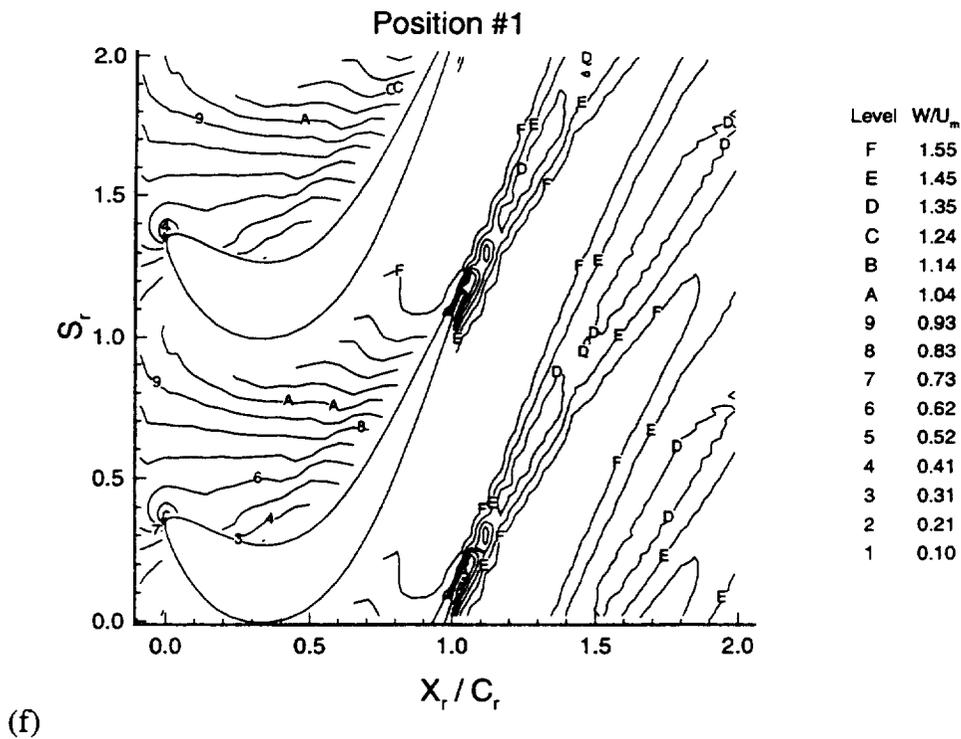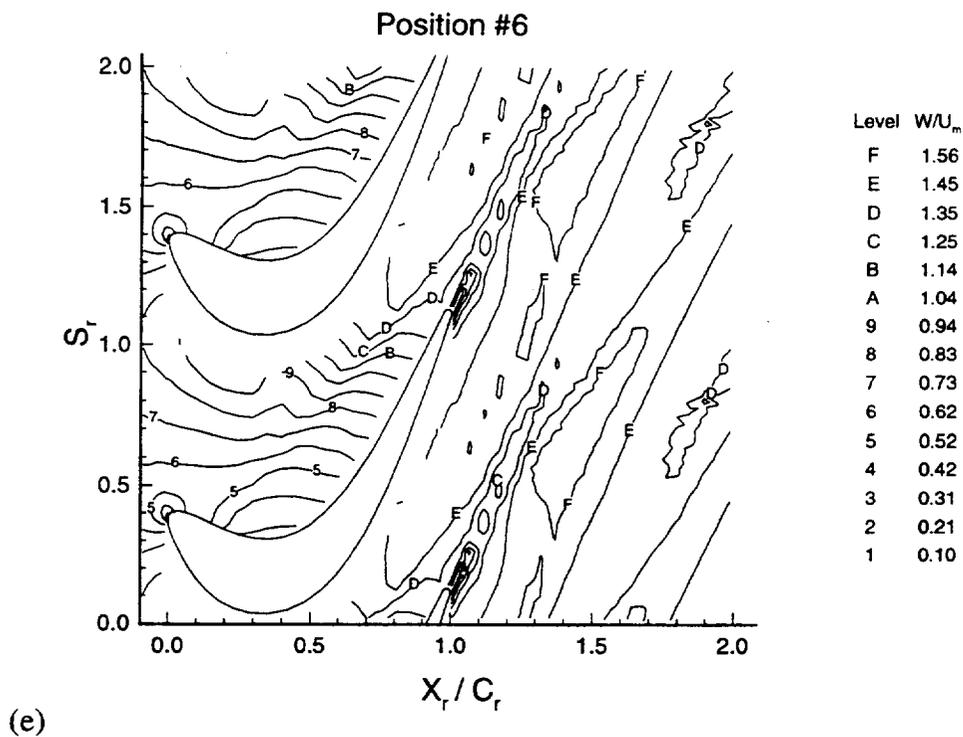
Figure 6.20 (Cont.). Relative Total Velocity $\left(\overline{W}/U_m\right)$ at the Six Nozzle/Rotor Positions

Blade-to-blade profiles of absolute total velocity for nozzle/rotor positions 4 and 1 are presented in Figures 6.21a and 6.21b at five different axial locations in the rotor passage. The profiles are plotted over two rotor blade pitches. These axial positions represent the location of the nozzle wake in the rotor passage. The nozzle wake is just downstream of the rotor leading edge at nozzle/rotor position 4 (see Figure 6.18), while it spans the rotor passage from $X_r/C_r = 0.2$ to 0.8 at position 1. The velocity defect and wake width varies over the rotor pitch at each location. Both the wake width and the velocity defect grow larger as one moves from the rotor pressure to the suction side, which results from the nozzle wake acting like a negative jet and drawing the low momentum fluid from the rotor pressure side boundary layer to the suction side. The addition of this low momentum boundary layer fluid to the nozzle wake cause its defect and width to increase.

6.3.3 Relative Flow Angle

The relative flow angle is presented in Figures 6.22a through 6.22f. Starting with nozzle/rotor position 2, an overturning of the flow angle is associated with the regions that correspond to the nozzle wake as identified by the relative total unsteadiness and velocity. Flow overturning in the rotor is identified by a lower relative flow angle (or higher negative angle), since a lower angle indicate more turning of the flow in the rotor. This overturning in the nozzle wake results from the slip velocity toward the rotor suction surface shown in Figure 6.2. This causes the nozzle wake to act like a negative jet drawing fluid from the rotor pressure side to the suction side.

Figure 6.23 presents the relative flow angle in the nozzle wake upstream of
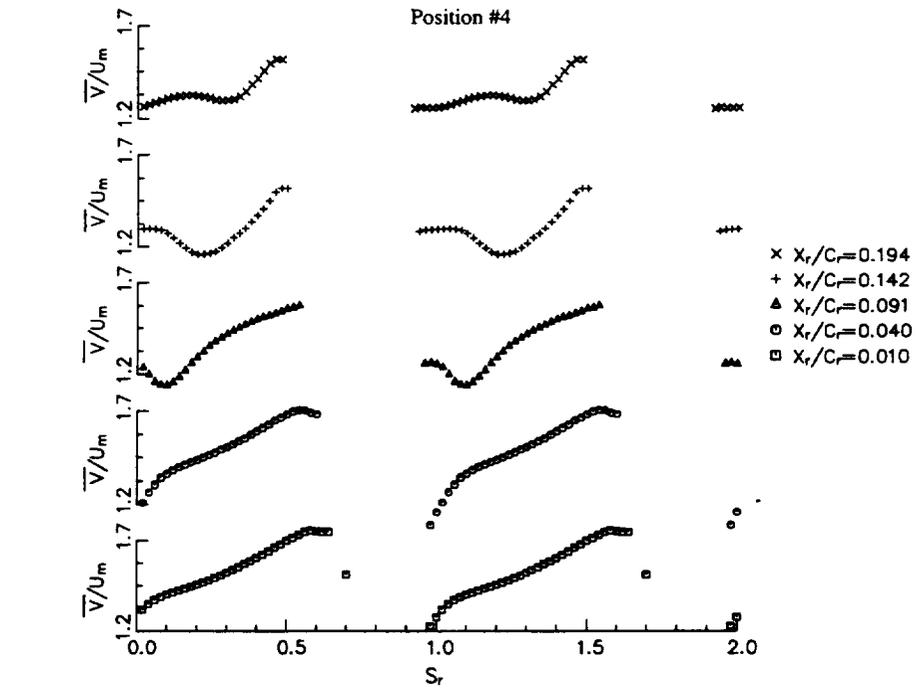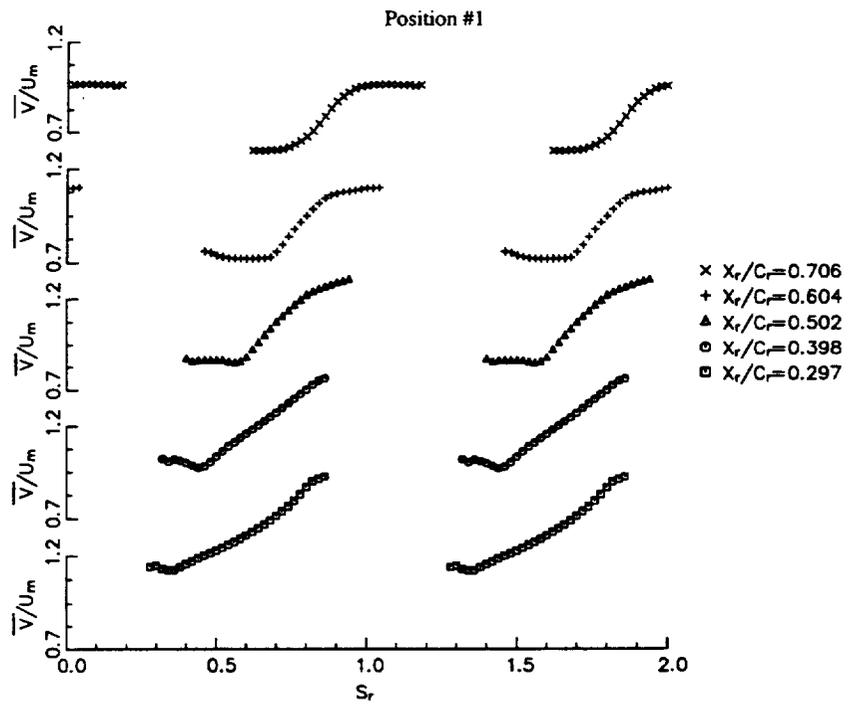
Figure 6.21. Blade to Blade Profiles of Absolute Total Velocity $\left(\overline{V}/U_m\right)$

(a)

(b)
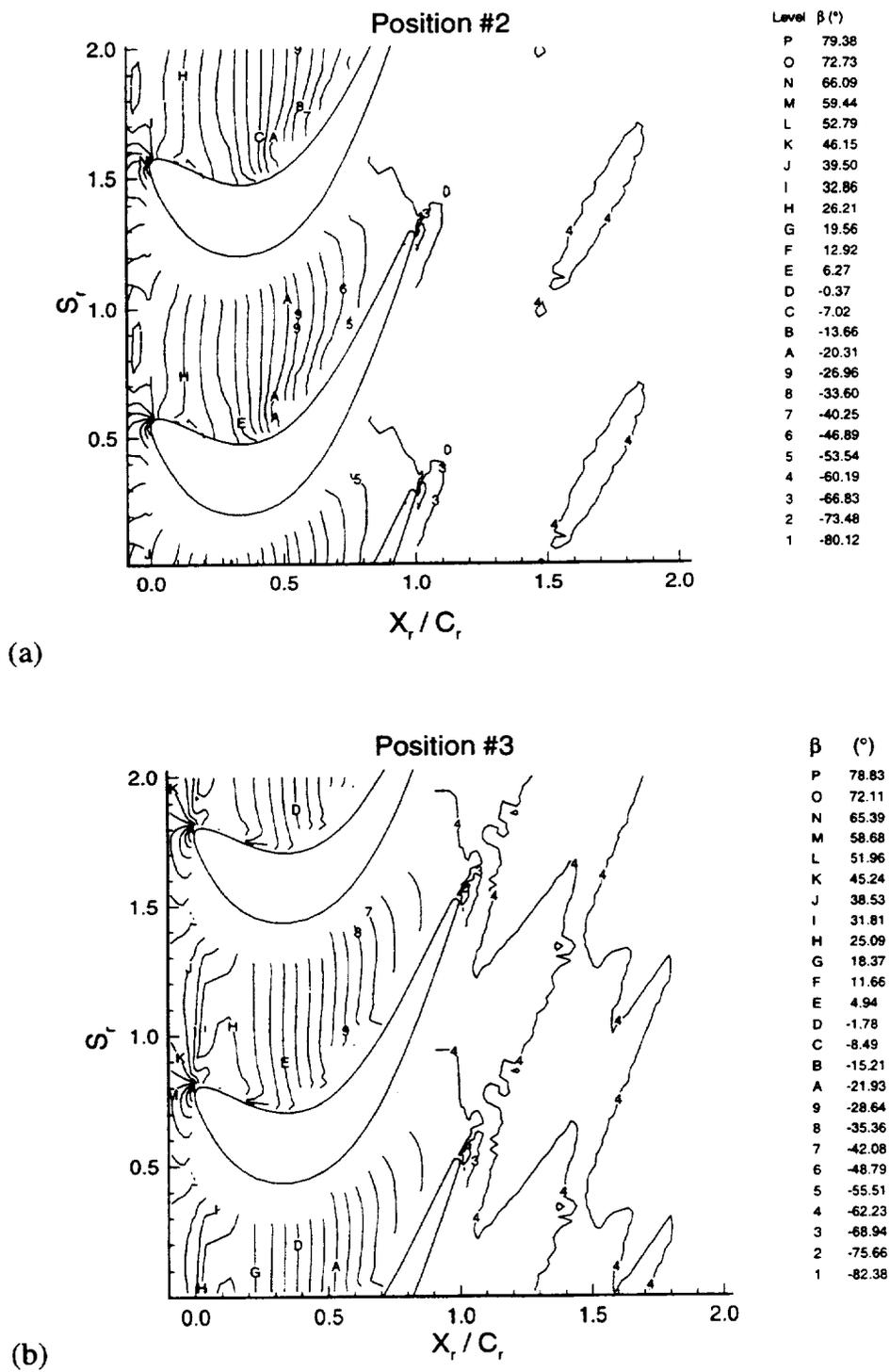
Figure 6.22. Relative Flow Angle ($\bar{\beta}$) at the Six Nozzle/Rotor Positions

Position #4

β	(°)
P	65.22
O	59.52
N	53.81
M	48.11
L	42.41
K	36.71
J	31.00
I	25.30
H	19.60
G	13.90
F	8.19
E	2.49
D	-3.21
C	-8.91
B	-14.62
A	-20.32
9	-26.02
8	-31.72
7	-37.42
6	-43.13
5	-48.83
4	-54.53
3	-60.23
2	-65.94
1	-71.64

(c)

Position #5

β	(°)
P	66.39
O	60.71
N	55.03
M	49.35
L	43.66
K	37.98
J	32.30
I	26.62
H	20.94
G	15.25
F	9.57
E	3.89
D	-1.79
C	-7.48
B	-13.16
A	-18.84
9	-24.52
8	-30.21
7	-35.89
6	-41.57
5	-47.25
4	-52.94
3	-58.62
2	-64.30
1	-69.98

(d)

Figure 6.22 (Cont.). Relative Flow Angle ($\bar{\beta}$) at the Six Nozzle/Rotor Positions

Position #6

Level	β (°)
K	65.85
J	58.36
I	50.86
H	43.37
G	35.88
F	28.38
E	20.89
D	13.39
C	5.90
B	-1.59
A	-9.09
9	-16.58
8	-24.08
7	-31.57
6	-39.06
5	-46.56
4	-54.05
3	-61.54
2	-69.04
1	-76.53

S_r vs X_r / C_r

(e)

Position #1

β	(°)
P	73.28
O	66.88
N	60.49
M	54.10
L	47.70
K	41.31
J	34.91
I	28.52
H	22.12
G	15.73
F	9.33
E	2.94
D	-3.46
C	-9.85
B	-16.25
A	-22.64
9	-29.03
8	-35.43
7	-41.82
6	-48.22
5	-54.61
4	-61.01
3	-67.40
2	-73.80
1	-80.19

S_r vs X_r / C_r

(f)

Figure 6.22 (Cont.). Relative Flow Angle $(\overline{\beta})$ at the Six Nozzle/Rotor Positions
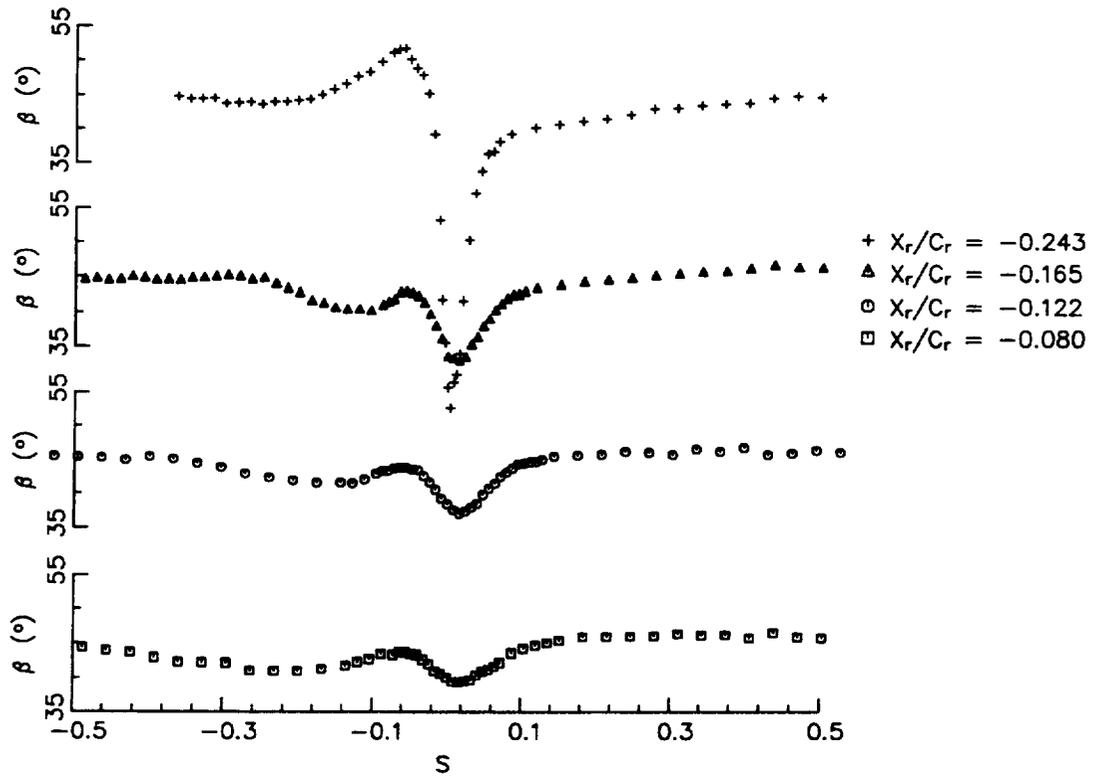
Figure 6.23. Relative Flow Angle (β) Upstream of Rotor (Five Hole Probe
Measurements)

the rotor, that was measured by the five hole probe. Close to the nozzle trailing edge, there is a large change in angle across the wake, which decreases as the wake travels downstream. At the closest measuring location to the rotor ($X_r/C_r = -0.08$), overturning in the nozzle wake still exists, with the flow being overturned by 4 degrees at this location. When the nozzle wake is at the rotor leading edge, the overturning in the nozzle wake causes the flow to enter the rotor at a negative incidence. Both Hodson and Dominy (1987) and Tremblay, Sjolander and Moustapha (1990) observed that at negative incidence a large separation bubble occurs on the pressure side of the blade. This separation bubble causes the losses to increase in the blade passage thus causing a decrease in performance. Thus the nozzle wake passing through the rotor blade is detrimental to the turbine performance.

The blade to blade profiles of relative flow angles in the nozzle wake at positions 4 and 1 are presented in Figures 6.24a and 6.24b, respectively. The overturning in the nozzle wake, which results from the nozzle wake acting as a negative jet, is seen clearly. The overturning in the nozzle wake at position 4 is greater than the overturning in the nozzle wake at position 1. This results from the decrease in the slip velocity (the negative jet) in the nozzle wake as the nozzle wake travels through the rotor passage.

6.3.4 Unresolved Velocity Cross Correlations

The axial-tangential cross component of the unresolved velocity correlation for each nozzle/rotor position is shown in Figures 6.25a through 6.25f. The unresolved velocity cross correlation in the nozzle wake is higher than in the surrounding fluid. These higher velocity cross correlation regions are located in the same regions as where the nozzle wake was identified using the relative total

Position #4

× X_r/C_r=0.194
+ X_r/C_r=0.142
▲ X_r/C_r=0.091
⊙ X_r/C_r=0.040
⊡ X_r/C_r=0.010

(a)

Position #1

× X_r/C_r=0.706
+ X_r/C_r=0.604
▲ X_r/C_r=0.502
⊙ X_r/C_r=0.398
⊡ X_r/C_r=0.297

(b)
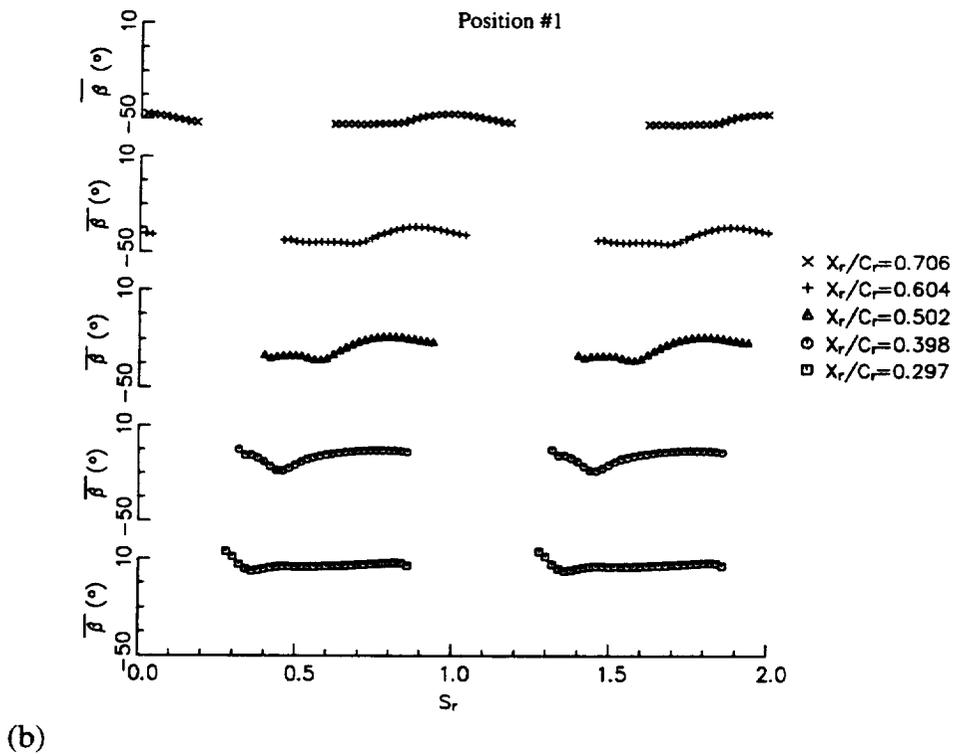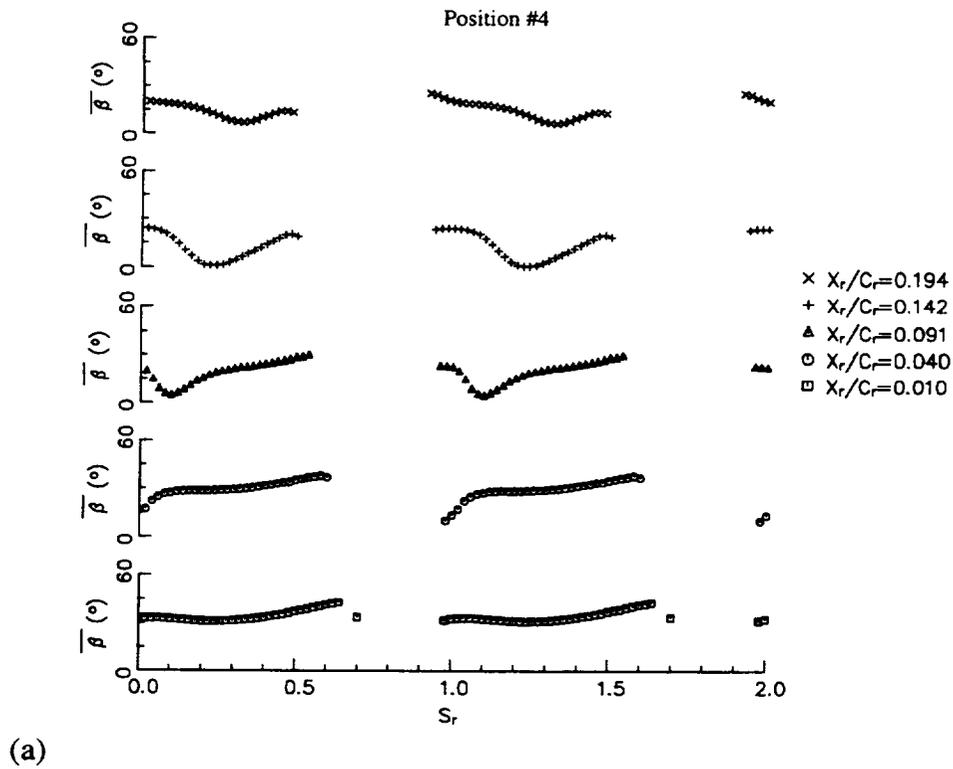
Figure 6.24. Blade to Blade Profiles of Relative Flow Angle $(\overline{\beta})$

Position #2
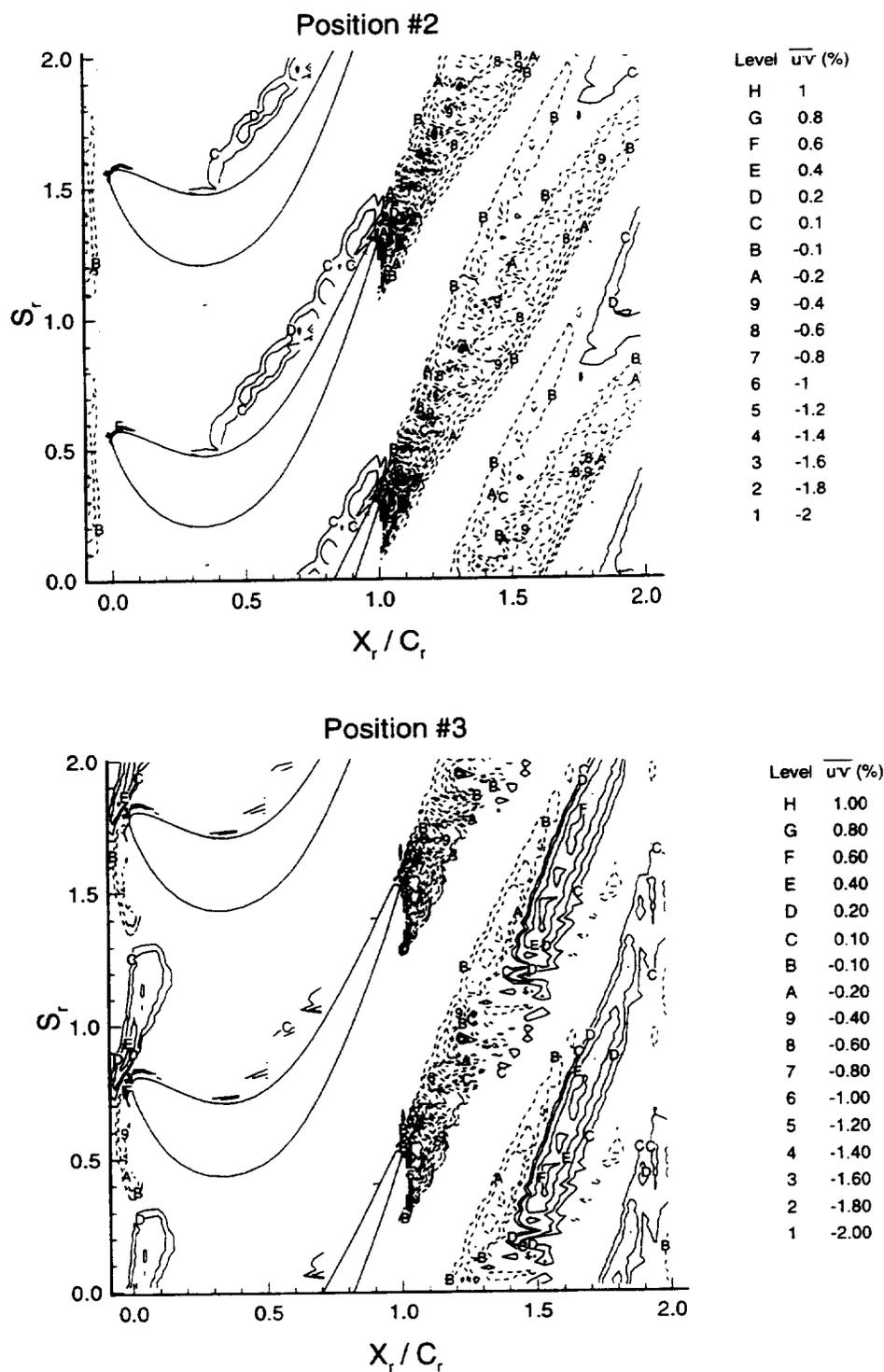
Position #3

(b)

Figure 6.25. Unresolved Velocity Correlation $\left(\overline{u'v'}\right)$ at the Six Nozzle/Rotor Positions
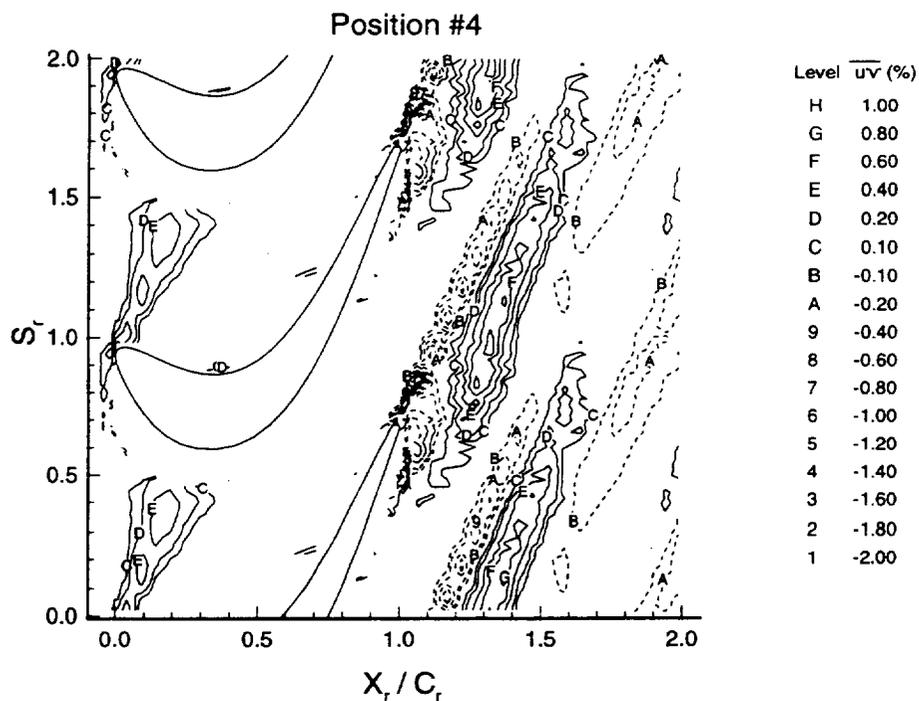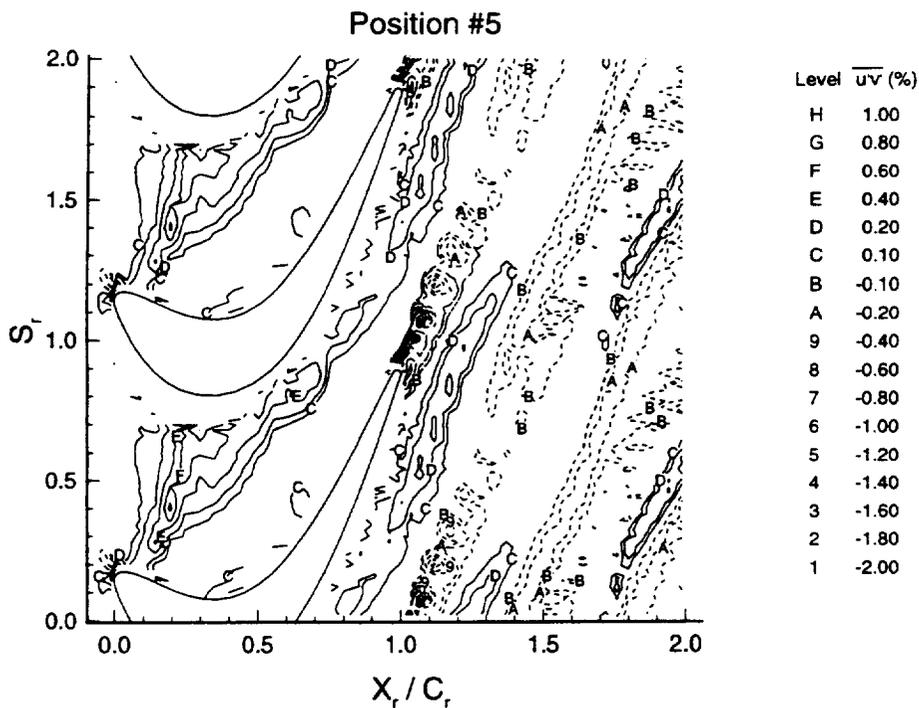
Position #4

(c)

Level	$\overline{u'v'}$ (%)
H	1.00
G	0.80
F	0.60
E	0.40
D	0.20
C	0.10
B	-0.10
A	-0.20
9	-0.40
8	-0.60
7	-0.80
6	-1.00
5	-1.20
4	-1.40
3	-1.60
2	-1.80
1	-2.00

Position #5

(d)

Level	$\overline{u'v'}$ (%)
H	1.00
G	0.80
F	0.60
E	0.40
D	0.20
C	0.10
B	-0.10
A	-0.20
9	-0.40
8	-0.60
7	-0.80
6	-1.00
5	-1.20
4	-1.40
3	-1.60
2	-1.80
1	-2.00

Figure 6.25 (Cont.). Unresolved Velocity Correlation $\left(\overline{u'v'}\right)$ at the Six Nozzle/Rotor Positions

Position #6

Level	$\overline{u'v'}$ (%)
H	1.00
G	0.80
F	0.60
E	0.40
D	0.20
C	0.10
B	-0.10
A	-0.20
9	-0.40
8	-0.60
7	-0.80
6	-1.00
5	-1.20
4	-1.40
3	-1.60
2	-1.80
1	-2.00

(e)

Position #1

Level	$\overline{u'v'}$ (%)
H	1.0
G	0.8
F	0.6
E	0.4
D	0.3
C	0.1
B	-0.1
A	-0.3
9	-0.5
8	-0.7
7	-0.9
6	-1.1
5	-1.3
4	-1.4
3	-1.6
2	-1.8
1	-2.0

(f)
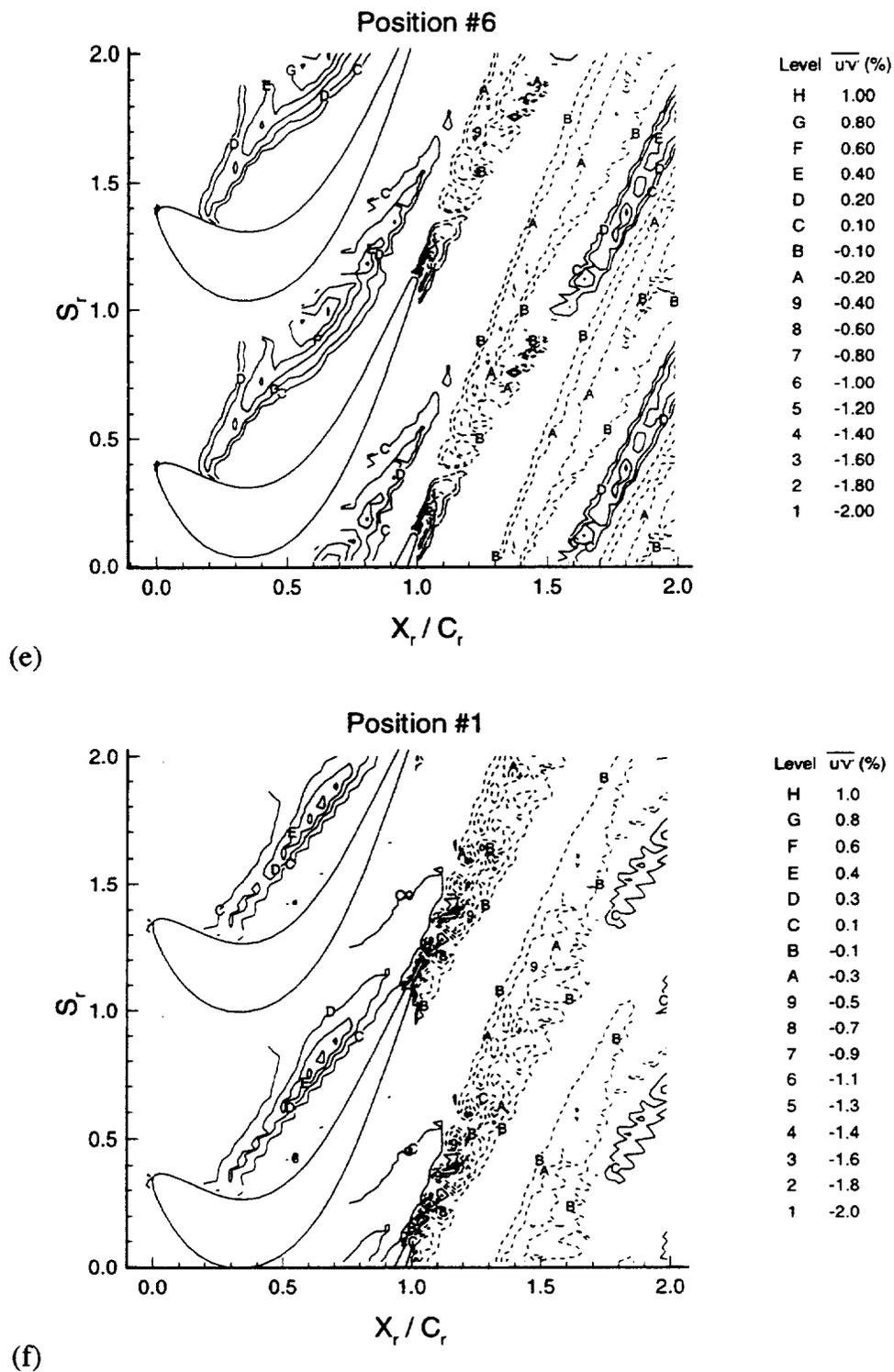
Figure 6.25 (Cont.). Unresolved Velocity Correlation $\left(\overline{u'v'}\right)$ at the Six Nozzle/Rotor Positions

unsteadiness, relative total velocity and relative flow angle, thus providing added confidence for the existence the nozzle wake. The unresolved velocity cross correlation starts out being negative in the nozzle wake at position 2. (The nozzle wake is located upstream of the rotor blade at this position.) At position 3, the velocity cross correlation changes sign in the region of the nozzle wake near the pressure surface, with this region being positive while the region of the nozzle wake near the suction surface is negative. Continuing on to the next locations, the turning and the distortion of the nozzle wake can be seen. These figures show that as the nozzle wake travels downstream through the rotor passage it thins out near the rotor pressure surface and thickens near the rotor suction surface. This is due to the nozzle wake acting like a negative jet as discussed in the previous paragraph. Examining positions 1 and then 2, the nozzle wake is seen to have elongated and thinned out considerably. This is a result of two reasons. The first is an inviscid phenomena which was discussed by Smith (1966), and is due to the fact that vorticity must be conserved in the nozzle wake, thus as the wake length grows, the wake width must become smaller. The second is a result of the large variation in convective velocity across the rotor pitch. Since the velocity is faster along the rotor suction surface than near the pressure surface, the region of the wake near the suction surface moves faster than the region near the pressure surface. Thus the wake stretches, becoming narrower and longer.

Downstream of the rotor trailing edge, one can see the flow field is not the same at every nozzle/rotor position, but changes from one position to another, similar to the total unsteadiness and relative velocity plots. For the region just downstream of the trailing edge at the maximum interaction (position 2), the unresolved velocity cross correlation is high in the near rotor wake (at $X_r/C_r = 1.04$ it is a maximum of -3.0) and is low (zero) in the free stream region outside of the rotor wake. This low unresolved velocity cross correlation region takes up over

60% of the rotor pitch at $X_r/C_r = 1.12$. The minimum interaction position (position 5) has a maximum unresolved velocity cross correlation that is lower in the rotor wake (maximum unresolved velocity cross correlation of -2.0 at $X_r/C_r = 1.04$) and a higher unresolved velocity cross correlation in the region between the rotor wake (maximum unresolved velocity cross correlation of 0.40 at $X_r/C_r = 1.12$) as compared to the maximum interaction position. The low unresolved velocity cross correlation ($\overline{u'v'} = 0$) occupies only 25% of the blade pitch at $X_r/C_r = 1.1$. This is because at the maximum interaction position, the nozzle wake is inside of the rotor wake, thus causing higher unresolved velocity cross correlations in the wake and outside of the rotor wake the unresolved velocity cross correlations are low, while at the minimum interaction position the nozzle wake is located in between the rotor wake, thus causing higher unresolved velocity cross correlations in the region between the rotor wake.

Figures 6.26a and 6.26b show the blade to blade profiles of unresolved velocity cross correlation in the nozzle wake at positions 4 and 1, respectively. The increase in unresolved velocity cross correlation in the nozzle wake is easily identifiable. Outside the wake the cross correlation is zero, while inside the wake it has a value of 0.5% which is constant in the nozzle wake as it migrates from the rotor leading edge to the trailing edge. As with the total unsteadiness, this shows that the unresolved velocity cross correlation does not decay any significant amount in the rotor passage. This is discussed in more detail in Chapter 7.

6.3.5 Axial and Tangential Components of Unresolved Velocity Correlations

The axial and tangential components of the unresolved velocity correlations are given in Figures 6.27a through 6.27f and 6.28a through 6.28f, respectively. The axial and tangential components of the unresolved velocity correlations are defined
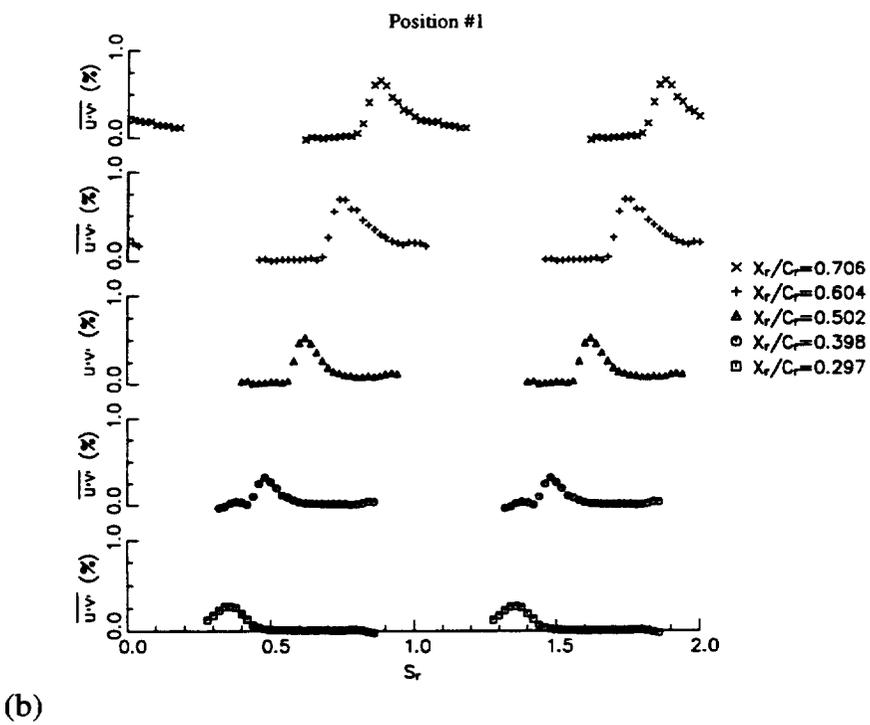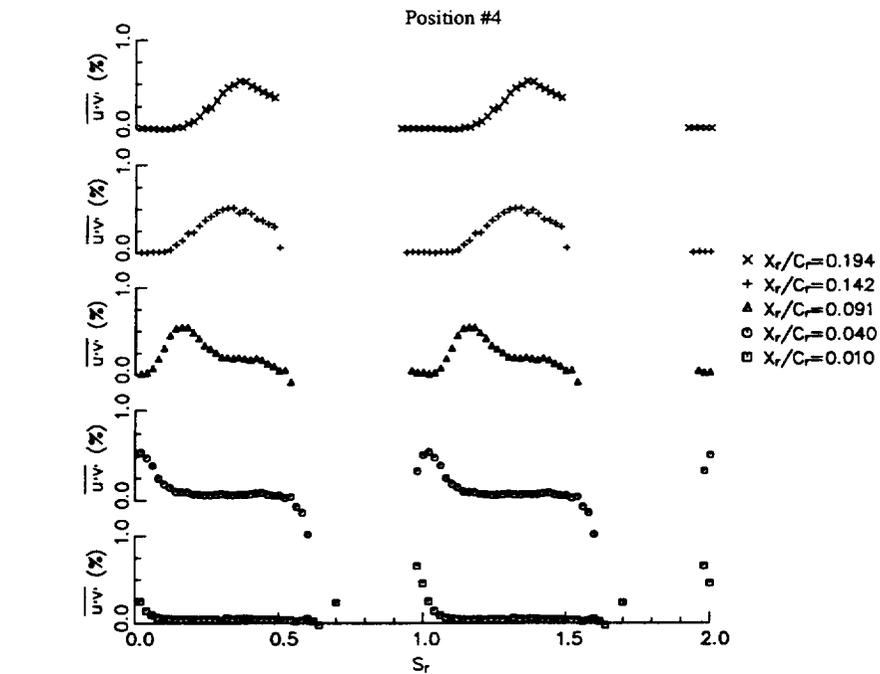
Figure 6.26. Blade to Blade Profiles of Unresolved Velocity Correlation $\left(\overline{u'v'}\right)$

Position #2
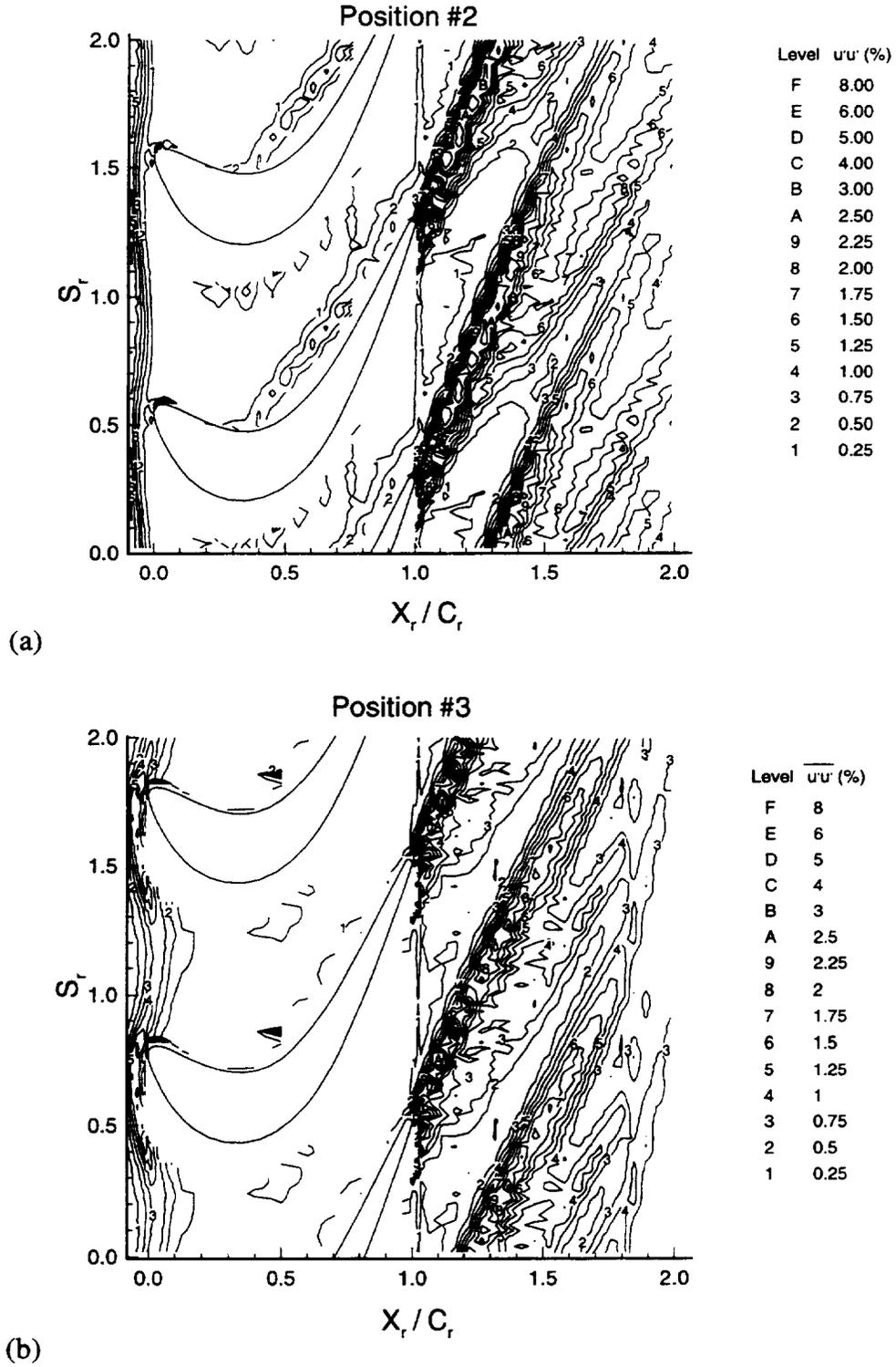
Position #3

Figure 6.27. Unresolved Velocity Correlation $\left(\overline{u'u'}\right)$ at the Six Nozzle/Rotor Positions
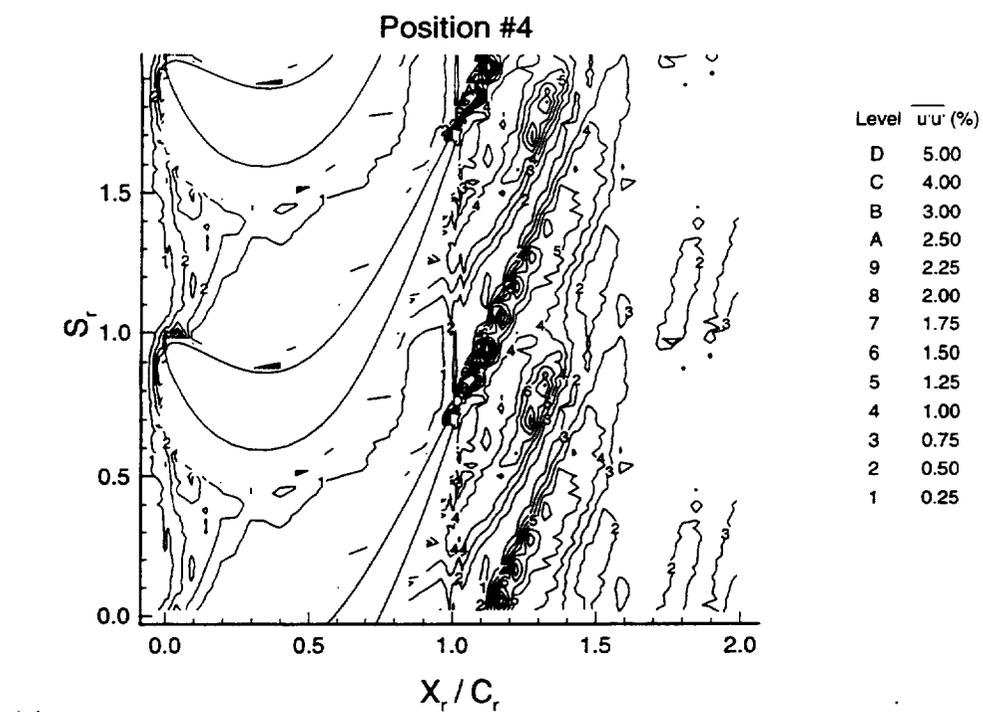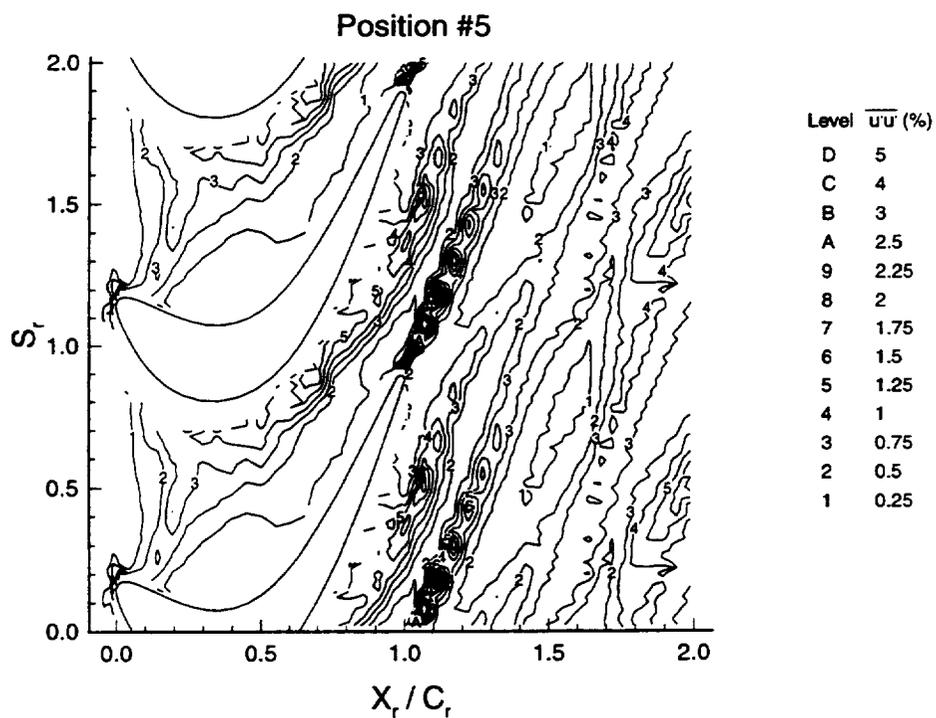
(a)

(b)

Position #4

Level	$\overline{u'u'}$ (%)
D	5.00
C	4.00
B	3.00
A	2.50
9	2.25
8	2.00
7	1.75
6	1.50
5	1.25
4	1.00
3	0.75
2	0.50
1	0.25

(c)

Position #5

Level	$\overline{u'u'}$ (%)
D	5
C	4
B	3
A	2.5
9	2.25
8	2
7	1.75
6	1.5
5	1.25
4	1
3	0.75
2	0.5
1	0.25

(d)

Figure 6.27 (Cont.). Unresolved Velocity Correlation $\left(\overline{u'u'}\right)$ at the Six
Nozzle/Rotor Positions

Position #6

Level	$\overline{u'u'}$ (%)
D	5.00
C	4.00
B	3.00
A	2.50
9	2.25
8	2.00
7	1.75
6	1.50
5	1.25
4	1.00
3	0.75
2	0.50
1	0.25

(e)

Position #1

Level	$\overline{u'u'}$ (%)
G	10
F	8
E	6
D	5
C	4
B	3
A	2.5
9	2.25
8	2
7	1.75
6	1.5
5	1.25
4	1
3	0.75
2	0.5
1	0.25

(f)

Figure 6.27 (Cont.). Unresolved Velocity Correlation $\left(\overline{u'u'}\right)$ at the Six Nozzle/Rotor Positions

Position #2

Level	$\overline{v'v'}$ (%)
E	6.00
D	5.00
C	4.00
B	3.00
A	2.50
9	2.25
8	2.00
7	1.75
6	1.50
5	1.25
4	1.00
3	0.75
2	0.50
1	0.25

(a)

Position #3

Level	$\overline{v'v'}$ (%)
F	7
E	6
D	5
C	4
B	3
A	2.5
9	2.25
8	2
7	1.75
6	1.5
5	1.25
4	1
3	0.75
2	0.5
1	0.25

(b)
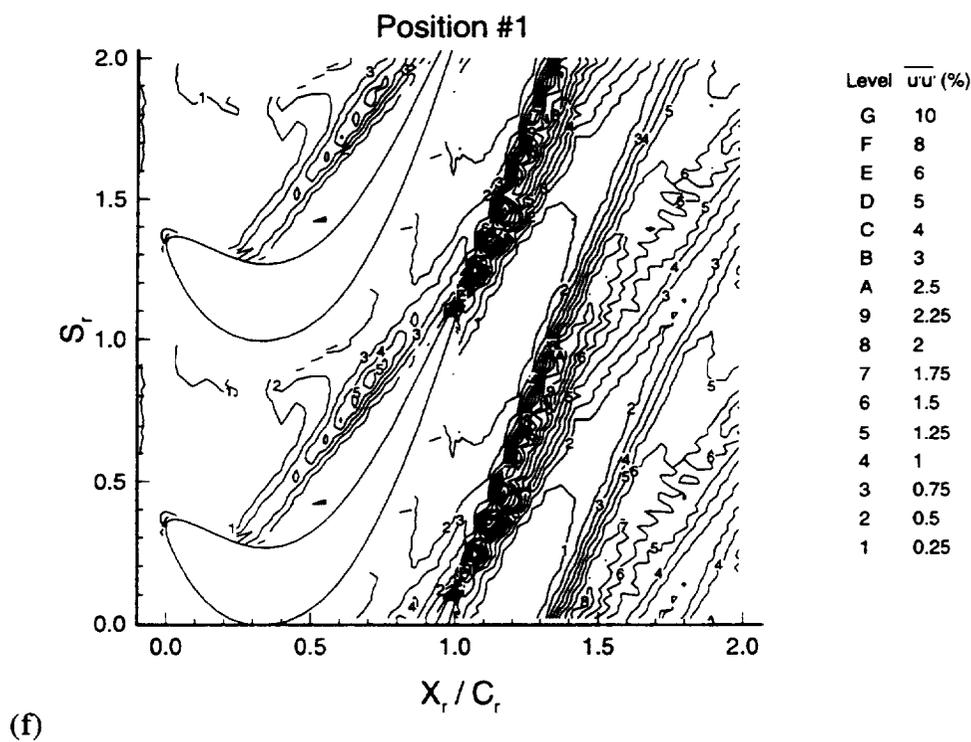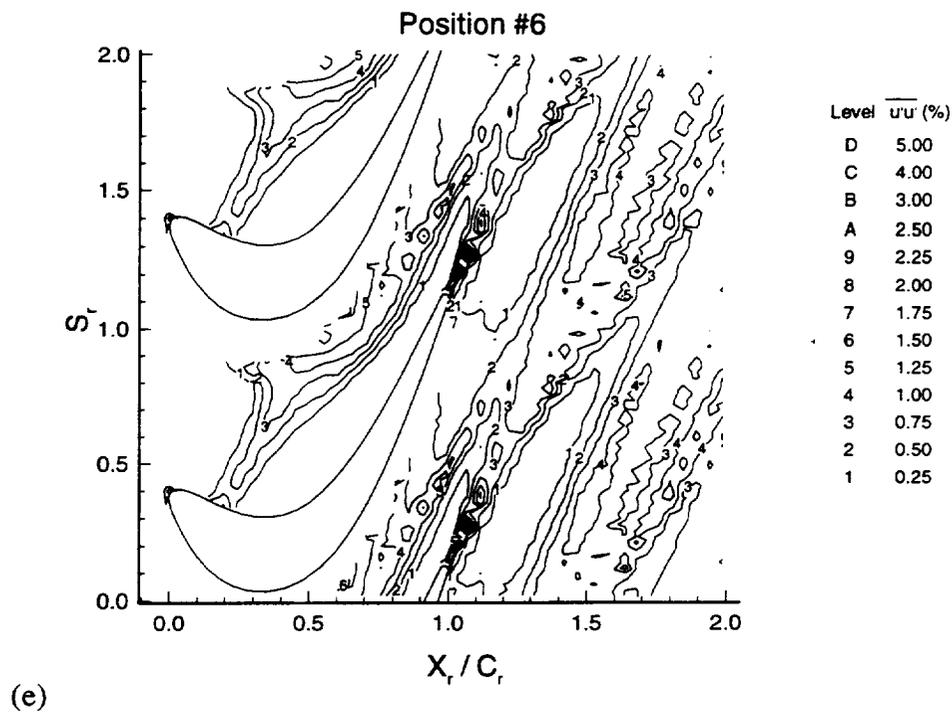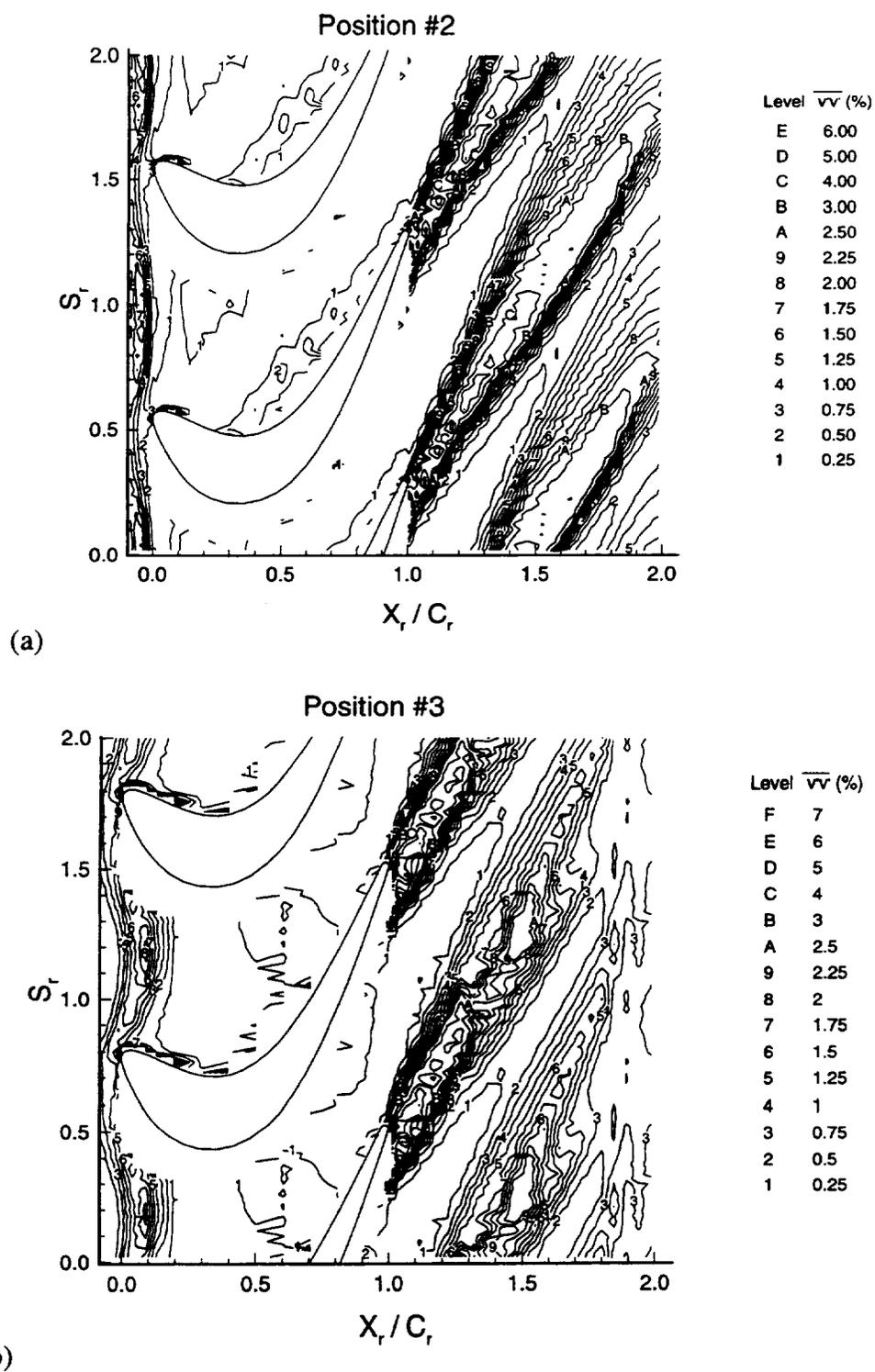
Figure 6.28. Unresolved Velocity Correlation $\left(\overline{v'v'}\right)$ at the Six Nozzle/Rotor Positions
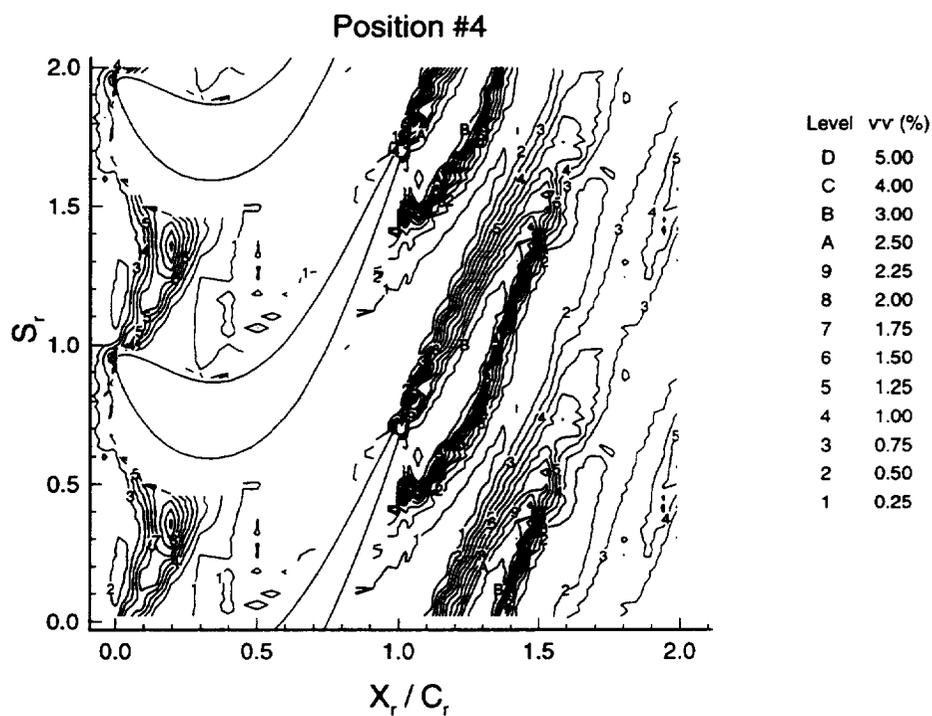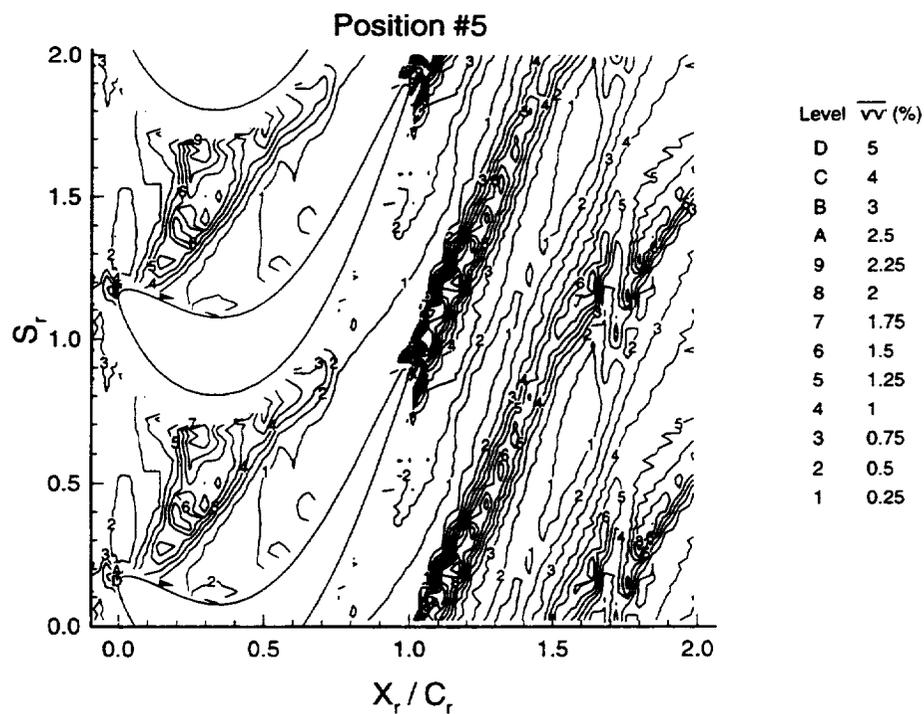
Position #4

Level	vv (%)
D	5.00
C	4.00
B	3.00
A	2.50
9	2.25
8	2.00
7	1.75
6	1.50
5	1.25
4	1.00
3	0.75
2	0.50
1	0.25

(c)

Position #5

Level	$\overline{vv}$ (%)
D	5
C	4
B	3
A	2.5
9	2.25
8	2
7	1.75
6	1.5
5	1.25
4	1
3	0.75
2	0.5
1	0.25

(d)

Figure 6.28 (Cont.). Unresolved Velocity Correlation $\left(\overline{v'v'}\right)$ at the Six
Nozzle/Rotor Positions

Position #6

Level	$\overline{v'v'}$ (%)
D	5.00
C	4.00
B	3.00
A	2.50
9	2.25
8	2.00
7	1.75
6	1.50
5	1.25
4	1.00
3	0.75
2	0.50
1	0.25

(e)

Position #1

Level	$v'v'$ (%)
D	5
C	4
B	3
A	2.5
9	2.25
8	2
7	1.75
6	1.5
5	1.25
4	1
3	0.75
2	0.5
1	0.25
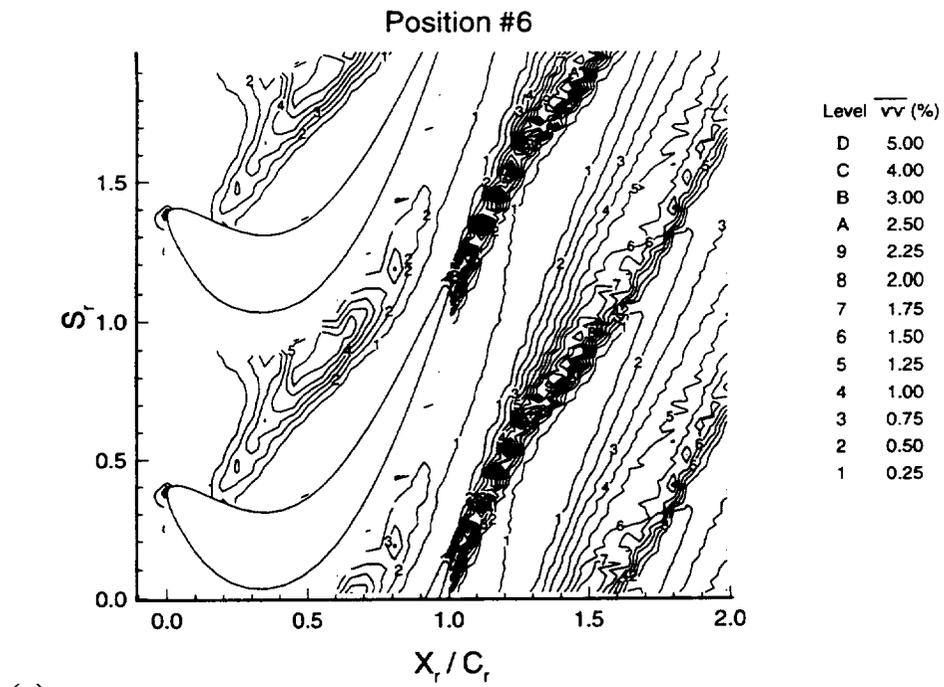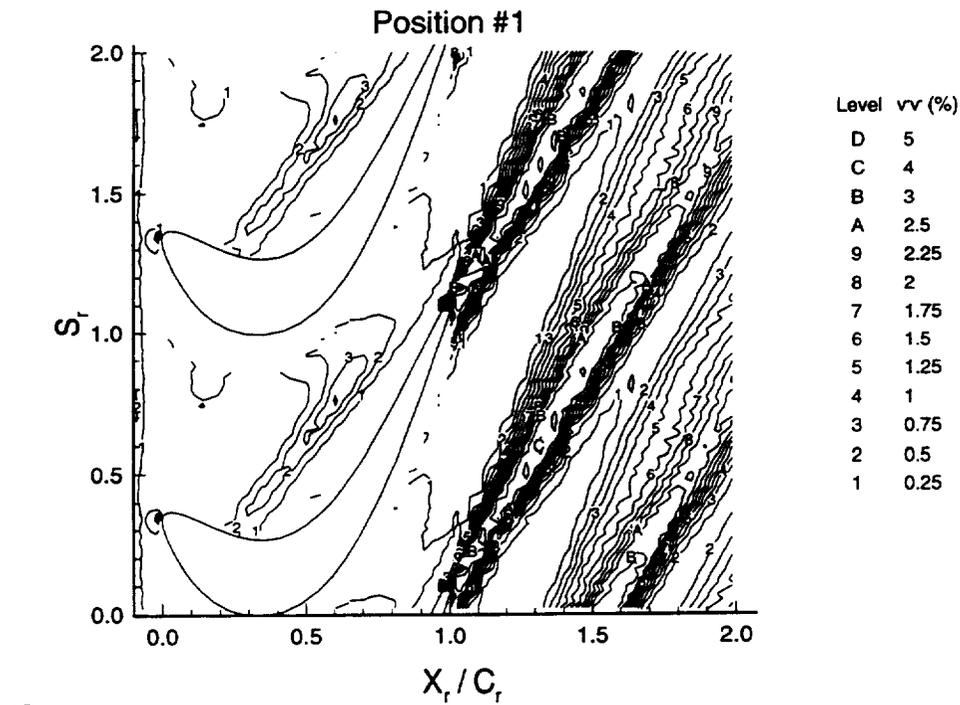
(f)

Figure 6.28 (Cont.). Unresolved Velocity Correlation $\left(\overline{v'v'}\right)$ at the Six
Nozzle/Rotor Positions

as follows:

$$\overline{V_p' V_q'} = \frac{\overline{(V_i - \overline{V})_p (V_i - \overline{V})_q}}{U_m^2} \times 100\% \qquad (6.16)$$

where the subscripts p and q correspond to the axial and /or tangential velocity components. The nozzle wake and its propagation through the rotor passage can be clearly identified by the higher unresolved velocity that occurs in the nozzle wake as compared to the surrounding fluid. Starting from position 2, where the nozzle wake is upstream of the rotor, and continuing onto the successive positions, it can beseen that where the nozzle wake interacts with the rotor leading edge an increase in the magnitude of the velocity fluctuations occur for both the axial and tangential components of unresolved velocity correlations.

Another interesting feature is the increase in the tangential component of the unresolved velocity correlation in the nozzle wake at rotor midpitch (shown in Figure 6.28) . At position 2 (where the nozzle wake is located upstream of the rotor), the maximum tangential component of the unresolved velocity correlation is 1.75. Continuing onto positions 3 and 4 where the nozzle wake moves into the rotor passage, the maximum tangential component of the unresolved velocity is 2.0 and 2.5, respectively. Binder et al. (1987) and Hathaway (1986) also notice this feature. While Hathaway does not provide an explanation for this feature in his compressor, Binder attributes this increase in random velocity fluctuations within the chopped nozzle wake segments at the turbine rotor leading edge midpitch to the cutting of the secondary flow vortices by the rotor resulting in the vortices breaking down. While this is a plausible explanation for the increase in random velocity fluctuations in Binder's turbine, it is not a correct explanation for this phenomena in the present turbine. This is because the nozzle secondary flow vortices were

located at midspan in Binder's axial flow turbine, which was his measurement location, while for the present turbine there are no nozzle secondary flow vortices at midspan (the measurement location). The increase in fluctuating velocity can be explained by looking at the nozzle wake as a negative jet drawing fluid from the rotor pressure to the rotor suction surface as discussed earlier. This movement of low momentum fluid toward the suction surface causes the high momentum fluid in the free stream to move in an opposite direction to replace the migrated wake fluid. This interaction induces two counter-rotating vortices, one on either side of the nozzle wake. The generation of these vortices causes an increase in the velocity fluctuations. Moving on from position 4 to position 5 the maximum tangential component of unresolved velocity correlation in the nozzle wake decreases and this decrease continues as the nozzle wake travels downstream in the rotor until position 2 where the maximum tangential component of the unresolved velocity in the nozzle wake is 0.50%.

The flow field downstream of the rotor trailing edge shows different features at each nozzle/rotor location due to the nozzle wake interaction with the rotor wakes. As with the previous properties, the maximum interaction position occurs at nozzle/rotor position 2 (for the near wake region). The unresolved unsteadiness is low between the rotor wakes and high in the rotor wakes since the nozzle wake is located inside of the rotor wake at this position. The minimum interaction for the near wake region occurs at nozzle/rotor position 5. Compared to the maximum interaction position the unresolved unsteadiness is lower in the rotor wake and higher in between the rotor wakes, since the nozzle wake is located in the free stream region between the rotor wakes.

6.3.6 Periodic Velocity Correlations

The periodic velocity correlations include the variation of velocity across the passage caused by potential and viscous effects. This is substantial even in the absence of the nozzle wake. This quantity is useful in evaluating the average passage equations used in industry for prelimary design (see Suder et al., 1987). The effect of the nozzle wake on rotor relative mean flow is also captured in this correlation.

The axial and tangential components of the periodic velocity correlation are presented in Figures 6.29a through 6.29f and 6.30a through 6.30f, respectively. The periodic velocity correlations are about five times higher than the unresolved velocity correlations in the rotor. This is due to the large variation of the rotor flow field in the pitchwise direction which is a steady flow field phenomena in the relative frame and can also be seen in the cycle averaged periodic velocity correlation presented in Figures 6.15 and 6.16. One can also see that while the nozzle wake can be identified in the tangential component of periodic velocity correlation plots, it cannot in the axial component of periodic velocity correlation plots. The reason for this is that the axial velocity has a much larger pitchwise variation in the rotor blade passage than the tangential velocity, thus the nozzle wake is obscured in the plots. Comparing the tangential component of the periodic and unresolved velocity correlations in the nozzle wake, it is clear that their magnitudes are similar. This can be seen clearly at positions 4, 5 and 1. Inside the nozzle wake at position 4, the maximum tangential component of unresolved velocity correlation ($\overline{v'v'}$) is 2.5 while the maximum tangential component of periodic velocity correlation ($\overline{\tilde{v}\tilde{v}}$) is 3.0. Inside the nozzle wake at position 5, $\left(\overline{v'v'}\right)_{max} = 2.25$ and $\left(\overline{\tilde{v}\tilde{v}}\right)_{max} = 3.0$. And at position 1, $\left(\overline{v'v'}\right)_{max} = 1.0$ and $\left(\overline{\tilde{v}\tilde{v}}\right)_{max} = 1.0$ inside the nozzle wake. Thus both the tangential component of the periodic and
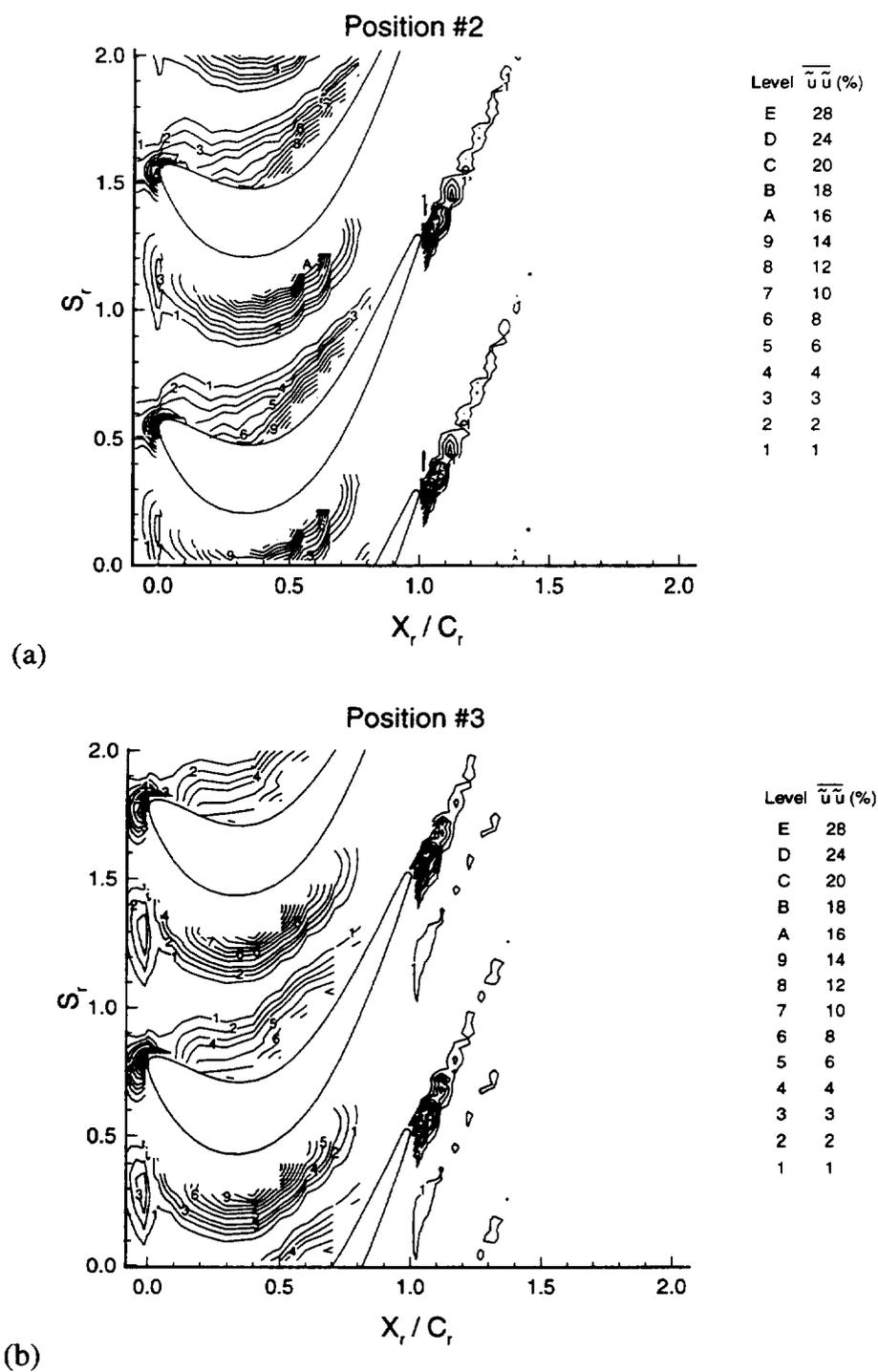
Figure 6.29. Periodic Velocity Correlation $\left(\overline{\tilde{u}\tilde{u}}\right)$ at the Six Nozzle/Rotor Positions
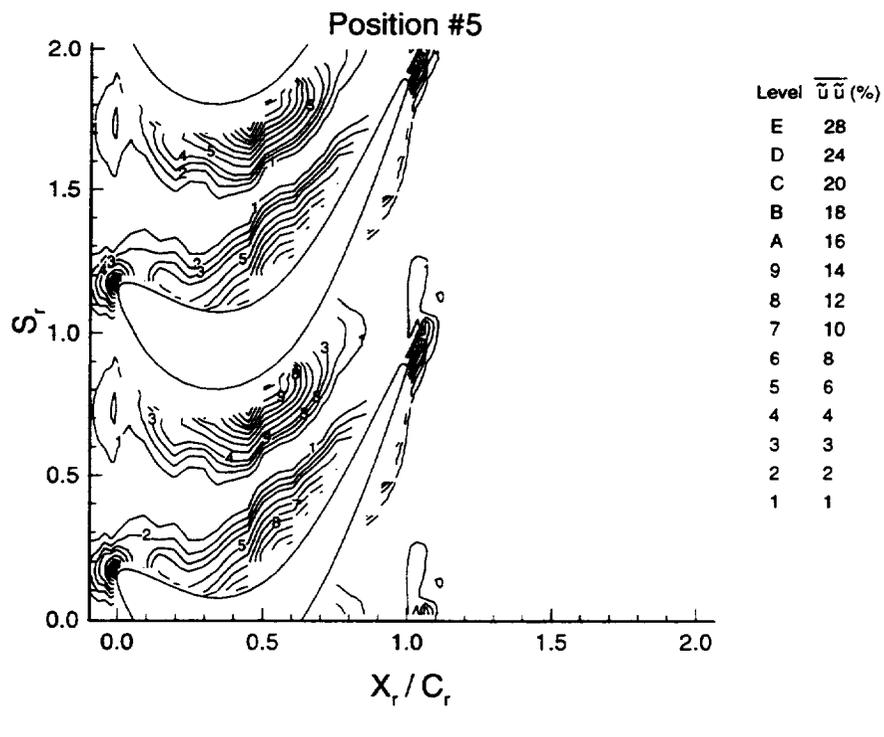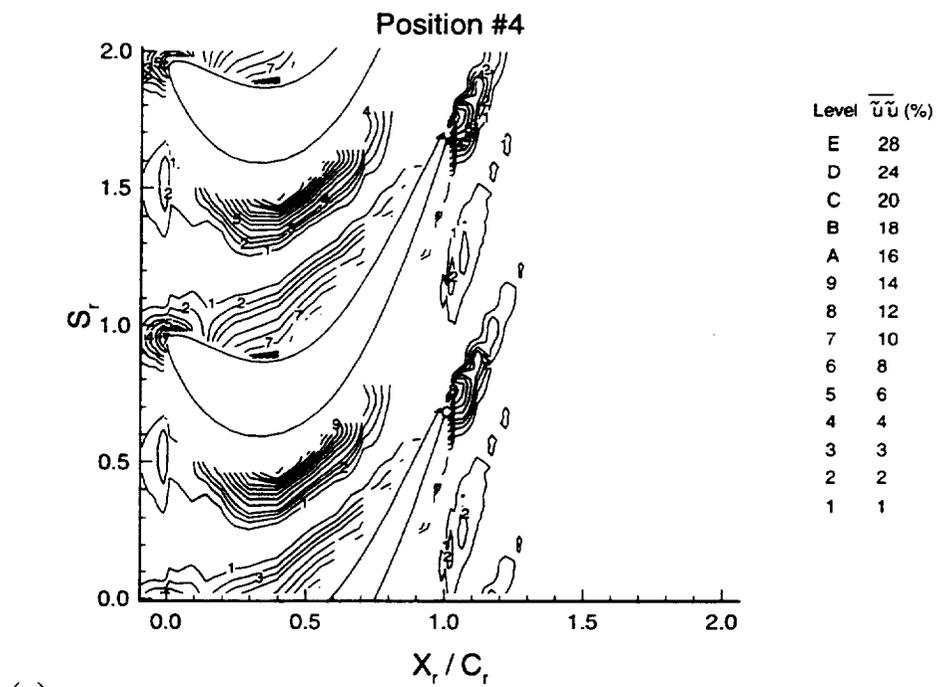
Position #4

Level	$\overline{\tilde{u}\tilde{u}}$ (%)
E	28
D	24
C	20
B	18
A	16
9	14
8	12
7	10
6	8
5	6
4	4
3	3
2	2
1	1

(c)

Position #5

Level	$\overline{\tilde{u}\tilde{u}}$ (%)
E	28
D	24
C	20
B	18
A	16
9	14
8	12
7	10
6	8
5	6
4	4
3	3
2	2
1	1

(d)

Figure 6.29 (Cont.). Periodic Velocity Correlation $\left(\overline{\tilde{u}\tilde{u}}\right)$ at the Six Nozzle/Rotor Positions

Position #6

Level	$\overline{\tilde{u}\tilde{u}}$ (%)
D	28
C	24
B	20
A	18
9	16
8	14
7	12
6	10
5	8
4	6
3	4
2	2
1	1

(e)

Position #1

Level	$\overline{\tilde{u}\tilde{u}}$ (%)
E	28
D	24
C	20
B	18
A	16
9	14
8	12
7	10
6	8
5	6
4	4
3	3
2	2
1	1

(f)

Figure 6.29 (Cont.). Periodic Velocity Correlation $\left(\overline{\tilde{u}\tilde{u}}\right)$ at the Six Nozzle/Rotor Positions

Position #2

Level	$\overline{\overline{\tilde{v}\tilde{v}}}$ (%)
E	28
D	24
C	20
B	18
A	16
9	14
8	12
7	10
6	8
5	6
4	4
3	3
2	2
1	1

S_r

X_r / C_r

(a)

Position #3

Level	$\overline{\tilde{v}\tilde{v}}$ (%)
E	28
D	24
C	20
B	18
A	16
9	14
8	12
7	10
6	8
5	6
4	4
3	3
2	2
1	1

S_r

X_r / C_r
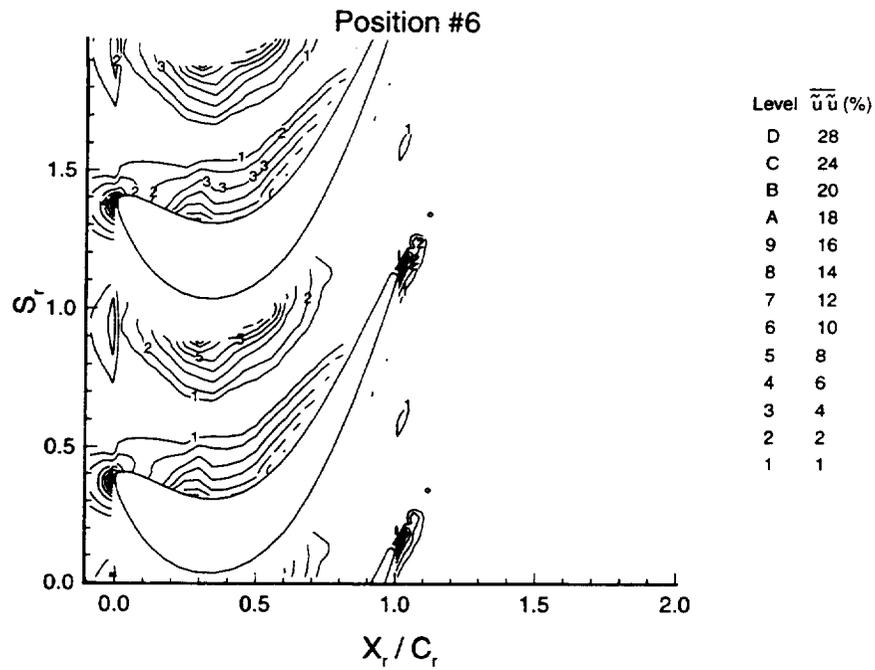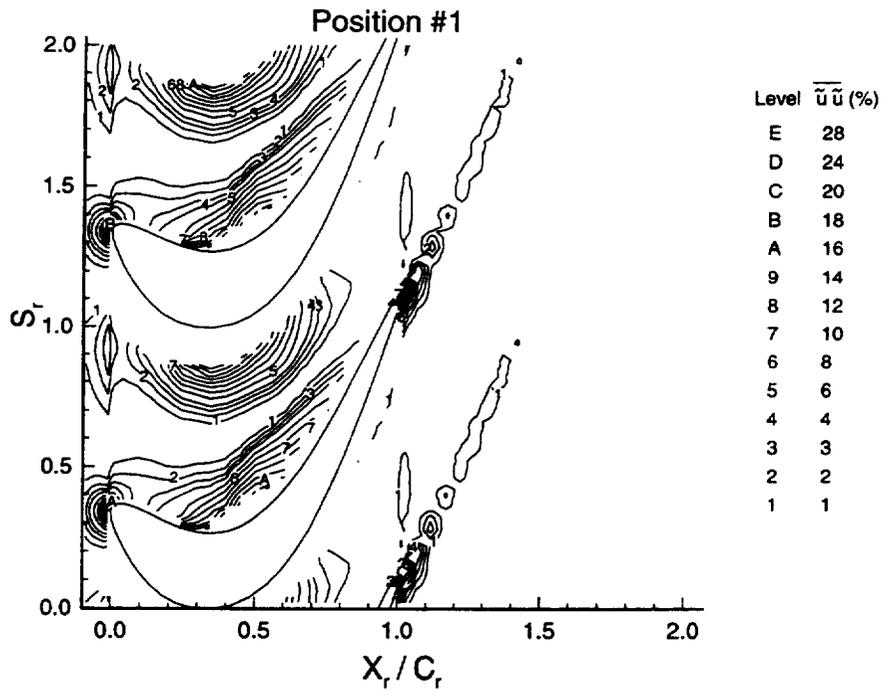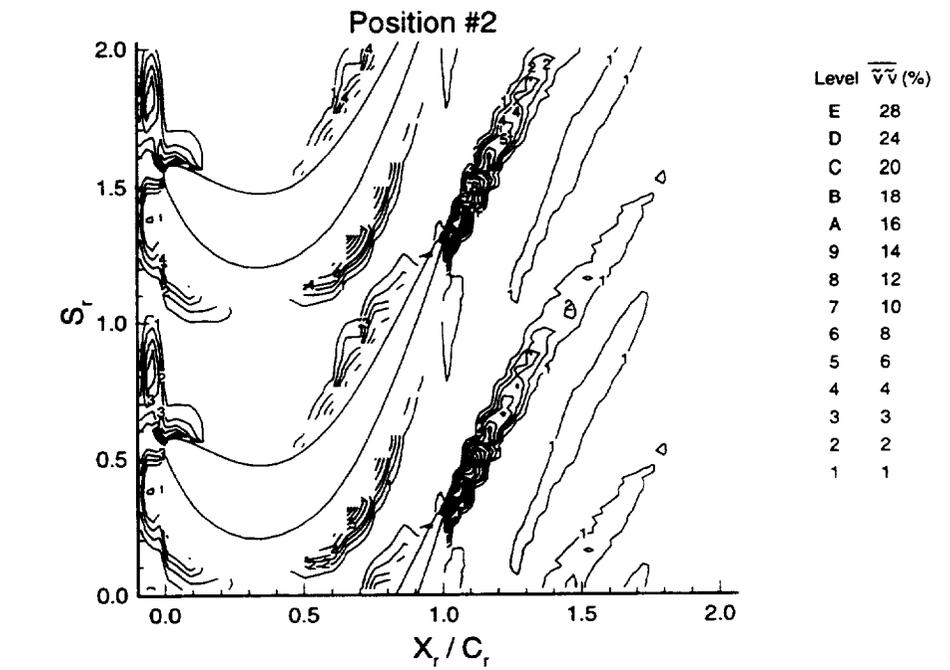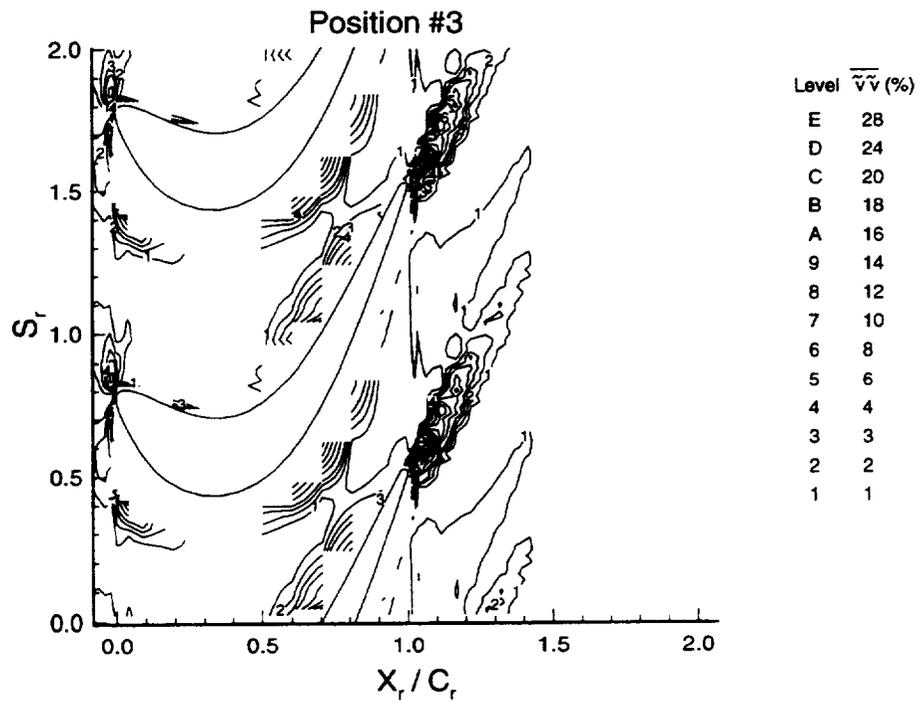
(b)

Figure 6.30. Periodic Velocity Correlation $\left(\overline{\tilde{v}\tilde{v}}\right)$ at the Six Nozzle/Rotor Positions
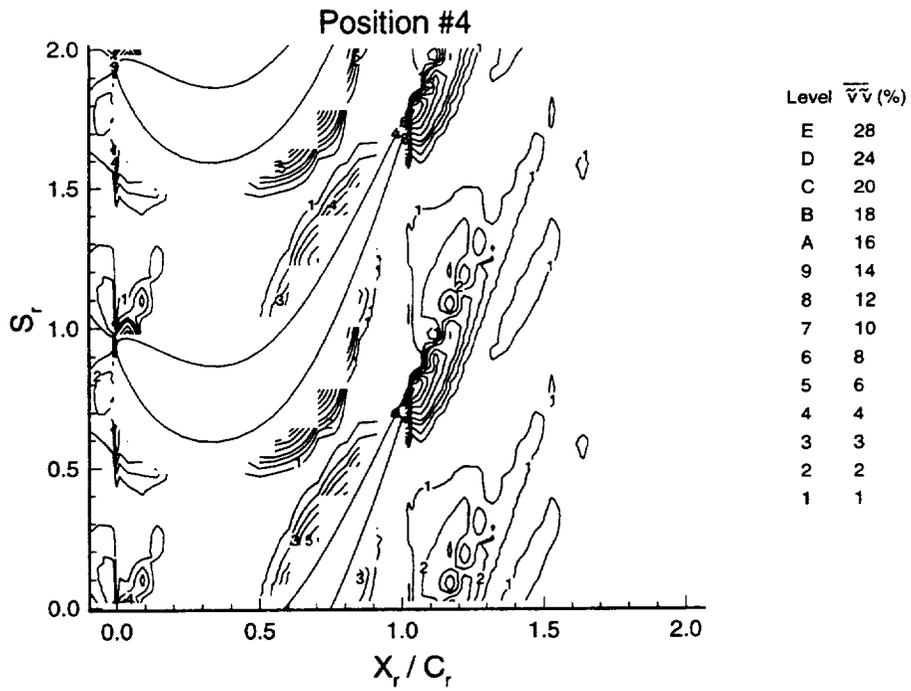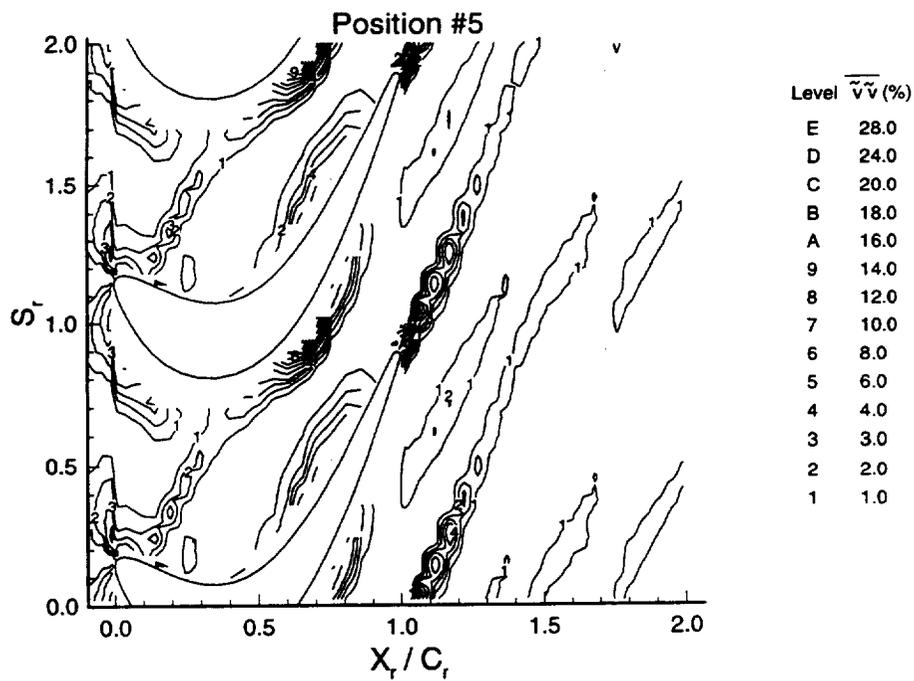
Position #4

Level	$\overline{\overline{v}\,\overline{v}}$ (%)
E	28
D	24
C	20
B	18
A	16
9	14
8	12
7	10
6	8
5	6
4	4
3	3
2	2
1	1

(c)

Position #5

Level	$\widetilde{v}\widetilde{v}$ (%)
E	28.0
D	24.0
C	20.0
B	18.0
A	16.0
9	14.0
8	12.0
7	10.0
6	8.0
5	6.0
4	4.0
3	3.0
2	2.0
1	1.0

(d)

Figure 6.30 (Cont.). Periodic Velocity Correlation $\left(\overline{\widetilde{v}\widetilde{v}}\right)$ at the Six Nozzle/Rotor Positions

Position #6

Level	$\overline{\tilde{v}\tilde{v}}$ (%)
E	28
D	24
C	20
B	18
A	16
9	14
8	12
7	10
6	8
5	6
4	4
3	3
2	2
1	1

(e)

Position #1

Level	$\overline{\tilde{v}\tilde{v}}$ (%)
E	28
D	24
C	20
B	18
A	16
9	14
8	12
7	10
6	8
5	6
4	4
3	2
2	1
1	0.2
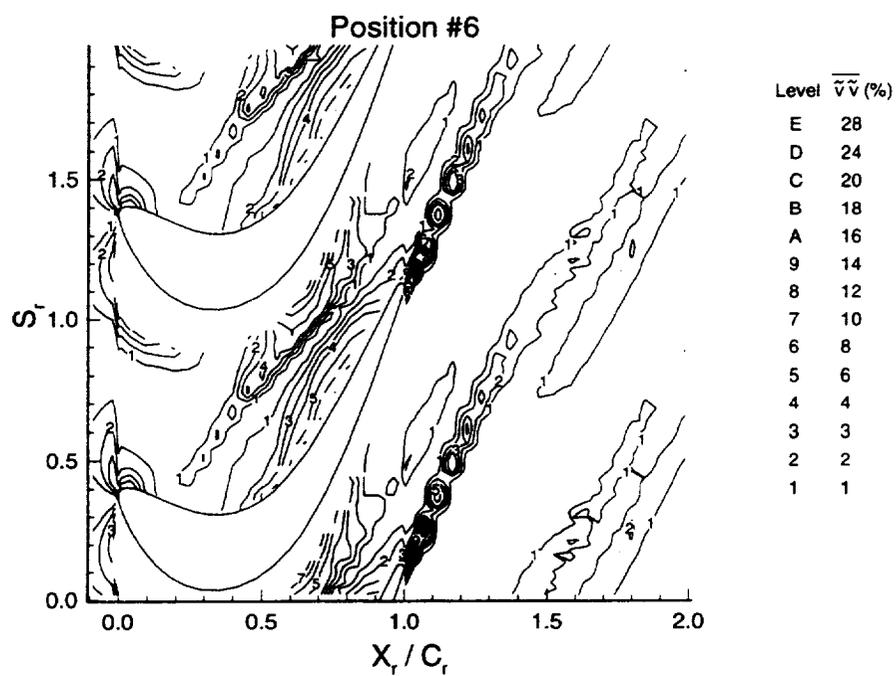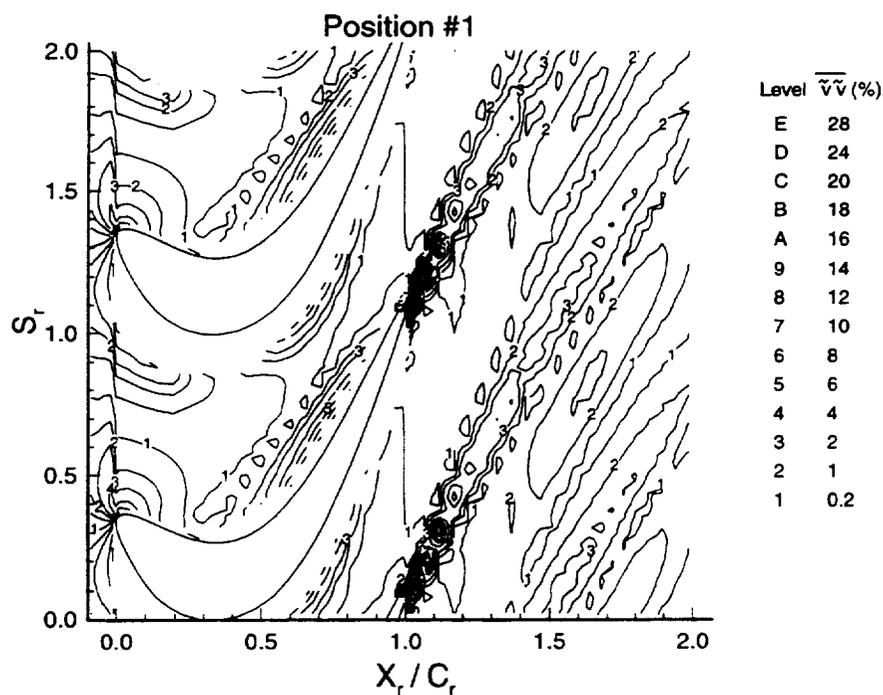
(f)

Figure 6.30 (Cont.). Periodic Velocity Correlation $\left(\overline{\tilde{v}\tilde{v}}\right)$ at the Six Nozzle/Rotor Positions

unresolved velocity correlations have an equal impact on the nozzle wake propagation through the rotor.

Figures 6.31a through 6.31f show the axial tangential cross components of the periodic velocity correlations for all six nozzle/rotor positions. In contrast to the plots of unresolved velocity cross correlations shown in Figures 6.25a through 6.25f, the nozzle wake cannot be identified in all the periodic velocity plots. Since the periodic velocity cross correlations are an order of magnitude greater than the unresolved cross correlations (due to the large pitchwise variation in the flow field), the effect of the nozzle wake would be hard to discern in the regions where there are large values of periodic velocity cross correlations. When the nozzle wake is in the areas where the periodic cross correlations are small, the nozzle wake can be seen. At nozzle/rotor locations 4, 5, 6 and 1, an increase in periodic cross correlations occurs in the region where the previous plots identified the nozzle wake. The magnitude of the periodic cross correlations in the nozzle wake is similar to the magnitude of the unresolved cross correlations in the nozzle wake, also providing added proof that the periodic and unresolved velocities have an equal impact on the nozzle wake propagation through the rotor.

6.3.7 Unsteady Velocity Vectors

The unsteady velocity vector field at the six different nozzle/rotor locations are presented in Figures 6.32a through 6.32f. The axial and tangential components of the unsteady velocity vector is calculated first as follows:

$$V_{x_{unsteady_k}} = \overline{V}_{x_k} - \overline{\overline{V}}_x \qquad (6.18)$$

$$W_{\theta_{unsteady_k}} = \overline{W}_{\theta_k} - \overline{\overline{W}}_\theta \qquad (6.19)$$

(a)

(b)
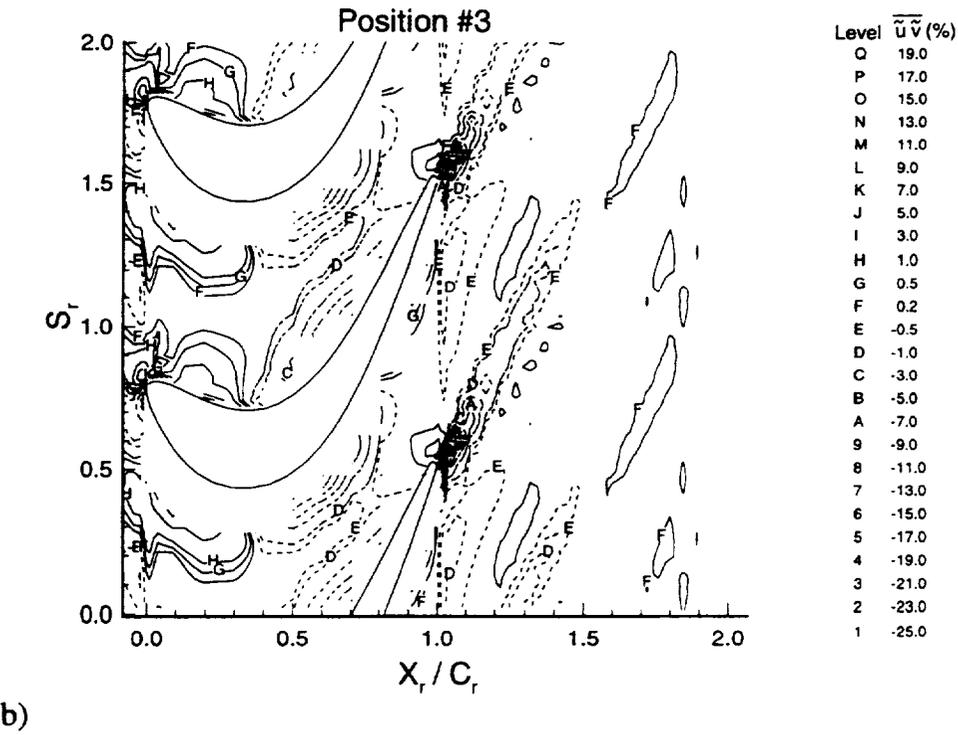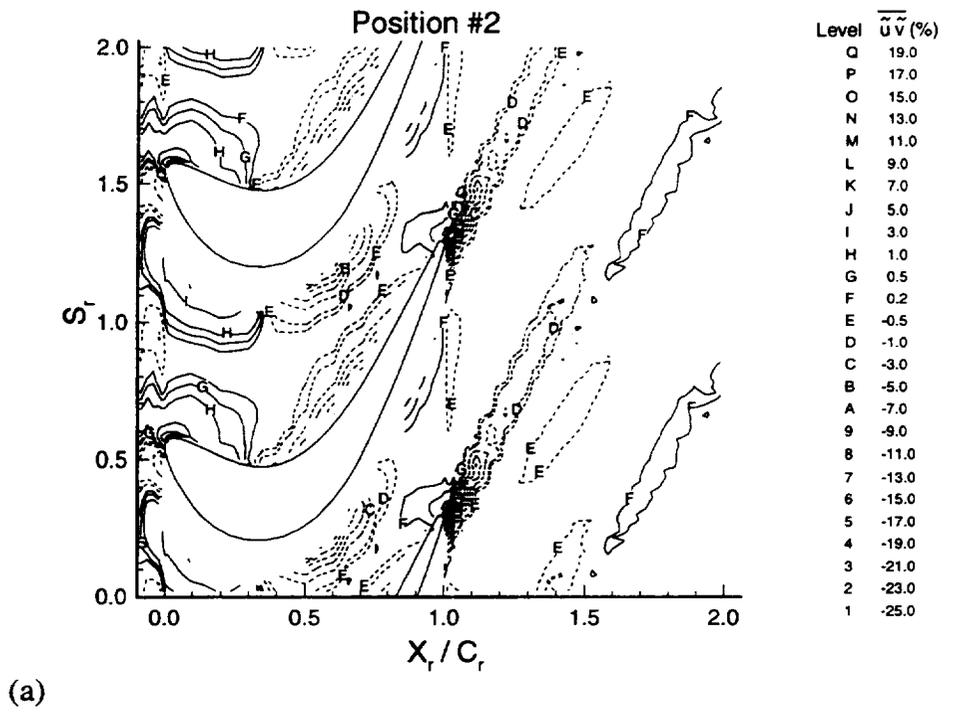
Figure 6.31. Periodic Velocity Correlation $\left(\overline{\tilde{u}\tilde{v}}\right)$ at the Six Nozzle/Rotor Positions
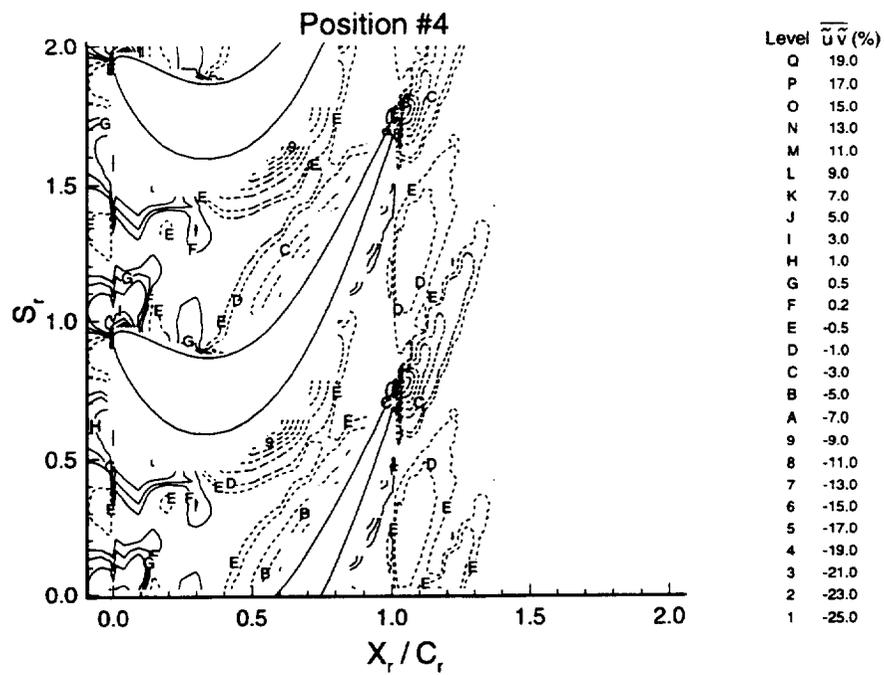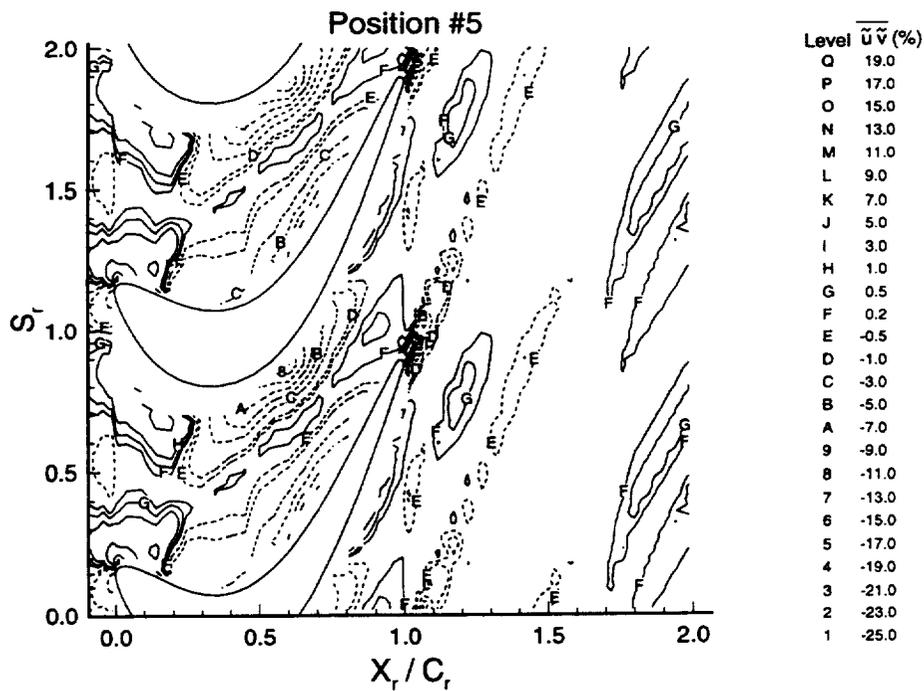
Position #4

S_r

X_r / C_r

Level	$\overline{\tilde{u}\tilde{v}}$ (%)
Q	19.0
P	17.0
O	15.0
N	13.0
M	11.0
L	9.0
K	7.0
J	5.0
I	3.0
H	1.0
G	0.5
F	0.2
E	-0.5
D	-1.0
C	-3.0
B	-5.0
A	-7.0
9	-9.0
8	-11.0
7	-13.0
6	-15.0
5	-17.0
4	-19.0
3	-21.0
2	-23.0
1	-25.0

(c)

Position #5

S_r

X_r / C_r

| Level	$\overline{\tilde{u}\tilde{v}}$ (%)
Q	19.0
P	17.0
O	15.0
N	13.0
M	11.0
L	9.0
K	7.0
J	5.0
I	3.0
H	1.0
G	0.5
F	0.2
E	-0.5
D	-1.0
C	-3.0
B	-5.0
A	-7.0
9	-9.0
8	-11.0
7	-13.0
6	-15.0
5	-17.0
4	-19.0
3	-21.0
2	-23.0
1	-25.0

(d)

Figure 6.31 (Cont.). Periodic Velocity Correlation $\left(\overline{\tilde{u}\tilde{v}}\right)$ at the Six Nozzle/Rotor Positions

Position #6

| Level	$\overline{\tilde{u}\tilde{v}}$ (%)
Q	19.0
P	17.0
O	15.0
N	13.0
M	11.0
L	9.0
K	7.0
J	5.0
I	3.0
H	1.0
G	0.5
F	0.2
E	-0.5
D	-1.0
C	-3.0
B	-5.0
A	-7.0
9	-9.0
8	-11.0
7	-13.0
6	-15.0
5	-17.0
4	-19.0
3	-21.0
2	-23.0
1	-25.0

(e)

Position #1

| Level	$\tilde{u}\tilde{v}$ (%)
Q	19.0
P	17.0
O	15.0
N	13.0
M	11.0
L	9.0
K	7.0
J	5.0
I	3.0
H	1.0
G	0.5
F	0.2
E	-0.5
D	-1.0
C	-3.0
B	-5.0
A	-7.0
9	-9.0
8	-11.0
7	-13.0
6	-15.0
5	-17.0
4	-19.0
3	-21.0
2	-23.0
1	-25.0

(f)

Figure 6.31 (Cont.). Periodic Velocity Correlation $\left(\overline{\tilde{u}\tilde{v}}\right)$ at the Six Nozzle/Rotor Positions

(a)

(b)
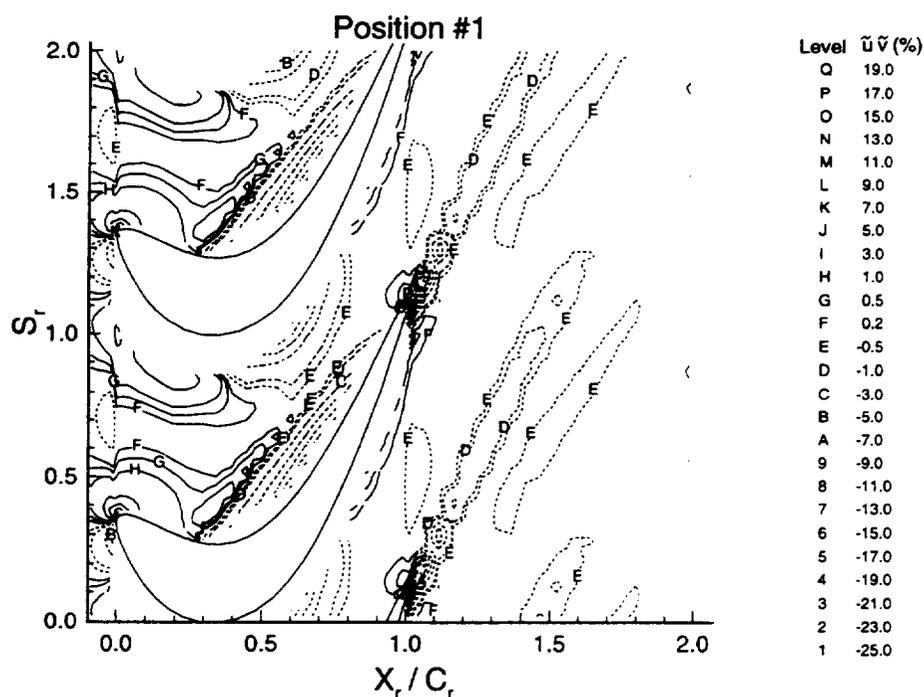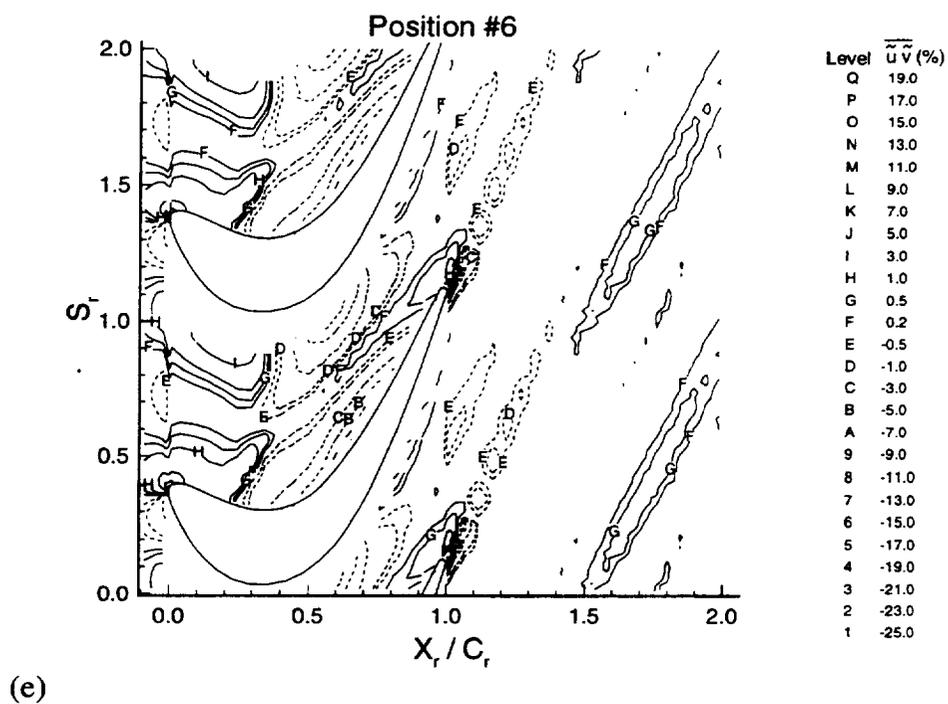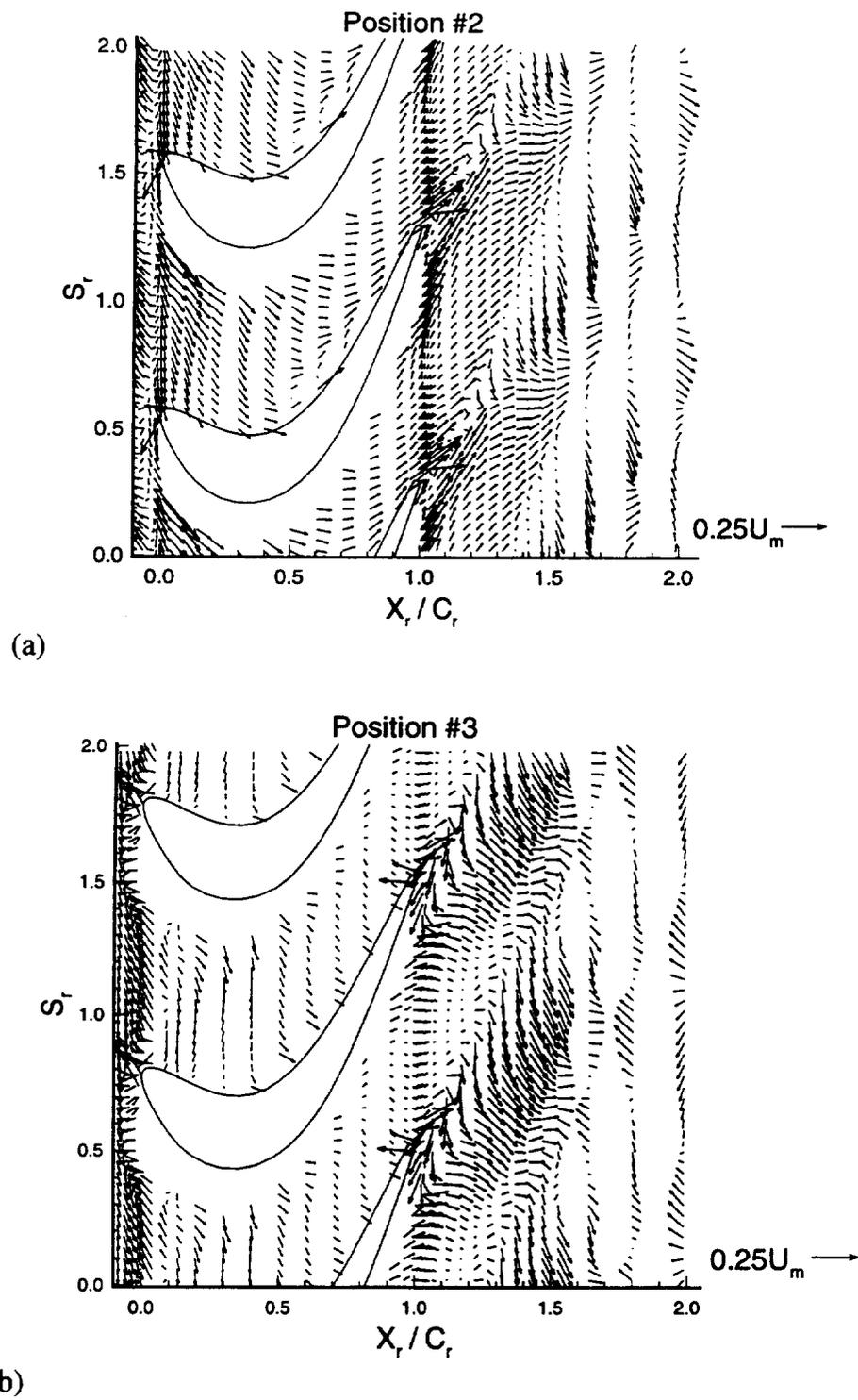
Figure 6.32. Unsteady Velocity Vectors at the Six Nozzle/Rotor Positions
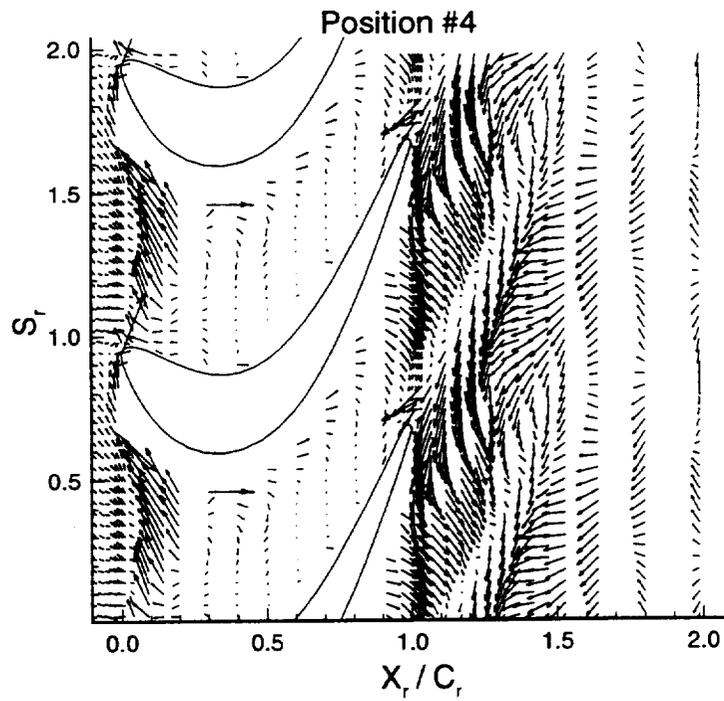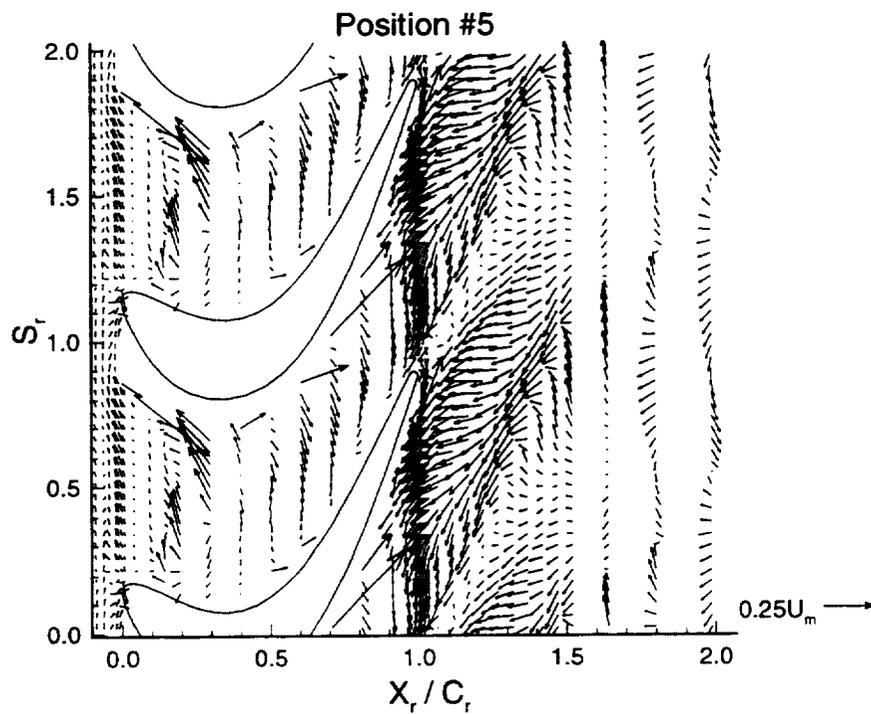
Position #4

(c)

Position #5

(d)

Figure 6.32 (Cont.). Unsteady Velocity Vectors at the Six Nozzle/Rotor Positions

Position #6

S_r

X_r / C_r

$0.25U_m \longrightarrow$

(e)

Position #1

S_r

X_r / C_r

$0.25U_m \longrightarrow$
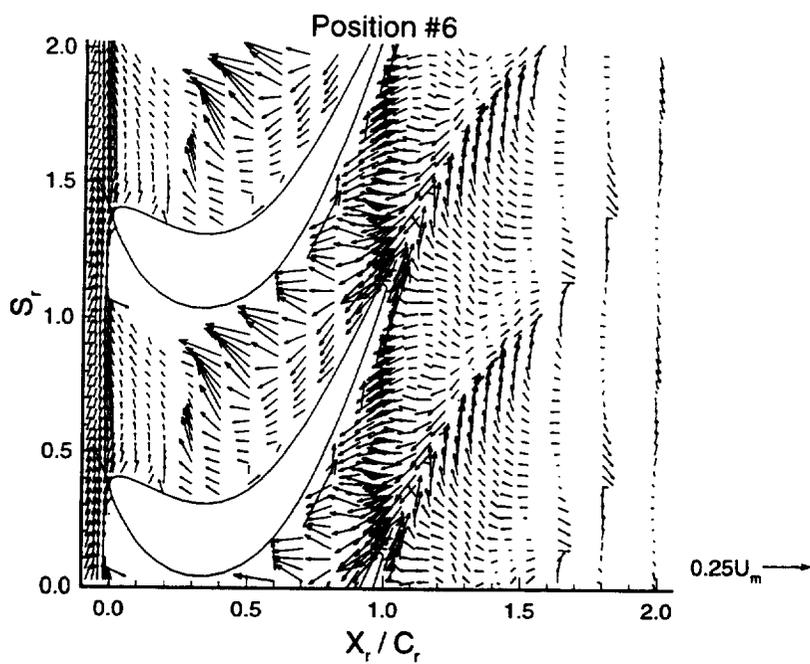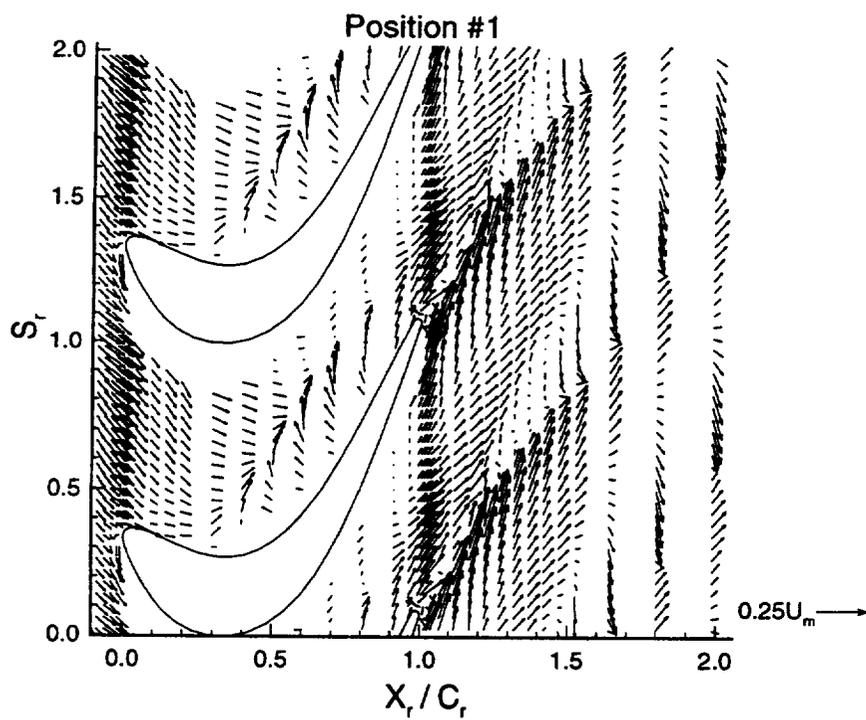
(f)

Figure 6.32 (Cont.). Unsteady Velocity Vectors at the Six Nozzle/Rotor Positions

where k is the nozzle/rotor location, — stands for the ensemble averaged velocity at each nozzle/rotor location and ... represents the cycle averaged velocity. These two components are then combined to form to unsteady velocity vector using the equation:

$$W_{\underline{unsteady}_k} = \underline{x}V_{x_{unsteady_k}} + \underline{\theta}W_{\theta_{unsteady_k}} \tag{6.20}$$

Since the cycle averaged velocities were only averaged over six positions, the unsteady velocity vectors should be looked at qualitatively, not quantitatively.

At position 2, the nozzle wake was identified upstream of the rotor leading edge by the relative total unsteadiness and shear stress plots, among others. Examining this region upstream of the rotor leading edge at position 2, the unsteady velocity vectors are seen to be moving from the pressure to the suction surface, which is a result of the slip velocity in the nozzle wake, discussed earlier (see Figure 6.2). Proceeding onto positions 3, 4 and 5 the slip velocity in the nozzle wake continues, causing the nozzle wake to act as a negative jet drawing fluid from the pressure to the suction surface, as discussed earlier. The two counter-rotating vortices on either side of the nozzle wake can be seen also. As the nozzle wake propagates through the rotor passage the counter-rotating vortex that is upstream of the nozzle wakes decays faster than the counter-rotating vortex that is downstream of the nozzle wake. At nozzle/rotor position 6, the upstream vortex has decayed and is not visible anymore. The nozzle wake is parallel to the rotor pressure surface and the downstream vortex is still strong, drawing fluid upstream along the pressure surface into the nozzle wake. Moving onto position 1, the downstream vortex has decayed considerably and by position 2 it is not visible anymore.

6.4 Mass-Averaged Properties

The mass-averaged properties are obtained by circumferentially mass-averaging each property over one rotor blade pitch as follows:

$$\hat{Q} = \frac{\int_0^{S_r} Q V_x r d\theta}{\int_0^{S_r} V_x r d\theta} \tag{6.21}$$

where Q is any property, the superscript $\cap$ represents mass-averaging, r is the radius (midspan), θ is the tangential distance, V_x is the local axial velocity and S_r is the rotor pitch. The mass-averaged cycle averaged relative total velocity is presented in Figure 6.33a. The data measured with the LDV is also compared to the mass-averaged relative velocity derived from the five hole probe in the nozzle wake. The comparison between the data derived from the two measuring techniques is excellent, being within 1.0% of each other at $X_r/C_r = -0.08$. The velocity is fairly constant from the nozzle trailing edge (which occurs at $X_r/C_r = -0.27$) through the rotor passage to about $X_r/C_r = 0.40$ after which it accelerates rapidly, with an almost linear velocity distribution, until trailing edge. Just downstream of the blade the velocity drops rapidly until $X_r/C_r = 1.05$ after which is decreases gradually until 1.0 chord downstream of the trailing edge.

The mass-averaged relative velocity for each nozzle/rotor location is shown in Figure 6.33b. The position of the nozzle wake can be identified by a dip in velocity. Using this method, the propagation of the nozzle wake through the rotor passage is clearly shown in this figure. At position 2, the nozzle wake is located upstream of the rotor leading edge. Continuing on to position 3, the nozzle wake has traveled downstream into the rotor passage. At position 3, the nozzle wake has
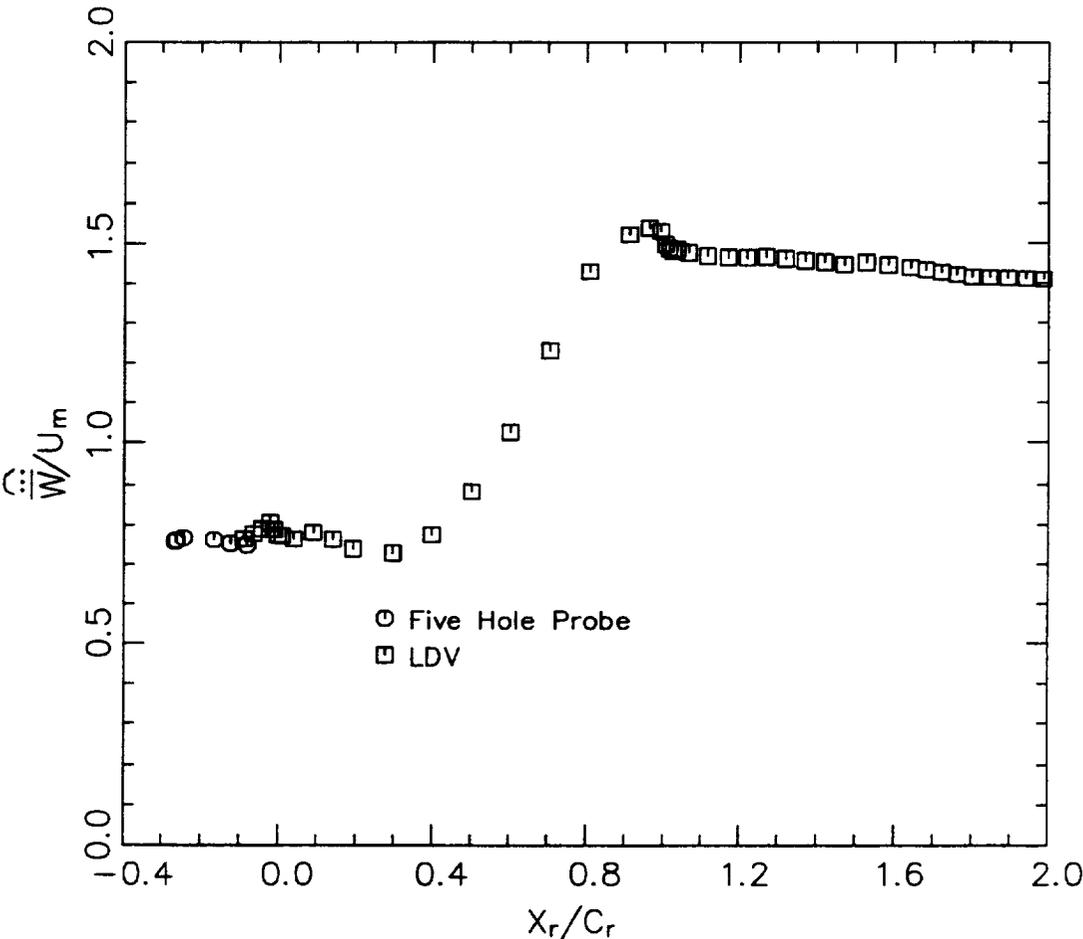
Figure 6.33a. Mass-Averaged, Cycle-Averaged Relative Total Velocity $\left(\widetilde{\overline{W}}/U_m\right)$
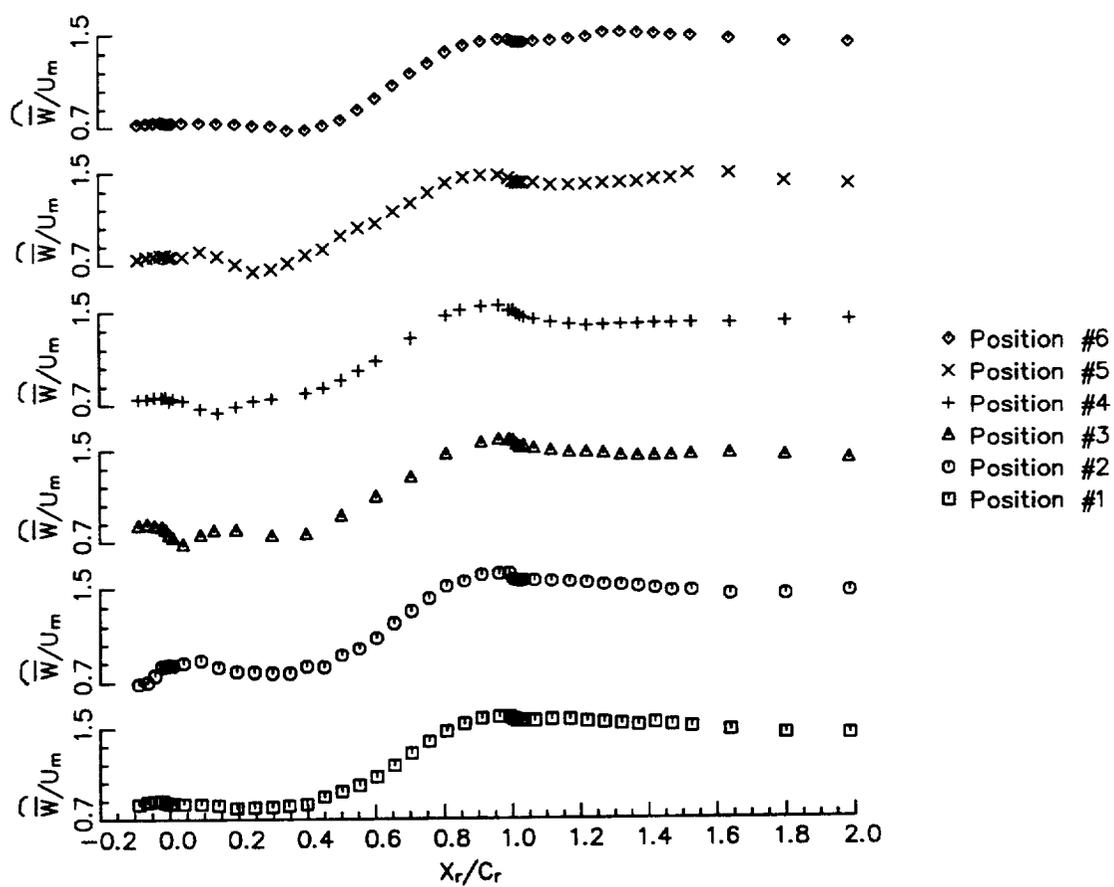
Figure 6.33b. Mass-Averaged Relative Total Velocity $\left(\widehat{\overline{\text{W}}}/\text{U}_\text{m}\right)$

moved to $X_r/C_r = 0.05$, while at position 4, the nozzle wake has traveled to $X_r/C_r = 0.10$. The nozzle wake continues moving downstream, reaching 20% rotor axial chord at position 5 and 40% rotor axial chord at position 6. By the time it has reached position 1, the nozzle wake has been sheared and rotated so that it is parallel to the rotor pressure surface. Thus the velocity defect would be spread out over a large axial distance, and it cannot be detected at position 1 and 2. Comparing this figure to the contour plots previously shown, the location of the nozzle wake coincides for both the contour and mass-average plots.

The mass-averaged cycle averaged absolute total velocity is shown in Figure 6.34. Upstream of the rotor, the comparison between the mass-averaged absolute velocity derived from the five hole probe and the mass-averaged cycle-averaged absolute velocity derived from the LDV is also excellent, being within 1.0% of each other. The absolute velocity is constant from the nozzle trailing edge (at $X_r/C_r =$ -0.27) to the rotor leading edge. In contrast to the relative total velocity, the absolute velocity drops through the rotor. This is because a turbine extracts kinetic energy from the flow field to produce work.

Figure 6.35a presents the mass-averaged cycle average relative flow angles. The mass-averaged relative flow angles are calculated from the mass-averaged relative tangential velocity and axial velocity as follows:

$$\hat{\beta} = \text{ATAN}\left(\frac{\hat{W}_\theta}{\hat{V}_x}\right) \tag{6.22}$$

The large turning of the flow (110 degrees) that is a characteristic of turbine rotors is seen in this figure. (Higher flow turning produces larger pressure and temperature drops, and thereby higher work output.) Upstream of the rotor, the comparison between the mass-averaged relative flow angle derived from the five
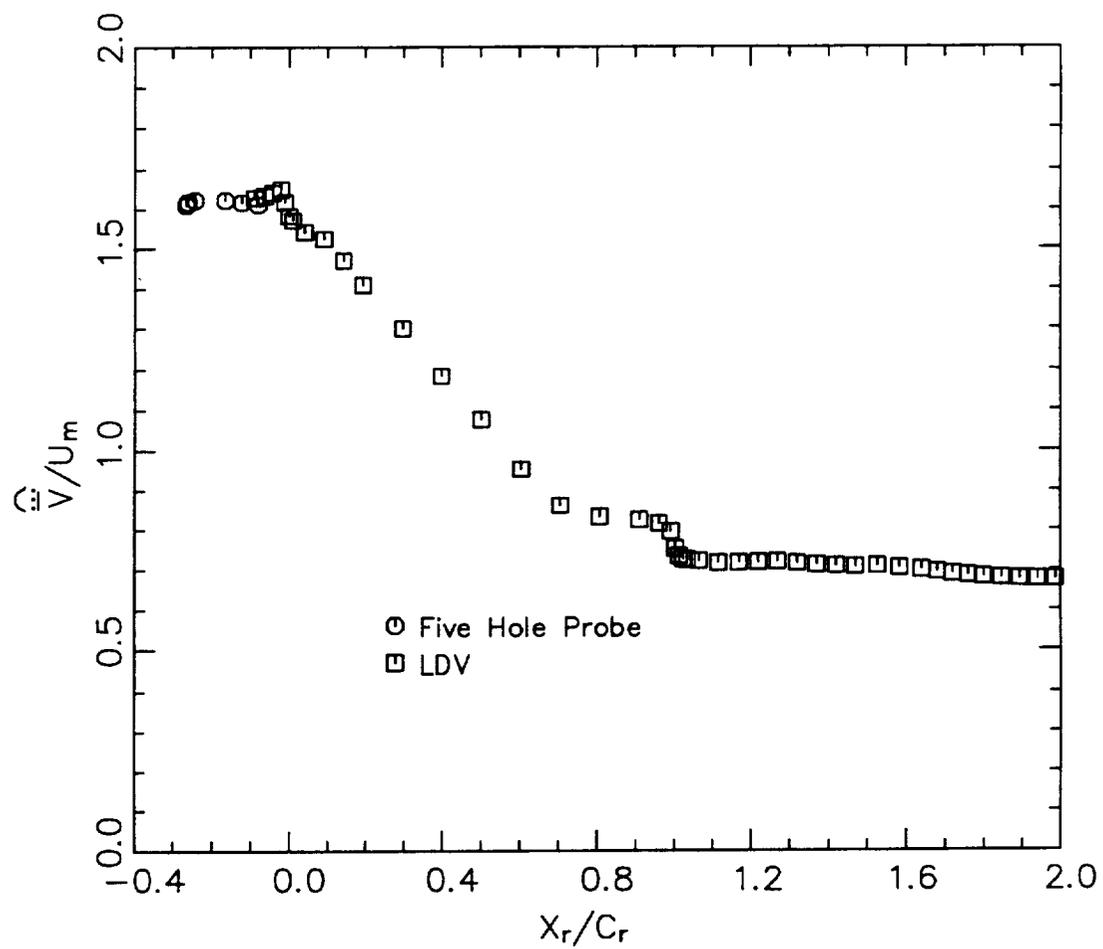
Figure 6.34. Mass-Averaged, Cycle-Averaged Absolute Total Velocity $\left(\widehat{\overline{\overline{V}}}/U_m\right)$
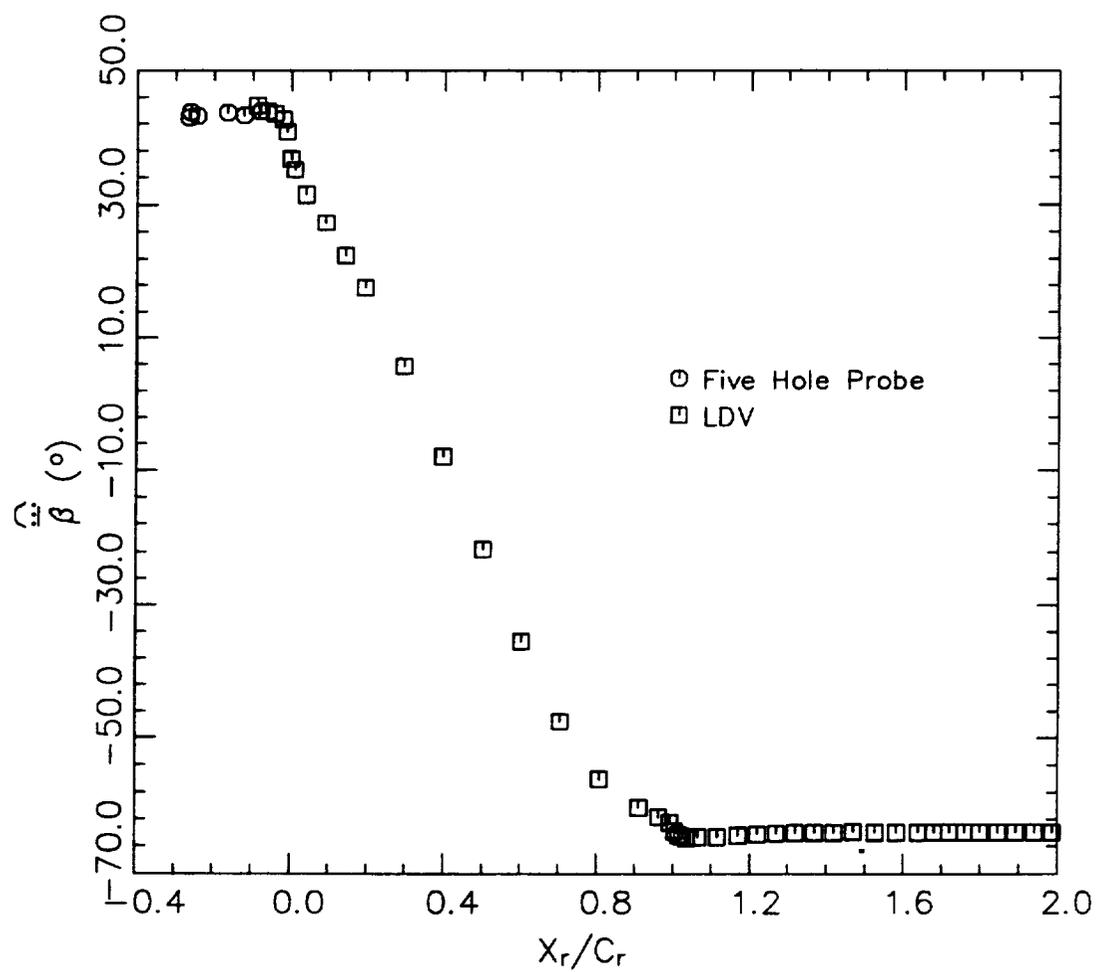
Figure 6.35a. Mass-Averaged, Cycle-Averaged Relative Flow Angle $\left(\overline{\overline{\beta}} \right)$

hole probe and the mass-averaged cycle-averaged relative flow angle obtained with the LDV is excellent being within 0.5% of each other.

The mass-averaged relative flow angle for each nozzle/rotor position are shown in Figure 6.35b. The location of the nozzle wake can be identified by the lower relative flow angle occurring at that axial location. This results from the overturning of the flow in the wake discussed earlier. Using this criteria the nozzle is seen upstream of the rotor leading edge at position 2. Continuing onto the next position, the nozzle wake is seen move through the passage until position 1, where it cannot be identified any longer. This is because the nozzle wake has rotated until it is parallel to the rotor pressure surface as discussed earlier.

Figure 6.36a presents the mass-averaged cycle-averaged axial velocity in the rotor. Just as with the previously discussed mass-averaged values the comparison between the mass-averaged axial velocity derived from the five hole probe and the LDV is excellent upstream of the rotor. Just upstream of the rotor leading edge there is an increase in axial velocity. This is due to the potential effect of the rotor blade. Traveling downstream of the leading edge, the axial velocity increases steadily until 60% rotor axial chord, which is caused by the decreasing area of the rotor passage. The maximum velocity is at $X_r/C_r = 0.60$ which is just upstream of the blade throat (the blade throat is at $X_r/C_r = 0.65$). Downstream of 65% rotor axial chord until the trailing edge, the axial velocity decreases sharply due to the increase in rotor passage area. The axial velocity then level off to a fairly constant velocity downstream of the rotor trailing edge.

Examining the mass-averaged axial velocities for each nozzle/rotor position (presented in Figure 6.36b), the nozzle wake can be distinguished clearly by the velocity defect associated with it (as compared to the mass-averaged cycle-averaged axial velocity shown in Figure 6.36a). Using this method, the location of the nozzle wake in the rotor passage is the same as in the previous mass-averaged
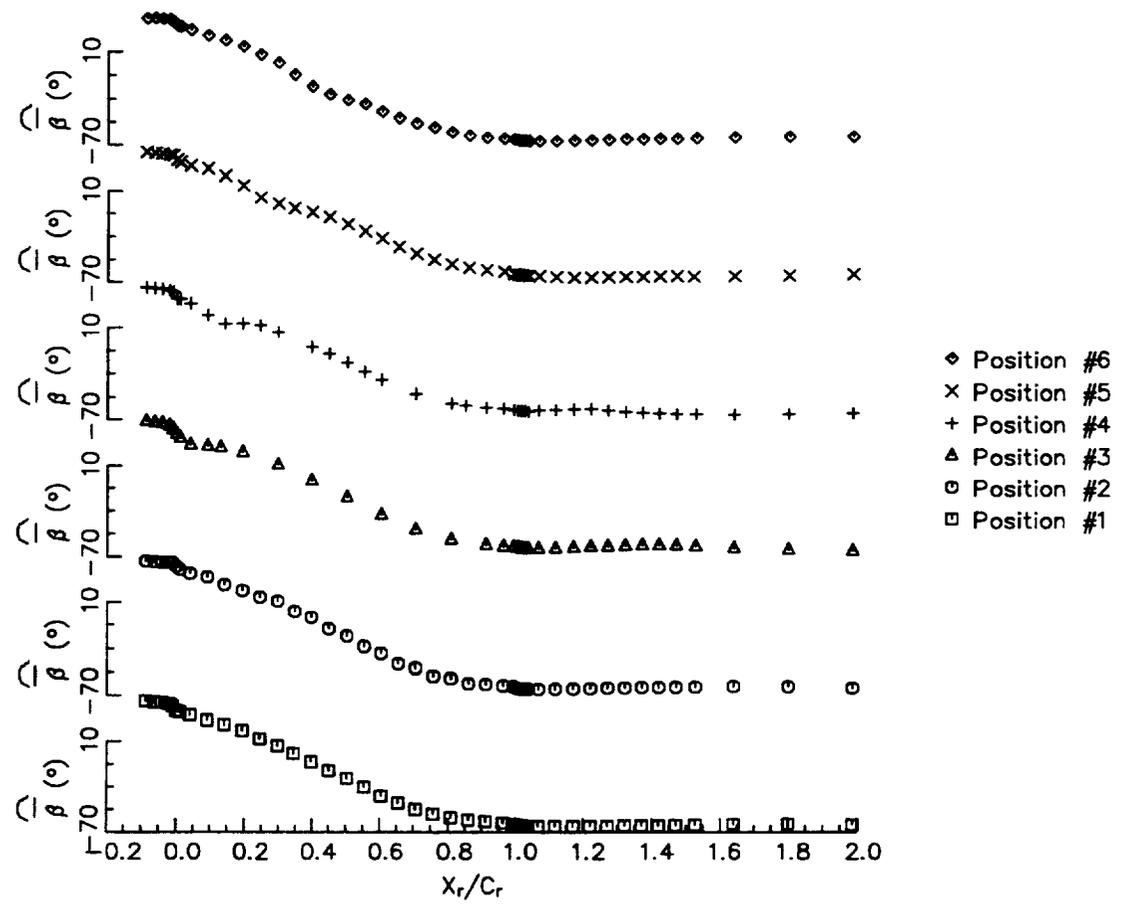
Figure 6.35b. Mass-Averaged Relative Flow Angle $\left(\overline{\overline{\beta}}\right)$
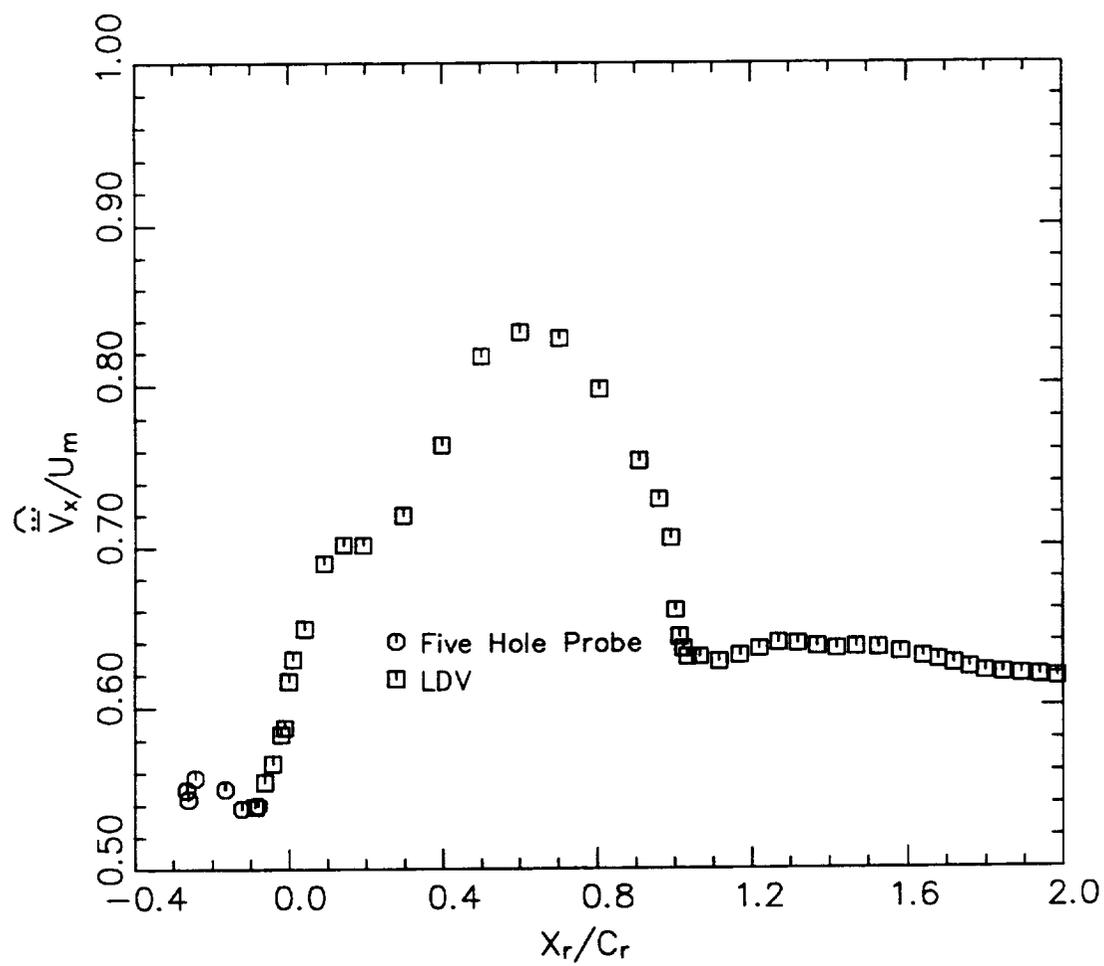
Figure 6.36a. Mass-Averaged, Cycle-Averaged Axial Velocity $\left(\overset{\approx}{\overline{V}}_x / U_m \right)$
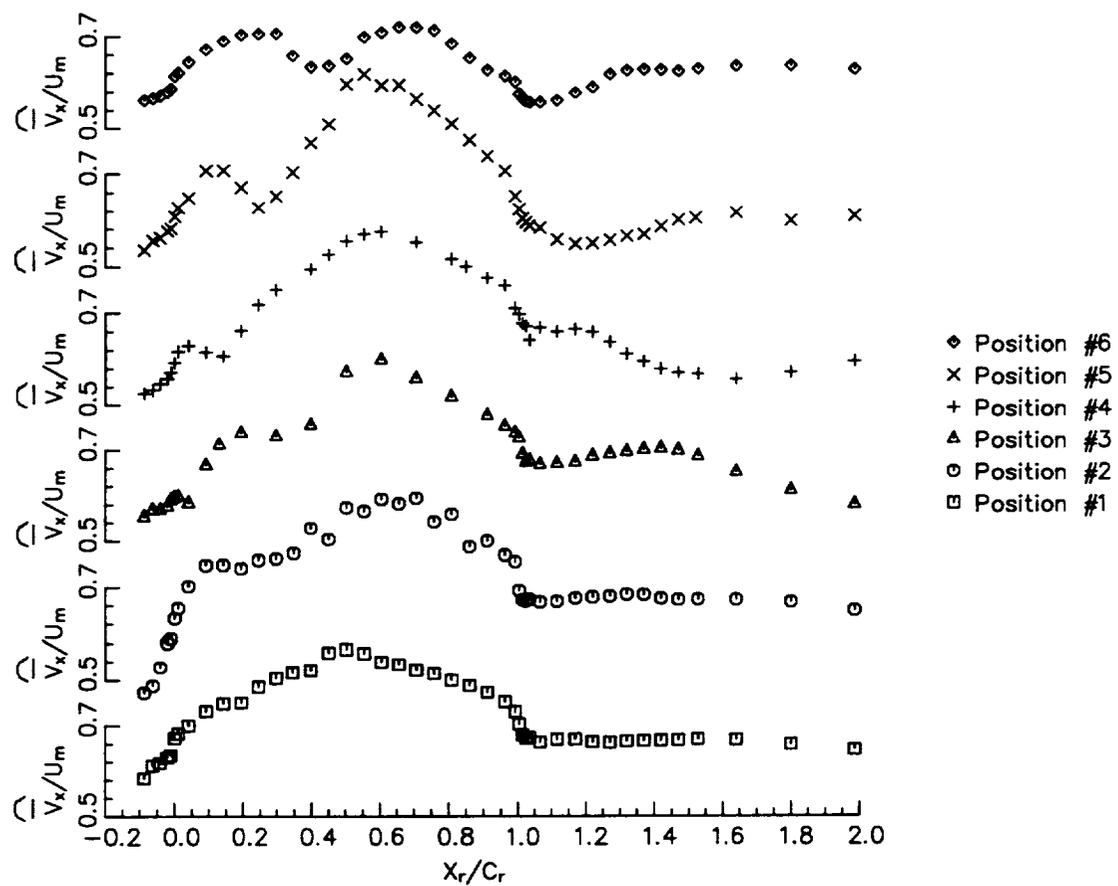
Figure 6.36b. Mass-Averaged Axial Velocity $\left(\hat{\overline{V}}_x / U_m \right)$

plots and the trajectory of the nozzle wake can be identified. While inside the rotor passage, the trajectory of the nozzle wake can be clearly seen, this is not the case downstream of the rotor. The nozzle wake trajectory downstream of the rotor is much more difficult to interpret for three reasons. The first is that the absolute flow angle changes direction (see Figure 6.37), which would cause the nozzle wake to move in the opposite direction downstream of the rotor as compared to inside the rotor passage (since the nozzle wake follows the flow direction), and the second is the absolute flow velocity decreases. The third reason is that in some nozzle/rotor positions, the nozzle wake is in the rotor wake freestream and decays slower (position 5), and in other locations (position 2), the nozzle wake is inside the rotor wake and decays faster. Despite this, the nozzle wake can be identified in the flow field downstream of the rotor at several locations. At nozzle/rotor position 5, there is an axial velocity defect at $X_r/C_r = 1.2$, which probably corresponds to the nozzle wake. At position 4, there is a defect at $X_r/C_r = 1.6$ and at position 3, there is a defect at $X_r/C_r = 2.0$, both of which could correspond to the nozzle wake.

The mass-averaged cycle-averaged absolute flow angle in the rotor is shown in Figure 6.37.The flow angle continuously decreases from the rotor leading edge to the trailing edge, changing sign just upstream of the rotor trailing edge (at $X_r/C_r = 0.8$). Downstream of the trailing edge the absolute flow angle remains constant. Figure 6.37 also shows the comparison between the mass-averaged absolute flow angle derived from the five hole probe and the mass-averaged cycle-averaged absolute flow angle obtained with the LDV upstream of the rotor. As with the previously discussed mass-averaged properties, the comparison is excellent being with 0.3% of each other at $X_r/C_r = -0.08$.

The mass-averaged cycle-averaged relative total unresolved unsteadiness is
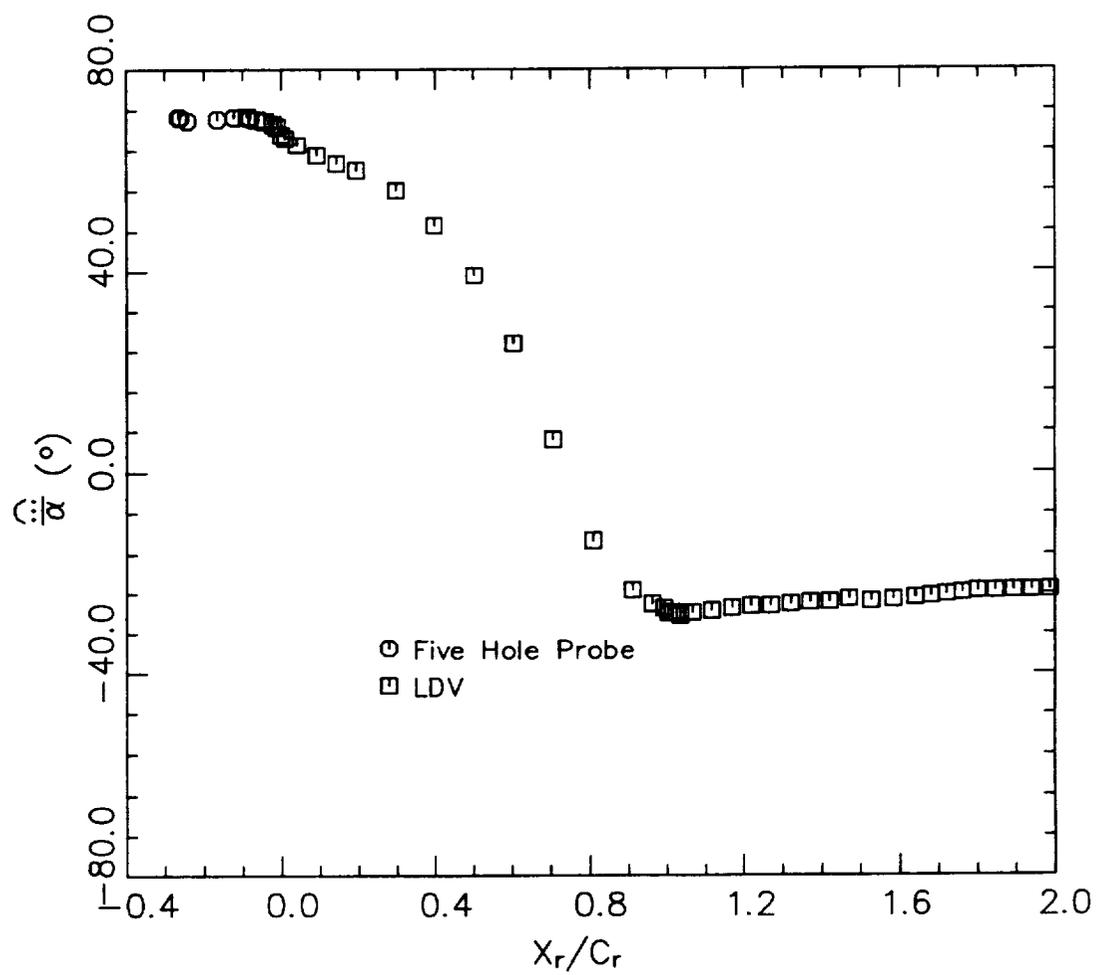
Figure 6.37. Mass-Averaged, Cycle-Averaged Absolute Flow Angle $\left(\overset{\approx}{\overline{\alpha}}\right)$

shown in Figure 6.38a. Starting from upstream of the rotor and moving downstream, the unresolved unsteadiness decreases as the rotor leading edge is approached. This is caused by the nozzle wake decay. At the leading edge there is a sharp increase in unresolved unsteadiness as discussed earlier. The total unresolved unsteadiness decreases as one continues to travel downstream, since the relative velocity increases. Downstream of the trailing edge there is a sharp increase between the trailing edge and 10% axial chord downstream. While the unsteadiness downstream of the rotor includes both nozzle wake and the rotor wake unsteadiness, this increase is only caused by the unsteadiness in the rotor wake. Continuing on downstream, the rate of increase in unresolved unsteadiness decreases until close to one chord downstream where the magnitude of relative total unsteadiness levels off.

Figure 6.38b presents the mass-averaged relative total unresolved unsteadiness for all six nozzle/rotor locations. Using the increase in total unresolved unsteadiness in the rotor blade passage to identify the nozzle wake, the position of the wake is at the same locations where the previous mass-average plots found it to be at. Downstream of the blade the nozzle wakes are harder to identify, since the overall level of unresolved unsteadiness is higher than in the blade passage and thus the nozzle wakes are not as noticeable. But looking closely at the plot, there are regions of higher unsteadiness that could be associated with the nozzle wake. Starting with position 5, there is a high unresolved unsteadiness region just downstream of the trailing edge (at $X_r/C_r = 1.10$). At position 4, there is a region at $X_r/C_r = 1.30$, while at position 3, the peak unsteadiness occurs at $X_r/C_r = 1.50$. At both nozzle/rotor positions 2 and 1, there are high unresolved unsteadiness regions (at $X_r/C_r = 1.8$ and 2.0, respectively), that possibly could correspond to the nozzle wake. While the regions of high unresolved unsteadiness matched the axial position of the other mass-averaged properties in the rotor blade,
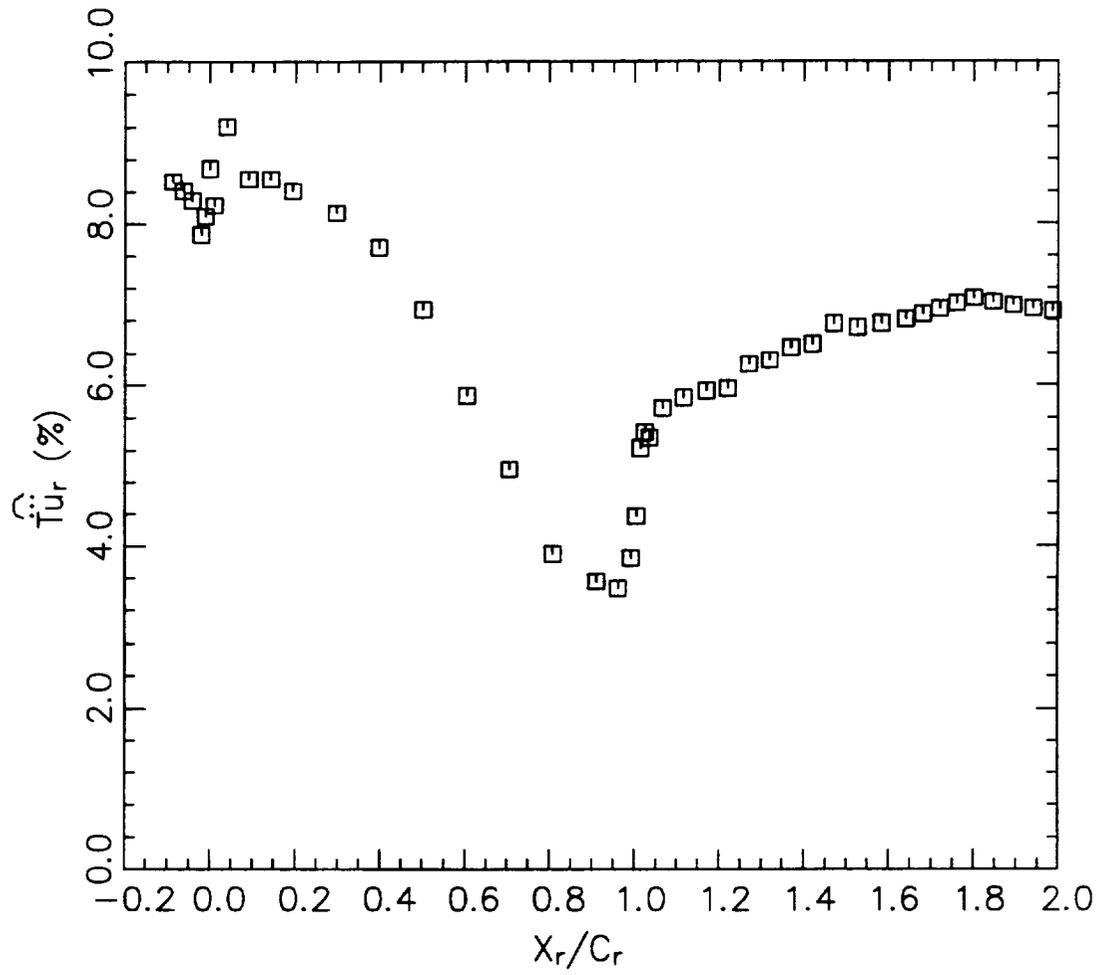
Figure 6.38a. Mass-Averaged, Cycle-Averaged Relative Total Unresolved
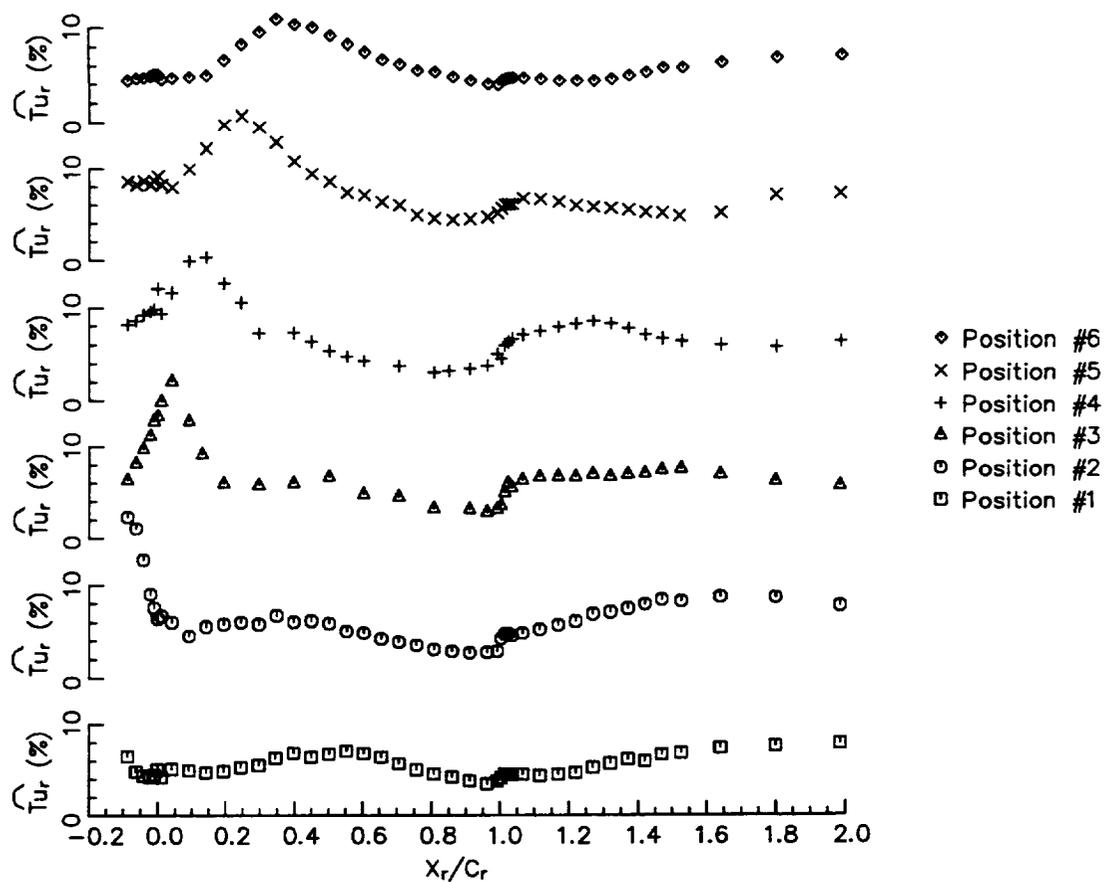
Unsteadiness ($\widehat{Tu}_r$)

Figure 6.38b. Mass-Averaged Relative Total Unresolved Unsteadiness $\left(\hat{Tu}_r\right)$

the region of high unsteadiness do not occur at the same location as the low axial velocity regions downstream of the rotor blade. This is because, although in the near wake the maximum unsteadiness occurs at the wake center (position where velocity defect is largest), far downstream of the nozzle the maximum turbulence intensity occurs away from the center due to the spread of the wake. Hah and Lakshminarayana (1982) also noticed this feature in the wake of an isolated airfoil.

The mass-averaged cycle averaged unresolved velocity cross-correlation $\overline{(\widehat{u'v'})}$ is presented in Figure 6.39a. The unresolved velocity cross correlation is zero upstream of the rotor leading edge. There is a sharp increase in unresolved velocity cross correlation at the leading edge due to the high unresolved velocity cross correlation in the stagnation region. The high levels of mass-averaged unresolved velocity correlation at midchord results from the high unresolved velocity cross correlation levels in the pressure surface boundary layer. The sharp increase in negative mass-averaged unresolved velocity cross correlations just downstream of the trailing edge is because high levels of negative unresolved velocity cross correlations in the rotor wake. Moving downstream of the trailing edge the mass-averaged unresolved velocity cross correlation decays very rapidly to zero at $X_r/C_r = 1.25$. This is mainly caused by the rapid decay of the rotor wake. The mass-averaged unresolved velocity cross correlation for each nozzle/rotor location is shown in Figure 6.39b. The regions of increased unresolved velocity cross correlation correspond to the nozzle wake location. These regions corresponds with the regions of increase total relative unsteadiness, thus giving added confirmation of the nozzle wake trajectory, especially downstream of the rotor.
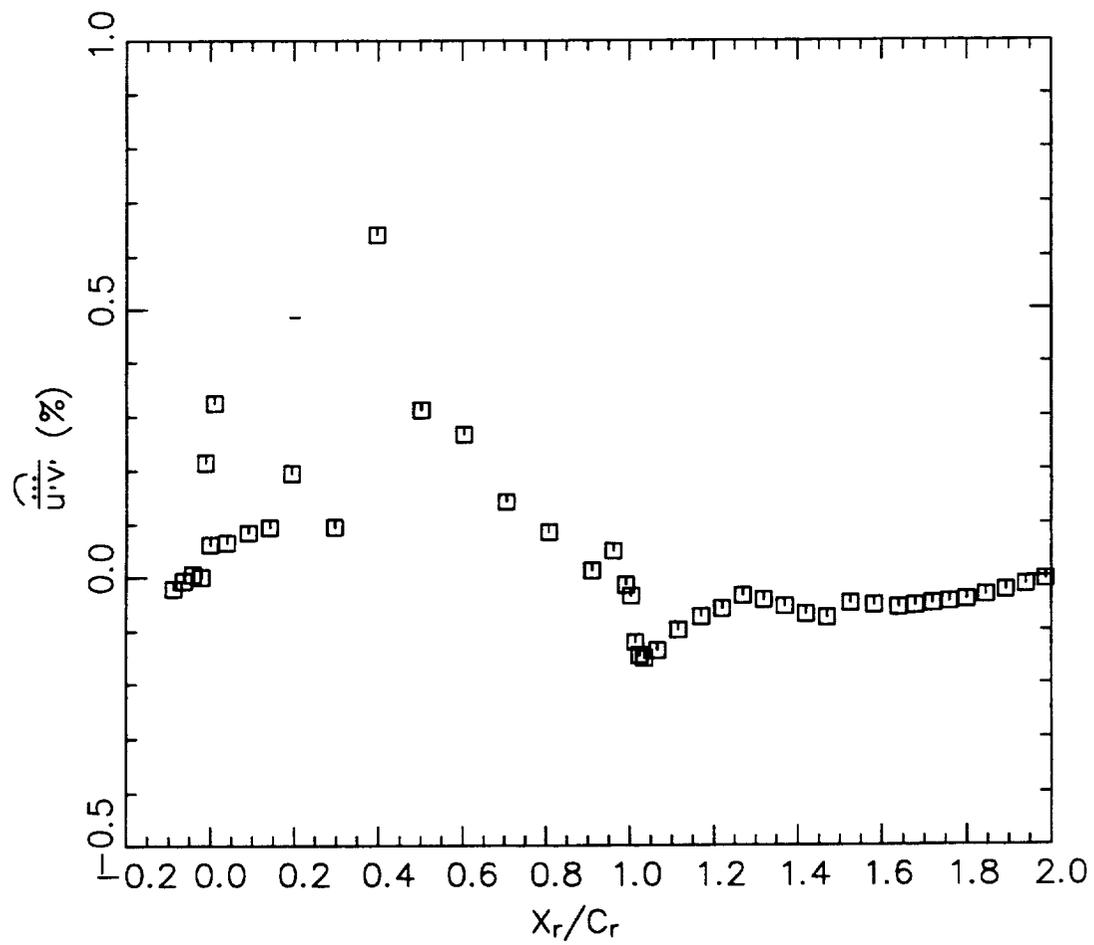
Figure 6.39a. Mass-Averaged, Cycle-Averaged Unresolved Velocity Correlation

$$\frac{\widehat{\overline{u'v'}}}{(\overline{u'v'})}$$
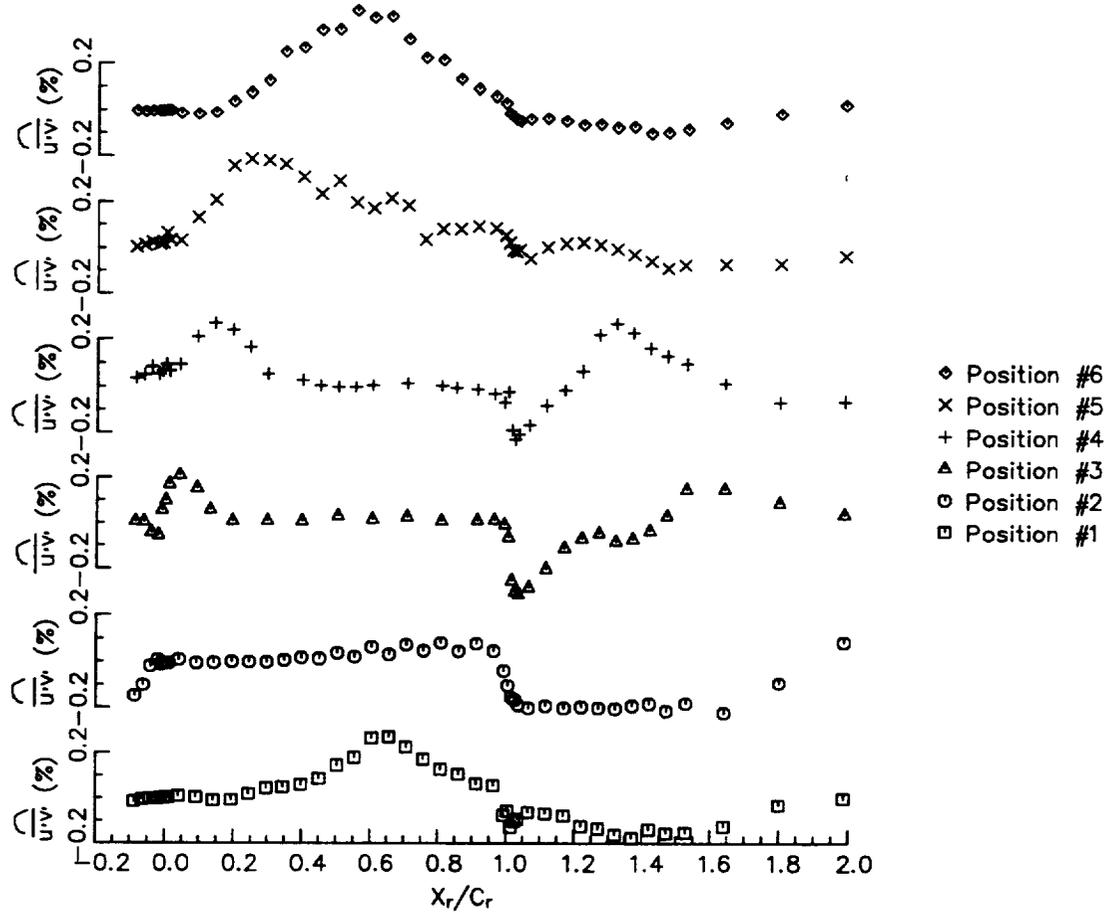
Figure 6.39b. Mass-Averaged Unresolved Velocity Correlation $\left(\overline{u'v'}\right)$

6.5 Nozzle Relative Flow Field (Time-Averaged Properties)

The time-averaged properties at each stationary measuring location are used to discern the wake pattern in the absolute frame without any reference to the rotor blade positions. The time-averaged values $\overline{\overline{Q}}$ are defined as

$$\overline{\overline{Q}} = \frac{1}{NW} \sum_{j=1}^{NW} \overline{Q} \qquad (6.23)$$

where $\overline{Q}$ is any ensemble averaged property and NW is the total number of measurement windows. The time-averaged velocity is a time average of all measurements acquired at a fixed point in space. This is equivalent to equation 6.6.

Figure 6.40 are the time-averaged total unresolved unsteadiness (normalized by U_m to see the nozzle wake more clearly). The data represents two nozzle pitches (the data from one pitch was doubled). The rotor blade is not visible due to the integration method. The nozzle wake, identified by increased unresolved unsteadiness, moves on a curved path through the rotor blade, changing direction from the inlet of the rotor to the exit. It seems to follows the path of the absolute flow. The absolute flow path can be seen more clearly by looking at the time-averaged absolute velocity vectors shown in Figure 6.41. By comparing the path of the nozzle wake with that of the absolute flow, the nozzle wake is seen to follow the absolute flow.

The time-averaged axial velocity is presented in Figure 6.42. The regions of low velocity correspond to the nozzle wake. By comparing the path of the low velocity regions with that of the high unresolved unsteadiness, the paths coincide in the rotor blade, while downstream of the rotor blade they deviated from one another. This is due to wake spreading which was discussed earlier. The time-
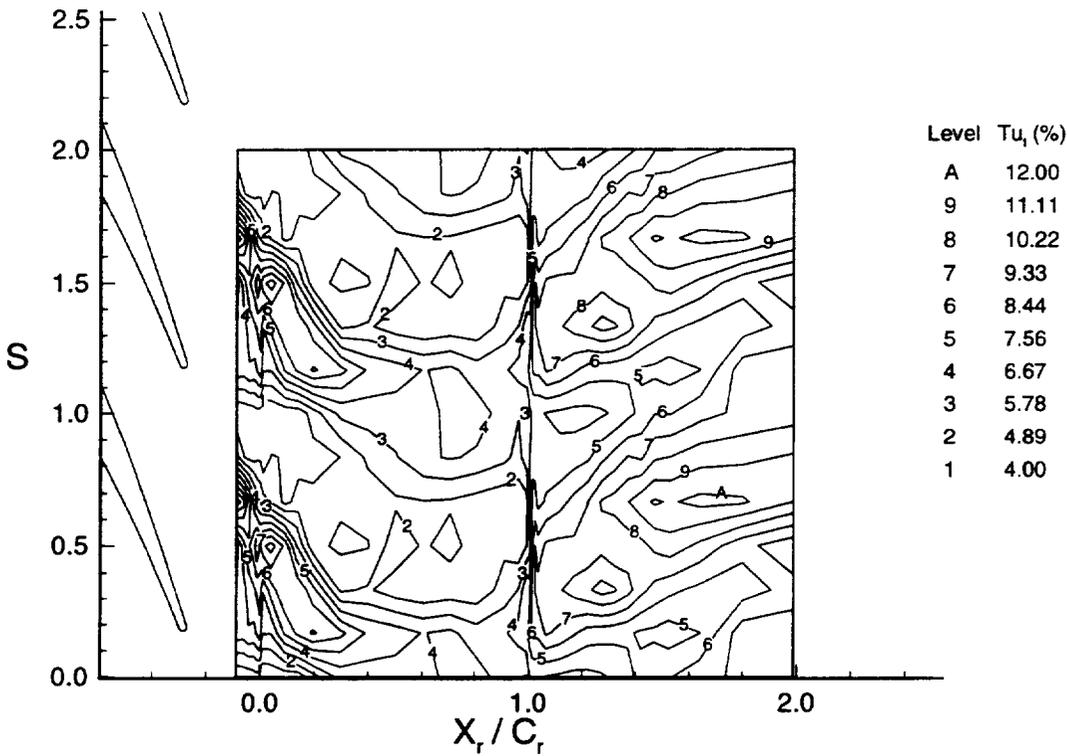
Figure 6.40. Time-Averaged Total Unresolved Unsteadiness $\left(\overline{\overline{Tu_t}}\right)$
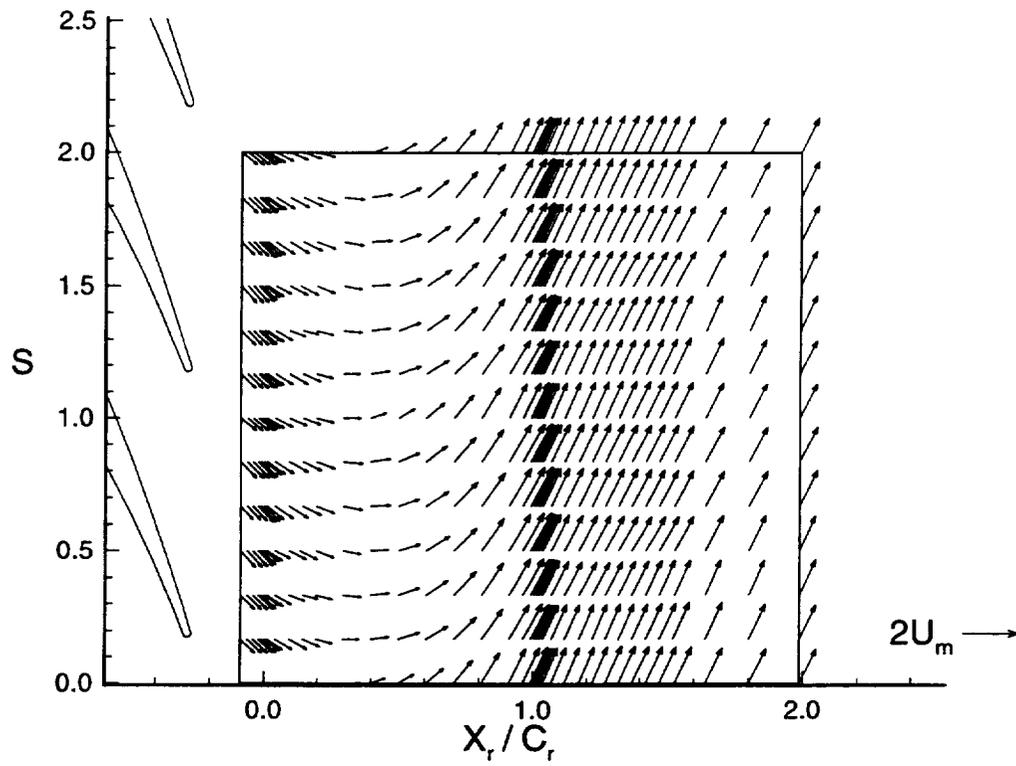
Figure 6.41. Time-Averaged Absolute Total Velocity Vectors
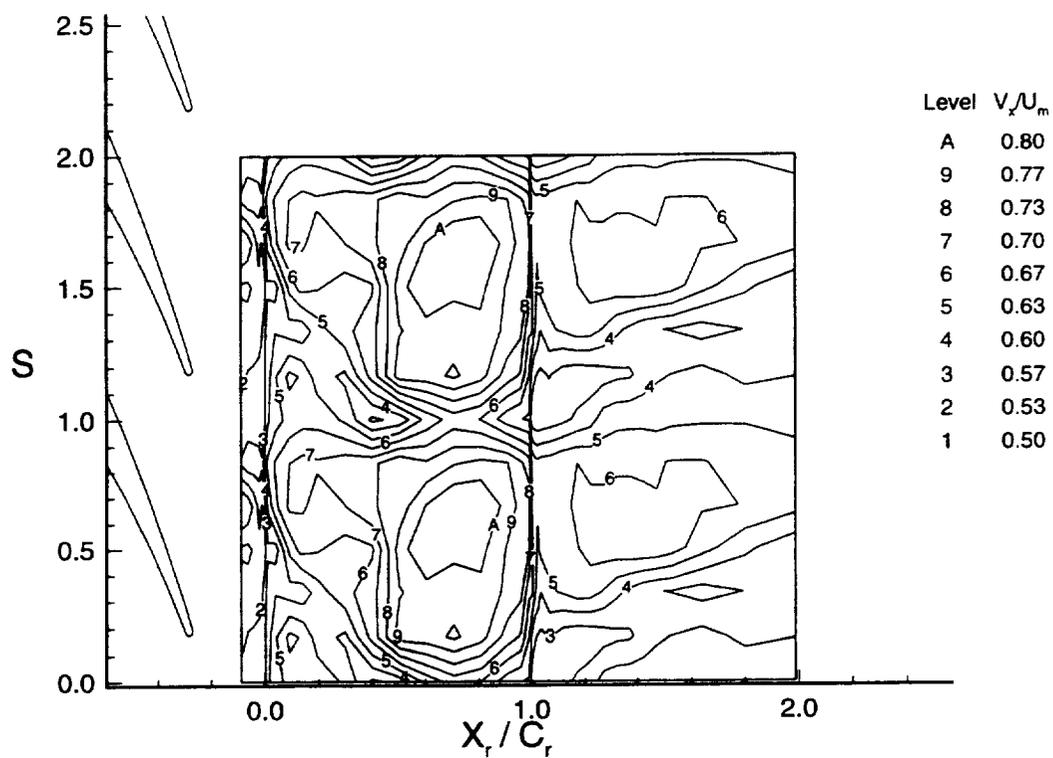
Figure 6.42. Time-Averaged Axial Velocity $\left(\overline{\overline{V}}_x/U_m\right)$

averaged unresolved velocity cross correlation is shown in Figure 6.43. The increased unresolved velocity cross correlation resulting from the nozzle wake can be seen. The path of the nozzle wake is clearly marked out downstream of the rotor, while in the rotor some of the high unresolved velocity cross correlation region result from the increased unresolved velocity cross correlation at the pressure surface, thus making the determination of the nozzle wake path more difficult.
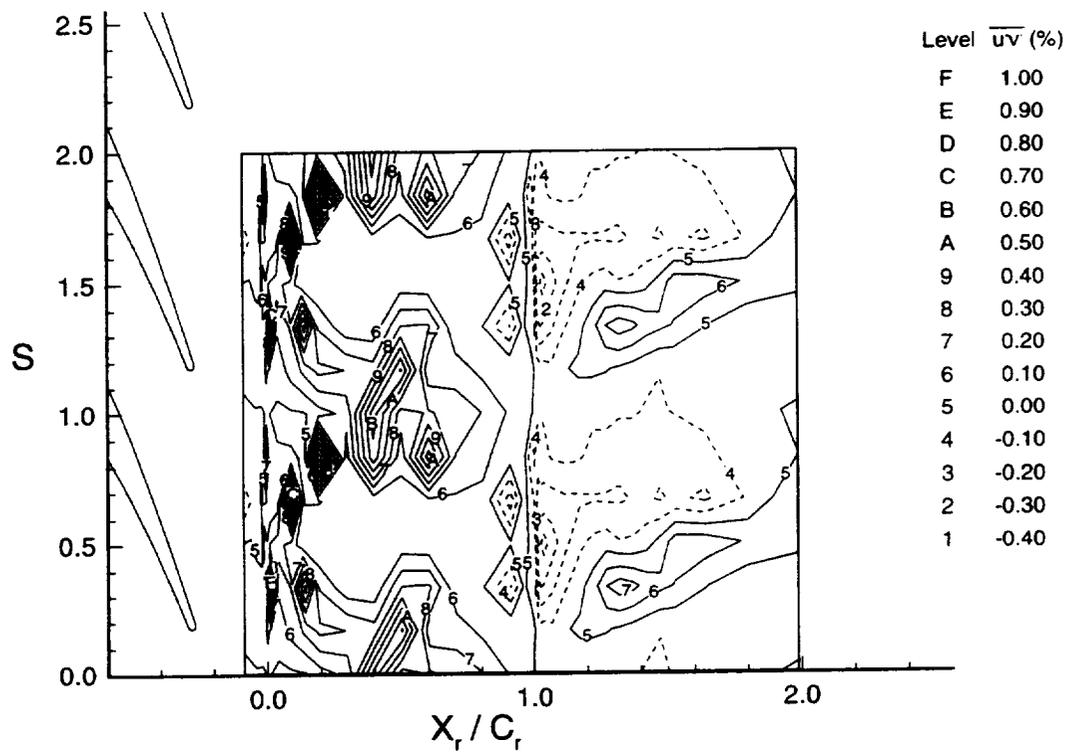
Figure 6.43. Time-Averaged Unresolved Velocity Correlation $\left(\overline{\overline{u'v'}}\right)$

CHAPTER 7

ROTOR FLOW FIELD WAKE CHARACTERISTICS

An understanding of the steady and unsteady characteristics of turbine nozzle and rotor wakes are important for the efficient design of axial flow turbomachinery. A major cause of noise and vibration characteristics of turbomachinery is caused by wakes. Turbine wakes represent a source of loss in efficiency, since the mixing of the wakes with the freestream dissipates energy. The three-dimensional characteristics of the wake, the decay characteristics and the path that it follows is important in the design of the following blade rows. This information is essential for both the prediction of the aerodynamic and mechanical performance of a turbine and for building quieter turbomachines.

7.1 Nozzle Wake Characteristics in Rotor Passage

The nozzle wake absolute velocity profiles upstream of the rotor blade, in the rotor blade passage and downstream of the rotor blade are presented in Figures 7.1 and 7.2a, and b respectively. (The bar over the velocity and angle notation in the figures in Chapter 7 represents ensemble averaging.) The measurement upstream of the rotor were acquired with the five hole probe which was discussed in Chapter 5. For the measurements in and downstream of the rotor, each axial location represents the axial location for each nozzle wake segment where the maximum velocity defect occurs. (A nozzle wake segment is defined as follows. As the nozzle wake enters the rotor passage, it is divided in to individual segments the rotor leading edge and these segments subsequently propagate through the rotor passage independent of each other.) The data is displayed over two rotor blade
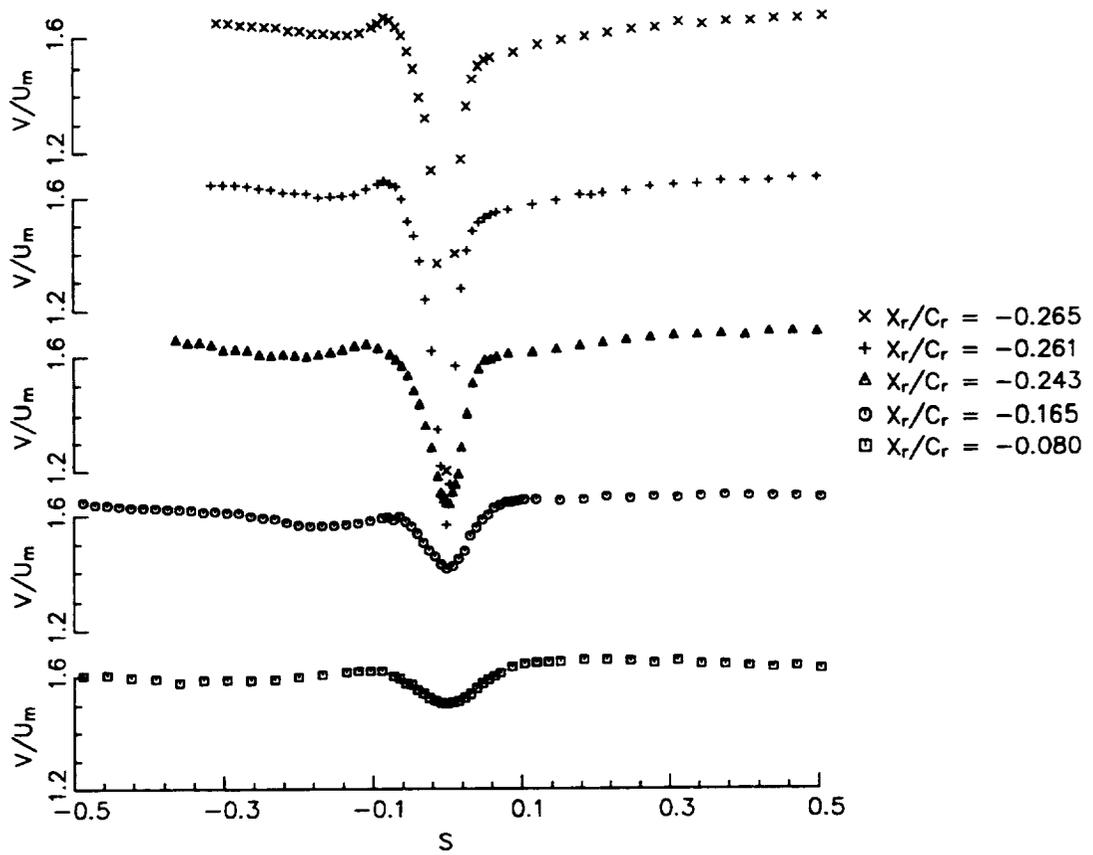
Figure 7.1. Nozzle Wake Total Velocity $\left(V/U_m\right)$ Profiles Upstream of Rotor (Five Hole Probe Measurements)
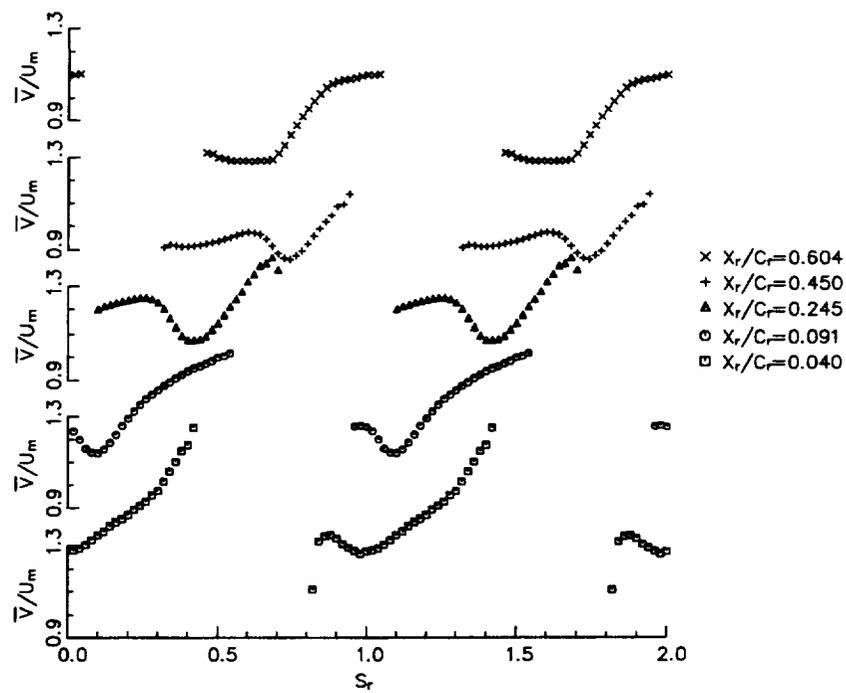
(a)
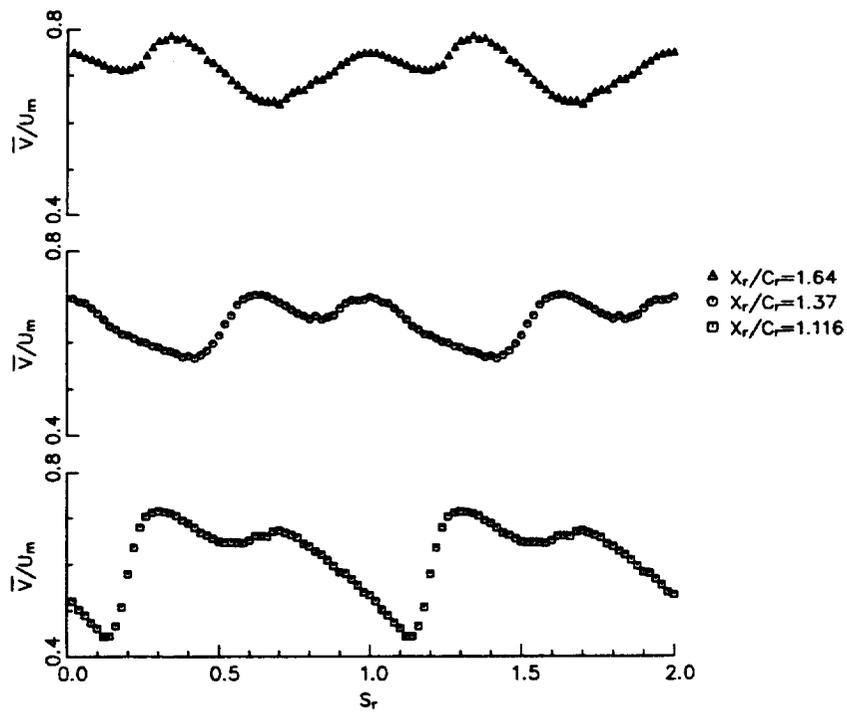
(b)

Figure 7.2 Nozzle Wake Total Velocity $\left(\overline{V}/U_m\right)$ Profiles in Rotor Passage

pitches (the data from one rotor pitch is doubled) to aid interpretation.

Upstream of the rotor, the nozzle wake decays very rapidly as the rotor leading edge is approached. As the nozzle wake moves through the rotor passage, the absolute magnitude of its defect grows and then decreases. Downstream of the rotor trailing edge, the nozzle wake defect remains constant until $X_r/C_r = 1.64$. (The nozzle wake is the smaller of the two velocity defects in the flow field downstream of the rotor while the rotor wake is the larger defect.) The variation in nozzle wake defect is demonstrated more clearly in Figure 7.3, which shows the nozzle wake defect normalized by the local maximum velocity. (The local maximum velocity is the velocity that would exist at the location where the nozzle wake occurs if the nozzle wake did not exist.) This is consistent with the normalization of the nozzle wake velocity defect upstream of the rotor measured by the five hole probe, which is also presented in this figure. Examining this figure, one can see that the velocity defect decreases sharply from the nozzle trailing edge (located at $X_r/C_r = -0.27$) to the rotor leading edge. This rapid decay is due to pressure gradients, high turbulence intensities and wake centerline curvature along with the effect of the rotor. The relative motion between the rotor and the nozzle causes periodic variations in the potential flow field around the blades which causes the wake to decay faster. A more detailed discussion of the nozzle wake decay between the nozzle and rotor is given in Chapter 5 of this thesis.

The nozzle wake then enters the rotor passage where the velocity defect increases from the rotor leading edge up to $X_r/C_r = 0.30$ and decreases after that until the trailing edge. Downstream of the trailing edge the velocity defect is constant. Matsuuchi and Adachi (1983) have observed a similar feature in their axial flow fan. The maximum velocity defect for each upstream stator wake segment in their axial flow fan rotor is presented also in Figure 7.3. As the stator
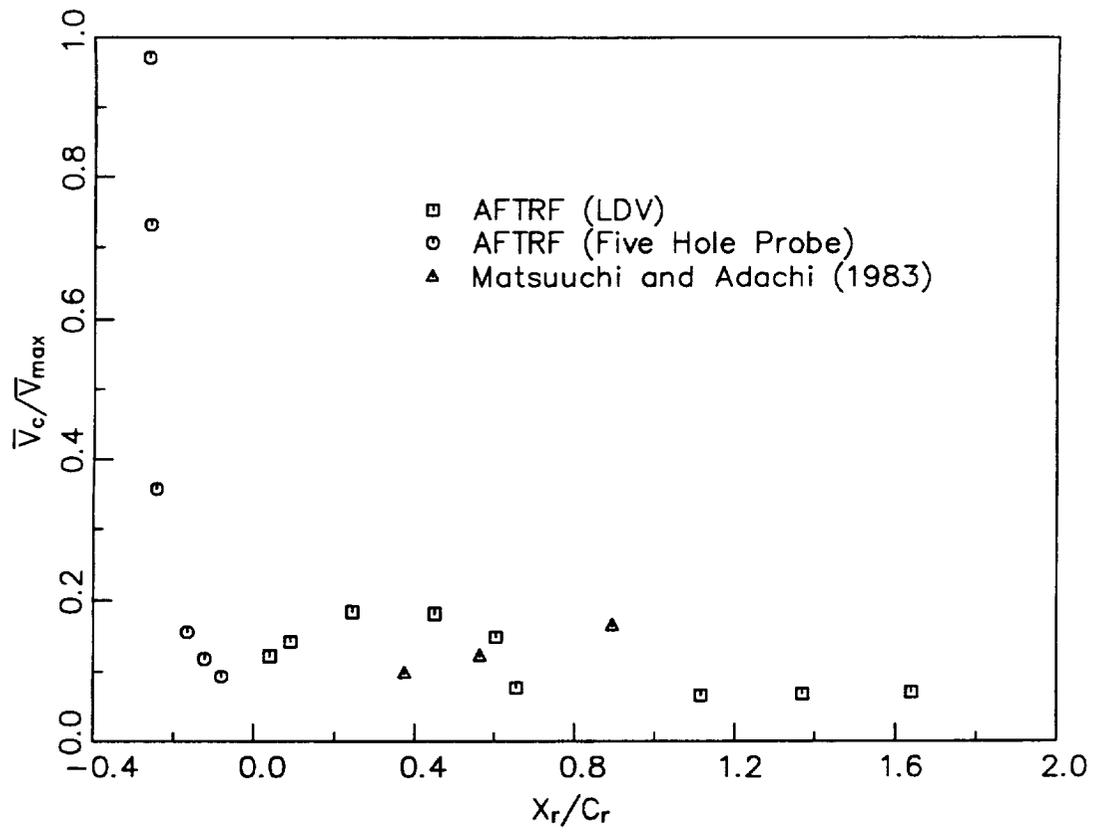
Figure 7.3. Variation of Peak Nozzle Wake Velocity Defect in Rotor Passage

wake travels through the rotor its velocity defect increases. This is because, according to Hill et al. (1963), a positive (adverse) pressure gradient slows the wake decay and if the pressure gradient is large enough the wake decay will be stopped completely and the wake will grow in size. This is what is happening here, since there is a positive pressure gradient in a compressor rotor.

The reasons for the velocity defect increase and decrease in the turbine rotor are more complex. A possible explanation can be given by looking at the mass averaged cycle-averaged relative velocity, presented in Figure 6.33a. The relative velocity slightly decreases from the leading edge until $X_r/C_r = 0.30$, increases sharply from $X_r/C_r = 0.40$ until the trailing edge and then is constant downstream of the trailing edge. The change in wake defect seems to correspond to the relative velocity change, with the defect increasing until $X_r/C_r = 0.30$ and then decreasing downstream of $X_r/C_r = 0.40$. Downstream of the rotor trailing edge, the wake defect is constant. As discussed earlier, Raj and Lakshminarayana (1973) found that the wake decay rate corresponds to the variation in wake edge velocity. In the region where the relative velocity decreases, an adverse pressure gradient occurs, thus causing the nozzle wake velocity defect to increase. Between $X_r/C_r = 0.40$ and the trailing edge, the relative velocity increases, resulting in a favorable pressure gradient which causes the nozzle wake to decay.

Blade to blade profiles of total unresolved unsteadiness (defined by eqn. 6.12) at the axial location where the maximum total unresolved unsteadiness occurs in each nozzle wake segment are shown in Figure 7.4. The total unresolved unsteadiness is normalized by U_m here in order to compare the fluctuating velocity at different axial locations, since the velocity outside of the nozzle wake changes significantly in the rotor. One interesting feature is that the peak magnitude of total unresolved unsteadiness in the nozzle wake does not continuously decay as it

(a)

(b)
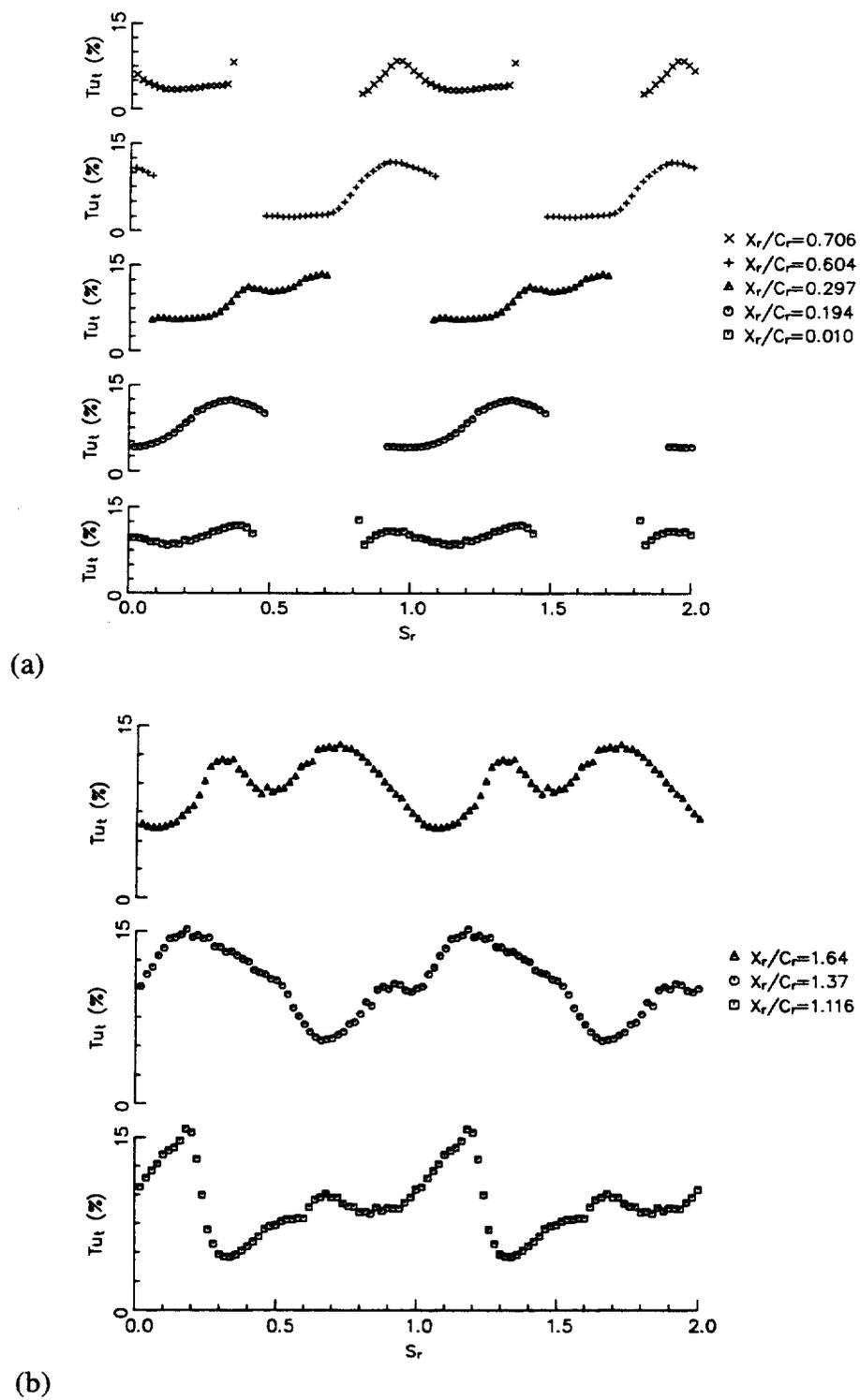
Figure 7.4. Nozzle Wake Total Unresolved Unsteadiness $\left(Tu_t\right)$ in Rotor Passage

travels through and downstream of the rotor passage. This is also established in Figure 7.5, which presents the peak total unresolved unsteadiness for each nozzle wake segment. The peak total unsteadiness increases slightly from the rotor leading edge to $X_r/C_r = 0.30$ after which it decreases dramatically.

This increase and decrease in total unresolved unsteadiness is related to the nozzle wake velocity defect increase and decrease in the rotor passage shown in Figure 7.3. Where the nozzle wake velocity defect increases in the rotor passage (from the rotor leading edge to $X_r/C_r = 0.30$) , the total unresolved unsteadiness increases and where the nozzle wake decays (from $X_r/C_r = 0.40$ to the rotor trailing edge) the nozzle wake total unresolved unsteadiness decays. An additional effect that could cause the decrease in total unresolved unsteadiness from $X_r/C_r = 0.40$ to the rotor trailing edge can be seen by examining Figure 6.33a, which is the mass-averaged cycle-averaged relative velocity in the rotor. The relative velocity increases sharply downstream of $X_r/C_r = 0.30$ and since the total unsteadiness decays in an accelerating flow field, the maximum total unsteadiness in each nozzle wake segment decreases also. Downstream of the rotor, the nozzle wake total unsteadiness increases in magnitude until at one half chord downstream of the rotor it is at the same value as it is at the rotor inlet. Sharma et al. (1985) also notice in their axial flow turbine that the nozzle wake total unsteadiness downstream of the rotor is the same order of magnitude as it is upstream of the rotor. Another interesting feature of this flow field can be seen downstream of the rotor in Figure 7.4. Close to the trailing edge, the total unsteadiness of the rotor wake is much higher than the nozzle wake. As the wakes travel downstream, the rotor wake total unsteadiness decreases while the nozzle wake total unsteadiness increases until at one half chord downstream of the rotor the total unsteadiness for both the nozzle and rotor wakes are equal in magnitude.
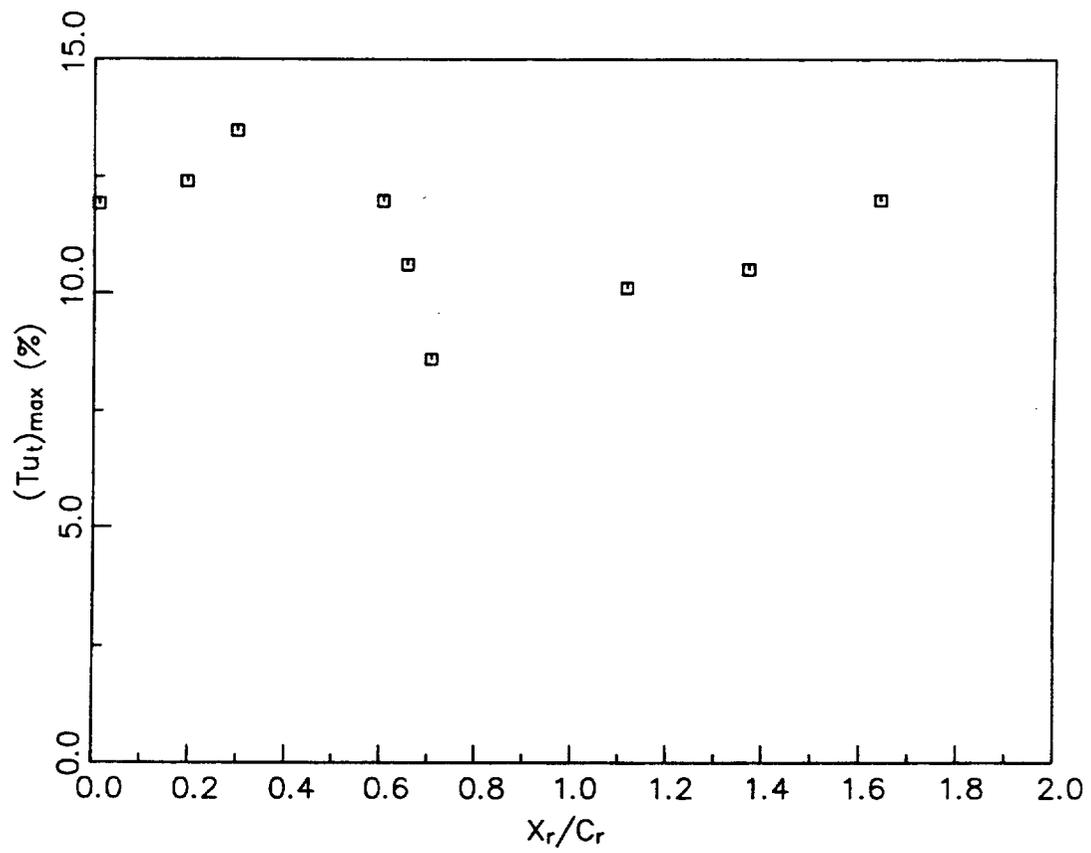
Figure 7.5. Variation of Peak Nozzle Wake Total Unresolved Unsteadiness $\left(Tu_t\right)_{max}$ in Rotor Passage

Blade to blade profiles of unresolved velocity cross correlation (defined by eqn. 6.14) at the axial location where the maximum unresolved velocity cross correlation occurs in each nozzle wake segment are presented in Figures 7.6a and b. As the nozzle wake travels through the rotor passage, the velocity cross correlation grows until midchord, after which is decreases sharply. This is clear from Figure 7.7, which is the variation of peak unresolved velocity cross correlation in each nozzle wake segment. The unresolved velocity cross correlation increases as the nozzle wake travels through the rotor passage until midchord, after which is decreases. This decrease occurs at the same location as the decrease in total unresolved unsteadiness and they are probably related.

7.2 Rotor Wake Characteristics

The rotor wake can be classified into three different categories, the trailing edge region, the near wake and the far wake. The trailing edge region is confined to the area just downstream of the trailing edge. The velocity defect is very large in the region. In the near wake region, the physical characteristics of the blade and the aerodynamic loading on the blade have a major impact on the development of the wake, causing the wake to be asymmetric. The wake defect is of the same order of magnitude as the mean velocity in this region. In the far wake the wake structure is almost symmetric and the physical characteristics and the aerodynamic loading have minor effects on the development of the wake. The velocity defect is also small in the far wake region. For the turbine rotor wake data presented in this thesis, the individual regions are defined as follows:

a)

(b)
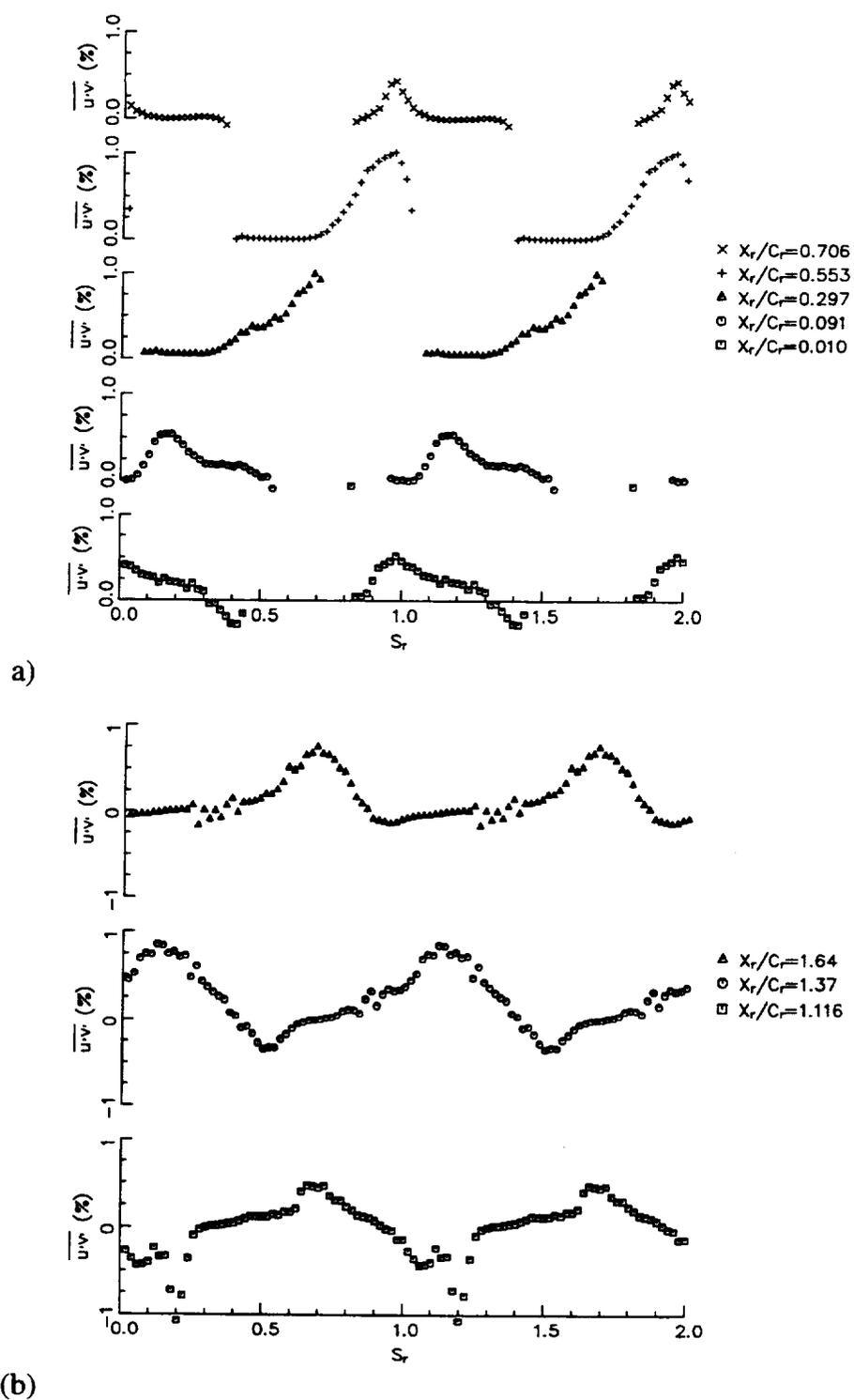
Figure 7.6. Nozzle Wake Unresolved Velocity Correlation $\left(\overline{u'v'}\right)$ in Rotor Passage
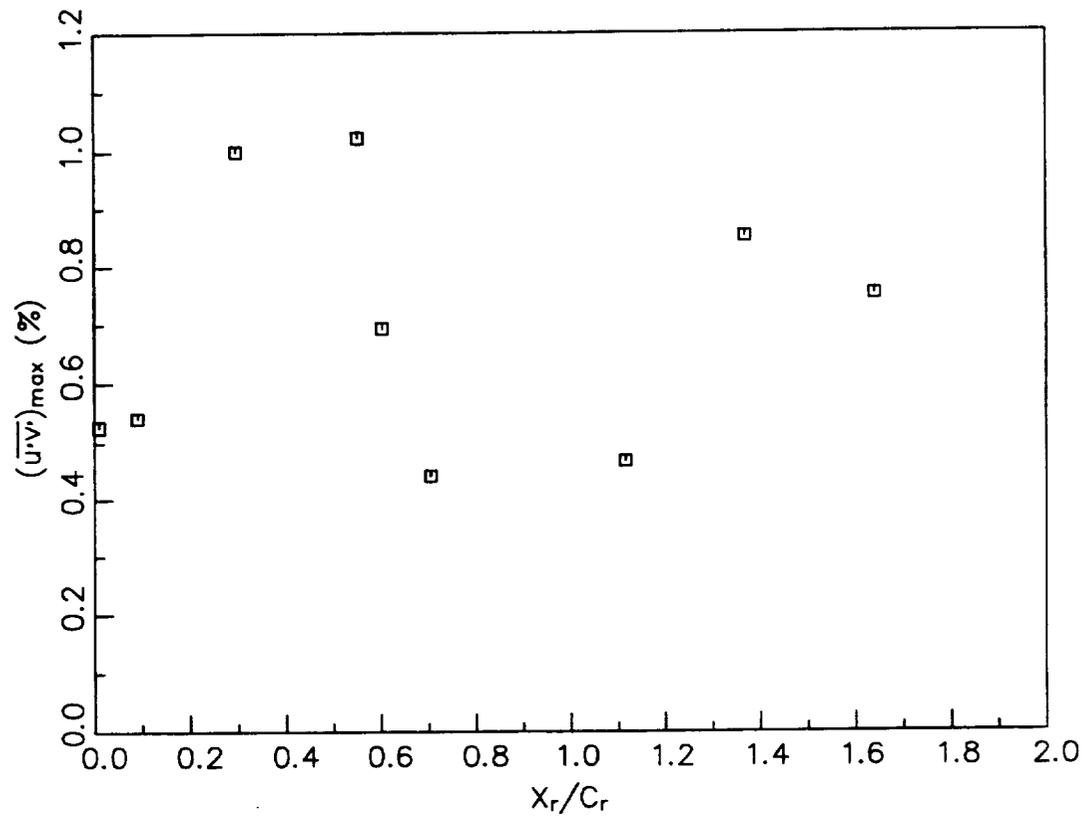
Figure 7.7. Variation of Peak Nozzle Wake Unresolved Velocity Correlation
$\left(\overline{u'v'}\right)_{max}$ in Rotor Passage

Trailing Edge Region: $X_r/C_r < 1.014$

$$(Z/\cos\beta_o < 0.035)$$

Near Wake Region: $1.014 < X_r/C_r < 1.22$

$$(0.035 < Z/\cos\beta_o < 0.555)$$

Far Wake Region: $X_r/C_r > 1.22$

$$(Z/\cos\beta_o > 0.555)$$

where $Z/\cos\beta_o$ is the streamwise distance downstream of the rotor (Z is the axial distance downstream of the rotor with $Z = 0.0$ at the trailing edge and β_o is the rotor blade outlet angle).

7.2.1 Cycle-Averaged Properties

Figures 7.8a and 7.8b show the cycle-averaged relative velocity profiles at several axial locations in the rotor wake. (As in chapter 6, all velocities presented in chapter 7 are ensemble averaged.) The abscissa in the figure represents the tangential distance normalized by the rotor blade pitch, with Y equal to 0.0 at the wake center. The velocity gradients in the tangential direction are very large just downstream of the rotor trailing edge. This feature results from the development of the flow as it transitions from the blade boundary layer to the wake. Farther downstream the gradient becomes much smaller due to wake spreading and mixing with the freestream as well as interchange of momentum and energy on either side of the wake. Also, the wake profiles are asymmetrical about the wake center due to the differential growth of the boundary layer on the two surfaces of the blade. The suction side of the wake has a larger width than the pressure side wake width since the suction surface boundary layer at the blade trailing edge is larger than the
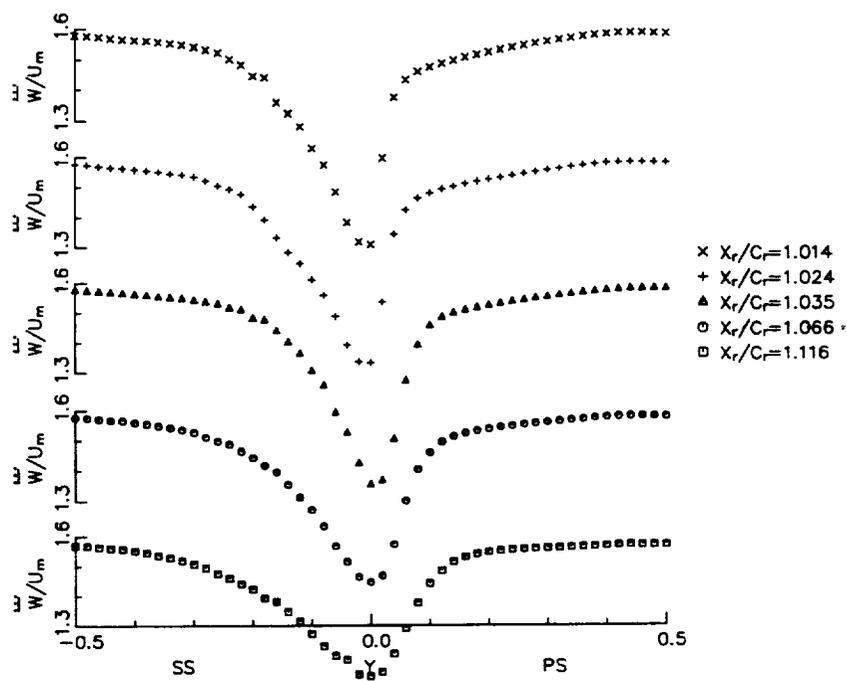
(a)
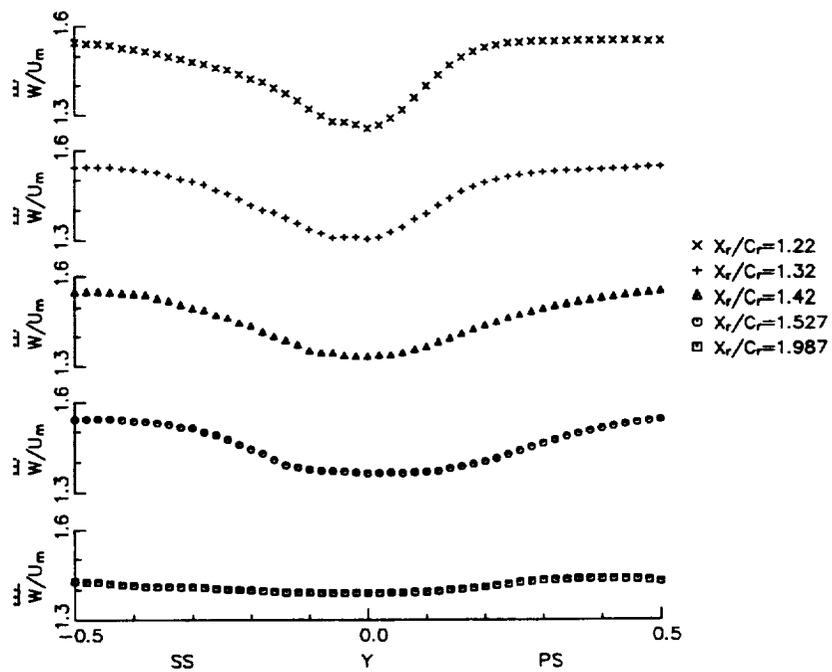
(b)

Figure 7.8. Rotor Wake Cycle-Averaged Relative Velocity $\left(\overline{\overline{W}}/U_m\right)$ Profiles

pressure surface boundary layer. As the wake moves downstream, the differences between the pressure side and the suction side of the wake diminish until $X_r/C_r =$ 1.22, where the wake profile becomes symmetrical about the wake center. This also results from wake spreading and mixing as discussed earlier.

The cycle-averaged total unresolved unsteadiness (normalized by U_m to show the absolute level of the fluctuations and defined by equation 6.12) is presented in Figures 7.9a and 7.9b. The total unresolved unsteadiness is highest near the trailing edge and decreases further downstream. The high values near the trailing edge result from the vortex street shed from the trailing edge and the high production of turbulence in this region. The unsteadiness profiles are asymmetric about the wake center in the near wake becoming symmetric farther downstream. This results from the differential growth of the boundary layer on the pressure and suction surfaces of the blade. The unsteadiness profiles have a dip in unsteadiness at the wake center with higher values of unsteadiness on either side of the dip. This is to be expected since the total unsteadiness is zero on the blade surface with the maximum value occurring slightly away from the surface. This dip in total unsteadiness disappears due to wake spreading and mixing, as the wake travels downstream. The highest total unsteadiness is observed on the pressure side of the wake which demonstrates that the pressure surface boundary layer has a higher total unsteadiness than the suction surface boundary layer. This is due to the concave curvature effect on the pressure surface and the interaction of the nozzle wake with the pressure surface boundary layer, discussed earlier. This increases the unresolved unsteadiness which persists even in the wake. The maximum total unsteadiness occurs close to the wake center in the near wake. Farther downstream, the maximum total unsteadiness occurs away from the wake center due to the spread of the wake.
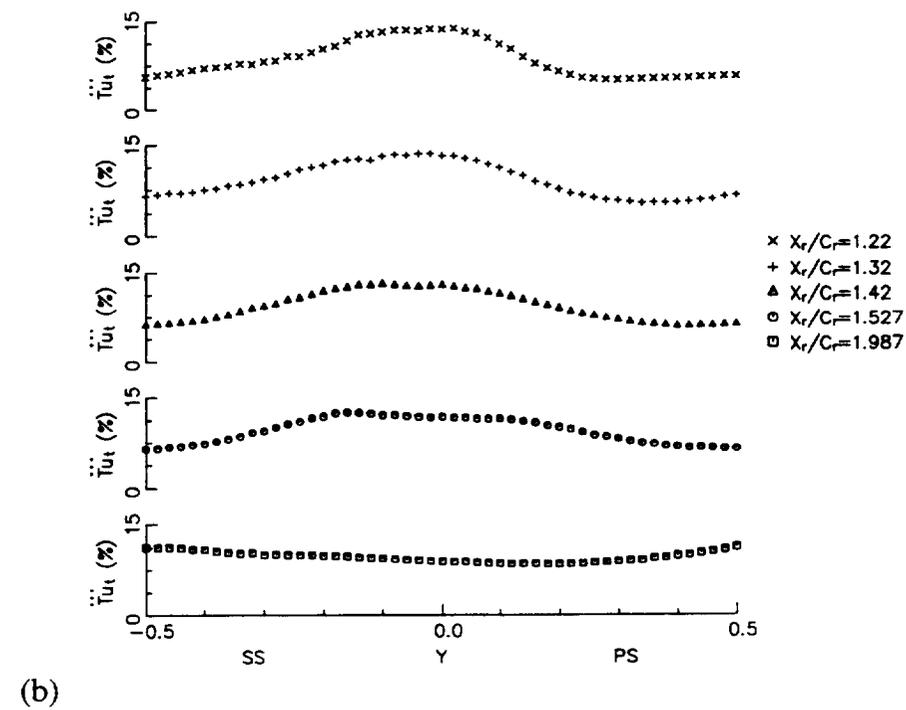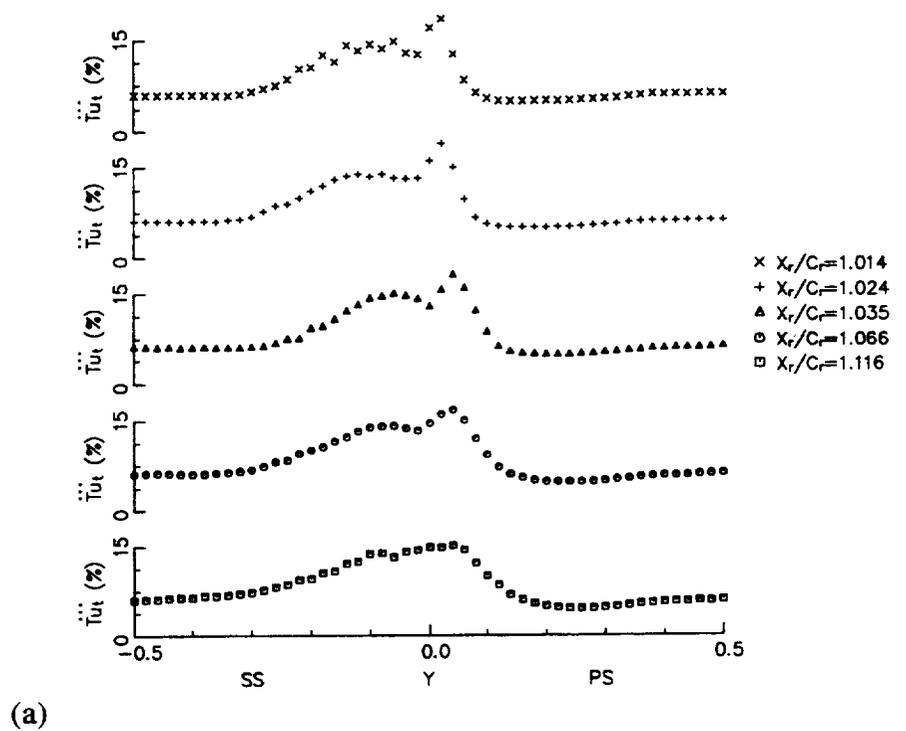
Figure 7.9. Rotor Wake Cycle-Averaged Total Unsteadiness $\left(\overset{\bullet\bullet\bullet}{Tu_t}\right)$ Profiles

The cycle-averaged unresolved velocity cross correlation in the streamwise-normal coordinate system (defined by equation 6.15) is shown in Figures 7.10a and 7.10b. The streamwise-normal coordinate system is used to aid physical interpretation. The unresolved velocity cross correlation is very small in the free stream and reaches a maximum value in the wake center. This is to be expected since the unresolved velocity cross correlation results from velocity and turbulence intensity gradients. The velocity cross correlation changes sign near the wake center due to the opposite velocity gradients on either side of the wake center, but close to the trailing edge the zero unresolved velocity cross correlation does not occur at the point of minimum velocity. Other researchers, such as Lakshminarayana and Reynolds (1979) also see this feature in their rotor wakes. Beyond $X_r/C_r = 1.035$, the maximum value of unresolved velocity cross correlation occurs at the point of minimum velocity. In the near wake, the unresolved velocity cross correlation profiles are asymmetric about the wake center, with the magnitude of the cross correlation on the pressure side being larger than the magnitude on the suction side. The difference in the unresolved velocity cross correlation between the pressure and suction side of the wake decreases as the wake travels downstream until $X_r/C_r = 1.22$, where the cross correlation profile becomes symmetric about the wake center. The unresolved velocity cross correlation decays rather slowly with significant values of this correlation still occurring one half chord downstream of the rotor.

The relative flow angle in the cycle-averaged rotor wake is presented in Figure 7.11. Just downstream of the rotor trailing edge, the flow is overturned on the suction side of the wake and underturned on the pressure side of the wake. This is due to the difference in flow direction on the pressure and suction surface of the
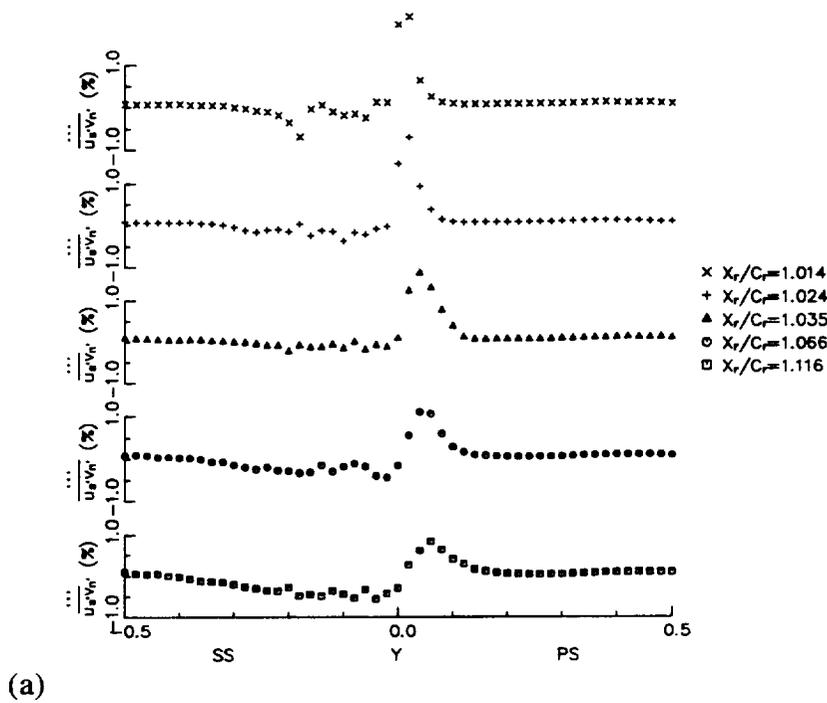
(a)
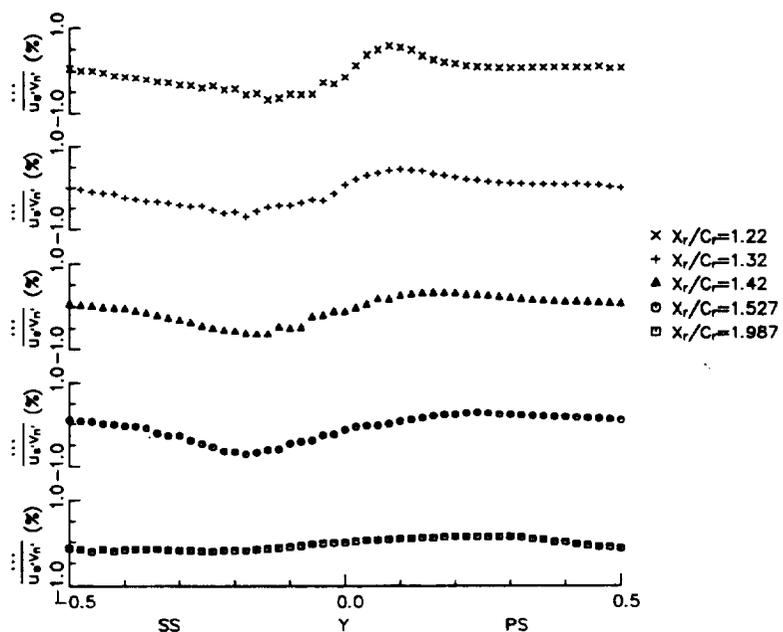
(b)

Figure 7.10. Rotor Wake Cycle-Averaged Unresolved Streamwise-Normal

Velocity Correlation $(\overline{\overline{u'_s v'_n}})$ Profiles

$\overset{\cdots}{\overline{\beta}}$ (°)

$\overset{\cdots}{\overline{\beta}}$ (°)

$\overset{\cdots}{\overline{\beta}}$ (°)

$\overset{\cdots}{\overline{\beta}}$ (°)

$\overset{\cdots}{\overline{\beta}}$ (°)

−50

−70

−50

−70

−50

−70

−50

−70

−50

−70

× X_r/C_r=1.014
+ X_r/C_r=1.024
▲ X_r/C_r=1.035
⊙ X_r/C_r=1.066
□ X_r/C_r=1.527

0.5   0.0   0.5

SS   Y   PS
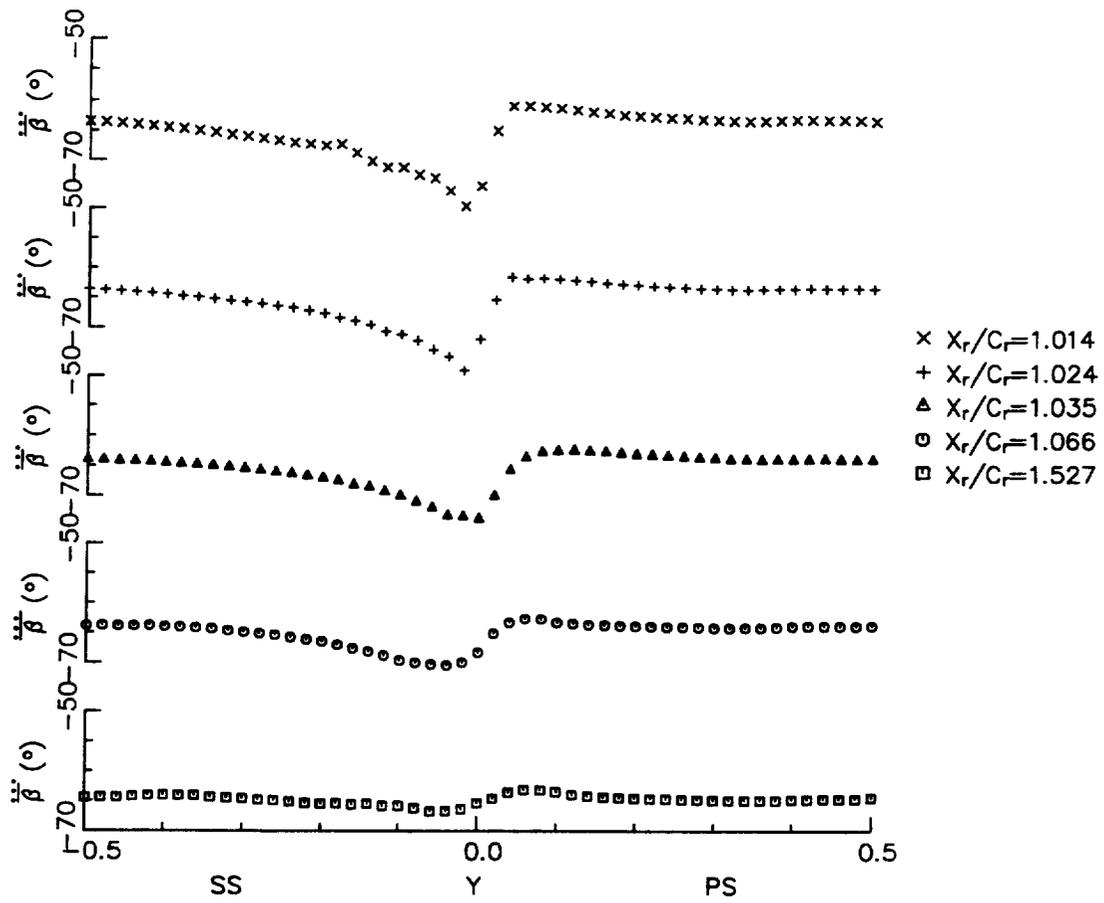
Figure 7.11. Rotor Wake Cycle-Averaged Relative Flow Angle ($\overset{\cdots}{\overline{\beta}}$) Profiles

rotor. This over and underturning of the flow angle decreases rapidly from a maximum of 17 degree difference at the trailing edge to a three degree difference in flow angle at 10 % chord downstream.

7.2.2 Cycle-Averaged Wake Decay Properties

A knowledge of the rate of decay for the rotor wake defect is necessary for an understanding of the rotor-stator interaction as discussed earlier. The decay of the velocity defect is influenced by the pressure gradient, turbulence intensity, curvature and viscous effects. The velocity defect decay for the cycle-averaged rotor wake is shown in Figure 7.12. The very rapid decay in the trailing edge region results from the high unresolved unsteadiness and possibly the three dimensional effects in this region. In the near and far wake regions, the velocity defect decay is less rapid. The rotor wake velocity defect is also compared to the decay of the AFTRF nozzle wake, and the decay of two linear rotor cascades, Sitaram and Govardhan's (1986) and Ho and Lakshminarayana's (1994) who computed the flow field in Gregory-Smith's rotor cascade, which has similar flow turning as the present turbine rotor. The AFTRF rotor velocity defect decays much slower than the velocity defects of the other blades. This is in contrast to a compressor rotor wake which decays faster than the wake of a compressor cascade. This reason for this is not understood as of yet. It is possible that the low momentum fluid from other spanwise locations is being convected into the midspan wake and thus causing the midspan wake to be deeper and to decay slower. Future measurements at midspan and other spanwise locations that include the radial velocity are needed to verify this.
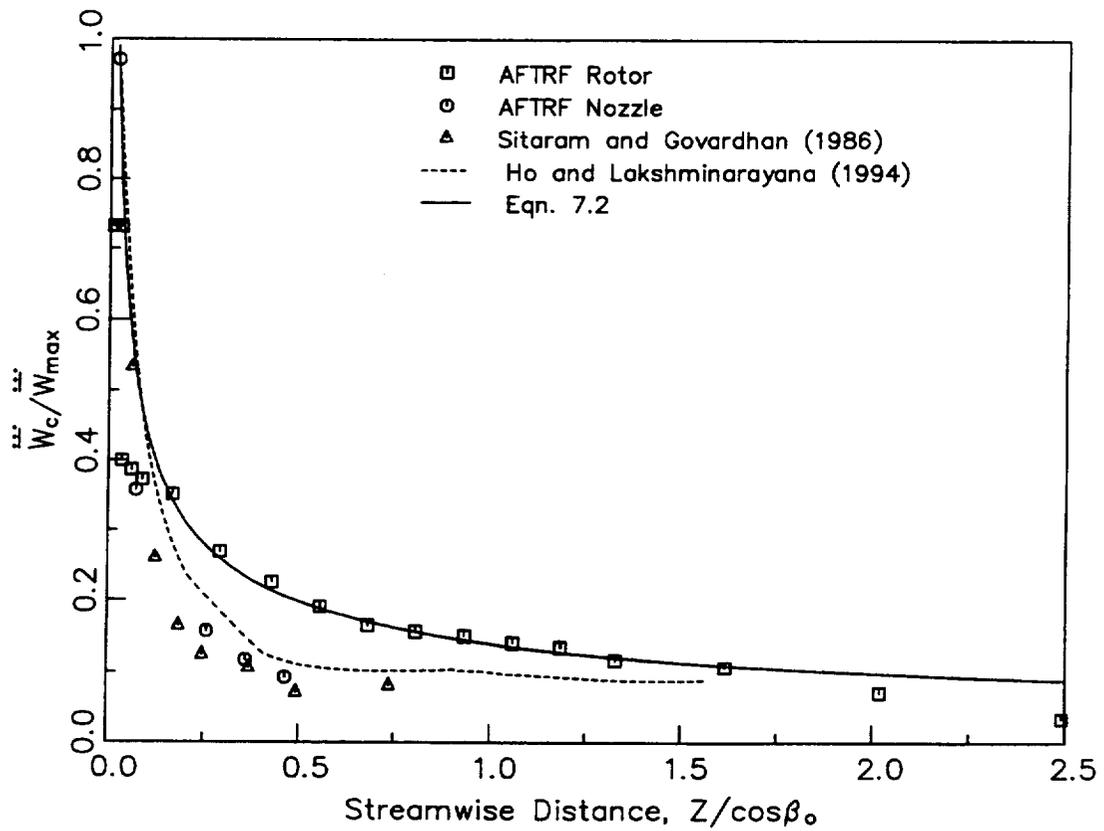
Figure 7.12. Decay of Cycle-Averaged Rotor Wake Velocity Defect

Schlichting's (1979) analysis indicates that a plane wake defect decays far downstream according to

$$\frac{V_c}{V_{max}} \propto S^{-\frac{1}{2}} \qquad (7.1)$$

where V_c is the velocity defect, V_{max} is the maximum velocity in the free stream outside of the wake, and S is streamwise distance. Using this relationship to correlate the rotor wake velocity defect results in the following equation

$$\frac{\overset{\bullet\bullet\bullet}{\overline{W}_c}}{\overset{\bullet\bullet\bullet}{\overline{W}}_{max}} = 0.14 \left(\frac{Z}{\cos\beta_o} \right)^{-\frac{1}{2}} \qquad (7.2)$$

where $\overset{\bullet\bullet\bullet}{\overline{W}_c}$ is the cycle-averaged velocity defect, $\overset{\bullet\bullet\bullet}{\overline{W}}_{max}$ is the cycle-averaged maximum relative velocity in the free stream outside of the wake, $Z/\cos\beta_o$ is the streamwise distance downstream of the rotor (Z is the axial distance downstream of the rotor with Z = 0.0 at the trailing edge and β_o is the rotor blade outlet angle). This correlation can be seen to match the data quite well over most the region downstream of the rotor in Figure 7.12. It is not very good just downstream of the rotor trailing edge. In this region, the flow is very complex and is dominated by flow separation and trailing edge vortices along with the high levels of total unsteadiness, thus the wake decays much faster than farther downstream. And since the correlation was developed for a far wake, it does not hold in the trailing edge region. The constant in eqn. 7.2, 0.14, probably depends on the aerodynamic properties of the blade such as blade loading and turbulence intensity. These properties need to be varied for a more general wake decay correlation to be derived.

The variation of the cycle-averaged rotor semi-wake width with streamwise

distance is shown in Figure 7.13. Semi-wake width is defined as the width of the wake where the total relative velocity defect is half. The data from the Sitaram and Govardhan's (1986) rotor cascade is also presented there for comparison. Both wake width's increase rapidly just downstream of the trailing edge (in the trailing edge region) and then grow more gradually in the near and far wake regions. Very far downstream (beyond $Z/\cos\beta_0 = 1.5$), the AFTRF rotor wake width grows at a much slower rate. Since the interchange of mass, energy and momentum is continuous on both side of the wake as the wake travels downstream, the growth should be continuous and this is seen in Figure 7.12.

Schlichting's (1979) analysis indicates that the increase of rotor semi-wake width is proportional to streamwise distance as follows,

$$L \propto S^{\frac{1}{2}}$$ (7.3)

where S is streamwise distance and L is semi-wake width (the wake width at half the maximum velocity defect). Using equation (7.3), the variation of semi-wake width over most of the streamwise distance can be represented quite accurately by the equation

$$L/S = 0.389 (Z/\cos\beta_0)^{\frac{1}{2}}$$
$$\text{for } 0.088 < (Z/\cos\beta_0) < 2.5$$ (7.4)

The semi-wake width variation of Sitaram and Govardhan (1986) turbine rotor also matches this equation. Their turbine rotor has similar loading as the AFTRF turbine rotor (AFTRF rotor flow turning is 110 degrees and Sitaram and Govardhan's rotor flow turning is 120 degrees). Since wake width depends on the
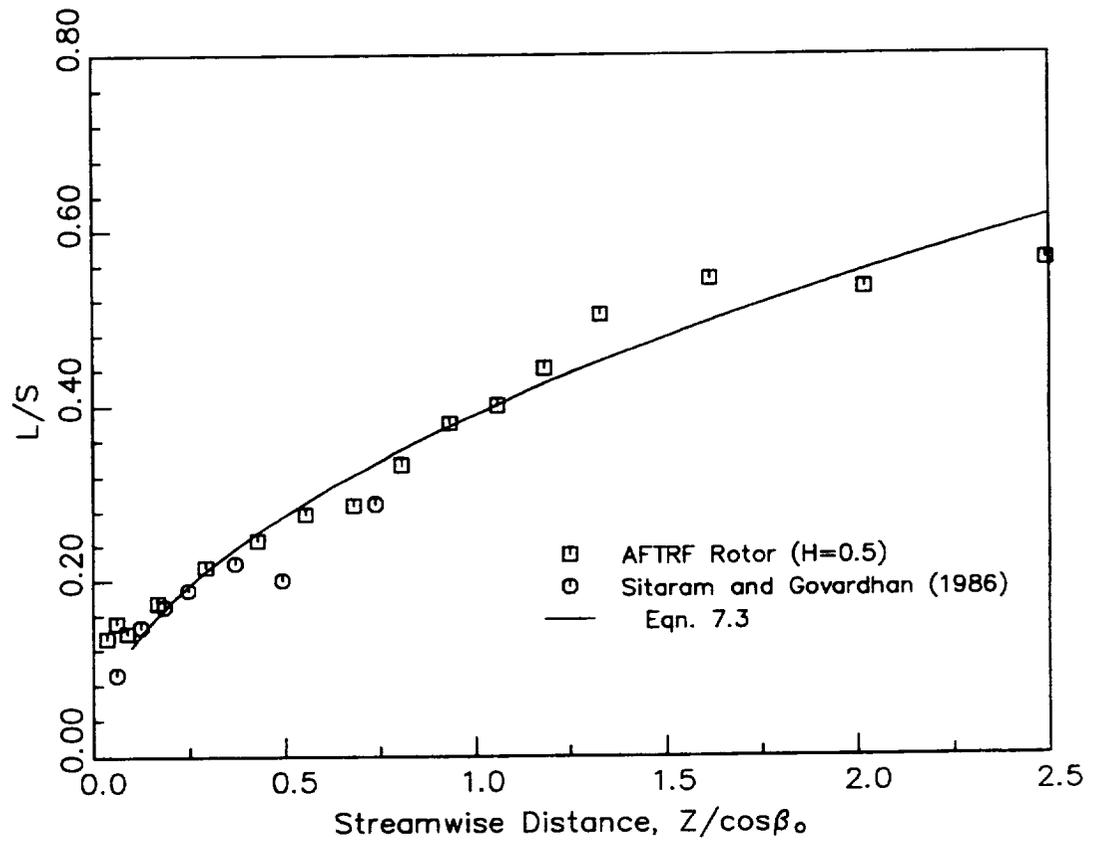
Figure 7.13. Variation of Cycle-Averaged Semi-Wake Width with Streamwise
Distance

aerodynamic properties of the blade and this should be a function of the blade loading, equation (7.4) probably would need to be modified to match the wake width data of a turbine rotor with different loading.

An interesting feature in the variation of semi-wake width is observed between the trailing edge and near wake regions. The semi-wake width grows rapidly in the trailing edge region (from the trailing edge to $Z/\cos\beta_o = 0.061$) and then decreases sharply between the trailing edge region and the near wake region (between $Z/\cos\beta_o = 0.061$ and 0.088). It then increases more gradually beyond $Z/\cos\beta_o = 0.088$. Reynolds et al. (1979) also see this feature in their compressor rotor wake width. This phenomenon is a characteristic of rotor wakes, since the two turbine cascade wake widths do not have this decrease in wake width. It is caused by the effect of three-dimensional flow (radial flows) on the wake which are not present in cascade wakes. The radial transport of mass, momentum and energy could be responsible for the small decrease in wake width between the trailing edge and near wake regions, although the wake defect is decaying steadily there.

The decay of the maximum cycle-averaged relative total, axial and tangential unsteadiness is presented in Figure 7.14. The relative total unresolved unsteadiness is defined by equation (6.9) while the relative unresolved axial and tangential unsteadiness is defined as follows:

$$Tu_x = \frac{\sqrt{\overline{u'^2}}}{W} \times 100\%$$

$$Tu_\theta = \frac{\sqrt{\overline{v'^2}}}{W} \times 100\%$$
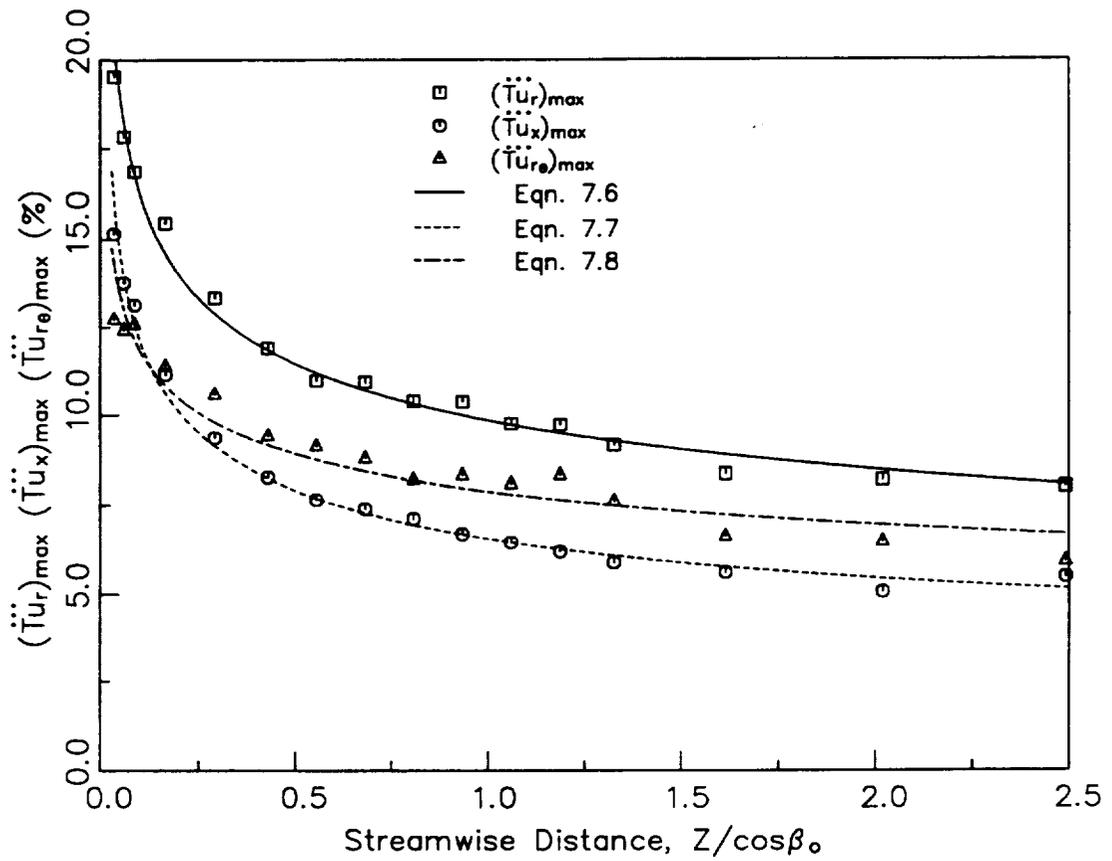
Figure 7.14. Decay of Rotor Wake Cycle-Averaged Maximum Relative Total
Unresolved Unsteadinesses

The relative total, axial and tangential unresolved unsteadiness is then cycle-averaged using equation (6.8).While the unsteadiness is very high in the trailing edge region, it decays rapidly as the wake travels downstream. In the far wake region, beyond $Z/\cos\beta_o = 1.50$, the relative unsteadiness has decayed to its magnitude upstream of the rotor blade. Each of the relative unsteadinesses do not decay at the same rate but can be shown to decay at a rate given by

$$(Tu)_{max} = \left(\frac{Z}{\cos\beta_o}\right)^n \qquad (7.5)$$

according to Raj and Lakshminarayana (1976), where K and n assume different values for each unsteadiness. For the AFTRF turbine rotor, the rate of decay of the maximum cycle-averaged relative total, axial and tangential unsteadinesses are given by the following expressions, based on the data:

$$(\overset{\cdots}{Tu}_r)_{max} = 9.85\left(\frac{Z}{\cos\beta_o}\right)^{-0.219} \qquad (7.6)$$

$$(\overset{\cdots}{Tu}_x)_{max} = 6.56\left(\frac{Z}{\cos\beta_o}\right)^{-0.269} \qquad (7.7)$$

$$(\overset{\cdots}{Tu}_{\theta_r})_{max} = 7.87\left(\frac{Z}{\cos\beta_o}\right)^{-0.179} \qquad (7.8)$$

The above expressions match the data quite well, as seen in Figure 7.14. The good match of the equation (7.5) with both Raj and Lakshminarayana's (1976) compressor rotor maximum unsteadiness and the AFTRF turbine rotor data shown

here gives confidence that it can be used as a general equation for the decay of Reynolds' stresses downstream of turbine and compressor rotors. Since the exponent n varies from -0.18 to -0.22 for the turbine rotor and -0.19 to -0.24 for the streamwise and normal components of relative unsteadiness in the compressor rotor (see Raj and Lakshminarayana, 1976), assuming the exponent is equal to -0.2 will give a fairly good fit for the expression. The constant K probably depends on factors such as the blade drag coefficient, the inlet unsteadiness and the mean velocity. Including the effect of these factors into the equation could collapse the data into a universal curve and lead to good correlation. For this to be done, though, the unsteadiness in the rotor wake at other conditions, such as different blade loading, inlet unsteadiness and mean velocity needs to be measured since the turbine rotor data here represents the only turbine rotor unsteadiness data the author has knowledge of.

The decay of the maximum cycle-averaged streamwise-normal unresolved velocity cross correlation is presented in Figure 7.15. The unresolved velocity cross-correlation is very high in the trailing edge region and it decays very rapidly as the wake travels downstream. The rate of decay seems to follow the same trend as the decay of the relative unsteadinesses and using an equation of the form of equation (9.5), the maximum cycle-averaged unresolved velocity cross correlation decay rate can be given by

$$\left(\overline{\overline{u_s' v_n'}}\right)_{max} = 0.335\left(\frac{z}{\cos\beta_o}\right)^{-0.644} \tag{7.9}$$

This correlation agrees with the data quite well as can be seen in Figure 7.15.

The decay of the maximum cycle-averaged periodic and unresolved
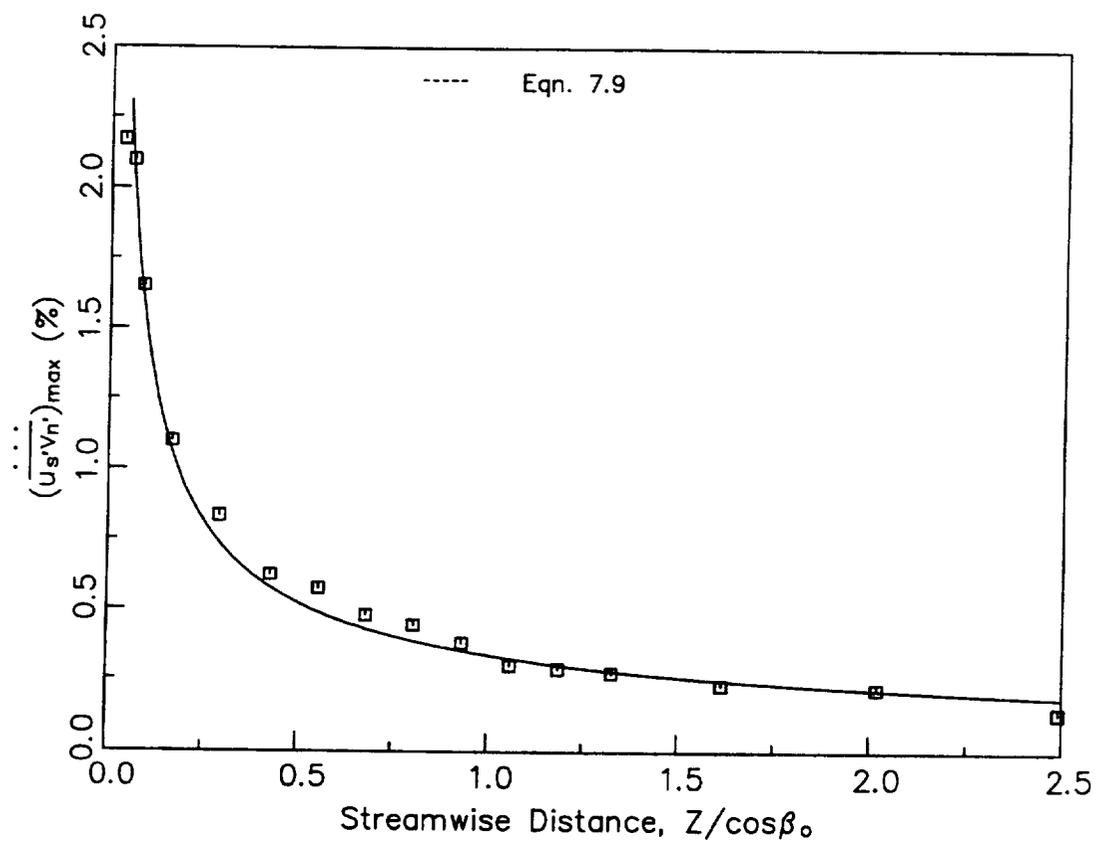
Figure 7.15. Decay of Rotor Wake Cycle-Averaged Maximum Unresolved

Velocity Correlation $\left(\overline{\overset{\cdots}{u_s' v_n'}}\right)_{max}$

unsteady velocity axial tangential and cross correlations are shown in Figures 7.16, 7.17 and 7.18. For all three correlations, the maximum periodic unsteady velocity correlations are much larger than the maximum unresolved correlations in the trailing edge region. This is because the periodic velocity correlations are due to the periodic variation in velocity over the rotor blade pitch, which is large in the rotor wake. But the periodic correlations decay much faster than the unresolved correlations so that the maximum periodic axial velocity correlation ($\overset{\bullet\bullet\bullet}{\overline{\tilde{u}\tilde{u}}}$) is less than the maximum unresolved axial velocity correlation ($\overset{\bullet\bullet\bullet}{\overline{u'u'}}$) downstream of $Z/\cos\beta_o =0.25$, while the magnitude of the maximum periodic tangential velocity correlation ($\overset{\bullet\bullet\bullet}{\overline{\tilde{v}\tilde{v}}}$) becomes lower than the maximum unresolved tangential velocity correlation ($\overset{\bullet\bullet\bullet}{\overline{v'v'}}$) downstream of $Z/\cos\beta_o=0.75$. While the maximum periodic unsteady velocity cross correlation ($\overset{\bullet\bullet\bullet}{\overline{\tilde{u}\tilde{v}}}$) decays more rapidly than the maximum unresolved velocity cross correlation ($\overset{\bullet\bullet\bullet}{\overline{u'v'}}$), the magnitude of the maximum periodic cross correlation never is lower than the magnitude of the maximum unresolved cross correlation. Both decay to negligible values in the far wake. The decay of the maximum cycle-averaged unresolved velocity correlation reflect the same trend as the relative unsteadiness and can be modeled using equation (7.5) as follows:

$$\left(\overset{\bullet\bullet\bullet}{\overline{u'u'}}\right)_{max} = 1.64\left(\frac{Z}{\cos\beta_o}\right)^{-0.368} \tag{7.10}$$

$$\left(\overset{\bullet\bullet\bullet}{\overline{v'v'}}\right)_{max} = 2.41\left(\frac{Z}{\cos\beta_o}\right)^{-0.158} \tag{7.11}$$

$$\left(\overset{\bullet\bullet\bullet}{\overline{u'v'}}\right)_{max} = 2.83\left(\frac{Z}{\cos\beta_o}\right)^{-0.704} \tag{7.12}$$
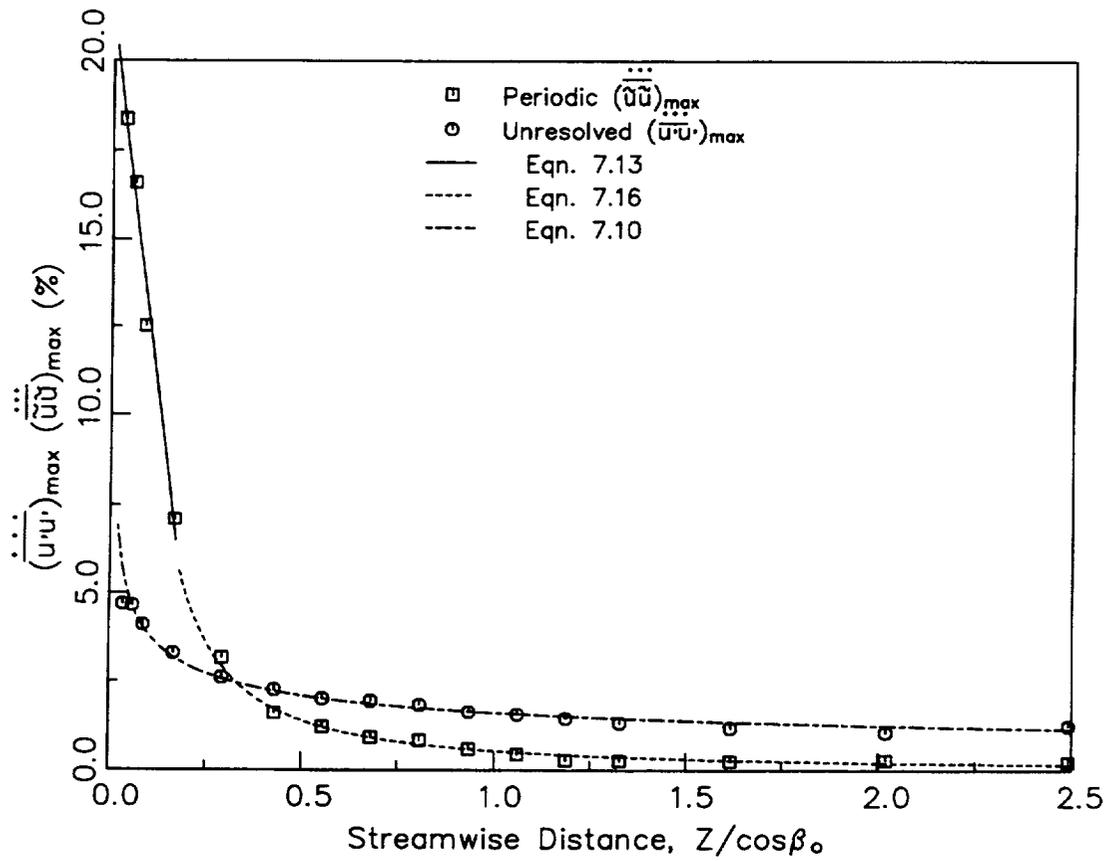
Figure 7.16. Decay of Rotor Wake Cycle-Averaged Maximum Unresolved $\left(\overline{u'u'}\right)_{max}$ and Periodic $\left(\overline{\tilde{u}\tilde{u}}\right)_{max}$ Velocity Correlations
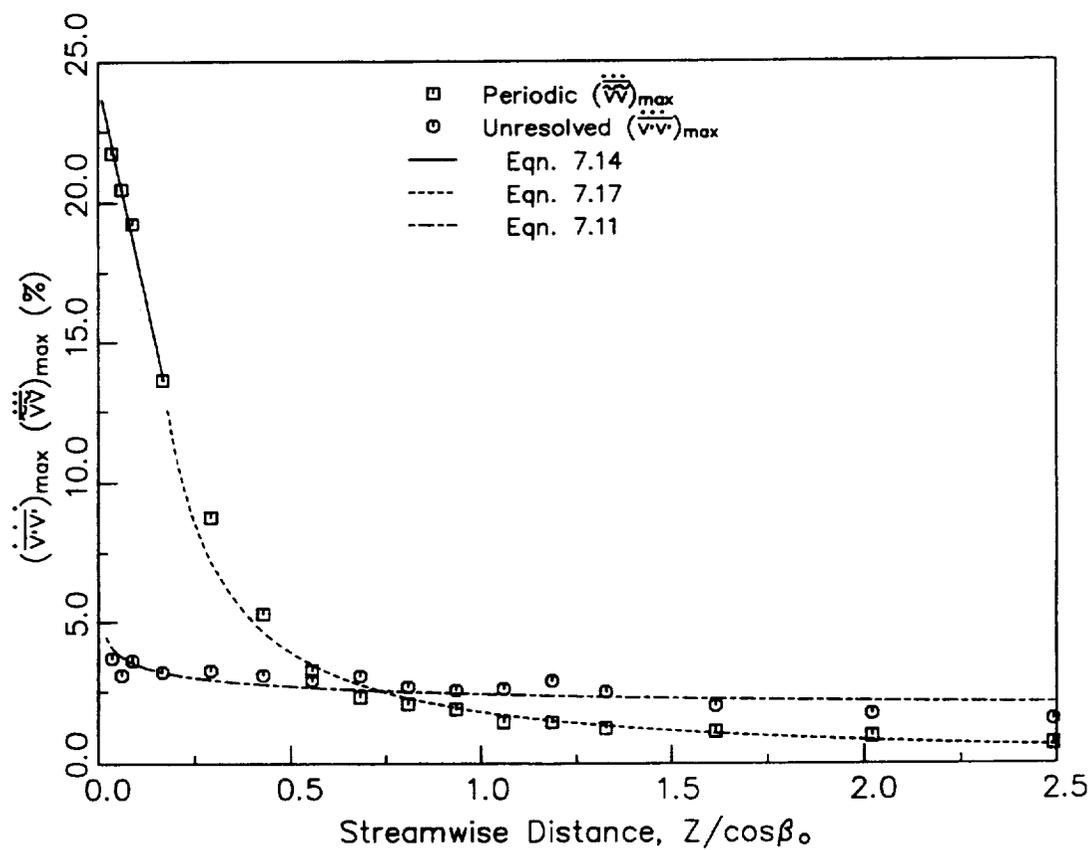
Figure 7.17. Decay of Rotor Wake Cycle-Averaged Maximum Unresolved $\left(\overline{\dddot{v'v'}}\right)_{max}$ and Periodic Velocity Correlation $\left(\overline{\dddot{\tilde{v}\tilde{v}}}\right)_{max}$
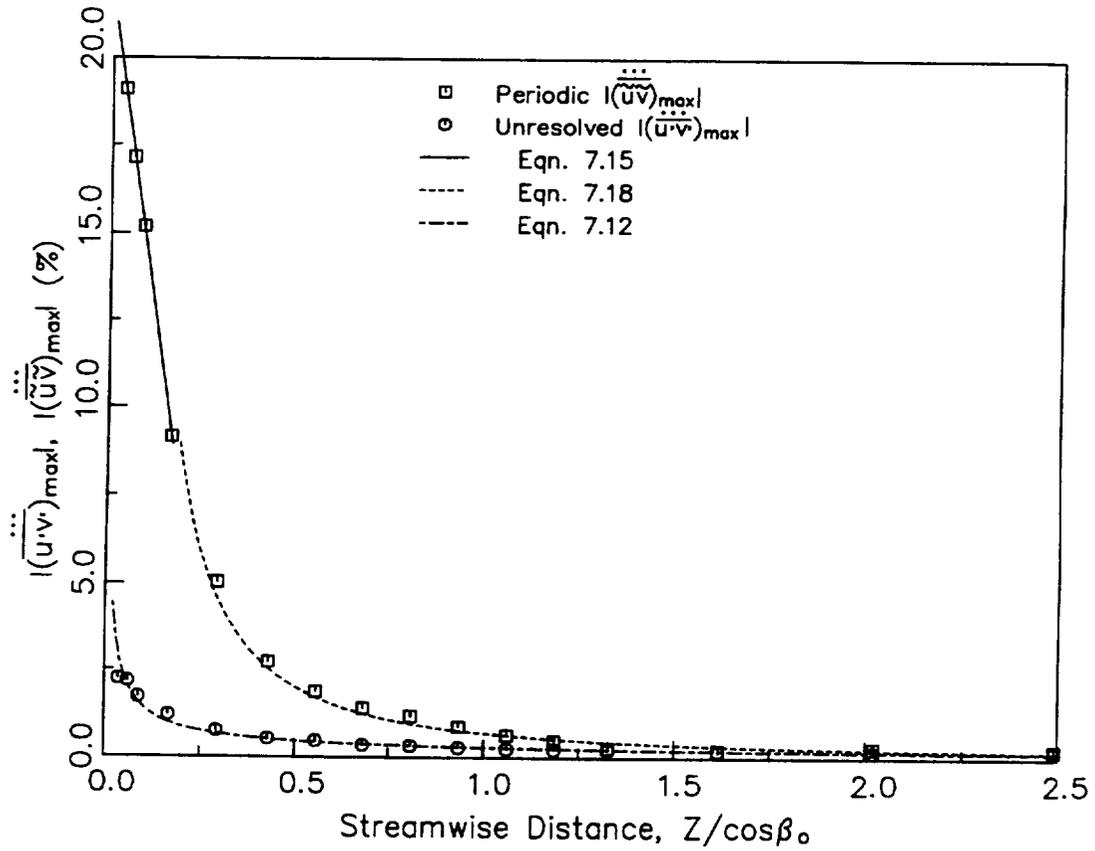
Figure 7.18. Decay of Rotor Wake Cycle-Averaged Maximum Unresolved $\left|\overline{\overset{\bullet\bullet\bullet}{u'v'}}\right|_{max}$ and Periodic Velocity Correlation $\left|\overline{\overset{\bullet\bullet\bullet}{\tilde{u}\tilde{v}}}\right|_{max}$

The decay of the maximum periodic velocity correlations, on the other hand, only follow this trend in the near and far wake regions; in the trailing edge region the decay is linear. Thus in the trailing edge region the maximum cycle-averaged periodic velocity correlation decay rates conform to the following relationships:

$$\left(\overline{\overset{\bullet\bullet\bullet}{\tilde{u}\tilde{u}}}\right)_{max} = -87.01\left(\frac{Z}{\cos\beta_o}\right) + 21.29 \tag{7.13}$$

$$\left(\overline{\overset{\bullet\bullet\bullet}{\tilde{v}\tilde{v}}}\right)_{max} = -62.59\left(\frac{Z}{\cos\beta_o}\right) + 24.26 \tag{7.14}$$

$$\left(\overline{\overset{\bullet\bullet\bullet}{\tilde{u}\tilde{v}}}\right)_{max} = -75.71\left(\frac{Z}{\cos\beta_o}\right) + 21.79 \tag{7.15}$$

while in the near and far wake regions the maximum periodic velocity decay rate correspond to the equations:

$$\left(\overline{\overset{\bullet\bullet\bullet}{\tilde{u}\tilde{u}}}\right)_{max} = 0.556\left(\frac{Z}{\cos\beta_o}\right)^{-1.35} \tag{7.16}$$

$$\left(\overline{\overset{\bullet\bullet\bullet}{\tilde{v}\tilde{v}}}\right)_{max} = 1.775\left(\frac{Z}{\cos\beta_o}\right)^{-1.14} \tag{7.17}$$

$$\left(\overline{\overset{\bullet\bullet\bullet}{\tilde{u}\tilde{v}}}\right)_{max} = 0.688\left(\frac{Z}{\cos\beta_o}\right)^{-1.55} \tag{7.18}$$

where $0.17 < Z/\cos\beta_o < 2.5$. The above correlations correspond the experimental data quite closely. They also give added confidence that equation (7.6) can be used to correctly model both the decay of each component of the Reynolds stress tensor

and the periodic velocity correlations, too. Since the periodic velocity correlations also correspond to the velocity defect, the above correlations could be used to model the total velocity defect decay, too.

The cycle-averaged wake momentum thickness and shape factor variations downstream of the rotor are shown in Figures 7.19 and 7.20. The momentum thickness for the rotor wake was determined using the equation,

$$\theta = \frac{1}{S_r} \int_0^{S_r} \frac{\overline{\overline{W}}}{\overline{\overline{W}}_c} \left(1 - \frac{\overline{\overline{W}}}{\overline{\overline{W}}_o} \right) r d\theta \tag{7.19}$$

where the integration was performed in the tangential direction over one blade spacing. The momentum thickness implies the loss of momentum in the wake as compared with potential flow. The wake shape factor in the wake was found using the following equation,

$$H = \frac{\delta^*}{\theta} \tag{7.20}$$

where δ^* is the displacement thickness. The displacement thickness is defined by the expression,

$$\delta^* = \frac{1}{S_r} \int_0^{S_r} \left(1 - \frac{\overline{\overline{W}}}{\overline{\overline{W}}_o} \right) r d\theta \tag{7.21}$$

where the integration was also performed over one blade spacing in the tangential direction.
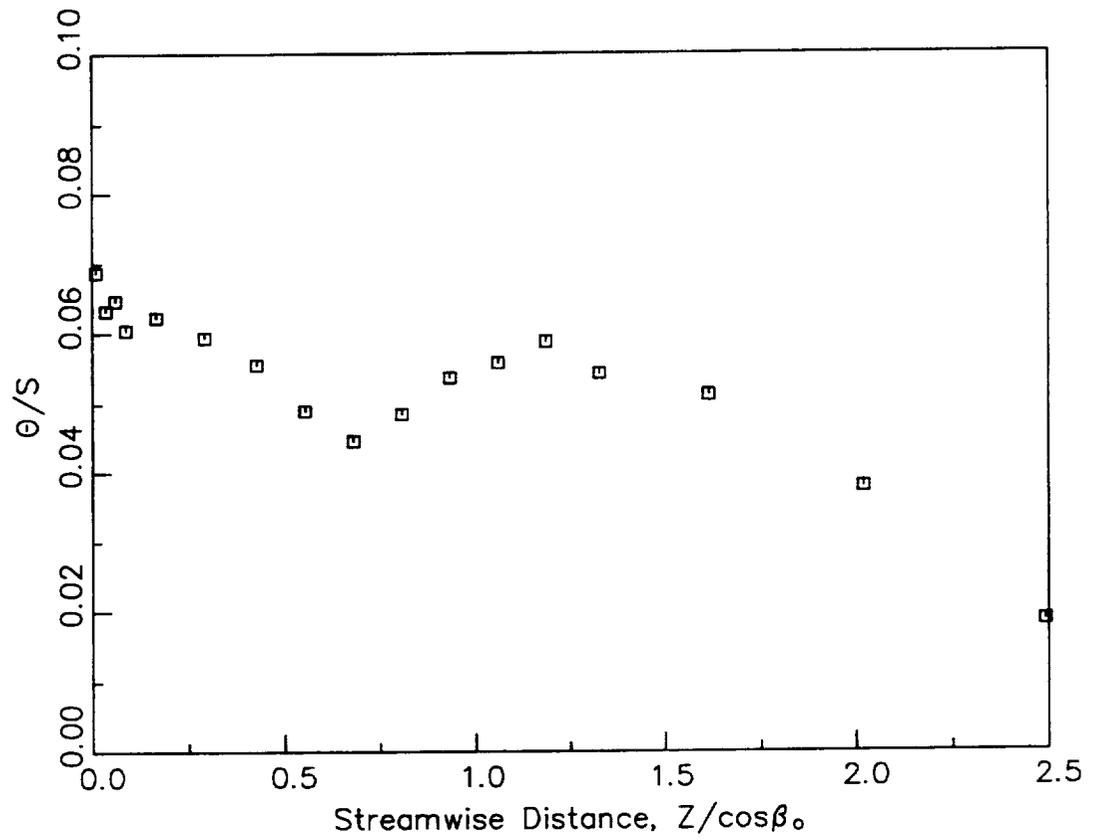
Figure 7.19. Variation of Rotor Wake Cycle-Averaged Momentum Thickness with Streamwise Distance
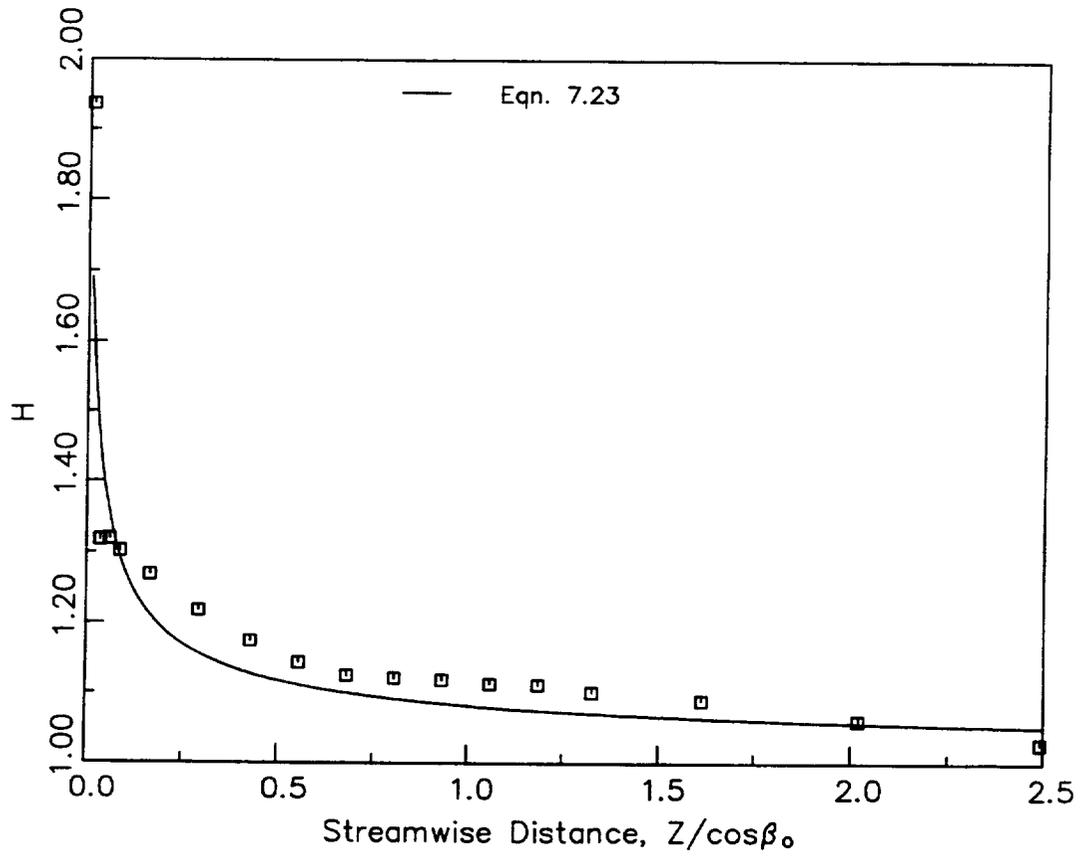
Figure 7.20. Variation of Rotor Wake Cycle-Averaged Shape Factor with Streamwise Distance

Figure 7.19 shows that the momentum thickness decreases in the trailing edge region, then increases as the wake travels downstream and then decreases in the far wake region. Both Raj and Lakshminarayana (1973) and Ravindranath (1979) explained the variation in momentum thickness in their compressor cascade and rotor wakes, respectively, on the basis of the von Karman momentum integral equation with zero wall shear stress as follows,

$$\frac{d\theta}{ds} + (2 + H)\frac{\theta}{W}\frac{dW_o}{ds} = 0 \qquad (7.22)$$

Equation (7.22) shows that the increase of decrease of θ depends on the variation of W_o. If W_o increases then θ decreases and if W_o decreases then θ increases. While this holds for both the compressor cascade and rotors, it does not hold for the turbine rotor wake presented here. The wake edge velocity continuously decreases downstream of this turbine rotor while the momentum thickness variation does not correspond to the wake edge velocity decrease. This is due to the radial transport of properties in the rotor wake which cause the variation in momentum thickness.

The variation of shape factor with streamwise distance is presented in Figure 7.20. The shape factor decreases sharply in the trailing edge region and then decreases at a slower rate as the wake travels downstream. The high value of shape factor just downstream of the trailing edge (H = 1.95) shows that the flow has a tendency to separate there. Since a turbine blade has a thick trailing edge, the flow does have a tendency to separate there. Other researchers such as Hobson and Lakshminarayana (1990) have also predicted flow separation at the trailing edge of a turbine blade.

The variation of the shape factor with streamwise distance downstream of

the trailing edge of an isolated airfoil was given by Spence (1953),

$$\left(1-\frac{1}{H}\right)=\left(1-\frac{1}{H_{te}}\right)\left[40\left(\frac{Z}{\cos\beta_o}\right)+1\right]^{-\frac{1}{2}}$$

(7.23)

where H_{te} is the shape factor at the trailing edge. Raj and Lakshminarayana (1973) demonstrated that eqn. (7.23) can be used to accurately used to predict the variation of shape factor downstream of a compressor cascade. Figure 7.20 shows the comparison of this equation with the experimentally measured shape factor. In the trailing edge region the comparison is not good, but farther downstream the agreement between eqn. (7.23) and the experimental data is better. In the rotor far wake region, eqn. (7.23) accurately predicts the magnitude of shape factor. The poor agreement in the trailing edge region is due to the large three-dimensional nature of the flow in the trailing edge region, while the good agreement in the far wake region results from the reduction of the three-dimensional effects far downstream of the trailing edge.

7.2.3 Rotor Wake Profiles at Individual Nozzle/Rotor Locations

Figures 7.21a and b show the relative velocity profiles in the rotor wake at different axial locations close to the rotor trailing edge. The data is presented at two selected nozzle/rotor locations that have large difference in flow properties between them (locations 3 and 5). The wake width at position 3 is wider than that at position 5. This is because the nozzle wake is located on the suction side of the rotor wake at position 3 and is located in the freestream region outside of the rotor wake at position 5. While the magnitude of the minimum velocity in the wake
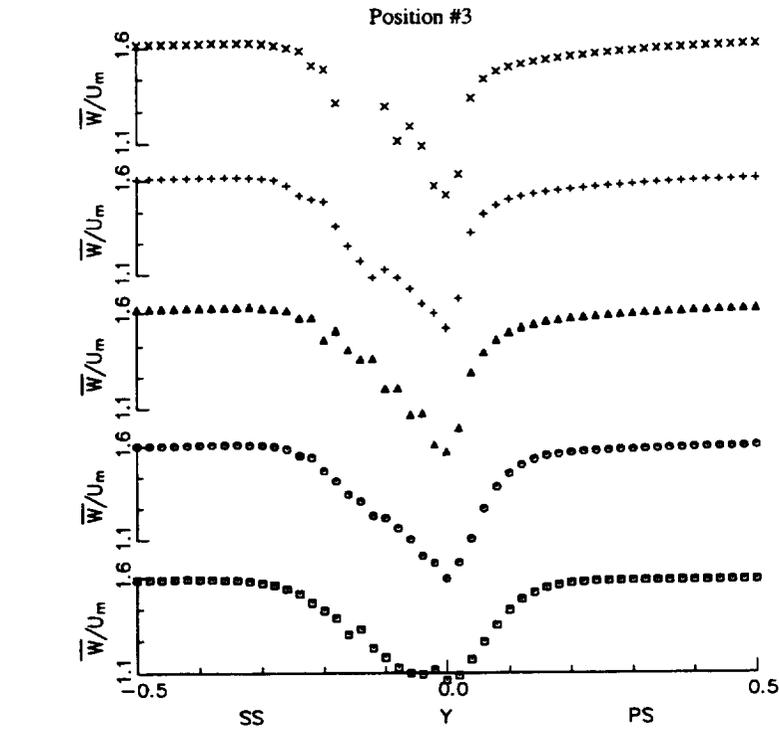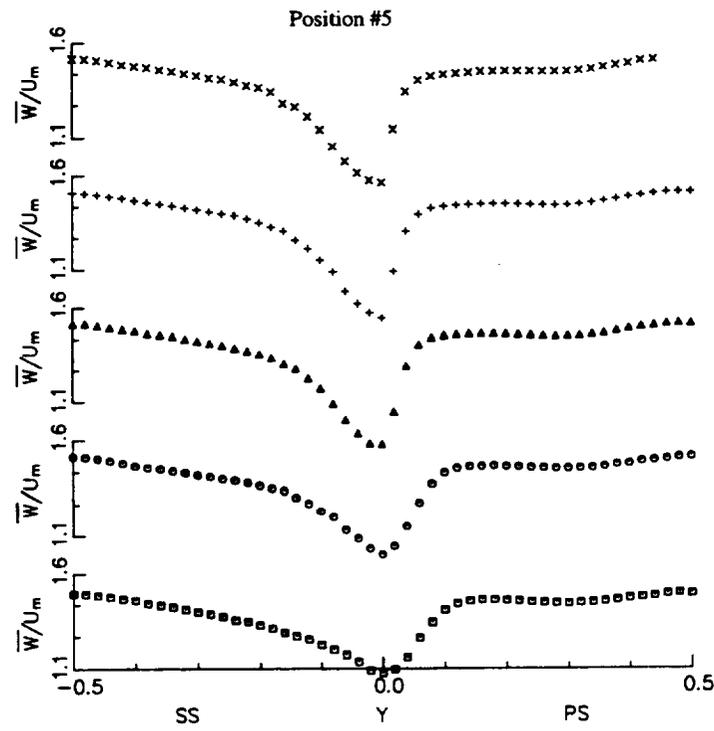
Figure 7.21. Rotor Wake Relative Velocity $\left(\overline{W}/U_m\right)$ Profiles

center is similar close to the trailing edge at both positions, the freestream velocity is quite different. The nozzle wake causes the freestream relative velocity to be lower at position 5 than the freestream velocity at position 3.

The total unresolved unsteadiness in the rotor wake at nozzle/rotor positions 3 and 5 are shown in Figure 7.22a and b. At both positions the unsteadiness profile is asymmetrical about the wake centerline which results from the different unresolved unsteadiness profiles in the blade surface boundary layers upstream of the trailing edge. The unsteadiness is much higher in the rotor wake and the region of increased unsteadiness occurs over a larger area at position 3 than at position 5 due to the presence of the nozzle wake inside of the rotor wake at position 3. On the other hand, the free stream region of position 5 contains twice the magnitude of total unresolved unsteadiness as the free stream region of position 3. This also results from the nozzle wake which is located in the free stream region of position 5.

Figures 7.23a and b and 7.24a and b present the streamwise-normal unresolved velocity cross correlation and the relative flow angle, respectively, at nozzle/rotor positions 3 and 5. The magnitude of unresolved velocity cross correlation in the pressure side of the rotor wake at position 3 is twice that in the pressure side of the rotor wake at position 5. On the suction side of the rotor wake at position 5 the unresolved velocity cross correlation is negligible while the suction side of the wake at position 3 contains a large area of negative unresolved velocity cross correlation. The higher unresolved velocity cross correlation in the position 3 rotor wake results from the presence of the nozzle wake inside the rotor wake at this position.

A noticeable difference between the relative flow angle in the rotor wake at these two nozzle/rotor positions is also seen in Figures 7.24a and b. At position 3, the overturning in the suction side rotor wake is larger than the overturning in the
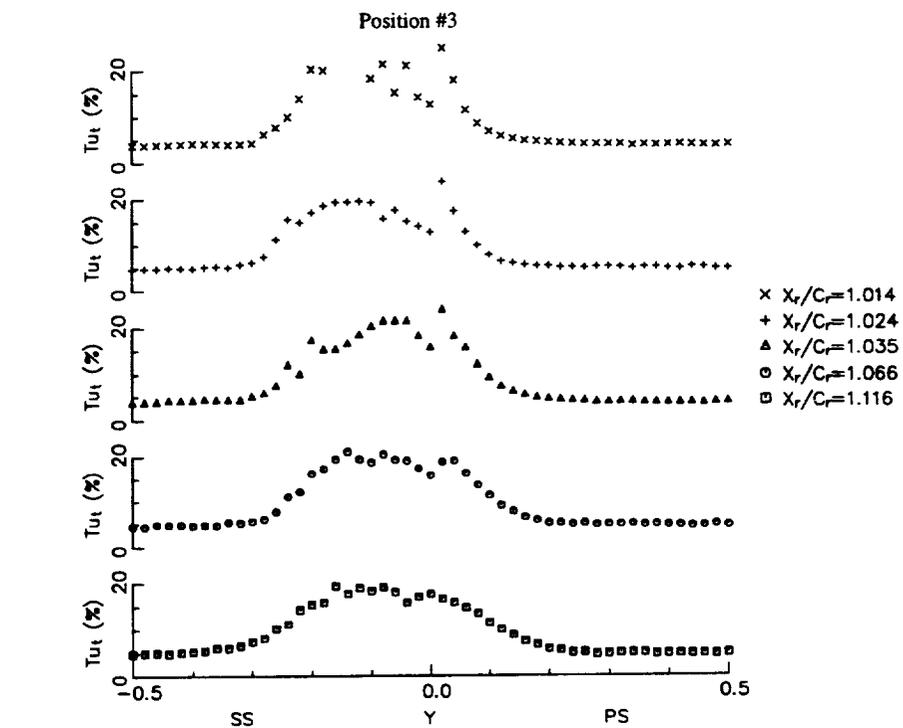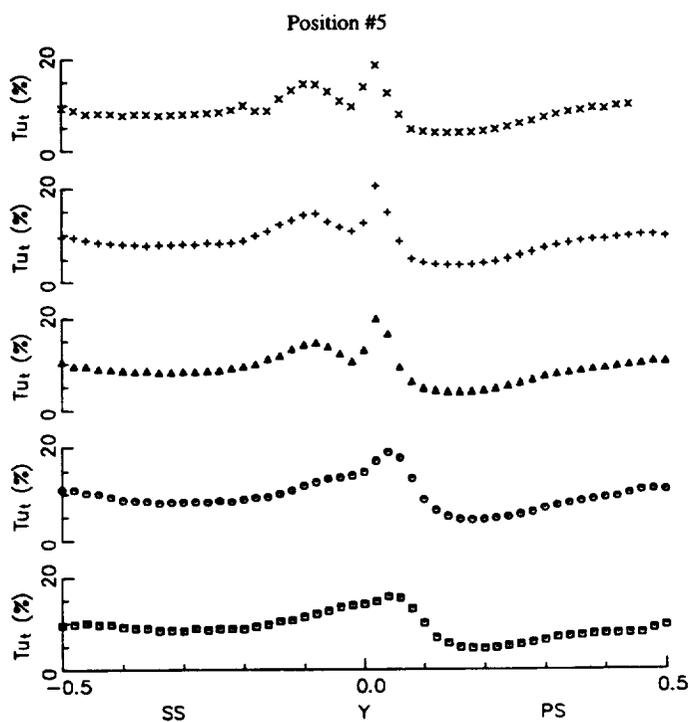
Figure 7.22. Rotor Wake Total Unresolved Unsteadiness (Tu_t)

Position #3

(a)

Position #5

(b)
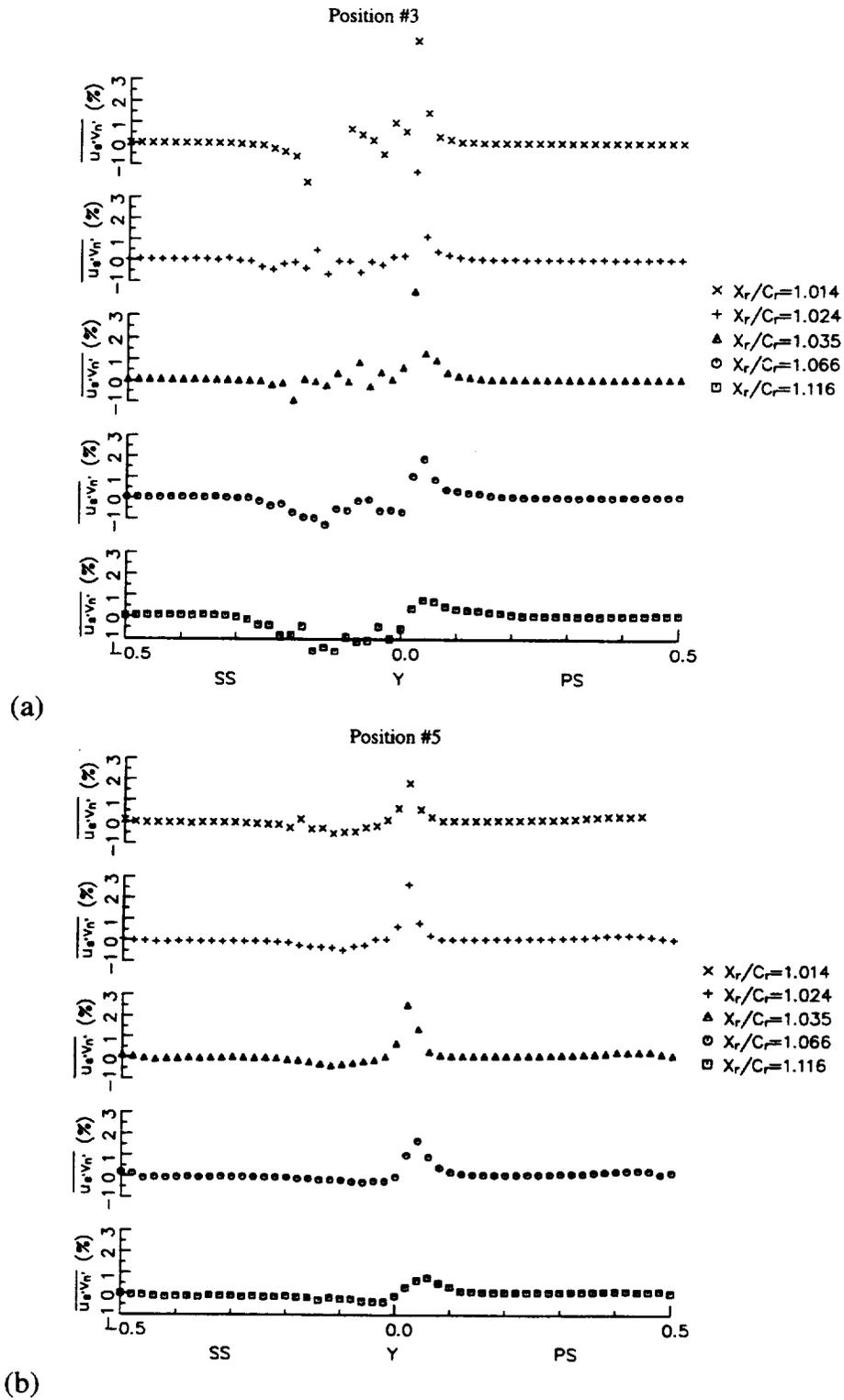
Figure 7.23. Rotor Wake Unresolved Velocity Correlation $\left(\overline{u_s' v_n'}\right)$

Figure 7.24. Rotor Wake Relative Flow Angle $(\bar{\beta})$

suction side rotor wake of position 5, while the overturning in the freestream region outside of the rotor wake at position 5 is higher than that in the freestream region of position 3. The higher overturning regions result from the presence of the nozzle wake in these areas.

Figure 7.21 through 7.24 show that rotor wake varies between individual nozzle/rotor positions. Thus one can conclude that the rotor wake is not steady in the rotor time frame. This can be seen more clearly by looking at Figures 7.25 and 7.26 which show the rotor wake relative total velocity and total unresolved unsteadiness just downstream ($X_r/C_r = 1.066$) of the rotor trailing edge at all six nozzle/rotor positions. There is a variation in both the velocity inside the wake and in the freestream for all six positions (there is an 8% difference between the highest and lowest freestream velocity and an 18% difference in velocity inside the wake). The lowest velocity at the wake center occurs at position 3 due to the presence of the nozzle wake inside the rotor wake at this position. At position 4, the nozzle wake has moved toward the rotor wake freestream region. This causes the suction side wake width to increase and the freestream velocity to decrease, since the nozzle wake is located partly in the suction side of the rotor wake and partly in the freestream region. The nozzle wake has moved out of the rotor wake at position 5, since the wake center velocity has increased and into the freestream region where the velocity has decreased.

The total unresolved unsteadiness, presented in Figure 7.26, shows the increased levels of unsteadiness in suction side of the rotor wake at position 3 due to the nozzle wake. At position 4, the level of the unsteadiness has decreased in the wake but has increased in the freestream region since the nozzle wake now is in both the rotor wake and freestream region. And at position 5, the nozzle wake has moved entirely into the freestream region as shown by the higher level of
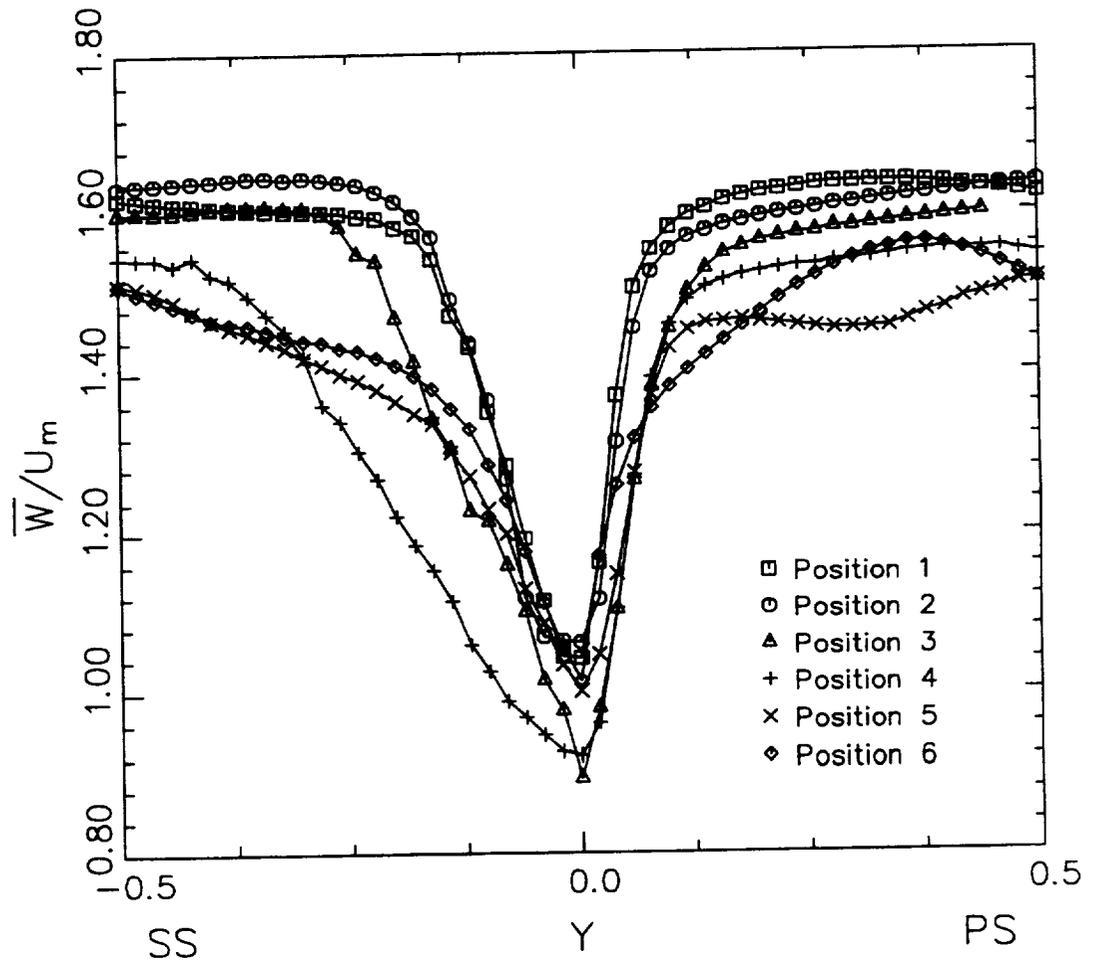
Figure 7.25. Rotor Wake Relative Velocity $(\overline{W}/U_m)$ Profiles at $X_r/C_r = 1.066$
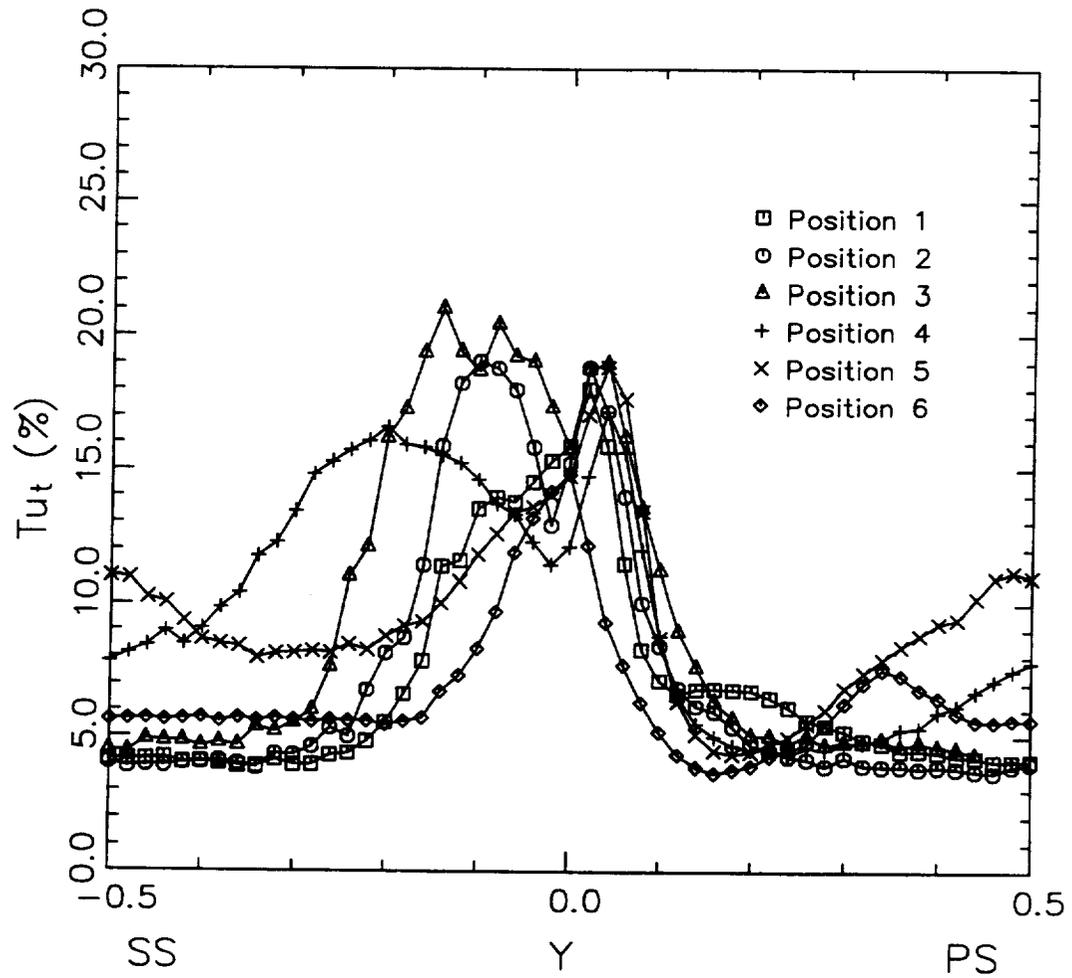
Figure 7.26. Rotor Wake Total Unresolved Unsteadiness (Tu_t) at $X_r/C_r = 1.066$

unsteadiness in the freestream region and lower level in the rotor wake.

The decay of the rotor wake velocity defect with streamwise distance is shown in Figure 7.27 for each of the different nozzle/rotor positions. The decay rate for each of the positions is similar but the magnitude of the velocity defects are different at each streamwise location. In the trailing edge and near wake region the defects for positions 3 and 4 are larger than the defects at 5 and 6 due to the presence of the nozzle wake inside the rotor wake at positions 3 and 4. Thus while the nozzle wake does not seem to have an impact on the velocity defect decay rate it does influence the magnitude of the velocity defect.

The nozzle wake interaction with the rotor wake also affects the rotor wake semi-wake width as shown in Figure 7.28. The semi-wake width is defined as the width of the wake at half the defect of total velocity. The rate of increase in wake width for each of the nozzle/rotor positions is similar but the magnitude of the semi-wake width at each streamwise location is not the same for each nozzle/rotor location. In the trailing edge and near wake regions, the rotor semi-wake width for positions 3 and 4 are larger in magnitude than the semi-wake width for positions 5 and 6 due to the presence of the nozzle wake inside the rotor wake at positions 3 and 4. Thus, just as for the velocity defect, the nozzle wake influences the magnitude of the semi-wake width but does not affect the semi-wake width rate of increase.

Figures 7.29 and 7.30 present the decay of the maximum total unresolved unsteadiness and streamwise-normal shear stress, respectively. Just as with the velocity defect and the semi-wake width, the rate of decay is similar for all six nozzle/rotor positions; just the magnitude of the unsteadiness and shear stress is different for each streamwise location. Therefore, the nozzle wake interaction with
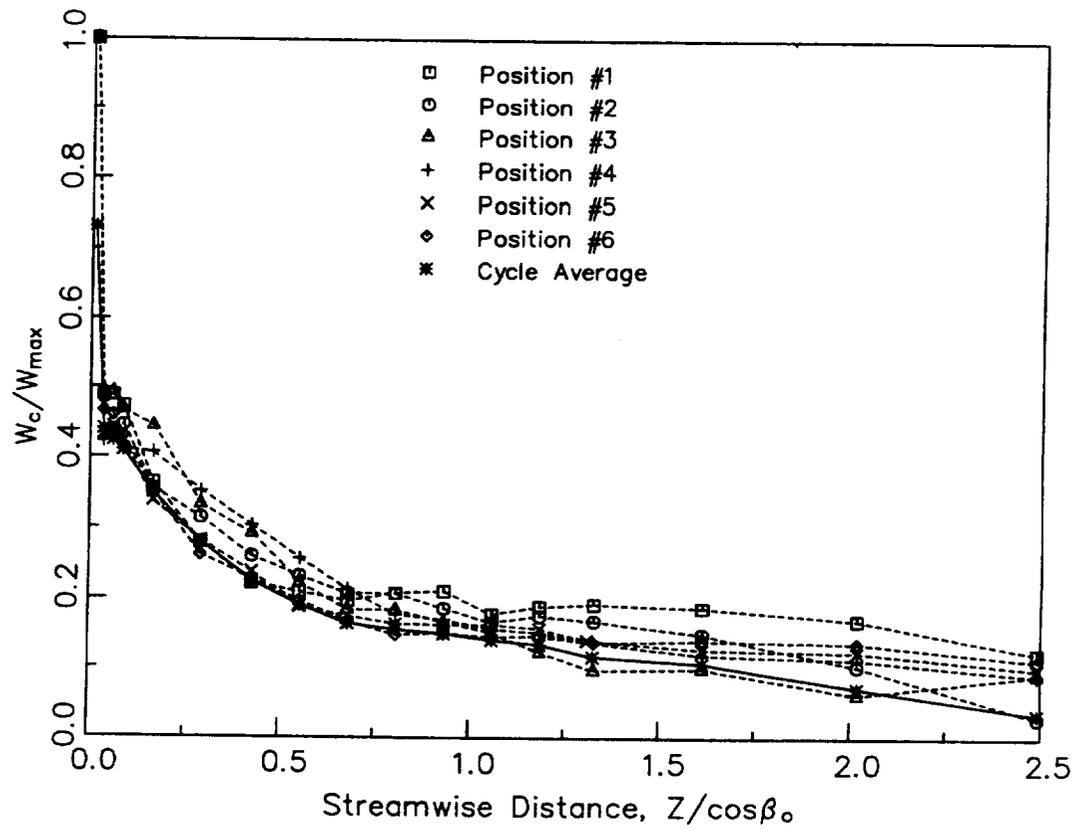
Figure 7.27. Decay of Rotor Wake Velocity Defect with Streamwise Distance for Each Nozzle/Rotor Location
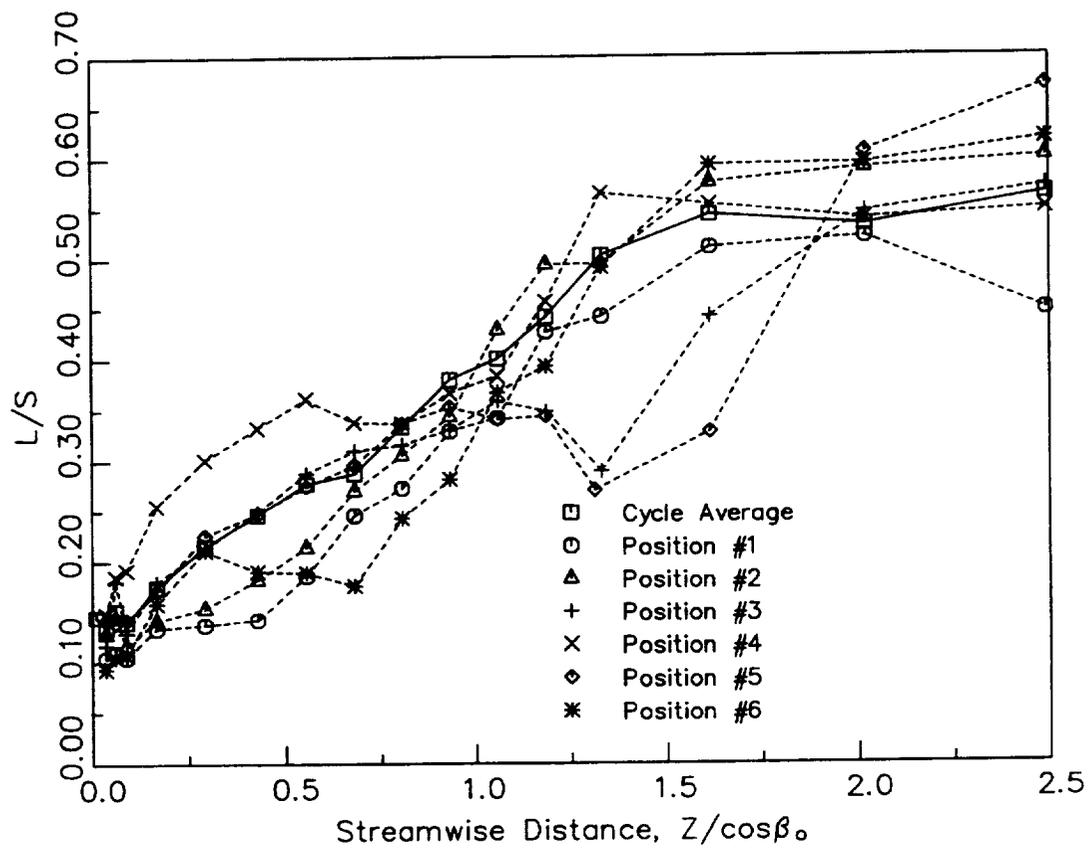
Figure 7.28. Variation of Rotor Wake Semi-Wake Width with Streamwise Distance for Each Nozzle/Rotor Location
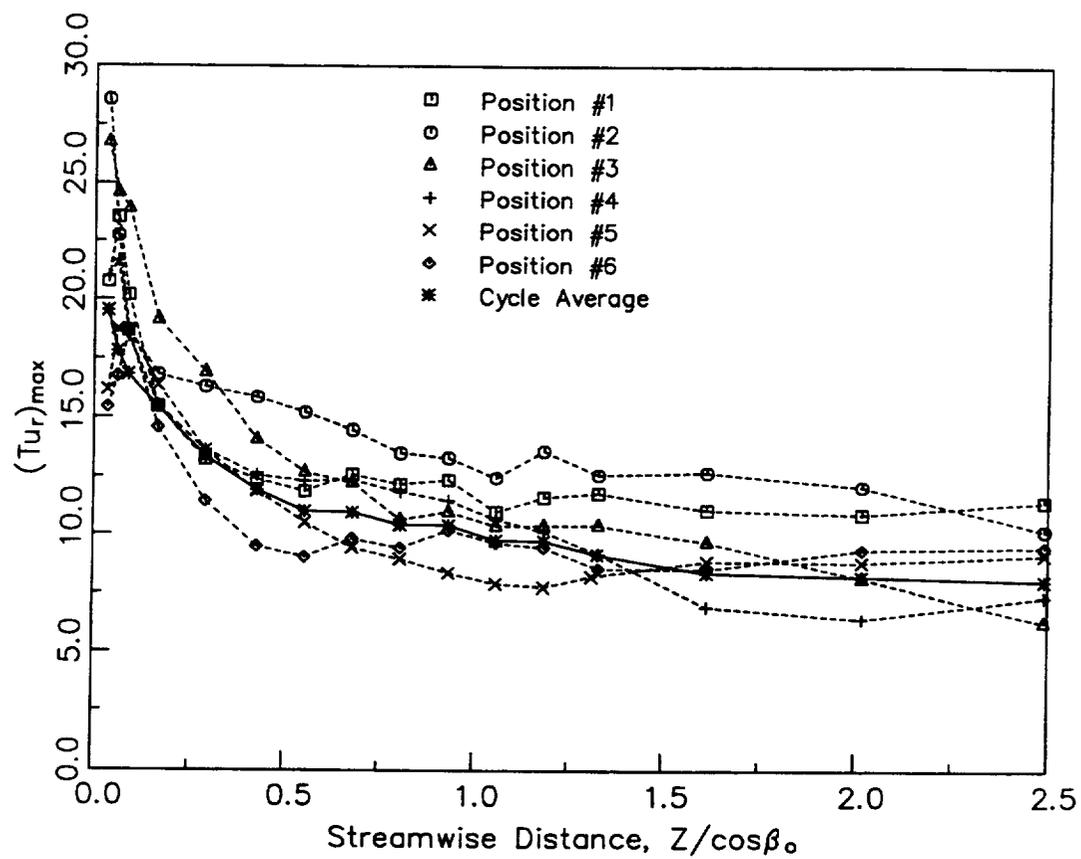
Figure 7.29. Decay of Maximum Relative Total Unresolved Unsteadiness
$(Tu_r)_{max}$ with Streamwise Distance for Each Nozzle/Rotor Location
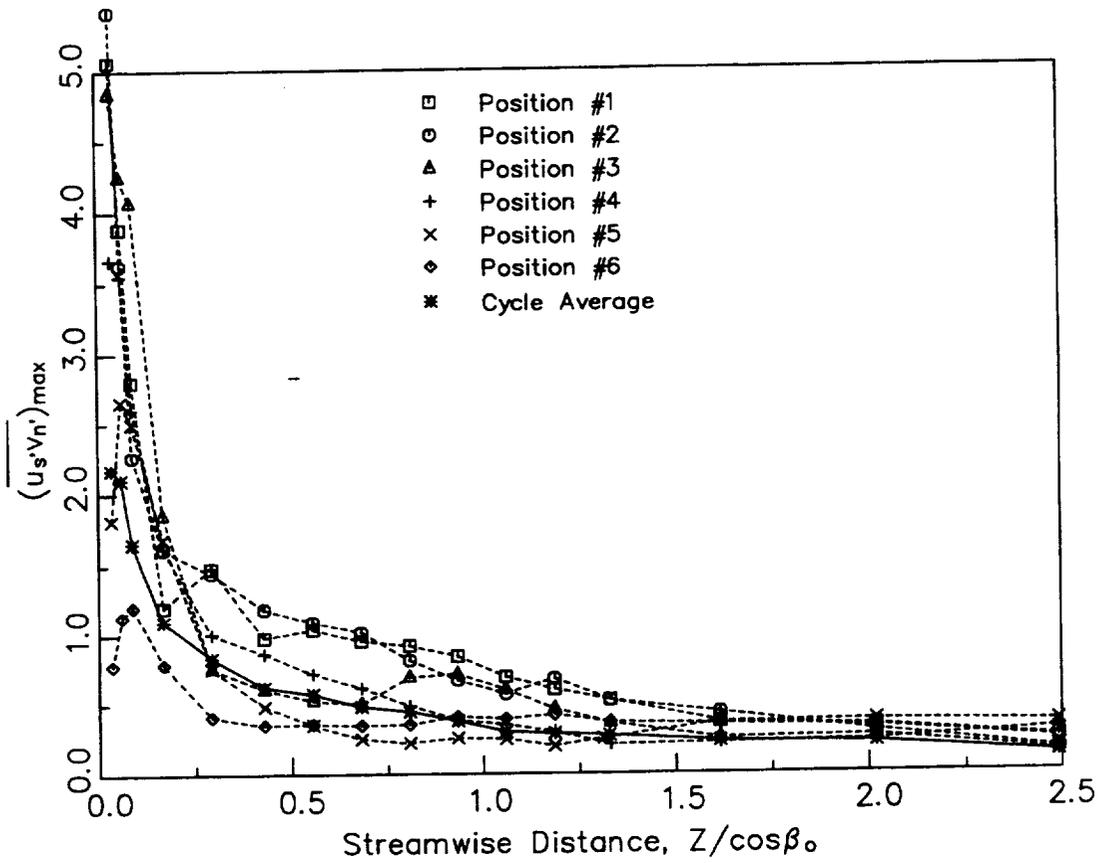
Figure 7.30. Decay of Maximum Unresolved Velocity Correlation $\left(\overline{u'_s v'_n}\right)$ with Streamwise Distance for Each Nozzle/Rotor Location

the rotor wake does not change the rate of decay or increase of the various properties, but it does change the magnitude of the properties for each nozzle/rotor position at each streamwise location.

CHAPTER 8

SUMMARY AND CONCLUSIONS

The three-dimensional steady flow field inside an axial flow turbine nozzle and the two-dimensional unsteady flow field inside a turbine rotor have been investigated experimentally. The nozzle flow field was studied in order to better understand the nozzle secondary flow and the nozzle wake properties. A complete flow field survey was carried out at two locations inside the nozzle passage at X/C = 0.56 and 0.935 and at two locations downstream of the nozzle at X/C = 1.025 and 1.09. The nozzle surface and endwall static pressures were also measured. The nozzle flow field measurements were carried out with a five hole probe, a single sensor hot wire and a two component LDV.

The rotor flow field was measured at midspan with a two component LDV in order to better understand the steady and unsteady flow field in a turbine rotor. Measurements were acquired at 37 axial locations from just upstream of the rotor to one chord downstream of the rotor and at 50 tangential locations (relative to the rotor) over one rotor pitch. To account for the non-uniformity of the rotor inlet flow field (due to the nozzle wake), measurements were made at six tangential locations (relative to the nozzle) equally spaced over one nozzle pitch. The rotor wake was also studied in detail in order to understand the rotor wake properties and its decay characteristics. Some important conclusions that can be drawn based on the results of the present investigations are presented below.

8.1. Nozzle Flow Field

The major conclusions of the nozzle flow field investigation are as follows:

1. The nozzle surface static pressures were predicted better by the three dimensional inviscid code of Katsanis than by the panel code, thus demonstrating that some of the departure between the design and the measured data is caused by the three-dimensional inviscid effects. The agreement of the yaw angle and the total velocity prediction by Katsanis' code and the experimental data is excellent, demonstrating the usefulness of using an inviscid code in early design.

2. The endwall static pressures show that the minimum static pressure on both endwalls occurs at the hub wall/suction surface corner. The minimum static pressure location on the hub occurs downstream (X/C = 0.80) of the minimum static pressure region on the casing, which occurs at midspan. This low pressure region is the location where the passage vortex lifts off the endwall and begins to grow rapidly as it moves up the suction surface. Thus the casing passage vortex covers a larger area than the hub passage vortex by the time it reaches the nozzle trailing edge, due to the longer distance it has traveled between the endwall/suction surface intersection point and the trailing edge.

3. Near midchord, the LDV measurements indicate the existence of the casing passage vortex by the high turbulence intensities and the underturning of the flow in the casing wall/suction surface corner. On the other hand, at the hub there is no indication of the hub wall passage vortex. This is in agreement with the endwall static pressure distribution, discussed above. While the casing passage vortex meets the suction surface at midchord, where it begins to grow rapidly and starts to move up the suction surface (away from the endwall), the hub passage

vortex is still being convected across the passage at midchord and is small. Thus the hub passage vortex should be rather weak and hard to detect at midchord.

4. Just upstream of the trailing edge (X/C = 0.935), the five hole probe data clearly show that the casing passage vortex is very strong. Radially inward flow in the suction surface boundary layer augments the casing passage vortex. The suction side leg of the horseshoe vortex is not visible near the casing. On the other hand, the passage vortex in the hub/suction surface corner is very weak. The radially inward flow in the suction surface boundary layer is in the opposite direction as those induced by the passage vortex and thus counteracts it. A vortex rotating in the opposite direction as the hub passage vortex is visible above the passage vortex. This might be the suction side leg of the horseshoe vortex.

5. Downstream of the nozzle, weak radial inward flow was observed over the whole span, which was more pronounced in the wake. Casing and hub passage vortices have been identified on the suction side of the wake. There is also indication of other vortices located in the wake center, near the casing and the hub. They rotate opposite to the passage vortices and are caused by the interaction of the passage vortices and the wake. On the other hand, there is conflicting evidence on the existence of the suction side leg of the horseshoe vortex. While there is no evidence for its existence at the hub, there is a region of negative vorticity near the casing at X/C = 1.025 that could correspond to this vortex, but the secondary flow vectors do not show the existence of a vortex. It has probably decayed by the time it has reached this axial location (X/C = 1.025).

6. Comparing the nozzle flow field just upstream of the trailing edge to that downstream of the nozzle, the casing passage vortex is seen to remain strong as it progresses and no dramatic change in secondary flow occurs at the tip. At the hub, however, the radially inward flow of the suction surface boundary layer has

reversed direction and is moving outward as a result of the rotating hub located downstream of the nozzle. The rotating hub also causes the hub passage vortex to dissipate, which can be seen from the secondary velocity vectors at X/C = 1.09.

7. A nozzle wake survey was also done at several axial locations at midspan to determine the wake decay characteristics. The AFTRF nozzle wake decays much faster than a compressor cascade wake, an annular turbine nozzle cascade wake or a turbine nozzle wake with a large rotor-nozzle spacing. This is due to the presence of a rotor in close vicinity, as well as the influence of a favorable pressure gradient downstream.

8. The radial variation of nozzle wake total velocity defect shows larger velocity defects in the hub and casing secondary flow regions. These larger defects result from the interaction of the passage vortices and the wake which cause deeper and wider wakes.

8.2 Rotor Passage Steady and Unsteady Flow Field

The major conclusions of the rotor passage flow field investigation are as follows:

1. Detailed measurements were made near the rotor leading edge. These measurements showed that the rotor leading edge has a major influence on the flow field, with large velocity gradients and flow angle changes in the vicinity of the leading edge. The axial velocity in the stagnation region decelerates to a value of 30% of the freestream axial velocity. The rotor leading edge has an influence on the flow field even 9% of the rotor axial chord upstream of the rotor leading edge, with the change in flow angle between the freestream and stagnation region being 18 degrees at this location. This effect increases as the rotor leading edge is

approached with the change in flow angle increasing to 35 degrees just upstream of the rotor leading edge.

2. High levels of relative total unresolved unsteadiness are observed at the leading edge. This is caused not only by a reduction in relative velocity, but also by an increase in the absolute magnitude of the velocity fluctuations at the leading edge. As the leading edge is approached, this large increase in the mean flow velocity gradients cause an increase in the production of unresolved unsteadiness which overshadows its dissipation.

3. Higher levels of relative total unresolved unsteadiness are also observed near the rotor pressure surface. This increase in unresolved unsteadiness is due to the interaction of the nozzle wake with the pressure surface boundary layer, along with the concave curvature effects, which destabilize the flow. Concave curvature effects results from the fact that the unresolved unsteadiness in thin shear layers is highly sensitive to streamline curvature in the plane of the mean shear. The unresolved shear stress and unsteadiness are increased due to curvature when the angular momentum of the flow decreases in the direction of the radius of curvature.

4. The nozzle wake can be clearly identified in the rotor passage. Compared to the flow field outside of the wake, the nozzle wake has a velocity defect, a higher unresolved unsteadiness, overturning of the flow angle and a higher unresolved velocity cross correlation.

5. As the nozzle wake enters the rotor passage, it is chopped into individual segments by the rotor blades. These individual segments can now move independently of each other. At the rotor inlet, the nozzle wake becomes bowed because the convection velocity at midpitch is higher than at the rotor leading edge. As the nozzle wakes travels further through the rotor passage, it becomes distorted with the region of the nozzle wake near the rotor suction surface moving faster than

the region near the pressure surface. This is due to the large differential in the convection velocity between the pressure and suction surface. Inside the rotor passage, the nozzle wake acts like a negative jet, drawing fluid from the rotor pressure surface to rotor suction surface, which causes the nozzle wake to thin out near the rotor pressure surface and thicken near the suction surface. This movement of low momentum fluid toward the suction surface also causes the high momentum fluid in the free stream to move in an opposite direction to replace the migrated wake fluid.

6. The nozzle wake propagates through the turbine rotor until it has turned more than 30 degrees from its orientation at the rotor leading edge and is spread out along the rotor pressure surface from midchord to the trailing edge. This is in contrast to other measurements of the nozzle wake in the rotor passage (Hodson, 1984 and Binder et al., 1985) who show that at the rotor trailing edge, the nozzle wake still spans the rotor passage in the pitchwise direction, from the pressure surface to the suction surface. This is caused by the large difference in velocity between the rotor suction and pressure surfaces. In the present turbine, the ratio of suction surface velocity to pressure surface velocity is twice the suction to pressure surface velocity ratio of Hodson's and Binder's turbine rotors. This large difference between the velocities near the suction and pressure surfaces of the author's turbine, causes the region of the nozzle wake near the rotor suction surface to travel much more rapidly than the region of the nozzle wake near the rotor pressure surface. Thus the nozzle wake rotates about the region of the nozzle wake near the rotor pressure surface, ending up spread out along the pressure surface. In Hodson's and Binder's turbine rotors, the difference between the suction and pressure surface velocities is not as great, thus the nozzle wake does not turn as much in the rotor

passage and by the time it reaches the rotor trailing edge it still spans the rotor passage in the pitchwise direction, from the pressure to suction surfaces.

7. By the time the nozzle wake has propagated through the rotor passage and is spread out along the rotor pressure surface from midchord to the trailing edge, it has elongated and thinned out considerably (compared to its shape at the rotor leading edge). This results from two reasons. The first is the fact that vorticity must be conserved in the nozzle wake, thus as the wake length grows, the wake width must become smaller. The second is due to the large variation in convective velocity across the rotor pitch. Since the velocity is faster along the rotor suction surface than near the pressure surface, the region of the wake near the suction surface moves faster than the region near the pressure surface. Thus the wake stretches, becoming narrower and longer.

8. As the nozzle wake interacts with the rotor leading edge, an increase in unresolved unsteadiness at the leading edge is observed. The tangential component of the unresolved unsteadiness also increases in the region of the nozzle wake at rotor midpitch. This increase in unresolved unsteadiness results from the two counter-rotating vortices, one on each side of the nozzle wake. The generation of these vortices cause an increase in the velocity fluctuations.

9. The periodic velocity correlations are similar in magnitude to the unresolved velocity correlations in the nozzle wake, which indicates that both have an equal impact on the through-flow mixing in this turbine rotor.

10. As the nozzle wake moves through the rotor passage the magnitude of the velocity defect increases from the leading edge until $X_r/C_r = 0.30$, after which it decreases. This can be explained by examining the mass-averaged cycle-averaged relative velocity. The relative velocity decreases from the rotor leading edge until $X_r/C_r = 0.30$, causing an adverse pressure gradient, which causes the

nozzle wake velocity defect to increase. Downstream of $X_r/C_r = 0.30$, the relative velocity increases, resulting in a favorable pressure gradient, which causes the nozzle wake to decay. Downstream of the rotor trailing edge the nozzle wake velocity defect is constant.

11. The peak magnitude of the total unresolved unsteadiness in the nozzle wake increases initially and then decreases as the nozzle wake travels through the rotor passage, until at one half chord downstream of the rotor trailing edge it is at the same value as it was upstream of the rotor.

12. Both the mass-averaged and time-averaged properties show that inside the rotor blade, the region of high unresolved unsteadiness that corresponds to the nozzle wake occurs at the same location as the low velocities due to the nozzle wake. On the other hand, downstream of the rotor, the region of high unresolved unsteadiness due to the nozzle wake does not occur at the same location as the low velocities due to the nozzle wake. This is because, although in the near wake the maximum unresolved unsteadiness occurs at the wake center (position where the velocity defect is largest), far downstream of the nozzle, the maximum unresolved unsteadiness occurs away from the center of the wake due to the spread of the wake.

8.3. Rotor Wake Properties and Characteristics

The major conclusions based on the rotor wake investigation are as follows:

1. The rotor wake mean velocity profiles in the trailing edge and near wake regions are asymmetrical and tend to become symmetrical in the far wake region.

2. The rotor wake total unresolved unsteadiness is highest in the trailing edge region and decreases further downstream. This is caused by the vortex street

shed from the trailing edge and the production of turbulence in this region. Also in the trailing edge region, the unresolved unsteadiness profiles are asymmetric with a dip in unsteadiness at the wake center. The asymmetry results from the differential boundary layer growth on the pressure and suction side of the rotor blade, while the dip in unsteadiness is due to the fact that the total unresolved unsteadiness is zero on the blade surface with a maximum value occurring slightly away from the blade surface. The asymmetry and dip in unresolved unsteadiness disappear as the rotor wake travels downstream.

3. The streamwise-normal unresolved velocity cross correlation in the rotor wake is also asymmetric close the rotor trailing edge, becoming symmetric farther downstream. Close to the trailing edge, the zero unresolved velocity cross correlation point does not occur at the point of minimum velocity, but farther downstream it does. The unresolved velocity cross correlation decays rather slowly with significant values still occurring one half chord downstream of the rotor.

4. The rotor wake velocity defect decays very rapidly in the trailing edge region, becoming less rapid in the near and far wake regions. The very rapid decay in the trailing edge region results from the high unresolved unsteadiness, separation and possibly the three dimensional effects in this region. The rotor wake velocity defect decays much slower than the velocity defect of turbine cascades. The decay of the rotor wake velocity defect decays according to $1/\sqrt{z/\cos\beta_o}$ where $z/\cos\beta_o$ is the streamwise distance downstream of the rotor blade. Using this property of the rotor wake, a correlation has been presented which matches the decay of the velocity defect in the near and far wake regions.

5. The rotor wake semi-wake width increases rapidly in the trailing edge region and then grows less rapidly in the near and far wake regions. The rate of semi-wake width increase is proportional to $\sqrt{z/\cos\beta_o}$. Using this property of the

rotor wake, a correlation has been presented which matches the growth of the semi-wake width.

6. Decay of the maximum unresolved unsteadiness and maximum unresolved velocity cross correlation is very rapid in the trailing edge region and this trend slows in the far wake region. Equations have been presented which match their decay rates.

7. In the trailing edge region, the maximum periodic velocity correlations are much larger than the maximum unresolved velocity correlations. But the periodic velocity correlations decay much faster than the unresolved correlations. Equations were presented that matched the experimental decay of the maximum periodic and unresolved velocity correlations in the rotor wake.

8. The rotor wake shape factor decreases sharply in the trailing edge region and then decreases at a slower rate farther downstream. The high value of shape factor just downstream of the rotor trailing edge indicates that the flow has a tendency to separate there. The variation of the rotor wake shape factor with streamwise distance downstream of the rotor was found to match the correlation developed by Spence (1953) quite well in the far wake region and not as good in the near wake region.

9. While the interaction of the nozzle wake with the rotor wake does not influence the decay rate of the various wake properties, it does change the magnitude of the properties.

CHAPTER 9

RECOMMENDATIONS FOR FUTURE RESEARCH

The present investigation has provided a good understanding of the whole nozzle flow field. One unanswered question in the nozzle flow field is what happens to the suction side leg of the horseshoe vortex. Flow visualization on the nozzle endwall surfaces and hot wire or five hole probe surveys close to the endwalls could be used to trace the path of the suction side leg of the horseshoe vortex as it travels through the nozzle passage.

The nozzle wake could be investigated in more detail. By measuring the properties of the nozzle wake with the rotor removed, the difference between the nozzle wake decay with and without the rotor could be quantified.

This investigation has also provided an understanding of the rotor flow field at midspan and the interaction of the nozzle wake with the rotor flow field. To better understand the rotor flow field including the secondary flow and the tip leakage vortex, a knowledge of the flow field at other radii is critical. Measurement of the radial velocity component is also essential for a complete understanding of the flow field. The LDV can be used to measure the radial velocity and to measure the flow field at other spanwise locations. Measurement of the losses in and downstream of the rotor would also be useful. This could be accomplished with a rotating five hole probe. The AFTRF has a rotating traverse that the five hole probe could be installed in. With this traverse the losses in the entire flow field could be measured.

There are numerous static pressure taps on the rotor blade surface and endwalls which should be used to measure the pressure distribution on the rotor blade. The unsteady pressures and the shear stress on the rotor blade surface can be

measured by the Kulite transducers and the shear stress gauges, respectively on the rotor blade surface. The rotor blade boundary layers could also be measured by using a two sensor hot wire mounted in the rotating traverse. By completing all these measurements, the complete flow field in the rotor could be measured.

The influence of the inlet turbulence intensity on the flow field could be quantified by repeating selected measurements with the inlet turbulence grid installed and comparing them with the measurements completed without the turbulence grid. The influence of the Reynolds number and the incidence angle on the turbine flow field could also be quantified by measuring the flow field at several locations at off-design conditions.

APPENDIX A

ERROR ANALYSIS

All experimental results have a certain degree of error associated with them. This error needs to be quantified in order for the results to be correctly interpreted. Thus an error analysis based on the ASME measurement uncertainty methodology (Abernathy et al., 1985) is given below.

An error is the difference between the measurement and the true value. Uncertainty is the maximum error that might be expected from a measured quantity. The total error is a combination of both bias (fixed) and precision (random) errors. The precision error, S, is the random part of the total error which for N measurements $(X_1, X_2, ..., X_N)$ of the parameter X , is

$$S = \sqrt{\frac{\sum_{i=1}^{N}(X_i - \overline{X})^2}{N-1}} \tag{A.1}$$

where $\overline{X}$, the average value (mean) of X is

$$\overline{X} = \frac{1}{N}\sum_{i=1}^{N} X_i \tag{A.2}$$

The precision index of the sample mean $\overline{X}$ can be also found from

$$S_{\overline{x}} = \frac{S}{\sqrt{N}} \tag{A.3}$$

The bias error is a fixed or systematic error. It remains constant during an experiment. In repeated measurements, each measurement has the same bias. There is no statistical equation, as for the precision error, to define the bias error, B. It must be estimated. This estimate can be based on calibrations or comparison with other experimental techniques, but in general the estimate of bias must be based on judgment.

To obtain the precision error of a given parameter, the root sum square (RSS) method is used to combine the precision errors from K sources of error as follows,

$$S = [S_1^2 + S_2^2 + ... + S_K^2]^{\frac{1}{2}} \qquad (A.4)$$

The bias of a given parameter can be similarly found as

$$B = [B_1^2 + B_2^2 + ... + B_K^2]^{\frac{1}{2}} \qquad (A.5)$$

The total uncertainty is obtained for a 95% confidence level) by combining the precision an bias errors in the following manner

$$U = [B^2 + P^2]^{\frac{1}{2}} \qquad (A.6)$$

where $P = tS_{\bar{x}}$. For a large number of samples (>30), t=2.0. U is then the uncertainty in the measured value of a single variable. If, on the other hand, the value of the experimental result is not directly measured, but the values of several variable are measured and then they are combined into a data reduction equation to obtain the value of the desired variable, the following is used.

Consider a general case in which an experimental result, r, is a function of J variables X_i

$$r = r(X_1, X_2, ..., X_J) \qquad (A.7)$$

The precision limit of the result is given by

$$S_r = \left[\left(\frac{\partial r}{\partial X_1} S_{x_1} \right)^2 + \left(\frac{\partial r}{\partial X_2} S_{x_2} \right)^2 + \cdots + \left(\frac{\partial r}{\partial X_J} S_{x_J} \right)^2 \right]^{\frac{1}{2}} \qquad (A.8)$$

where the S_{x_i} are the precision limits in the measured variables X_i. It is assumed that the relationship given by equation (A.7) is continuous and has continuous derivatives in the domain of interest and that the precision limits S_{x_i} are independent of one another.

This same method can be used to calculate the experimental bias error from the bias limits of each measured variable that the experimental result is a function of (shown in equation A.7) as is done as follows

$$B_r = \left[\left(\frac{\partial r}{\partial X_1} B_{x_1} \right)^2 + \left(\frac{\partial r}{\partial X_2} B_{x_2} \right)^2 + \cdots + \left(\frac{\partial r}{\partial X_J} B_{x_J} \right)^2 \right]^{\frac{1}{2}} \qquad (A.9)$$

The uncertainty of the result is again given by (for 95% confidence level)

$$U = [B_r^2 + P_r^2]^{\frac{1}{2}} \qquad (A.10)$$

where $P_r = tS_r$ and t=2.0 when N>30.

If it is difficult to separately estimate the bias errors and the precision errors for each measured variable, an uncertainty which is a combination of the bias and precision errors can be estimated for each measured variable as follows,

$$U_{x_i} = [U_1^2 + U_2^2 + ... + U_j^2]^{\frac{1}{2}} \qquad (A.11)$$

where $U_1, U_2, ..., U_j$ are the sources of error for the measured variable X_i, and U_{x_i} is the uncertainty in X_i. Then the total uncertainty of the experimental result, r, which is a function of J variables X_i as shown in equation (A.7), is then

$$U_r = \left[\left(\frac{\partial r}{\partial X_1} U_{x_1} \right)^2 + \left(\frac{\partial r}{\partial X_2} U_{x_2} \right)^2 + \cdots + \left(\frac{\partial r}{\partial X_J} U_{x_J} \right)^2 \right]^{\frac{1}{2}} \qquad (A.12)$$

APPENDIX B

FIVE-HOLE PROBE AND STATIC PRESSURE UNCERTAINTY ANALYSIS

B.1 Sources of Error

A detailed discussion on the errors involved in the five hole probe and static pressure measurements in given by Sitaram, Lakshminarayana and Ravindranath (1981) and by Zierke, Straka and Taylor (1993). The present discussion is based on the above mentioned references using the ASME measurement uncertainty analysis described in Appendix A to calculate the uncertainty.

The accuracy of the five hole probe measurements is dependent on several factors including transducer error, wall and blade vicinity effects, Reynolds number and compressibility effects, misalignment of problem probe blockage effects and turbulence effects. Each of these factors are discussed in detail below:

(1) Transducer uncertainty: The error in the transducer is 0.15 inches of water. This error affects both the five hole probe and static pressure measurements. The remaining errors discussed below only affect the five hole probe measurements.

(2) Wall Vicinity Effect: When a probe is located near a solid surface, the flow accelerates in that region introducing errors in the measurements. Sitaram, Lakshminarayana and Ravindranath (1981) found that for a five hole probe, the error is negligible when the distance between the probe and the solid surface is more than two probe diameters. Thus this error is negligible since all measurements were made at a distance greater than two probe diameters from the wall.

(3) Reynolds number effects: The calibration of the five hole probe was carried out at a Reynolds number approximately equal to that in the measured flow. Thus the Reynolds number effects are accounted for in the calibration.

(4) Compressibility effects: Although the five hole probe was calibrated at the same Reynolds number as that in the measured flow, the calibration was done in an incompressible flow (water). To account for compressibility effects of the flow, the pitch and yaw calibration constants were modified using the Prandtl-Glauert rule as follows,

$$C_{P_{pitch,c}} = \frac{C_{P_{pitch,i}}}{\sqrt{1 - M_\infty^2}}$$ (B.1)

$$C_{P_{yaw,c}} = \frac{C_{P_{yaw,i}}}{\sqrt{1 - M_\infty^2}}$$ (B.2)

where the subscripts c and i represent compressible and incompressible calibration coefficients. The total velocity is then calculated using,

$$V^2 = \frac{2c^2}{\gamma - 1}\left[\left(\frac{P_o}{p}\right)^{\frac{(\gamma-1)}{\gamma}} - 1\right]$$ (B.3)

Thus the error due to compressibility can be neglected since it is accounted for.

(5) Misalignment of the probe: The probe was aligned using a protractor. The error in aligning the probe is 0.25 degrees.

(6) Probe and stem blockage effects: The error in probe and stem blockage is negligible since the probe was calibrated with its stem and the ratio of the probe diameter to both the vane spacing and pitch is 1.4% and 1.5%, respectively.

(7) Turbulence Effects: The five hole probe was calibrated in a low turbulence calibration tunnel. Measurements were taken in the nozzle wake where the turbulence intensity is around 10%. Goldstein (1936) has theoretically investigated the effect of turbulent velocity components on pressure probe measurements. Sitaram, Lakshminarayana, and Ravindranath (1981) have modified Goldstein's analysis to estimate the error due to turbulence on the five hole probe measurements. Based on their analysis, the error in the calibration angle and pressure coefficients is 0.67%, assuming 10% turbulence intensity in the nozzle wake.

(8) Pressure and Velocity Gradient Error: The five hole probe used in this investigation was calibrated in a uniform flow, but was used to measure flow where steep gradients in pressure and velocity exist (such as in the nozzle wake). Since each hole is located in a differing pressure field, an error is introduced. This is corrected by using a linear interpolation of the pressures at two adjacent measuring locations in the direction of the gradient, as devised by Prato (1992). Thus, the pressure and velocity gradient error can be neglected.

B.2 Uncertainty Analysis

The error in static pressure results mainly from the error in the pressure transducer which is 0.15 inches of water. Thus for the static pressure measurements

$$\frac{U_p}{p} = 1.0\%$$
(B.4)

For the five hole probe measurements, the data reduction equations are based on the method of Treaster and Yocum (1979) which is modified to include

compressibility and shear gradient effects. The equations for this analysis are presented and then the propagation of uncertainty from the measured variable is given.

The first step in the five hole probe data analysis is to calculate an average pressure,

$$\bar{p} = \frac{1}{4}(p_2 + p_3 + p_4 + p_5) \tag{B.5}$$

where $\bar{p}$ is the average pressure, p_2 and p_3 are the pressures measured in the yaw plane, and p_4 and p_5 are the pressure measured in the pitch plane. The uncertainty equation is then

$$U_{\bar{p}} = \frac{1}{2}U_{p_2} \tag{B.6}$$

Next, the yaw and pitch calibration coefficients are calculated as

$$C_{P_{yaw}} = \frac{\left(\dfrac{p_2 - p_3}{p_1 - \bar{p}}\right)}{\sqrt{1 - M_\infty^2}} \tag{B.7}$$

$$C_{P_{pitch}} = \frac{\left(\dfrac{p_4 - p_5}{p_1 - \bar{p}}\right)}{\sqrt{1 - M_\infty^2}} \tag{B.8}$$

The general uncertainty equation for these coefficients is then

$$U_{C_{P_{yaw}}} = \left[\left(\frac{U_{p_2}}{p_2 - p_3}\right)^2 + \left(\frac{-U_{p_3}}{p_2 - p_3}\right)^2 + \left(\frac{-U_{p_1}}{p_1 - \bar{p}}\right)^2 + \left(\frac{U_{\bar{p}}}{p_1 - \bar{p}}\right)^2 + \left(\frac{-MU_M}{1 - M^2}\right)^2\right]^{\frac{1}{2}} \tag{B.10}$$

and

$$U_{C_{P_{pitch}}} = \left[\left(\frac{U_{p_4}}{p_4 - p_5}\right)^2 + \left(\frac{-U_{p_5}}{p_4 - p_5}\right)^2 + \left(\frac{-U_{p_1}}{p_1 - \bar{p}}\right)^2 + \left(\frac{U_{\bar{p}}}{p_1 - \bar{p}}\right)^2 + \left(\frac{-MU_M}{1 - M^2}\right)^2\right]^{\frac{1}{2}} \tag{B.11}$$

After the uncertainty in $C_{P_{yaw}}$ and $C_{P_{pitch}}$ are computed, then the uncertainty in the angles can be calculated. Since the values for the pitch angle, γ, and yaw angle,

α, come from the calibration plots, the partial derivatives in the general uncertainty equation are replaced with finite differences to obtain

$$U_\gamma = \left[\left(\frac{\Delta\gamma}{\Delta C_{P_{yaw}}} U_{C_{P_{yaw}}} \right)^2 + \left(\frac{\Delta\gamma}{\Delta C_{P_{pitch}}} U_{C_{P_{pitch}}} \right)^2 \right]^{\frac{1}{2}} \tag{B.12}$$

$$U_\alpha = \left[\left(\frac{\Delta\alpha}{\Delta C_{P_{yaw}}} U_{C_{P_{yaw}}} \right)^2 + \left(\frac{\Delta\alpha}{\Delta C_{P_{pitch}}} C_{P_{pitch}} \right)^2 \right]^{\frac{1}{2}} \tag{B.13}$$

The calibration pressure coefficients, which are used to compute the pressures from five hole probe calibration plots, are calculated next. The uncertainty in these coefficients are

$$U_{C'_{P_{total}}} = \left[\left(\frac{\Delta C'_{P_{total}}}{\Delta\gamma} U_\gamma \right)^2 + \left(\frac{\Delta C'_{P_{total}}}{\Delta\alpha} U_\alpha \right)^2 \right]^{\frac{1}{2}} \tag{B.14}$$

and

$$U_{C'_{P_{static}}} = \left[\left(\frac{\Delta C'_{P_{static}}}{\Delta\gamma} U_\gamma \right)^2 + \left(\frac{\Delta C'_{P_{static}}}{\Delta\alpha} U_\alpha \right)^2 \right]^{\frac{1}{2}} \tag{B.15}$$

The total and static pressures are then calculated using the following equations

$$P_o = p_1 - C'_{P_{total}} (p_1 - \overline{p}) \tag{B.16}$$

$$p = \overline{p} - C'_{P_{static}} (p_1 - \overline{p}) \tag{B.17}$$

Thus the general uncertainty equations for the total and static pressures are

$$U_{P_o} = \left[\left(\left(1 - C'_{P_{total}}\right) U_{P_1} \right)^2 + \left(\left(C'_{P_{total}}\right) U_{\bar{p}} \right)^2 + \left((\bar{p} - p_1) U_{C'_{P_{total}}} \right)^2 \right]^{\frac{1}{2}} \qquad \text{(B.18)}$$

$$U_p = \left[\left(\left(-C'_{P_{static}}\right) U_{P_1} \right)^2 + \left(\left(1 + C'_{P_{static}}\right) U_{\bar{p}} \right)^2 + \left((\bar{p} - p_1) U_{C'_{P_{static}}} \right)^2 \right]^{\frac{1}{2}} \qquad \text{(B.19)}$$

The total velocity can then be calculated as follows,

$$V^2 = \frac{2\gamma RT}{\gamma - 1} \left[\left(\frac{P_o}{p} \right)^{\frac{\gamma-1}{\gamma}} - 1 \right] \qquad \text{(B.20)}$$

and the uncertainty equation for V^2 is

$$U_{V^2} = V^2 \left[\left(\frac{U_T}{T} \right)^2 + \left(\frac{2RT}{V^2 \left(\frac{P_o}{p}\right)} U_{P_o} \right)^2 + \left(\frac{2RT}{V^2 \left(\frac{P_o}{p}\right)^{\frac{1-2\gamma}{\gamma}}} U_p \right)^2 \right]^{\frac{1}{2}} \qquad \text{(B.21)}$$

Finding the magnitude of the velocity vector from the squared value leads to

$$U_V = \frac{U_{V^2}}{2V} \qquad \text{(B.22)}$$

Next, the axial, radial and tangential components of velocity in the probe coordinate system are computed as

$$V_{x_1} = V \cos\gamma \, \cos\alpha \qquad \text{(B.23)}$$

$$V_{r_1} = V \sin\gamma \qquad \text{(B.24)}$$

$$V_{\theta_1} = V \cos\gamma \, \sin\alpha \qquad \text{(B.25)}$$

The uncertainty equations for these components are then

$$U_{V_{x_1}} = \left[\left(U_V \cos\gamma\cos\alpha\right)^2 + \left(-U_\gamma V \sin\gamma\cos\alpha\right)^2 + \left(-U_\gamma V \cos\gamma\sin\alpha\right)^2\right]^{\frac{1}{2}} \quad (B.26)$$

$$U_{V_\eta} = \left[\left(U_V \sin\gamma\right)^2 + \left(U_\gamma V \cos\gamma\right)^2\right]^{\frac{1}{2}} \quad (B.27)$$

$$U_{V_{\theta_1}} = \left[\left(U_V \cos\gamma\sin\alpha\right)^2 + \left(-U_\gamma V \sin\gamma\sin\alpha\right)^2 + \left(-U_\alpha V \cos\gamma\cos\alpha\right)^2\right]^{\frac{1}{2}} \quad (B.28)$$

The final step in the five hole probe data analysis is to convert the velocities from the five hole probe coordinate system to the turbine coordinate system. This is done as follows,

$$V_x = \left[V_{x_1} \cos a - V_{\theta_1} \sin a\right]\cos\delta - V_{r_1} \sin\delta \quad (B.29)$$

$$V_r = \left[V_{x_1} \cos a - V_{\theta_1} \sin a\right]\sin\delta - V_{r_1} \cos\delta \quad (B.30)$$

$$V_\theta = V_{\theta_1} \cos a - V_{x_1} \sin\delta \quad (B.31)$$

where a and δ are the yaw and pitch angle offset, respectively, of the five hole probe relative to the turbine coordinate system. The uncertainty equations for these components are then calculated as

$$U_{V_x} = \left[\left(U_{V_{x_1}} \cos a \cos \delta \right)^2 + \left(\left(-V_{x_1} \sin a \cos \delta - V_{\theta_1} \cos a \cos \delta \right) U_a \right)^2 + \right.$$

$$\left(\left(-V_{x_1} \cos a \sin \delta + V_{\theta_1} \cos a \sin \delta - V_{r_1} \cos \delta \right) U_\delta \right)^2 +$$

$$\left. \left(-\sin a \cos \delta \, U_{V_{\theta_1}} \right)^2 + \left(-\sin \delta \, U_{V_{r_1}} \right)^2 \right]$$

$$(B.32)$$

$$U_{V_r} = \left[\left(U_{V_{x_1}} \cos a \sin \delta \right)^2 + \left(\left(-V_{x_1} \sin a \sin \delta - V_{\theta_1} \cos a \sin \delta \right) U_a \right)^2 + \right.$$

$$\left(\left(V_{x_1} \cos a \cos \delta - V_{\theta_1} \cos a \cos \delta - V_{r_1} \sin \delta \right) U_\delta \right)^2 +$$

$$\left. \left(-\sin a \sin \delta \, U_{V_{\theta_1}} \right)^2 + \left(\cos \delta \, U_{V_{r_1}} \right)^2 \right]^{\frac{1}{2}}$$

$$(B.33)$$

$$U_{V_\theta} = \left[\left(U_{V_{x_1}} \sin \delta \right)^2 + \left(-U_a V_{\theta_1} \sin a \right)^2 + \left(U_\delta V_{x_1} \cos \delta \right)^2 + \left(U_{V_{\theta_1}} \cos a \right)^2 \right]^{\frac{1}{2}}$$

$$(B.34)$$

Using equations (B.12), (B.13), (B.18), (B.19), (B.22), (B.32), (B.33). and (B.34),
the uncertainties for the properties measured by the five hole probe are calculated
to be

$$U_\alpha = 0.5 \text{ degrees}$$

$$U_\gamma = 0.5 \text{ degrees}$$

$$U_{P_o} = 30 \text{ Pa}$$

$$U_p = 33 \text{ Pa}$$

$$U_V = 1 \text{ m/s}$$

$$U_{V_x} = 0.78 \text{ m/s}$$

$$U_{V_\theta} = 0.45 \text{ m/s}$$

$$U_{V_r} = 0.78 \text{ m/s}$$

Using typical values downstream of the nozzle, the percentage uncertainty for the
velocities are:

$$\frac{U_v}{V} = 0.6 \%$$

$$\frac{U_{v_x}}{V_x} = 2.5 \%$$

$$\frac{U_{v_\theta}}{V_\theta} = 0.5 \%$$

$$\frac{U_{v_r}}{V_r} = 22 \%$$

APPENDIX C

HOT WIRE UNCERTAINTY ANALYSIS

The accuracy of hot wire measurements can easily be quantified and are limited only by the accuracy of the calibration, the anemometer and voltmeter error and by ambient temperature drift. Each of these factors are discussed below.

C.1 Probe Calibration

The single sensor hot wire was calibrated in a low turbulence ($< 1.0 \%$) calibration jet. The sensor was placed perpendicular to the flow. The probe was calibrated over a range from 0 to $0.6U_m$. A pitot-static probe connected to a manometer was used to measure the calibration jet velocity. The air velocity measured by the pitot-static probe is given by

$$V = \left(\frac{2RT\rho_{H_2O}gh}{p} \right)^{\frac{1}{2}} \qquad (C.1)$$

where h is the manometer reading in inches of water. The manometer is used to measure the difference between the static and total pressures for the pitot-static probe. The error in reading the manometer is

$$U_{h_1} = 0.025 \text{ inches } H_2O \qquad (C.2)$$

The uncertainty for the thermometer and barometer that are given by the manufacturer are respectively.

$$U_{T_1} = 0.1 \text{ degrees } K \qquad (C.3)$$

$$U_{P_1} = 0.05 \text{ inches Hg} \qquad\qquad (C.4)$$

The significant source of error results from the pitot-static tube installation. According to Holman (1994) and Bradshaw (1970), the major source of error in a low turbulence flow away from solid surfaces is due to probe misalignment. The error due to the pitot-static installation is then

$$U_{h_2} = 0.01h = 0.02 \text{ inches } H_2O \qquad\qquad (C.5)$$

since h=2.0 inches of water is the h corresponding to the maximum velocity measured by the hot wire.

The uncertainties in each of the measured variables is

$$U_h = \left(U_{h_1}^2 + U_{h_2}^2\right)^{\frac{1}{2}} \qquad\qquad (C.6)$$

$$U_T = \left(U_{T_1}^2 + U_{T_2}^2\right)^{\frac{1}{2}} \qquad\qquad (C.7)$$

$$U_P = \left(U_{P_1}^2 + U_{P_2}^2\right)^{\frac{1}{2}} \qquad\qquad (C.8)$$

and the uncertainty in the calibration velocity measured by the pitot-static probe is

$$\frac{U_V}{V} = \left[\frac{1}{4}\left(\frac{U_T}{T}\right)^2 + \frac{1}{4}\left(\frac{U_h}{h}\right)^2 + \frac{1}{4}\left(\frac{U_P}{P}\right)^2\right]^{\frac{1}{2}} \qquad\qquad (C.9)$$

Substituting the nominal values for T, h and P and equations (C.8), (C.9), and (C.10) into (C.11) gives

$$\frac{U_v}{V} = 0.8 \%$$ (C.10)

C.2 Measurement Errors

The velocity measured by the hot wire sensor is obtained from King's law which is

$$E^2 = A + BV^{0.45}$$ (C.11)

where E is the anemometer output voltage taken across the Wheatstone bridge in the anemometer, V is the fluid velocity and A and B are the calibration constants. The uncertainty in the measured velocity is thus

$$U_v = \left[\left(\frac{\partial V}{\partial E} U_E\right)^2 + \left(\frac{\partial V}{\partial A} U_A\right)^2 + \left(\frac{\partial V}{\partial B} U_B\right)^2\right]^{\frac{1}{2}}$$ (C.12)

To find U_v, the uncertainties in E, A and B need to be found first. The error stated by the manufacturer for the anemometer bridge output voltage and the voltmeter output voltage are

$$U_{E_1} = 0.0002V$$ (C.13)

$$U_{E_2} = 0.002V$$ (C.14)

and the error due to reading the voltmeter is

$$U_{E_3} = 0.0005V \qquad (C.15)$$

Another source of error that can change the anemometer output voltage is ambient temperature drift. A change in ambient temperature causes a change in the heat transfer rate of the sensors. This results in a corresponding change in the measured output voltages from the anemometer. A correction scheme by Kristensen (1973) is used to correct the variation in anemometer output voltage due to temperature. Thus this error is neglected. The total uncertainty in E is then found from

$$U_E = \left(U_{E_1}^2 + U_{E_2}^2 + U_{E_3}^2\right)^{\frac{1}{2}} \qquad (C.16)$$

The calibration constants A and B are obtained by fitting a straight line in the form

$$\ln A = A \ln V + B \qquad (C.17)$$

through the calibration data. The uncertainty in A and B are then obtained from the equations

$$U_A = \left[\left(\frac{\partial A}{\partial E} U_E\right)^2 + \left(\frac{\partial A}{\partial V} U_V\right)^2\right]^{\frac{1}{2}} \qquad (C.18)$$

$$U_B = \left[\left(\frac{\partial B}{\partial E} U_E\right)^2 + \left(\frac{\partial B}{\partial V} U_V\right)^2\right]^{\frac{1}{2}} \qquad (C.19)$$

$(\partial A / \partial B$ and $\partial B / \partial A$ are assumed to be zero.) Thus, substituting the uncertainties in A, B and E into equation (C.12) along with the nominal values for A, B and E yields

$$\frac{U_v}{V} = 1.9 \% \tag{C.20}$$

which is the total uncertainty in the measured velocity. Yavuzkurt (1984) states that the mean and rms components of velocity have the same percent error, thus

$$\frac{U_{Tu}}{Tu} = 1.9 \% \tag{C.21}$$

which is the total uncertainty in the measured turbulence intensity.

APPENDIX D

LDV ERRORS

LDV measurements are subject to numerous errors, most of which can be qualified. The discussion here, which is based on the error analysis of Patrick (1987) uses the ASME measurement uncertainty analysis described in Appendix A to calculate the uncertainty. The errors are separated into both precision and bias errors. Bias errors include errors from laser beam geometry, counter processor errors and seeding bias errors. The laser beam geometrical errors consist of finite probe volume bias, beam location bias, beam orientation bias, fringe spacing uncertainty bias, negative velocity beam bias, angle bias and frequency broadening bias. The processor bias errors are made up of errors due to comparison accuracy, clock synchronization, quantizing, threshold limit, electronic noise and pedestal filter removal. Finally, the seeding bias errors include errors resulting from the flow distortion, particle lag, statistical or velocity bias and Bragg bias. Most of the bias errors are very small compared to the precision errors (discussed below), and thus are neglected. The bias errors which can be on the order of magnitude of the precision errors are discussed in detail below.

Statistical or velocity biasing was first mentioned by McLaughlin and Tiederman (1972). It occurs as a result of two reasons. The first is that the velocity magnitude varies with time. The second is that in a uniformly seeded flow, more particles pass through the probe volume per unit time during periods when the velocity is faster than the mean velocity than when the velocity is slower than the mean velocity. Thus a high data rate causes the measured values to be biased toward a higher value than the true mean. In the nozzle, where the turbulence intensity was less than 5 %, the error due to statistical bias is less than 0.5% based

on the analysis of Strazisar and Powell (1980). In the rotor, based on the same analysis, this error is about 1% outside the rotor wake and 5% inside the rotor wake (where the highest turbulence intensities occur). But in the rotor the need for statistical biasing corrections is questionable. According to Hathaway (1993) and Bell et al. (1993), measurements taken using conditional sampling techniques (such as with an optical shaft encoder) should not need this correction, since the velocity data is grouped into individual time windows and averaged for each window, and just because there are more measurements at higher velocities means there are more measurements at that particular window, but the average velocity is unbiased. Based on this, the velocity bias error is neglected.

Angle bias occurs when the flow is not parallel to the plane containing the laser beams. The factor controlling the angle bias is the ratio N/N_{fr}, where N is the minimum number of cycles required by the signal processor and N_{fr} is the number of measurable fringes. The angle bias can be minimized by reducing the N/N_{fr} ratio. Frequency shifting was used to minimize the angle bias, and thus this error is negligible also.

The precision errors in LDV measurement are data processing errors which result from averaging a finite number of data samples per data point. In LDV measurements, the velocity being measured does not remain constant during the sampling period but fluctuates due to turbulence. Thus the precision error is

$$S = \sqrt{\frac{\sum\limits_{i=1}^{N}\left(V_i - \overline{V}\right)^2}{N-1}} = v' \qquad (C.1)$$

where

$$\overline{V} = \frac{1}{N}\sum\limits_{i=1}^{N} V_i \qquad (C.2)$$

where V_i is the velocity of the i'th sample and $\overline{V}$ is the sample mean velocity. The precision error calculated by equation (C.1) is an estimate of the rms turbulence level. For an infinite number of samples, S becomes an exact measurement of the turbulence level. For a finite number of samples, both the rms turbulence level, v', and the mean sample velocity $\overline{V}$, will deviate from the true turbulence level and mean velocity of the flow field by precision errors $S_{v'}$ and $S_{\overline{V}}$, respectively.

Patterson (1982) states that the mean square turbulence intensity has a Chi-square distribution. Thus for a large sample size (N>50) the precision error of the turbulence intensity measurement can be found from

$$\frac{S_{v'}}{v'} = \frac{1}{\sqrt{2N}} \qquad (C.3)$$

Relative to the mean velocity measurements, the sampling distribution of $\overline{V}$ is normal about the population mean $\overline{V}_p$ (true mean) as a mean with a standard deviation of $v'_p/\sqrt{N}$. Thus the precision error in the mean velocity measurement can be estimated as

$$\frac{S_{\overline{V}}}{\overline{V}_p} = \frac{1}{\sqrt{N}}\left(\frac{v'_p}{V_p}\right) \qquad (C.4)$$

which is a function of the true turbulence intensity, $\left(v'_p/V_p\right)$. The quantity, $\left(v'_p/V_p\right)$, is unknown but can be approximated by the measured ratio of the turbulence to the mean velocity, $\left(v'/\overline{V}\right)$.

For the LDV measurements in the rotor, 120,000 axial and tangential coincident samples were taken at each measurement position for the entire rotor

revolution. Since the data were phase-locked averaged to obtain an "average" rotor blade passage with 50 measurement windows, there were on average 2400 samples per bin. Thus outside of the rotor wake, the precision errors in the mean velocity and turbulence intensity are less than 0.2% and 1.4% respectively. In the rotor wake, where the samples per bin are much smaller and the turbulence intensity is much higher, the precision errors in the mean velocity and turbulence intensity are 2% and 7%, respectively. For the LDV measurements in the nozzle, where the sample size was 200, the precision errors in the mean velocity and turbulence intensity are 0.1% and 5.0%, respectively. Thus using equation (A.6), the total uncertainty for a 95% confidence level is as follows,

$$\text{Nozzle flow field:} \quad S_{\bar{V}}/\bar{V} = 0.2\ \%$$

$$S_{v'}/v' = 10\ \%$$

Rotor flow field:

$$\text{Outside of rotor wakes:} \quad S_{\bar{V}}/\bar{V} = 0.4\ \%$$

$$S_{v'}/v' = 2.8\ \%$$

$$\text{Inside rotor wakes:} \quad S_{\bar{V}}/\bar{V} = 4.0\ \%$$

$$S_{v'}/v' = 14.8\ \%$$

REFERENCES

Bammert, K., and Sandstede, H., 1980, "Measurements of the Boundary Layer Development along a Turbine Blade with Rough Surfaces," ASME Paper 80-GT-40.

Belik, L., 1975, "Secondary Losses in Turbine Blade Cascade with Low Aspect Ratio and Large Deflection," Proc. 6th Conf. on Steam Turbines of Large Power Output, Plzen, Czechoslovakia

Bell, W. A., Lepicovsky, J., and Garnett, D., 1993, "The Laser Velocimeter, Conditional Sampling, and the Wavelet Transform," Fluid Measurement and Instrumentation, ASME

Binder, A., 1985, "Turbulence Production Due to Secondary Vortex Cutting in a Turbine Rotor," ASME Journal of Engineering for Gas Turbines and Power, Oct. Vol. 107, pp. 1039-1046

Binder, A., Forster, W., Kruse, H., and Rogge, H., 1985, "An Experimental Investigation Into the Effect of Wakes on the Unsteady Turbine Rotor Flow," ASME Journal of Engineering for Gas Turbines and Power, April, Vol. 107, pp. 458-466.

Binder, A., Forster, W., Mach, K., and Rogge, H., 1987, "Unsteady Flow Interaction Caused by Stator Secondary Vortices in a Turbine Rotor," ASME Journal of Turbomachinery, April, Vol. 109, pp. 251-257.

Binder, A. and Romey, R., 1982, "Secondary Flow Effects and Mixing of the Wake Behind a Turbine Stator", ASME Paper No. 82-GT-46, 1982.

Boletis, E. and Sieverding, C.H., 1991, "Experimental Study of the Three-Dimensional Flow Field in a Turbine Stator Preceded by a Full Stage," ASME Journal of Turbomachinery, Vol. 113, No. 1, pp. 1-9.

Came, P. M., and Marsh, H., 1974, "Secondary Flow in Cascades: Two Simple Derivations for the Components of Vorticity," Journal of Mechanical Engineering Sciences, Vol. 16, pp. 391-401.

Coleman, H. W. and Steele, W. G., 1989, Experimentation and Uncertainty Analysis for Engineers.

Dring, R. P., Joslyn, H. D. and Blair, M. F., 1987, "The Effects of Inlet Turbulence and Rotor/Stator Interactions on the Aerodynamics and Heat Transfer of a Large-Scale Rotating Turbine Model", NASA-CR-179469, Vol. 4.

Dring, R. P., Joslyn, H.D., Hardin, L.W. and Wagner, J.H., 1982., "Turbine Rotor-Stator Interaction", ASME Journal of Engineering for Power, Vol. 104, Oct. , pp. 729-742.

Dunham, J., 1970,"A Review of Cascade Data on Secondary Losses in Turbines," Journal of Mechanical Engineering Sciences, Vol. 12, No.1, p.48.

Gallus, H. E., 1987, "Unsteady Aerodynamic Measurements on Rotors," in AGARD Manual on Aeroelasticity in Axial-Flow Turbomachines, Volume 1, Unsteady Turbomachinery Aerodynamics, pp. 11-1 to 11-18.

Goldman, L. J. and Seasholtz, R. G., 1982, "Laser Anemometer Measurements in an Annular Cascade of Core Turbine Vanes and Comparison with Theory", NASA TP 2018.

Goldman, L. J. and Seasholtz, R. G., 1992, " Laser Anemometer Measurements and Computations in an Annular Cascade of High Turning Core Turbine Vanes," NASA TP 3252.

Graziani, R. A., Blair, M. F., Taylor, J. R., and Mayle, R. E., 1980, "An Experimental Study of Endwall and Airfoil Surface Heat Transfer in a Large Scale Turbine Blade Cascade," ASME Journal of Engineering for Power, Vol. 102, April, pp. 257-267.

Gregory-Smith, D. G. and Graves, C. P., 1983, "Secondary Flows and Losses in a Turbine Cascade," in Viscous Effects in Turbomachines, AGARD CP-351, Paper 17.

Gregory-Smith, D. G., Graves, C. P., Walsh, J. A., 1988, "Growth of Secondary Losses and Vorticity in an Axial Turbine Cascade", ASME Journal of Turbomachinery, Vol. 110, January, pp. 1-8.

Greitzer, E. M., 1985, "An Introduction to Unsteady Flow in Turbomachines," in

Thermodynamics and Fluid Mechanics of Turbomachinery, Vol. II, pp. 967-1025.

Hah, C. and Lakshminarayana, B., 1982, "Measurement and Prediction of Mean Velocity and Turbulent Structure in the Near Wake of an Airfoil," Journal of Fluid Mechanics, vol. 115, pp. 251-282.

Hathaway, M., 1986, "Unsteady Flows in a Single-Stage Transonic Axial-Flow Fan Stator Row," NASA TM-88929.

Hathaway, M. 1994, Private Communication.

Hawthorne, W.R., 1955, "Rotational Flow Through Cascades," Journal of Mechanics and Applied Mathematics, Vol. 3.

Hill, P. G., Schaub, U. W., and Senoo, Y., 1963 , "Turbulent Wakes in Pressure Gradients", ASME Journal of Applied Mechanics, December, pp. 518-524.

Ho, Y. H. and Lakshminarayana, B., 1994, "Computational Modelling of Three-Dimensional Flow Through a Turbine Rotor Cascade with Strong Secondary Flows," ASME-GT Paper (to be presented at 1994 Gas Turbine Conference).

Hobson, G and Lakshminarayana, B., 1990, "Computation of Turbine Flow Fields with Navier-Stokes Equations," AIAA Paper 90-2122.

Hodson, H. P., 1984, "Measurements of Wake-Generated Unsteadiness in the Rotor Passages of Axial Flow Turbines," 84-GT-189.

Hodson, H. P., 1985, "An Inviscid Blade-to-Blade Prediction of a Wake-Generated Unsteady Flow," ASME Journal for Gas Turbines and Power, April, Vol. 107, pp. 337-344.

Hodson, H. P. and Dominy, R. G., 1987, "The Off-Design Performance of a Low-Pressure Turbine Cascade," ASME Journal of Turbomachinery, Vol. 109, April, pp. 201-209.

Holman, J. P., 1984, Experimental Methods for Engineers, McGraw-Hill.

Horlock, J. H. and Lakshminarayana, B., 1973, "Secondary Flows: Theory, Experiment, and Application in Turbomachinery Aerodynamics," Annual Review of Fluid Mechanics, Vol. 5, pp. 247-280.

Hunter, I.H.,1982, "Endwall Boundary Layer Flows and Losses in an Axial Turbine Stage," Journal of Engineering for Power, Vol. 104, pp. 184-193, January .

Joslyn, D. and Dring, R., 1990. "Three-Dimensional Flow in an Axial Turbine," ASME Paper 90-GT-56.

Kacker, S.C. and Okapuu, U., 1982, "A Mean Line Prediction Method for Axial Flow Turbine Efficiency," Journal of Engineering for Power, Vol. 104, pp.111-119. January

Katsanis, T. and McNally, W., 1977, "Revised Fortran Program for Calculating

Velocities and Streamlines on the Hub-Shroud Midchannel Stream Surface of an Axial, Radial or Mixed Flow Turbomachine or Annular Duct, I-User's Manual", NASA TN D-8430.

Klein, A., 1966,"Investigation of the Entry Boundary Layer on the Secondary Flows in the Blading of Axial Turbines," BHRA T 1004.

Korakianitis, T., 1992, "On the Prediction of Unsteady Forces on Gas Turbine Blades: Part 1-Description of the Approach," ASME Journal of Turbomachinery, Jan., Vol. 114, pp. 114-122.

Lakshminarayana, B., Camci, C., Halliwell, I. and Zaccaria, M., 1992, "Investigation of Three Dimensional Flow Field in a Turbine Including Rotor/Stator Interaction", Part 1: Design, Development and Performance of Turbine Facility, AIAA paper 92-3325.

Lakshminarayana, B. and Davino, R., 1980, "Mean Velocity and Decay Characteristics of the Guidevane and Stator Blade Wake of an Axial Flow Compressor", ASME Journal of Engineering for Power, Vol. 102, January, pp. 50-60.

Lakshminarayana, B. and Reynolds, B, 1979, "Turbulence Characteristics in the Near Wake of a Compressor Rotor Blade," AIAA Journal, Vol. 18, No. 11,November, pp. 1354-1362.

Langston, L. S., 1980, "Crossflows in a Turbine Cascade Passage," ASME Journal

of Engineering for Power, Vol. 102, No. 4, Oct., pp. 866-874.

Langston, L. S., Nice, M. L., and Hooper, R. M., 1977, "Three-Dimensional Flow Within a Turbine Blade Passage," ASME Transations, Series A: Journal for Engineering for Power, Vol. 99, No. 1, Jan., pp. 21-28.

Matsuuchi, K. and Adachi, T., 1983, "Measurement of the Three-Dimensional Unsteady Flow Inside a Rotor Blade Passage of an Axial Flow Fan, presented at the 1983 Tokyo International Gas Turbine Congress, JSME Paper 83-TOKYO-IGTC-67.

McFarland, E. R., 1981, "Solution of Plane Cascade Flow Using Improved Surface Singularity Methods, ASME Paper 81-GT-169.

McLaughlin, D. K., Tiederman, W. G., 1973, "Biasing Correction for Individual Realization of Laser Anemometer Measurements in Turbulent Flow," Physics of Fluids, December, pp. 2082-2088.

Mee, D. J., Baines, N.C., Oldfield, M.L.G. and Dickens, T.E., 1990, "An Examination of the Contribution to Loss on a Transonic Turbine Blade in Cascade", ASME Paper 90-GT-264.

Moore, J. and Adhye, R., 1985, "Secondary Flows and Losses Downstream of a Turbine Cascade," ASME Journal of Engineering for Gas Turbines and Power, Vol. 109, pp. 961-969.

Niehuis, R, Lucking, P. and Stubert, B., 1990, "Experimental and Numerical Study on Basic Phenomena of Secondary Flows in Turbines," Secondary Flows in Turbomachines, AGARD-CP-469, pp. 5-1 to 5-17.

Patterson, R. W., 1982, "Turbofan Forced Mixer-Nozzle Internal Flowfied, I - A Benchmark Experimental Study" NASA CR-3492. April.

Patrick, W. P.,1987, "Flowfield Measurements in a Separated and Reattached Flat Plate Turbulent Boundary Layer," NASA Contractor Report 4052, March.

Prato, J., 1992, Private Communication

Rao, K. V., Delaney, R. A., and Dunn, M. G., 1992, "Vane-Blade Interaction in a Transonic Turbine, Part I - Aerodynamics," AIAA paper 92-3323.

Raj, R. and Lakshminarayana, B., 1973, "Characteristics of the Wake Behind a Cascade of Airfoils", J. Fluid Mech., Vol. 61, part 4, pp. 707-730.

Raj, R. and Lakshminarayana, B., 1976, "Three-Dimensional Characteristics of Turbulent Wakes Behind Rotors of Axial Flow Turbomachinery," ASME Engineering for Power, Vol, 98, No. 2, April, pp. 218-228.

Ravindranath, A., 1979, "Three-Dimensional Mean and Turbulence Characteristics of the Near Wake of a Compressor Rotor Blade," M. S. Thesis, Department of Aerospace Engineering, The Pennsylvania State University.

Ravindranath, A. and Lakshminarayana, B., 1980 , "Mean Velocity and Decay Characteristics of the Near and Far-Wake of a Compressor Rotor Blade of Moderate Loading", ASME Journal of Engineering for Power, Vol. 102, July, pp. 535-548.

Reynolds, B. D., 1978, "Characteristics of Lightly Loaded Fan Rotor Blade Wakes," M.S. Thesis, Department of Aerospace Engineering, The Pennsylvania State University.

Reynolds, B., Lakshminarayana, B. and Ravindranath, A., 1979, "Characteristics of the Near Wake of a Compressor of a Fan Rotor Blade," AIAA Journal, Vol. 17, No. 9, September, pp. 959-967.

Rodi, W., 1982, "Examples of Turbulence Models for Incompressible Flows," AIAA Journal, July, Vol. 20, No. 7, pp. 872-879.

Schlichting, H., 1979, Boundary Layer Theory, McGraw-Hill Publishers.

Sharma, O. P., and Butler, T. L., 1987, "Predictions of Endwall Losses and Secondary Flows in Axial Flow Turbine Cascades," ASME Journal of Turbomachinery, Vol. 109, April, pp. 229-236.

Sharma, O. P., Butler, T. L., Joslyn, H. D., and Dring, R. P.,1985, "Three-Dimensional Unsteady Flow in an Axial Flow Turbine," AIAA Journal of Propulsion, Jan.-Feb., pp. 29-38.

Sharma, O. P., Pickett, G. F., and Ni, R. H., 1992, "Assessment of Unsteady Flows in Turbines," ASME Journal of Turbomachinery, January, Vol. 114, pp. 79-90.

Sieverding C. H., 1985a, "Axial Turbine Performance Prediction Methods," Thermodynamics and Fluid Mechanics of Turbomachinery, Vol. II, pp.737-784.

Sieverding, C. H., 1985b, "Recent Progress in the Understanding of Basic Aspects of Secondary Flows in Turbine Blade Passages", Journal of Engineering for Gas Turbines and Power, Vol. 107, April, pp. 248 - 257.

Sieverding, C.H., Van Hove, W. and Boletis, E. 1984, "Experimental Study of the Three-Dimensional Flow Field in an Annular Turbine Nozzle Guidevane",ASME Journal of Engineering for Gas Turbines and Power, April, Vol. 106, pp. 437-444.

Sitaram, N. and Govardhan, M., 1986, "Effect of Incidence Angle on Wake Characteristics of High Deflection Turbine Rotor Linear Cascade", Paper presented at 9th Australasian Fluid Mechanics Conference, Auckland, Dec..

Sitaram, N., Lakshminarayana, B., and Ravindranath, A., 1981, "Conventional Probes for the Relative Flow Measurement in a Turbomachinery Rotor Blade Passage," ASME Journal of Engineering for Power, Vol. 103, April, pp. 406-414.

Sjolander, S. A., 1975, "The End Wall Boundary Layer in an Annular Cascade of Turbine nozzle Guide Vanes, " Carleton University, TRME/A 75-4, Dec.

Smith, L. H. Jr., 1966, "Secondary FLow in Axial-Flow Turbomachinery,"

Transactions of the ASME, 77, No. 7, Oct., 1065-1076.

Spence, D. A., 1953, Aero. Research Council C. P., no. 125.

Squire, H. and Winter, K.G., 1951, "The Secondary Flow in a Cascade of Airfoils in Non-Uniform Stream," J. Aero. Sci., Vol. 18, p. 271.

Strazisar, A. J., 1985, "Application of Laser Anemometry to Turbomachinery Flowfield Measurements," VKI LS 1985-03.

Strazisar, A. J., and Powell, J. A., 1981, "Laser Anemometer Measurements in a Transonic Axial Flow Compressor Rotor," ASME Journal of Engineering for Power, Vol. 103, No. 2, April, pp. 430-437.

Suder, K., L., Hathaway, M., D., Okiishi, T., H., Strazisar, A., J., and Adamczyk, J.J., 1987, "Measurements of the Unsteady Flow Field Within the Stator Row of a Transonic Axial Flow Fan I - Measurement and Analysis Technique", 87-GT-226.

Treaster, A. L., Yocum, A. M.,1979, "The Calibration and Application of Five-Hole Probes," ISA Transations, Vol. 18, No. 3, pp. 34.

Tremblay, B., Sjolander, S. A. and Moustapha, S. H., 1990, "Off-Design Performance of a Linear Cascade of Turbine Blades," ASME paper 90-GT-314.

TSI, 1987, "Manual for Six Jet Atomizer."

Wiedner, B., 1988, "Experimental Investigation of Velocity Biasing in Laser Doppler Anemometry," .M. S. Thesis.

Yamamoto, A. and Yanagi, R., 1986, "Production and Development of Secondary Flows and Losses Within a Three Dimensional Turbine Stator Cascade", International Journal of Turbo and Jet Engines, pp. 79-90.

Yavuzkurt, S., 1984, "A Guide to Uncertainty Analysis of Hot-Wire Data," Journal of Fluids Engineering, June, Vol. 106, 181-186.

Zaccaria, M. and Lakshminarayana, B., 1994, "Investigation of Three Dimensional Flow Field at the Exit of Turbine Nozzle," to be published in the AIAA Journal of Propulsion and Power.

Zierke, W. C., Straka, W. A.,and Taylor, P.D., 1993, "The High Reynolds Number FLow Through an Axial-Flow Pump," The Pennsylvania State University Applied Research Laboratory Technical Report No. TR 93-12

REPORT DOCUMENTATION PAGE

1. AGENCY USE ONLY (Leave blank)	2. REPORT DATE	3. REPORT TYPE AND DATES COVERED
	May 1997	Final Contractor Report

4. TITLE AND SUBTITLE

An Experimental Investigation of Steady and Unsteady Flow Field in an Axial Flow Turbine

6. AUTHOR(S)

M. Zaccaria and B. Lakshminarayana

5. FUNDING NUMBERS

WU–523–26–33
G–NAG3–555

7. PERFORMING ORGANIZATION NAME(S) AND ADDRESS(ES)

Pennsylvania State University
Department of Aerospace Engineering
University Park, Pennsylvania 16802

8. PERFORMING ORGANIZATION REPORT NUMBER

E–10771

9. SPONSORING/MONITORING AGENCY NAME(S) AND ADDRESS(ES)

National Aeronautics and Space Administration
Lewis Research Center
Cleveland, Ohio 44135–3191

10. SPONSORING/MONITORING AGENCY REPORT NUMBER

NASA CR–4778

11. SUPPLEMENTARY NOTES

Project Manager, Robert J. Boyle, Turbomachinery and Propulsion Systems Division, NASA Lewis Research Center, organization code 5820, (216) 433–5889.

12a. DISTRIBUTION/AVAILABILITY STATEMENT

Unclassified - Unlimited
Subject Category 34

This publication is available from the NASA Center for AeroSpace Information, (301) 621–0390.

12b. DISTRIBUTION CODE

13. ABSTRACT (Maximum 200 words)

Measurements were made in a large scale single stage turbine facility. Within the nozzle passage measurements were made using a five hole probe, a two-component laser doppler velocimeter (LDV), and a single sensor hot wire probe. These measurements showed weak secondary flows at midchord, and two secondary flow loss cores at the nozzle exit. The casing vortex loss core was the larger of the two. At the exit radial inward flow was found over the entire passage, and was more pronounced in the wake. Nozzle wake decay was found to be more rapid than for an isolated vane row due to the rotor's presence. The midspan rotor flow field was measured using a two-component LDV. Measurements were made from upstream of the rotor to a chord behind the rotor. The distortion of the nozzle wake as it passed through the rotor blade row was determined. The unsteadiness in the rotor flow field was determined. The decay of the rotor wake was also characterized.

14. SUBJECT TERMS	15. NUMBER OF PAGES
Turbine aerodynamics	385
	16. PRICE CODE A17

17. SECURITY CLASSIFICATION OF REPORT	18. SECURITY CLASSIFICATION OF THIS PAGE	19. SECURITY CLASSIFICATION OF ABSTRACT	20. LIMITATION OF ABSTRACT
Unclassified	Unclassified	Unclassified	